NASA TECHNICAL TRANSLATION

NASA TT F-656

NASA TT F-656

ELEMENTARY PARTICLES AND COSMIC RAYS

Collection of Articles, No. 2

Edited by A. M. Gal'per and A. K. Ponosov

Atom Press, Moscow, 1969

NATIONAL AERONAUTICS AND SPACE ADMINISTRATION • WASHINGTON, D. C. • FEBRUARY 1972

ELEMENTARY PARTICLES AND COSMIC RAYS

Collection of Articles, No 2

Edited by A. M. Gal'per and A. K. Ponosov

Translation of "Elementarnyye Chastitsy i Kosmicheskiye Luchi - Sbornik Statey, Vypusk 2." Atom Press, Moscow, 1969

NATIONAL AERONAUTICS AND SPACE ADMINISTRATION

For sale by the National Technical Information Service,
Springfield, Virginia 22151 $3.00

This collection presents papers on the physics of cosmic rays and elementary particles, written by the Department of Experimental Nuclear Physics of the Moscow Engineering Physics Institute. The greater part of the collection deals with descriptions of experimental work on cosmic rays and in the use of an accelerator. A number of the articles are devoted to theoretical questions and experiment methodology. As in preceding issues (Fizika elementarnykh chastits [Physics of Elementary Particles], Moscow, Atom Press, 1966; Elementarnyye chastitsy i kosmicheskiye luchi [Elementary Particles and Cosmic Rays], Moscow, Atom Press, 1967), a good deal of space is given to articles that are reviews, or semi-reviews, in nature. /2

The collection reviews questions concerned with the investigation of μ-mesons, electrons, photons, with the search for quarks and fireballs in cosmic rays, as well as with the study of the interactions of elementary particles in accelerators, topics of great interest that will undoubtedly prove useful to scientific workers, graduate students, and to students concerned with the physics of elementary particles and cosmic rays.

TABLE OF CONTENTS

Page

MEASUREMENT OF ELECTRON FLUXES AND GAMMA RAYS OF ENERGY GREATER THAN 100 MEV AT VARIOUS HEIGHTS IN THE ATMOSPHERE

V. A. Bezus, A. M. Gal'per, N. L. Grigorov, V. V. Dmitrenko, L. F. Kakinkin, V. G. Kirillov-Ugryumov, B. I. Luchkov, A. S. Melioranskiy, Yu. V. Ozerov, I. L. Rozental', I. A. Savenko, E. M. Shermanzon

ABSTRACT. An experiment conducted in 1967-1968, using balloons to measure the intensities and energy spectra of electrons and gamma rays of a direct vertical flow, and the electrons of a return (albedo) flow is described.

Study of the electron-photon components of cosmic rays at various heights /3* in the atmosphere has been in progress for many years [1-14]. The majority of recent investigations with balloons that have reached heights of from 30 to 40 km (residual pressure about 10 g/cm^2) were for purposes of determining flows of primary cosmic electrons and gamma rays. Naturally, the secondary electron-photon component generated by the cosmic rays in the upper layers of the atmosphere contributes to the flow investigated. The effect [15, 16] of the nuclear component was evaluated in order to separate the primary component. Moreover, it has been demonstrated [9, 12, 17] that electrons returned to the atmosphere by the magnetic field (the so-called double albedo electrons) make a definite contribution to the flow of electrons in the atmosphere. The intensity of this return depends on the condition of the earth's magnetosphere and differs in different geomagnetic latitudes. Bremsstrahlung from the double albedo electrons also causes an additional flow of gamma radiation at high altitudes [10].

Artificial earth satellites have been used recently to measure the flows of electrons and gamma rays beyond the limits of the atmosphere [18-20]. Specifically, the flights of Proton-1 and Proton-2 at a height of about 500 km recorded a definite flow of electrons of greater than 300 MeV [20]. The measurements made by the satellites make for a much better understanding of the process involved in the occurrence and change that takes place in the flows of electrons

*Numbers in the right margin indicate pagination in the foreign text.

and gamma rays recorded in the atmosphere. Despite the great number of papers in this field, far from all the details of how these flows of electrons and gamma rays of energies of the order of 100 MeV pass through the atmosphere are clear. The effect of the magnetosphere on recorded flows is far from fully studied because of the complexity of the processes taking place in the magnetosphere. Unclear is the contribution of the double albedo electrons in the flow recorded on the earth. The role of captured radiation in the formation and change of flows of electrons and gamma rays is unknown.

This article will describe an experiment conducted to measure the intensities and energy spectra of electrons and gamma rays of a direct vertical flow, and the electrons of a return (albedo) flow, conducted in 1967-1968, with high altitude balloons. The preliminary results were discussed in [21]. /4

1. The Instrument

Figure 1 is the block diagram of the recording instrument. The instrument comprises the following components, CC - the Cerenkov directional action threshold counter with an organic glass radiator (refractive index k = 1.5). Counter directivity is the result of blackening the upper surface of the radiator and setting the threshold for the electronic circuit such that only particles passing through the counter from top to bottom will be recorded. SC_1, SC_2, SC_3, and SC_4 are polystyrene scintillation counters. SCh is a multi-layer spark chamber with lead plates, electrodes the total thickness of which is 3.7 radiation

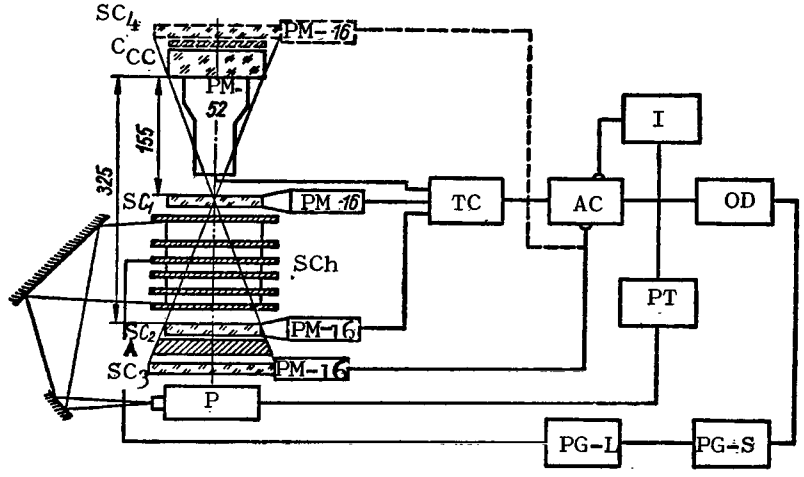

Figure 1. Block diagram of the instrument.

lengths (rl). A is a lead absorber 3 rl thick. P is a photographic monitor that photographs the spark chamber in two orthogonal projections with a system of mirrors.

The instrument operates in two modes: it records (1) electrons; and (2) gamma rays. The first mode utilizes counters CC, SC_1, SC_2, and SC_3 for recording. An electron causes counters CC and SC_1 to function, then, passing through the spark chamber, will create an electron-photon shower on the plates. /5 Electrons in the shower are recorded by counter SC_2 and are absorbed in A without striking counter SC_3. Events of the CC $SC_1SC_2\overline{SC}_3$ type (the bar over the counter symbol means that that counter is included in the anticoincidence circuit) are segregated by an electronic circuit consisting of TC, the triple coincidence circuit with a resolution time of some 50 nsec, and the anticoincidence circuit, AC. This segregation method precludes the recording of other particles passing through because their path, at a velocity exceeding the threshold velocity for the recording of a particle by the Cerenkov counter (β_t = 0.67), is so much longer than the total of the substance in the instrument (some 6.7 rl of lead) that they are "cut out" by counter SC_3. However, there will be nuclear interactions between cosmic particles (protons) in the SC and A, in addition to the electrons of the CC $SC_1SC_2\overline{SC}_3$ event, during which not a single charged product will strike SC_3, as well as μ-mesons of energies of 55 to 80 MeV remaining in A. The final selection of cases with electrons among the recorded CC $SC_1SC_2\overline{SC}_3$ event is made from the photographs of the spark chamber.

The gamma ray recording condition is taken care of by counters CC, SC_1, SC_2 and counter SC_4, which is installed together with the lead converter (1 rl of lead), C, above the Cerenkov counter. SC_4 is connected to the anticoincidence channel of the AC circuit along with SC_3. Events of the SC_4CC $SC_1\overline{SC}_2$ type, caused by gamma rays being converted into an electron-position pair in converter C, can be recorded.

Subsequent instrument operation takes place regardless of the recording condition. A pulse from the AC circuit triggers the output device, OD, the photographic monitor trigger circuit, PT, and the interlock circuit, I. A pulse from the output device with an amplitude of about 150 volts now causes the small and large pulse voltage generators, PG-S and PG-L [22, 23] to

function and generate the high-voltage supply pulse for the spark chamber. All electronic circuits, voltage converters, and supply pulse generators are based on cold-cathode elements, such as transistors, tunnel diodes, dynistors, and vacuum spark relays.

The effective recording area of the instrument is approximately 110 cm^2, the solid angle about 0.12 ster. The overall dimensions of the instrument are 60 x 30 x 30 cm, its weight is 35 kg, and the total power demand is 12 watts [23].

2. The Spark Chamber

The principal component of the instrument, the purpose of which is to make the final segregation of the events in need of investigation, is the spark chamber. The chamber is a rectangular box made of organic glass with internal volume of 12 x 12 x 12 = 1728 cm^3, containing six 6 mm thick plates. The upper and lower plates are made of Dural. Each of the four interior plates contains a 4 mm thick lead layer. The plates divide the chamber into five compartments. One (the upper) is 3 cm high, and four are 1.5 cm high. The upper compartment is used to measure the direction of the incoming electron, or electron-positron pair. The electron shower developing in the lead plates is recorded in the next four small compartments. All of the internal plates have outside taps to which Dural straps are secured, thus becoming external extensions of the electrodes, as it were. The external straps provide the necessary homogeneity for the electric field in the chamber's working expanse. The chamber is filled with exceptionally pure neon to a pressure of 1 atm. /6

The upper and lower electrodes are connected to the instrument's local "ground." The high-voltage pulses are supplied to the plate third from the top, that is, to the heart of the chamber. The gap between this plate and any of the grounded electrodes is 4.5 cm. Thus, high-voltage pulses are supplied at once to the two upper, and the three lower compartments and are distributed among them in accordance with their capacitances. Given this supply mode, the chamber functions as a spark chamber with a large interelectrode gap with its distinguishing feature the movement of the sparks following the particle tracks and a high shower efficiency value. The plates are connected to each other through 100 kohm resistors in order to discharge the charge remaining on the

electrodes in event of breakdown.

The pulse supplied to the spark chamber has an amplitude of some 25 kv, with an approximately 30 nsec leading edge and a duration of about 0.5 μsec. The electronic delay in delivery of the high-voltage pulse is approximately 0.5 μsec. The "life" of one filling of the chamber is 2 to 3 weeks. At the expiration the chamber must be refilled with fresh gas because the neon becomes contaminated by emissions from the organic glass and chamber efficiency and spark brilliancy diminish.

3. Instrument Calibration

The physical characteristics of the instrument were measured while it was functioning on cosmic μ-mesons and electrons with energies of 100 to 600 MeV (the synchrotron at the P. N. Lebedev Physics Institute of the Academy of Sciences of the USSR) and of 500 to 1500 MeV (the linear accelerator in the Physicotechnical Institute of the Academy of Sciences of the Ukrainian SSR).

Calibration of the telescope for the CC, SC_1, SC_2, SC_3, and SC_4 counters. Figure 2 shows the efficiency with which the instrument records electrons (η_e) /7 and gamma rays (η_γ) in terms of their energy. The efficiency with which electrons were recorded was measured directly in electron beams. As will be seen from the graph, η_e rises sharply at first from zero when $E \approx 100$ MeV to a maximum of $\eta_e = 0.3$ for $E \approx 400$ MeV, and then decreases smoothly to zero. The reduction in η_e when $E > 400$ MeV is the result of the increase in the probability of the penetration of the absorber (A) by the electron shower and of hitting the "anticoincidence" counter SC_3. The efficiency with which the instrument records gamma rays, η_γ, cannot be obtained directly because of the absence of beams of monoenergetic gamma rays of the needed energy, so is computed by using the data for electron beam calibration (see Appendix 1). η_γ rises smoothly from zero when $E \approx 100$ MeV to approximately 0.5 when $E \approx 1500$ MeV. What follows from the relationships in Figure 2 is that the instrument records electrons in the energy range between 100 and 1500 MeV and gamma rays with energy $E > 100$ MeV.

Figure 3 shows the efficiency of the recording of electrons with 435 MeV /8 of energy in terms of the angle of entry into the instrument. The electrons pass through the center of the radiator of the Cerenkov counter at various

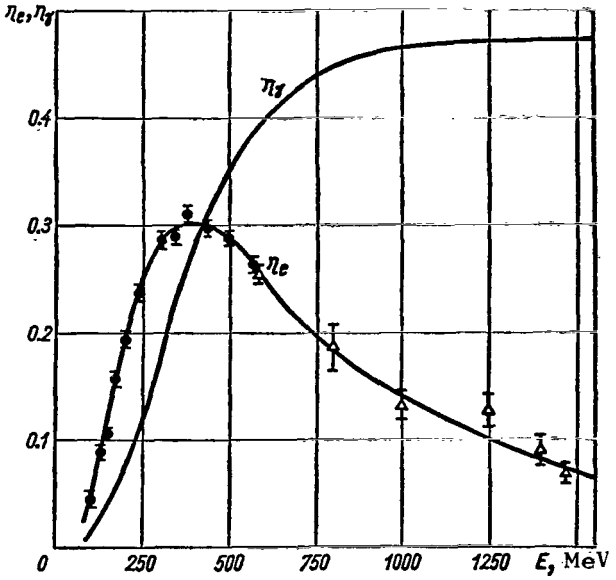

Figure 2. Recording of electrons (η_e) and gamma rays (η_γ) by the instrument in terms of energy.

● - electron synchrotron (P. N. Lebedev Physics Institute);

Δ - electron linear accelerator (Physicotechnical Institute).

angles, φ, to the axis of the instrument in one projection, and at a fixed angle, $\psi = 0$, in the other orthogonal projection. As will be seen from Figure 3, the effectiveness changes little in the range of angles φ from -10 to +10°, and drops off sharply when $|\varphi|$ is increased from 10 to 30°. The effectiveness with which the return flow of electrons is recorded ($\varphi = 180°$) is less than $2 \cdot 10^{-4}$. The angular relationship of the effectiveness of the recording of gamma rays will be practically the same because of the smallness of the angle of divergence of the electron-positron pair for given energies. The geometric factor for the instrument, computed from calibration measurements for electrons with an energy of 435 MeV, is equal to $G = 14.5 \pm 1.0$ cm^2-ster (see Appendix 2).

An important quantity, measured on cosmic μ-mesons, is the efficiency of the "anticoincidence" counter SC_4 when there are counting errors caused by contaminated particles possibly simulating gamma rays. Counter efficiency proved to be 0.9993 ± 0.0005.

Spark chamber calibration. Demonstrated in the course of recording electrons and μ-mesons in the spark chamber was that the sparks follow the tracks of particles in the upper, large compartment to the maximum angle between the field and the particle, 20°, fixed by the instrument aperture. The accuracy /9 with which the particle track angle is measured in the upper compartment is approximately 2°. The spark moves through vertically in the small compartments. A comparison made between the shower curves obtained for electrons with energies from 100 to 1500 MeV during the calibration with those computed, or obtained by other experimental methods, revealed that the spark chamber has close to 100%

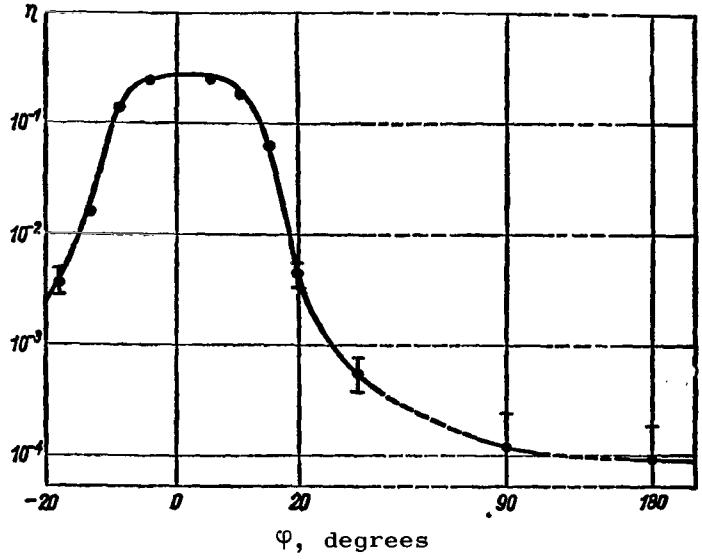

Figure 3. Instrument efficiency in terms of the angle of entry of electrons for E = 435 MeV.

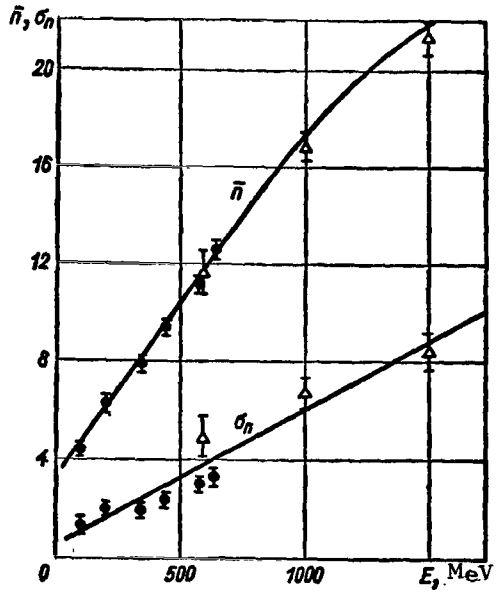

Figure 4. Average number of sparks, $\bar{n}$, root-mean-square scatter in the number of sparks, σ_n, in terms of electron energy.

● - electron synchrotron (P. N. Lebedev Physics Institute);

Δ - electron linear accelerator (Physicotechnical Institute)

efficiency for the simultaneous registration of many particles (so-called shower efficiency) [23, 24].

The total number of sparks n, in all five compartments, is the characteristic for the electron shower in a spark chamber. Figure 4 shows the change in the average number of sparks, $\bar{n}$, and in the root-mean-square scatter in the number of sparks, σ_n, with change in electron energy. $\bar{n}$ increases linearly with increase in energy between 100 and 1000 MeV. When E > 1000 MeV there is a slight deviation from the linear relationship, something that possibly is the result of the spark pileup and of errors in their /10 count in showers with a great many particles. The relative error in measuring the energy of the individual electron in terms of the number of sparks in a

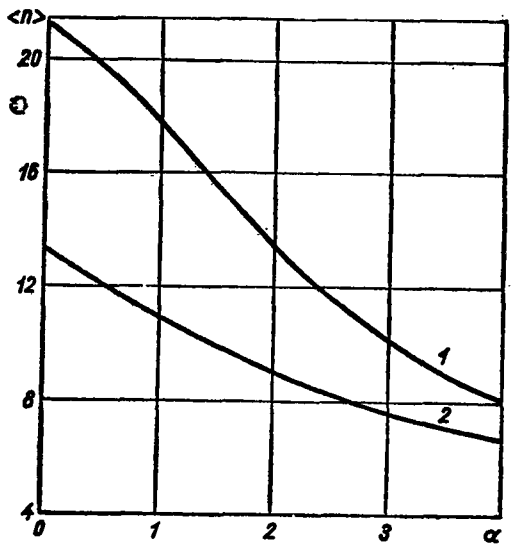

Figure 5. Average number of sparks in showers $< n >$ in terms of the index for a differential energy spectrum for gamma rays (1) and electrons (2).

shower recorded by the spark chamber is approximately 70% for E = 200 MeV, and about 50% for E = 1000 MeV. An error of this magnitude can be explained by the substantial fluctuations in the initial development of the electron shower. Yet even so unrefined a method of measuring energy can result in determination of the shape of the energy spectrum for the electrons recorded in the spark chamber with a fair degree of accuracy. The average number of sparks in showers $< n >$ in terms of the value of α (Figure 5) was obtained as a result of computation made on the basis of the calibration data shown in Figures 2 and 4 for a differential energy spectrum for electrons with a power form

$$N(E)\,dE = AE^{-\alpha}\,dE. \qquad (1)$$

4. Conditions for Conduct of the Experiment

The instrument was placed in an airtight duralumin container containing a rack for the auxiliary instruments, that is, for the clocks, thermometer, vacuum gage, compass, and a pendulum bob, the readings of which were photographed by a second photorecorder simultaneously with the functioning of the instrument and the photographing of the spark chamber. The metal container was covered on the outside by a layer of foam plastic for thermal insulation and to protect against shock upon launching. The measurements were made using controlled high-altitude balloons in the summer and fall of 1967, and in the summer of 1968, in the geomagnetic latitude of 46°. /11

Table 1 lists information on seven flights. Six measurements of electron fluxes were made, in the course of two of which the albedo electrons were measured, and in three of which the gamma ray fluxes were measured. With the

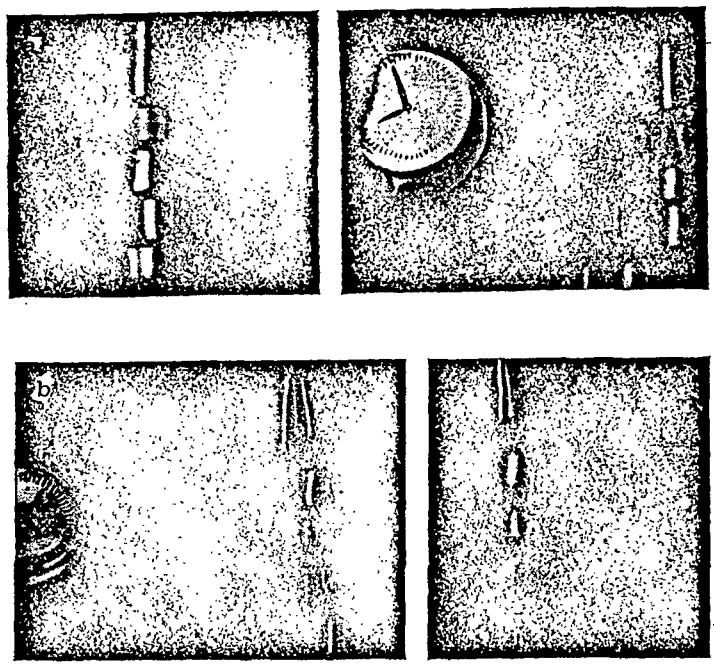

Figure 6. Photographs of events in the spark chamber.

exception of one flight (that of 28 April 1967) the instruments were energized on the ground prior to launch and functioned during the lift, which usually lasted for from 1.5 to 2.5 hours, as well as during the drift at the maximum altitude attained. Temperature and pressure inside the container remained normal, 10 to 15°C, 1 atm, in all measurements. Tilt of the axis of the instrument to the vertical was not in excess of 3°. The altitude at any moment in time can be /12 established from the barogram made during each flight. The container holding the instrument was turned 180° to measure albedo flux. Figure 6 shows the photographs of the events within the spark chamber obtained during measurements when recording electrons (a) and gamma rays (b).

TABLE 1

Date	Time of measurement (Moscow)		Height, km	Recorded radiation
	Beginning	End		
14 June 1967	0522	0730	0 - 25	Electrons, gamma rays
28 June 1967	0329	1100	20 - 26.5	Gamma rays
6 July 1967	0553	1000	0 - 27.5	Electrons, gamma rays
20 October 1967	0435	0730	0 - 27	Gamma rays
27 October 1967	0628	1000	0 - 26.5	Electrons
31 October 1967	0447	1200	0 - 28	Albedo electrons
9 July 1968	0616	~ 1200	0 - 32	Electrons, albedo electrons

5. Measurement Results

Index of the spectrum of electrons and gamma rays. The data obtained from the flights were used to find the intensity and energy spectrum of recorded particles at different altitudes. Since the electrons and gamma rays are recorded over a wide range of energies, their energy spectrum can be presented in the form

$$N(E)dE = A(E_0 + E^{\alpha})^{-1}\, dE \qquad (2)$$

which differs from the spectrum of Eq. (1) by the constant E_0, which takes into consideration the "pile up" that occurs in the spectrum at low energies. Processing the experimental data on three measurements of electrons "in the spectrum of Eq. (2)" using the results of the calibration showed that the average for all altitudes in the atmosphere was $\alpha \approx 2$, and $E_0 \lesssim 2$ if [E] = [MeV]. This indicates that the "pileup" in the spectrum is slight and that the purely power-law spectrum of Eq. (1) is sufficiently accurate for use.

The average number of sparks $< n >$ in the showers recorded in the spark chamber was computed in order to determine the index of the energy spectrum, α, and the relationship of $< n > = f(\alpha)$ (see Figure 5), computed from the results of the calibration was used. Figure 7 shows the values for α_e and α_γ, determined for different altitudes from all electron and gamma ray measurements. α_e and α_γ are in good concordance at all altitudes within the limits of statistical errors, /13

decreasing approximately from 2.5 at an altitude of 500 g/cm^2 to 1.7 to 2 at altitudes of 100 to 200 g/cm^2, and to about 3 at an altitude of approximately 20 g/cm^2.

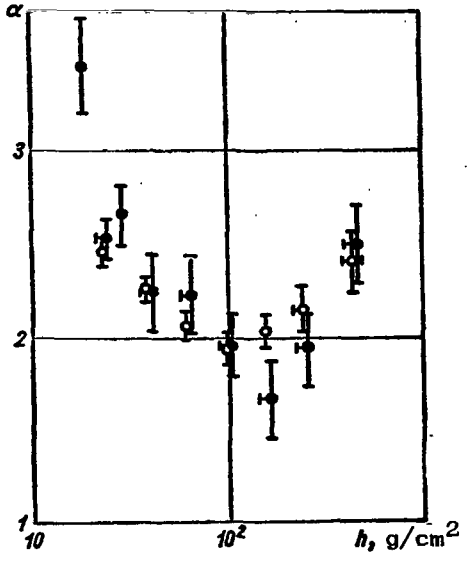

Figure 7. Measured values of the indexes of the differential energy spectra of electrons and gamma rays at different altitudes.

● - electrons (14 June, 6 July, 27 October 1967);

O - gamma rays (28 June, 6 July, 20 October 1967).

Intensity of gamma rays and electrons. The following formula was used to compute the intensity of electrons (gamma rays)

$$J_{e(\gamma)} = \frac{N_{e(\gamma)}}{(T - \tau N) G \eta_{e(\gamma)}} \qquad (3)$$

where

$N_{e(\gamma)}$ is the number of particles recording in time T = 10 minutes;

τ = 3.3 seconds is the time the instrument is blocked (movement of the photographic film); /14

N is the total number of times the instrument functions in time T;

G is the instrument's geometric factor;

$\eta_{e(\gamma)}$ is recording efficiency.

Since G and η are functions of energy, the value $\overline{G\eta}$ = 2.1 cm^2-ster, averaged over the spectrum of recorded particles, can be substituted in Eq. (3).

Figure 8 shows the relationship between altitude and gamma ray intensity, plotted from the measurements made on 6 July and 20 October 1967. The gamma ray intensity, increasing with altitude from ground level, passes through a maximum with a value of about 0.18 cm^{-2}-sec^{-1}-ster^{-1} at a height of 115 g/cm^2, then decreases smoothly. The solid line shows the altitude dependence of the secondary gamma rays generated in the atmosphere by the nuclear component of the cosmic rays as computed in [15]. Although the computations were made for electrons and gamma rays with an energy of some 1 GeV, as the comparison between the computed curve and experimental results [5 - 8] showed, the relative altitude dependence remains as it is in the case of lower energy electrons and

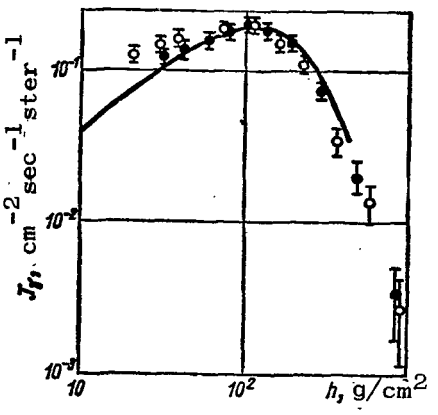

Figure 8. Intensity of the direct gamma ray flux with $E_\gamma \geq 100$ MeV at different altitudes: ● - 6 Jul 1967, O - 20 Oct 1967.

gamma rays [15]. The computed curve was normalized at the experimental value for 100 g/cm^2. The intensity values of the two measurements are in good concordance during the lift, and at the maximum, but there is some fixed difference (about 15%) beyond the maximum. At the same time, the data obtained on 6 July 1967, are in good concordance with the computed curve.

Figure 9 shows the change in the intensity of outgoing electron fluxes with height computed from the results of four flights. The solid line shows the altitude dependence of the secondary electrons [15], normalized by the experimental values obtained in this paper at 100 g/cm^2. As in the case of the gamma rays, we see a broad maximum with a value of about 0.11 cm^{-2}-sec^{-1}-ster^{-1} at a height of 120 g/cm^2. The results of all flights are in good concordance with each other and with the theoretical relationship before the maximum, but diverge markedly beyond the maximum. At the same time, the results of the measurements made on 14 June and 27 October 1967 coincide with the limits of /16 statistical errors at all heights, and differ from the results obtained on 6 July 1967, and on 9 July 1968, which repeat the expected altitude dependence of the secondary electrons. The divergence is retained for electrons with energies of from 500 to 1500 MeV generating showers with number of particles $n \geq 10$ (Figure 10) in the chamber, although the intensity of these electrons is markedly less, and the relative errors are high. The relationship between the intensities of the electron fluxes observed on 14 June, 27 October, and 6 July 1967, and on 9 July 1968, at a height of 20 g/cm^2 is 2.5 ± 0.5 for $E_e \gtrsim 100$ MeV, and 3 ± 1 for $E_e \gtrsim 500$ MeV.

The divergence cannot be explained by instrument errors. The readings obtained from the auxiliary instruments show that conditions inside the container were identical on all flights.

Another criterion by which to judge instrument operation is the particles that are nonelectron in nature that were recorded by the instrument and do not cause showers on the spark chamber plates. These particles, comprising 10% of

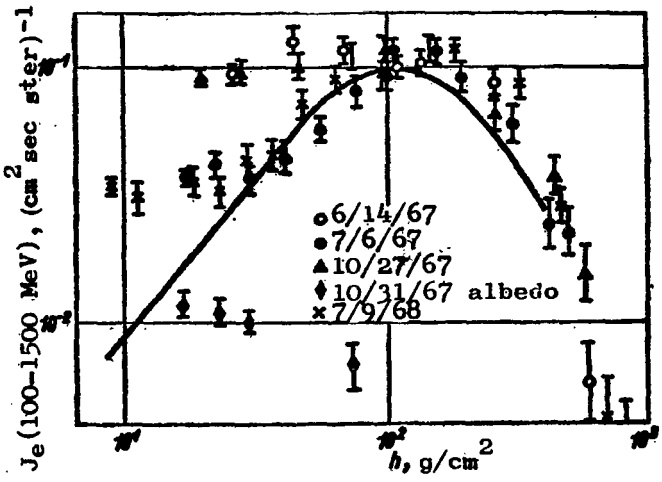

Figure 9. Intensity of outgoing and return (albedo) fluxes of electrons with $100 \leq E_e \leq 1500$ MeV at different altitudes.

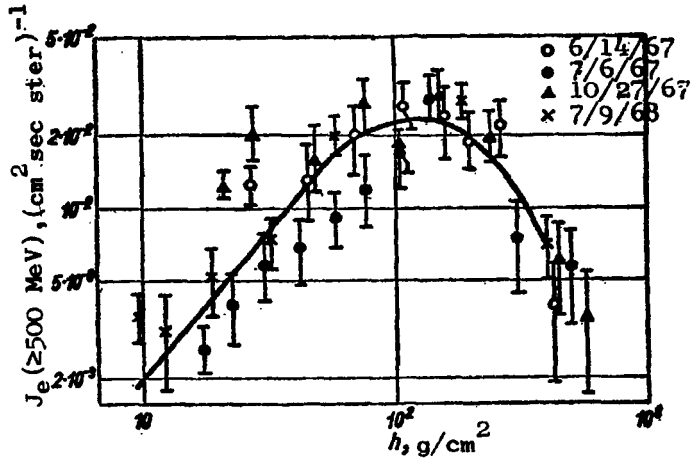

Figure 10. Intensity of the outgoing flux of electrons with $500 \leq E_e \leq 1500$ MeV at different altitudes.

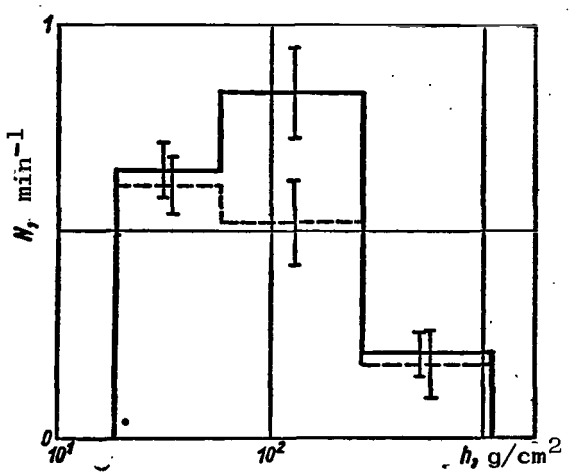

Figure 11. Particles nonelectron in nature recorded by the instrument in terms of height; - - - 6 July 1967; ___ 14 June and 27 October, 1967.

the total recorded, can be μ mesons, protons, and other particles that are arrested in the A unit, or that cause the instrument to function as a result of counting errors by the SC_2 counter. Figure 11 shows the change in the recording of nonelectron events by the instrument with height. As will be seen from the figure, the height curves for nonelectron events are in good concordance for the two groups of flights. Hence, it follows that, first, the instrument functioned normally, and, second, /17 that the total intensity of cosmic rays on all four flights was identical (also confirmed by the readings of the image monitors on the same days).

Albedo electrons. Figure 9 also shows the intensity of the albedo electron fluxes measured on 31 October 1967. As distinguished from the outgoing fluxes of electrons and gamma rays, the albedo electron flux has no sharply expressed maximum. The albedo electron energy spectrum proved to be very hard. The index for the spectrum, averaged for all altitudes traversed, is $\overline{\alpha}_{albedo} \leq 1.6 \pm 0.3$.

6. Discussion of the Results.

References [4, 11-13, 25, 26] have measured the energy spectra of electrons and gamma rays with energies greater than 100 MeV at different heights in the atmosphere. Table 2 lists the values of α_e and α_γ, the energy intervals for recorded particles, and heights in the atmosphere, obtained in our paper, and in the papers written by other authors. Our data coincide with the results con- /18 tained in the other papers in the range between 1000 and 100 g/cm^2, where reduction in $\alpha_{e(\gamma)}$ with height will be observed. Only in our measurements can the increase in $\alpha_{e(\gamma)}$ beyond the maximum for the development of a shower at heights $h < 100$ g/cm^2 be traced. It should be pointed out that in this paper the measurement of spectra at different heights was made with the same instrument, so that the measurement of the relative behavior of $\alpha_{e(\gamma)}$ with height is quite reliable.

The relationship between α and height obtained is qualitatively in concordance with the predictions contained in [27]. The energy spectrum of the electrons, and, accordingly, of the gamma rays, at sea level, and at mountain elevations, is determined chiefly by the basic spectrum of the μ-meson component. But at other heights the electron-photon component generates μ-, as well as π^0-mesons. The spectra of μ- and π^0-mesons duplicate the spectrum of the primary nucleon component with $\alpha \approx 2.5$ [28]. At the maximum for an electron-photon shower, that is, at heights of about 100 g/cm^2, the spectrum is determined by the nature of the development of the electron-photon shower in air, and has $\alpha \approx 2$.

So far as the measured altitude dependence of the intensities of electrons and gamma rays is concerned (see Figures 8 and 9), it is in good concordance with the results of other papers [5-8, 10, 11, 13] at heights of from 1000 to

TABLE 2

Energy interval, Mev	Height g/cm^2	α_e	α_γ	Literature
300—2000	1000	2,81±0,13	2,71±0,13	[25]
400—2000	670	—	2,5	[24]
100—200	355	—	1,7±0,3	[11]
500—2000	355	—	2,3±0,2	[11]
100—200	12	—	1,7±0,1	[4]
300—1000	12	—	2,0±0,1	[4]
500—3500	4	1,6	—	[32]
300—2000	2,6—4	1,8	—	[33]
⩾ 100	300—1000	2,5±0,2	2,40±0,16	this paper
	200—300	1,9±0,2	2,14±0,12	same
	120—200	1,7±0,2	2,02±0,08	»
	75—120	1,95±0,16	1,93±0,08	»
	48—75	2,2±0,2	2,06±0,07	»
	30—48	2,24±0,2	2,26±0,06	»
	20—30	2,6±0,1	2,46±0,07	»

Commas represent decimal points.

100 g/cm^2, and differs in a number of cases at heights from 100 to 20 g/cm^2. It was found that the measured flux exceeded the computed value for the secondary electron-photon component [15], especially in the case of the electron flux (by a factor of 2 to 3); that is, we have the additional fluxes i_e and i_γ. A check has shown that the appearance of these additional fluxes is not associated with fluctuations in the intensity of primary cosmic rays, established by neutron monitors, nor by solar activity, measured by the number of sun spots, for example. Table 3 lists measured values of additional fluxes $i_{e,\gamma}$, and various parameters that serve to characterize cosmic rays and the condition of the geomagnetic field on the day the experiment was conducted. As we see from Table 3, there is a correlation between the i_e and i_γ fluxes and magnetic measurement at ground level, specifically with the integral K-index (ΣK), characterizing the degree to which the earth's magnetosphere is disturbed. The correlation is such that the larger i_e and i_γ, the greater the change in the K-index prior to the days the measurements were made (see Table 3). Two possibilities can be assumed as leading to the appearance of the additional flux i_e. The first is associated with the flux of double albedo electrons, that is of earth albedo electrons with momenta less than the geomagnetic cutoff momentum, which are returned to the conjugate magnetic point by the geomagnetic field [9,12]. The assumption is that the additional flux, i_e, is a flux of double albedo electrons subjected to the strong influence of the geomagnetic field, an explanation that is, as is apparent, untenable because

/19

TABLE 3

Date of launch	i_e, cm^{-2}-sec^{-1}-ster^{-1}	i_γ, cm^{-2}-sec^{-1}-ster^{-1}	Neutron monitor reading (Moscow)	No sun spots	ΣK	$\Delta\Sigma K$
14 June 1967	0,06	–	1750	31	25	+6
6 July 1967	0,01	0,02	1740	97	25	+1
20 October 1967	—	0,025	—	83	12	–3
27 October 1967	0,06	—	1730	125	23	+10
31 October 1967	—	—	1680	100	16	–2
9 July 1968	0,01	—	—	—	20	+1

Commas represent decimal points.

changes in the magnetosphere close to the earth's surface at heights of one to two earth radii, where the trajectories of albedo electrons returning to the earth occur, are small. Moreover, the albedo electron flux we measured at a height of 17 g/cm^2 is 0.012 ± 0.002 cm^{-2}-sec^{-1}.$ster^{-1}$. Its extrapolation to the conjugate point at a depth of 2 x 17 g/cm^2 = 34 g/cm^2 yields a flux of about 0.015 cm^{-2}-sec^{-1} -$ster^{-1}$, or less than the additional flux, i_e, observed at this same depth on 14 June and 27 October 1967, by a factor of 4. Another, very real possibility of the appearance of the additional flux, i_e, correlating with the K-index, is associated with the electrons in near space, in particular with the electrons from the radiation belts "thrown" into the atmosphere when the geomagnetic field is disturbed. Electrons with energies greater than, or equal to, 100 MeV have not been directly recorded in the radiation belts. But they can exist there, because protons with the corresponding Larmor radii (out to 400 km, corresponding to electrons with energy E = 500 MeV) were observed experimentally in the inner radiation belt in the shell $L \approx 2$ [29, 30]. Our experiment was conducted at a geomagnetic latitude of 46°, which corresponds to this same shell. Moreover, electrons with energies greater than 300 MeV were observed during the flights of Proton-1 and Proton-2 /20 [18]. But even the experimental detection of high energy electrons in the inner radiation belt fails to provide a complete answer to the question because what is still unclear is whether comparatively small disturbances of the magnetosphere, characterized by change in the integral K-index $\Delta\Sigma K$ of 5 to 10 units, caused the appreciable discharge of these electrons into the atmosphere. Apparently, however, electrons with energies close to critical, at which they can still be kept within the inner radiation belt, should "spill out" of it, even when disturbances in the magnetosphere are slight.

The additional i_γ flux appears as a result of the bremsstrahlung of the additional electron flux in the rest of the atmosphere and consequently should correlate with the change in the integral K-index. Correlation such as this follows from the results of the work done by Ye. A. Chuykin, and others [10, 13] at the same geomagnetic point. The overall intensity of the gamma ray flux, as well as the nature of the altitude dependence in the upper atmosphere, changes with change in $\Delta\Sigma K$. Because of the difference in nuclear and radiation lengths there is an additional maximum for gamma radiation at a depth of $\sim$ 40 g/cm^2 [10, 13].

Final explanation of the question remains for additional experiments, not only in the upper layers of the atmosphere, but beyond the limits of the atmosphere as well.

APPENDICES

1. Computation of the Energy Dependence of the Efficiency with which the Instrument Records Gamma Rays

The dependence $\eta_\gamma (E_\gamma)$ can be obtained from the following expression

$$\eta(E_\gamma) = \int_0^{E_\gamma} d\varepsilon \int_0^{x_0} dx \cdot K(E_\gamma, x) \cdot \omega(E_\gamma - \varepsilon, \varepsilon) F(E_\gamma - \varepsilon, \varepsilon, x), \tag{A.1}$$

where

$K(E_\gamma, x)$ is the probability of the conversion of a gamma ray with energy E_γ in converter layer $(x, x + dx)$;

$\omega(E_\gamma - \varepsilon, \varepsilon)d\varepsilon$ is a function of the distribution of the energy of the gamma ray between the components of the pair $(E_\gamma - \varepsilon, \varepsilon)$;

$F(E_\gamma - \varepsilon, \varepsilon, x)$ is the probability that the instrument will record an electron-positron pair with energies $E_\gamma - \varepsilon$ and ε, occurring at depth x of the converter.

It will be accurate enough to take the distribution of the energy between the components the pair as equally probable. Then

$$\omega d\varepsilon = \frac{d\varepsilon}{E_\gamma}, \tag{A.2}$$

$$K\omega d\varepsilon dx = e^{-\sigma N x} \frac{\sigma N}{E_\gamma} d\varepsilon dx, \tag{A.3}$$

/21

where

$\sigma(E_\gamma)$ is the gamma ray conversion cross-section [31];

$N = 2.91 \cdot 10^{21}$ is the number of lead nuclei in 1 gram.

The function F can be expressed in terms of the measured efficiency of recording of electrons by counters CC, CS_1 and CS_2 $(i = 1, 2, 3)$, $\eta_i(E_\gamma, x) = 1 - \xi_i(E_\gamma, x)$, for $i = 1, 2, 3$, during the calibration, as follows:

$$F = \prod_l [1 - \xi_l(E_\gamma - \varepsilon, x)\xi_l(\varepsilon, x)]. \tag{A.4}$$

so far as this latter formula is concerned, it is sufficient that each of the three counters, CC, CS_1, and CS_2, record just one of the components of a pair

in order to record the electron-positron pairs occurring.

The numerical solution for the integral of Eq. (A.1), will result in the relationship shown in Figure 2 when Eqs. (A.3) and (A.4) are taken into consideration.

2. Determination of the Instrument's Geometric Factor

The following expression yields the instrument's geometric factor

$$G\eta = \int_0^{2\pi} \int_0^{\pi/2} \int_{-r}^{+r} \int_{-r}^{+r} f(x, y, \theta, \varphi)\, dx dy \sin\theta d\theta d\varphi, \qquad (A.5)$$

where

$f(x, y, \theta, \varphi)$ is the efficiency of the instrument in handling particles entering at point (x, y) in a direction fixed by the zenith angle θ, and the azimuth angle φ.

The function f was measured with the instrument functioning with a beam of electrons with E_e = 435 MeV.

Numerical integration resulted in G = 14.5 ± 1.0 cm^2-ster.

REFERENCES

1. Schein, M., et al., Phys. Rev., Vol. 59, 1941, p. 615.
2. Hulsizer, R. I., Rossi, B., Phys. Rev., Vol. 73, 1948, p. 1402.
3. Critchfield, C. L., et al., Phys. Rev., Vol. 85, 1952, p. 461.
4. Svenson, K., Arkiv Fysik, Vol. 13, 1958, p. 347.
5. Cline, T. L., Phys. Rev.,Lett., Vol. 7, 1961, p. 109.
6. Meyer, P., Vogt, R., Phys. Rev., Lett., Vol. 6, 1961, p, 193.
7. Meyer, P., Vogt, R. J., Geophys. Res., Vol. 66, 1961, p. 3950.
8. Duthie, J. G., et al., Phys. Rev., Lett., Vol. 10, 1963, p. 364.
9. Schmouer, J. W., Earl, J., Phys. Rev., Vol. 138B, 1965, p. 300.
10. Chuykin, Ye. A., et al., Izv. AN SSSR. Ser. fiz., Vol. 30, 1966. p. 1791.
11. Kohn, D., et al., Z. Phys., Vol. 193, 1966, p. 443.
12. Verma, C. D., J. Geophys. Res., Vol. 72, 1967, p. 915.
13. Chuykin, Ye. A., et al., Geomagnetizm i aeronomiya, Vol. 7, 1967, p. 815.
14. L'Heureux, J. Astron. J., Vol. 148, 1967, p. 399.
15. Okuda H., Yamamoto, Y., Report Ionosph and Space Res.,
16. Perola, G. C., Scarsi, L., Nuovo cimento, Vol. 46A, 1966, p. 718.
17. Jokipii, J. K., et al., Preprint EFINS 67-45, May 1967.
18. Kraushaar, W. L., Clark, G. W., Phys. Rev., Lett., Vol. 8, 1962, p. 8.
19. Grigorov, N. L., et al., Kosmicheskiye issledovaniya, Vol. 5, 1967, p. 124.
20. Grigorov, N. L., et al., Izv. AN SSSR. Ser fiz., Vol. 30, 1966, p. 1773.
21. Bezus, V. A., et al., Izv. AN SSSR. Ser fiz., Vol. 32, 1968, p. 1863. /22
22. Gal'per, A. M., et al., Pribory i tekhn. eksperim., No. 5, 1967, p. 186.

23. Gal'per, A. M., et al., Pribory i tekhn. eksperim., No. 3, 1969 p. 56.

24. Becklin, E. E., Earl, J. A., Phys. Rev., Vol. 136B, 1964, p. 237.

25. Chou, C. N., Phys. Rev., Vol. 90, 1953, p. 473.

26. Lovati, U. A., Nuovo cimento, Vol. 12, 1954, p. 526.

27. Rozental', I. L., Zh. eksperim. i teor. fiz., Vol. 22, 1952, p. 93.

28. Ginzburg, V. L., Syrovatskiy, S. I., Proiskhozhdeniye kosmicheskikh luchey, [The Origin of Cosmic Rays], Academy of Sciences of the USSR Press, Moscow, 1963.

29. Rosser, U., Uspekhi fiz. nauk, Vol. 85, 1965, p. 147.

30. Vernov, S. N., Izv. AN SSSR. Ser. fiz., Vol. 32, 1968, p. 1834.

31. Ritson, D., Eksperimental'nyye metody v fizike vysokikh energiy, [Experimental Methods in the Physics of High Energies], Nauka Press, Moscow, 1964.

32. L'Heureux, J., Meyer, P., Phys. Rev., Lett., Vol. 15, 1965, p. 93.

33. Webber, W. R., Chotkawski, J., Geophys. Res., Vol. 73, 1967, p. 2783.

THE EXISTENCE AND DETECTION OF FIREBALLS

Ye. I. Daybog and I. L. Rozental'

ABSTRACT. The experimental evidence in favor of the existence of fireballs is subjected to critical examination.

The hypothesis concerning the carrying away of much of the energy of /23
primary particles and the decaying into π-mesons when there is strong interaction between particles has been widely discussed in recent years (see [1-3], for example). Particles such as these have been called fireballs. Moreover, the very fact of the existence of superheavy resonances with fireballs is related to the fundamental question of the critical mass of the elementary particles [4].

The difficulty in approaching this question results from the fact that fireballs can be generated at quite high energy levels. Consequently, until recently, the search for them went on through the use of cosmic particles, when measurement accuracy is poor. Added to this basic technical difficulty is that associated with the inaccuracy and indeterminancy of the fireball concept itself. Two approaches can be taken to this question. The first of these, and the most persuasive, involves an a priori determination, and subsequent measurement, of the fireball quantum numbers. The second, or "empirical" approach reduces to an undecipherable property, that of the massiveness of this particle. It is precisely this latter approach that has been discussed in the main in connection with the double-hump in the angular distributions [1, 2], and with the other properties of the strong interactions in the case of very high energy levels (see [5], for example). The existence of this double-hump also served as the basis for the experimental introduction of the two-fireball hypothesis.[1]

Later on, N. A. Dobrotin, S. A. Slavatinskiy and their fellow workers (see [3, 5], for example) obtained new experimental data that, in their opinion, pointed to the existence of one fireball. Thus arose the conception of the rise in the number of fireballs with energy.

---

1. This hypothesis was postulated on a speculative basis in 1950 by G. T. Zatsepin.

It is the purpose of this paper to make a critical analysis of the experimental evidence in favor of the existence of fireballs. It is our view that /24 they either are the result of two well studied characteristics of strong interactions (the approximate independence of the magnitude of the transverse momenta of secondary particles from the energy of the primary particles, and the existence among the secondary particles of one that is isolated from the standpoint of energy), or they bear no relationship to the proof of the existence of fireballs. It is our opinion that certain serious arguments in favor of this assertion were cited earlier [6]. We intend to continue this analysis in this paper.

1. The Double-Hump in the Angular Distributions in Selected Theoretical Models.

The angular distribution of secondary particles in coordinates $\eta = -\log \tan (\theta_c/2)$, where θ_c is the angle of escape of secondary particles in the C-system,* sometimes discloses the double-hump.[2] This fact has also served as the beginning of lengthy searches for fireballs [1, 2]. The idea that fluctuations in energy [7], or angular [8, 9] distributions could transform a single-hump distribution into a double-hump distribution has been under discussion for a comparatively long time. However, the distinctive feature of the models used in [7 to 9] evidently served as the basis for the fact that these papers pretty much ignored the adherents of the existence of fireballs. Reference [6] took a new step along the road to the analysis of the general principles involved in the double-hump distribution, advancing the idea that the double-hump in the angular distribution was the result of approximate independence between transverse momentum distribution and the energy of the primary particles, although proof of this assertion was also based on a number of particular longitudinal momentum distributions

$$\Phi_1(p) = \delta\left(p - \frac{2E_0K}{N}\right), \qquad (1)$$

---

2. More precisely, the double-hump in logarithmic coordinates was disclosed in the L-system in the experiment. It has long been assumed that distribution was invariant in these coordinates, whereas in fact this was not so (see [6] and the end of section 1). However it is more convenient to do research in the C-system for a physical understanding of the principles of the double-hump in logarithmic coordinates.

* C-system - center-of-mass system; L-system - laboratory system.

in a "uniform" distribution

$$\Phi_2(p) = \begin{cases} \frac{N}{2E_0K} & \left(p < \frac{2E_0K}{N}\right), \\ 0 & \left(p > \frac{2E_0K}{N}\right), \end{cases} \qquad (2)$$

and $\Phi_3(p)$ corresponds to Landau's hydrodynamic theory. $p \sim p_{\parallel}^3$ is the momentum of the secondary particles; E_0 is the total energy of the colliding particles in the C-system; K is the coefficient of inelasticity; N is the multiplicity. The following general conclusion can be formulated. The double-hump should increase in the $\bar{p}_{\parallel}/\bar{p}_{\perp}$ ($\bar{p}_{\parallel}$ is the mean longitudinal momentum of the secondary particles). But the very magnitude of the double-hump depends significantly on K and, in particular, the magnitude of the double-hump should increase with increase in K. In the more general case it can be said that the more uniformly energy E_0 is distributed among the secondary particles, the greater the increase in the double-hump should be (see section 2). Thus it becomes clear why the double-hump is relatively neglected in Landau's theory, and it disappears completely in the L-system.[4] In hydrodynamic theory most of the energy is carried off by a small percentage of secondary particles. Since hydrodynamic theory agrees with the experiment at this point, there is nothing surprising about the fact that the double-hump phenomenon is quite rare (even at very high energies of some 10^{12} ev). /25

Although these conclusions are quite persuasive, the distinctive feature of the distributions mentioned above has made it possible for adherents of the proofs of the existence of fireballs to express doubt as to the generality of these conclusions, and the lack of an adequate link with the various theoretical models of the multiple processes deprives these conclusions of the necessary degree of persuasiveness. So far as this aspect is concerned, it can be pointed out in particular that the establishment of a link between the various empirical

---

3. This condition signifies that energy E_0 is adequately high.

4. This fact was noted by V. M. Maksimenko. We should emphasize that what we are discussing here is the nontrivial solution for hydrodynamic equations, that the simple wave computation reduces to the appearance of a small double-hump [7].

characteristics (in this particular case between transverse momenta and the double-hump phenomenon) is of incomparably greater significance than the use of models that usually provide poor concordance with experiment. However, since there is the point of view [9] that certain models (the multiperipheral Amati model, in particular, and others [10]) do not result in a double-hump at very high energies, we have once again made an analysis of this link in the Van Hove [11] and Amati and other [10], similar, models.

The Van Hove model. The distribution of the longitudinal (and, consequently, in our approximation the total) momenta in this theory is in the form

$$\Phi(p) \sim \frac{1}{p^{\alpha}} \qquad (1 < \alpha \leqslant 2). \tag{3}$$

Taking the distribution of the transverse momenta to be in the form /26

$$\frac{d^2N}{dp_{\perp}\,dp_{\parallel}} = \frac{p_{\perp}}{p_0^3}\, e^{-\frac{p_{\perp}}{p_0}}\, \frac{1}{p^{\alpha}}. \tag{4}$$

we obtain

$$N(p_{\perp})\,dp_{\perp} = \frac{p_{\perp}}{p_0^2}\, e^{-\frac{p_{\perp}}{p_0}}\, dp_{\perp}\,(p_0 \sim 0{,}15 \text{ GeV}), \tag{5}$$

In η coordinates

$$\frac{d^2N}{dp\,d\eta} = \frac{p^{2-\alpha}}{p_0^2}\, \frac{\operatorname{sh}\eta}{\operatorname{ch}^3\eta}\, \exp\left[-\frac{p}{p_0}\,\frac{1}{\operatorname{ch}\eta}\right]; \tag{6}$$

$$\frac{dN}{d\eta} = \frac{1}{p_0^2}\int_{p_{\min}}^{p_{\max}} \frac{\operatorname{sh}\eta}{\operatorname{ch}^3\eta}\, p^{2-\alpha} \exp\left[-\frac{p}{p_0 \operatorname{ch}\eta}\right] dp; \tag{7}$$

$$\frac{dN}{d\eta} = \frac{1}{p_0}\,\frac{\operatorname{sh}\eta}{\operatorname{ch}^2\eta}\left\{\exp\left[-\frac{p_{\min}}{p_0 \operatorname{ch}\eta}\right] - \exp\left[-\frac{p_{\max}}{p_0 \operatorname{ch}\eta}\right]\right\}, \qquad \alpha = 2; \tag{8}$$

$$\frac{dN}{d\eta} = \frac{1}{p_0}\,\frac{\operatorname{sh}\eta}{\operatorname{ch}^2\eta}\left\{\left[\left(\exp\left\{-\frac{p_{\min}}{p_0 \operatorname{ch}\eta}\right\} - \exp\left\{-\frac{p_{\max}}{p_0 \operatorname{ch}\eta}\right\}\right) p_0 \operatorname{ch}\eta\right] + \left[p_{\min}\exp\left\{-\frac{p_{\min}}{p_0 \operatorname{ch}\eta}\right\} - p_{\max}\exp\left\{-\frac{p_{\max}}{p_0 \operatorname{ch}\eta}\right\}\right]\right\}, \qquad \alpha = 1. \tag{9}$$

Although it is obvious that the distribution of Eq. (3) diverges when $p \to 0$, and consequently that $p_{min} \neq 0$, we have assumed that $p_{min} = 0$ in the computation for the illustrative graph for the angular distributions of Eq. (7) because this value corresponds to a minimal double-hump (see below). Figure 1 shows the

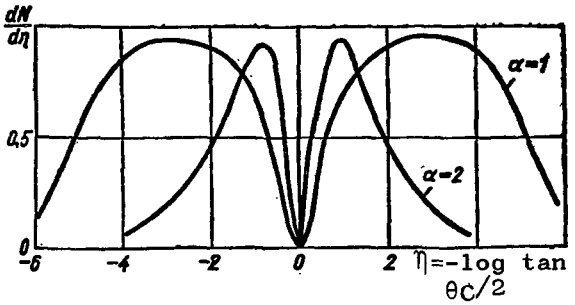

Figure 1. Angular distributions of secondary particles in accordance with Van Hove's theory.

angular distribution in a C-system in accordance with Van Hove's theory.

The multiperipheral model. The multiperipheral model predicts the same distribution as does the Van Hove model in a C-system for the function $\Phi(p)$, so this model too results in the double-hump in the angular distribution. But there has been a longstanding opinion (see [9], for example) that the multiperipheral model predicts a "table-shaped" and not a humped distribution in the coordinates $\lambda(\lambda = -\log \tan \theta_L)$. It would appear that this view is associated with the misunderstanding that only the particles of the leading cone were taken into consideration when the transition was made to the L-system. Let us use the approximation $p_\perp$ = constant, $p_\parallel = p$, introduced in this paper, in order to match the true results with the conclusions arrived at by Ciezewsky and Krzywiski [9]. The $dN/d\eta$ distribution will then be in the form

$$\frac{dN}{d\eta} = \begin{cases} B & \eta_{min} < \eta < \eta_{max}, \\ & -\eta_{max} < \eta < -\eta_{min}, \\ 0 & |\eta| > |\eta_{max}|, \\ & |\eta| < |\eta_{min}|, \end{cases} \tag{10}$$

that is, this distribution will have the form of two symmetrical "tables" in the C-system. The quantities η_{min} and η_{max} correspond to the values p_{min} and p_{max}. The two "tables" will merge into one only when $p_{min} = 0$, and this, as was pointed out above, contradicts the physical sense of the distribution of Eq. (3). Both "table-shaped" distributions are retained when the transition is made to the L-system, but they are no longer symmetrical. Figure 2 shows the angular distributions in accordance with a multiperipheral model in the C- and L-systems.

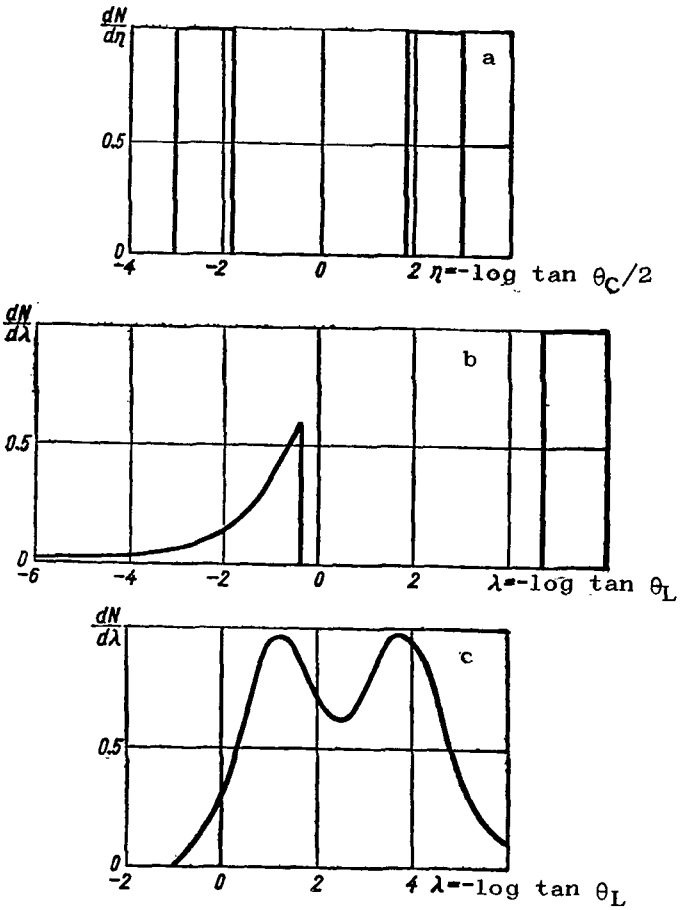

Figure 2. Angular distributions of secondary particles in accordance with the multiperipheral model [10].

a - C-system distribution; b - L-system distribution; c - L-system distribution if the transverse pulse distribution is in the form of Eq. (4) and $E_0/500 \leq p_{\parallel} \leq E_0/100$.

2. The Effect of Nonuniformity in the Distribution of Longitudinal Pulses on the Magnitude of the Double-Hump in the Angular Distributions

Since the double-hump is reflected by the relative paucity of particles escaping at an angle $\theta \sim \pi/2$ in the C-system, it is clear that the more particles there are which have high longitudinal momentum ($p_{\parallel} \gg p_{\perp}$), the more distinctly the double-hump is revealed. This condition corresponds to the requirement for a reduction in the difference in secondary particle energies. The distribution of Eq. (1) corresponds to the limit of a maximum double-hump when K = 1. The simplest form of nonuniformity is the generalization of this distribution for

the case when $K \neq 1$. Reference [6] demonstrated the fact that the double-hump is reduced when there is a reduction in K (an increase in the "nonuniformity" of the energy distribution).

It goes without saying that making an overall analysis of the effect of "nonuniformity" of distribution is made difficult because of the lack of clarity of this concept. We have, therefore, limited ourselves to an analysis of a special case, assuming that the sequence of momenta of secondary particles will form the geometric progression

$$\varepsilon_i = \varepsilon_1 b^{i-1}. \tag{11}$$

Assuming that $\varepsilon_1 = \mu_\pi$, we see that the magnitude b satisfies the condition /29

$$\frac{b^N - 1}{b - 1} - \frac{E_0}{\mu_\pi} = 1. \tag{12}$$

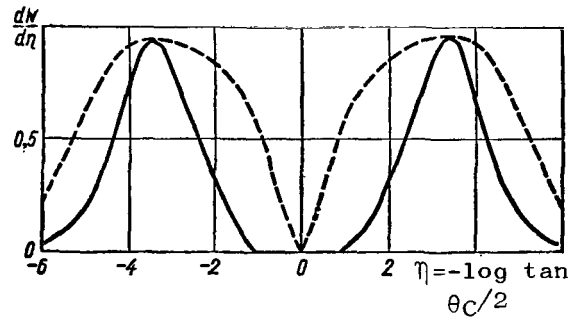

Figure 3. Angular distributions of secondary particles for various degrees of nonuniformity.
b = 1 (solid line); b = 1.73 (dashed line)

The condition $\varepsilon_1 = \mu_\pi$ corresponds to the maximum nonuniformity, b = 1 to the minimum. Figure 3 shows the angular distributions for energy $E_L = 10^{12}$ ev, N = 10, and two values b = 1 and b = 1.73, satisfying Eq. (12).

3. Other Proofs of the Existence of Fireballs

S. A. Slavatinskiy [5] has advanced several new arguments indicating his opinion that he is in favor of the occurrence of one fireball. Let us list these arguments.

1. The value of the coefficient of inelasticity, $K \sim 0.5$, is comparatively low.

2. There is inequality between the coefficients of inelasticity in the laboratory (K_L) and mirror (K_M) systems of coordinates.

3. There is a specific system of coordinates (the M-system) different from the C-system, in which the divergence is close to isotropic.

4. The shape of the energy spectrum (close to a Planckian distribution) in the M-system.

5. The mean multiplicity at energies of about 250 GeV (when, in accordance with the conception, one fireball forms), have approximately half the multiplicity of double-hump showers, interpreted as the formation of two fireballs.

It seems to us that these arguments have no relation to the problem of the existence of fireballs, and that some of these conclusions present their adherents with quite complex questions, to which it is difficult to find answers at this time. Let us, first of all, look at points 1 through 4. They all equate /30 to a completely defined energy, some (2 to 3)$\cdot 10^{11}$ ev [5]. But is is apparent that fireballs can occur for any coefficient of inelasticity ($K > 0$) when the condition is $K_M = K_L$ and in principle can have an angular and energy distribution (satisfying the laws of conservation, of course). There are no kinematic limitations on these characteristics. The theoretical forecasts, based on consideration of the dynamics of the processes, are definite enough to serve as persuasive arguments.

The situation is even more complicated if consideration is given to the characteristics (paragraphs 1 and 2) in terms of energy E_L. We know (see [12], for example) that the value $K \sim 0.5$ is retained over a very wide range of E_L energies, 3 to 1000 GeV. Question. Why is it that the value $K \sim 0.5$ is associated with the occurrence of fireballs when the energies are from 200 to 300 GeV, yet this property is retained when the occurrence of fireballs is not a topic of discussion when energies are $E_L < 10$ GeV? This same consideration can be applied to the property $K_L \neq K_M$, which shows up clearly, even at very low energies (1.5 GeV, for example [13]).

It should be pointed out with respect to the energy spectrum of secondary particles that the Planckian distribution does not describe the fastest π-mesons observed in [5]. To explain them calls for the introduction of a new hypothesis; the occurrence of an isobar with a cross section close to the total cross section. Although there are certain indirect arguments[5] in favor of the

---

5. The most persuasive argument, in our view, follows from an analysis of the properties of cosmic μ-mesons [14].

frequent occurrence of isobars when energies are very high, nevertheless, at this time this property is still only a hypothesis. The existence of a quasi-isotropic system of coordinates too can be explained by the distribution of transverse momenta (see [6]).

Let us move on to the last argument (paragraph 5). The multiplicity in terms of E_L is not associated with the existence of fireballs, in and of itself. For example, hydrodynamic theory predicts approximately the same quantitative multiplicity relationship. The multiplicity distribution in the case of a specified energy of some 10^{12} ev is more interesting. Not only one, but two fireballs should form in this energy region, depending on the concentrations. The share of the "two fireball" showers is approximately 0.3 to 0.5, according to various estimates (see [5]). One should be able to observe a very unique multiplicity distribution for fixed energy in this case. In fact, certain fluctuations in the multiplicity should be observed as each fireball decays. /31
We shall assume that these fluctuations can be described by Poisson's law for purposes of definiteness. Then the function f(N) describing the multiplicity distribution will be in the form

$$f(N) = \frac{e^{-\bar{N}}\bar{N}^N}{N!}[\alpha + (1-\alpha)e^{-N}\,2^N], \qquad (13)$$

where

$\bar{N} \sim 8$ is the average number of secondary charged particles in the decay of one fireball;

α is the share of "one fireball" showers.

It is obvious that this distribution has two maxima (if $\alpha \neq 0$, or $\alpha = 1$). Figure 4 shows Eq. (13) for $\alpha = 0.5$. The experimental data obtained during the fragmentation of primary heavy nuclei are shown in the form of a curve, and a comparison of the curves will show that they have nothing in common, although it should be pointed out that the experimental statistics are too meager to consider the judgment as final.

In conclusion, it must be emphasized that although the characteristics enumerated in the foregoing apparently have no relation to proof of the existence

of fireballs, they can play an important role in explaining the properties of fireballs, if their existence can be proven by using other methods.

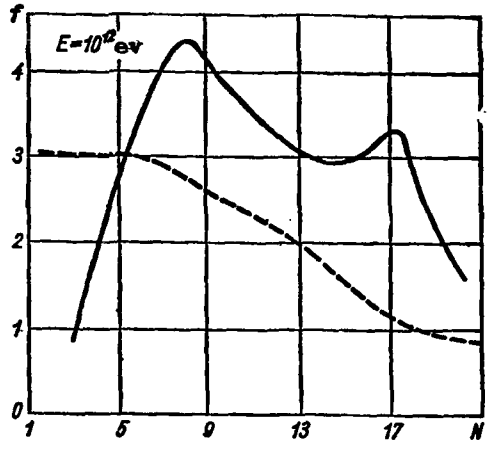

Figure 4. Multiplicity distribution for specified energy.

The computed curve (——) is from Eq. (13) for $\alpha = 0.5$. The experimental data (-----) were selected from a so-called "rich family" [15] obtained during the fragmentation of heavy nuclei.

4. Methodology for Fireball Searches

/32

Because of the heuristic value of the conception of fireballs, we shall, at this point introduce certain considerations with respect to a methodology for fireball searches, understanding them to be resonances with great masses.[6] It goes without saying, that these considerations are a very simplified arrangement, an outline of a methodology for detecting fireballs.

The investigation of resonances has to begin with a definition of the hypothesis describing resonance. Yet, today, fireballs are given so many different characteristics that their quantitative investigation is impossible without more or less strict definitions. Therefore, there must be a clear-cut formulation of the principal characteristics of fireballs before experimental verification is undertaken. We shall assume that:

(a) the number of fireballs is equal to 1 or 2;

(b) the angular distribution in the M-system is isotropic;

---

6. There is a point of view [16] that fireballs do not have discrete quantum numbers. In this case it is extraordinarily difficult to detect fireballs dependably (if they exist). If this point of view proves to be correct, the two maxima for the multiplicity distribution curve, for example, can prove to be practically insoluble.

(c) the energy distribution in the M-system can be expressed by a Planckian function, or by a δ-function;[7]

(d) the direction in which the fireballs move coincides with the direction in which the primary particles are moving;

(e) there are no isobars.[8]

The search for fireballs must be broken down into two periods: (a) definition of the physical characteristics establishing the proof of their existence; and (b) evaluation of the accuracy needed for measuring these characteristics. To be pointed out in connection with the first of these is that the search is primarily for those characteristics without dependence on the energy of the primary particles, E_0, if the latter exceed some threshold value corresponding to the appearance of fireballs. Included, for example, can be the mass of an assumed bunch, the energy-momentum distribution in some selected system of coordinates (with system establishment not dependent on E_0), and the distribution of the transverse momenta in terms of the multiplicity. The investigation of the multiplicity distribution for specified E_0, and information on these distributions when this parameter is changed, are of interest.

So far as the second of these is concerned (the evaluation of accuracy), /33 let us introduce certain leading considerations. Let us review two variants of the distribution of showers in terms of the "masses of the bunches."

1. Let there be a quasi-continuous series of "resonances." The distance between specific lines (SU_3 classification) within one supermultiplet is about 0.1 M (where M is the mean mass of the particles for the particular supermultiplet). We shall assume that in the C-system all secondary particles[9] form a single fireball, so that

$$|\Sigma p_i| \ll |\Sigma \varepsilon_i|, \quad M \sim \Sigma \varepsilon_i$$

---

7. Since the Planck function has a sharp maximum, it can be assumed, for the estimates, that the momentum of secondary particles in the M-system is equal to the mean value.

8. The methods proposed in what follows can also be used to verify other hypotheses.

9. Perhaps after the deduction of the primary nucleons.

and the error is

$$\delta M \sim \delta(\Sigma \varepsilon_i).$$

Needed for the solution is

$$\delta M \ll 0.1 M. \tag{14}$$

2. Let there be a fireball, "isolated" in terms of mass. The weaker condition

$$\delta M_1 \ll M. \tag{15}$$

should then be satisfied. At this point it is helpful to point out that when investigating resonances there is another characteristic magnitude, the width Γ of a "resonant" line, equal to 150 MeV, approximately. If $\Gamma < 0.1$ M, measurement accuracy needed is even higher, and is determined by the quantity Γ. On the other hand, if the existence of a supermultiplet as a whole is investigated (within the SU_3 classification framework), the characteristic width (the dispersion of the mass within the limits of the supermultiplet) is very great, about 0.2 to 0.3 M.

Let us consider the question of the feasibility of arriving at the necessary accuracy, using the approximate constancy of the average transverse momentum We shall use the approximations for the distribution of transverse momenta of Eq. (3) for purposes of simplicity. Now the dispersion is

$$D = 2p_0$$

and the root-mean-square error is

$$\sqrt{D} \sim 150 \text{ Мэв} \sim \bar{p}_\perp; \quad N \sim 15.$$

When $E_0 = 10^{12}$ ev

$$\delta \Sigma \varepsilon_i \sim \sqrt{\frac{D}{N}} \sim 0.2 \Sigma \varepsilon_i. \tag{16}$$

Let us point out that investigation of the distribution of the masses of the /34
resonances is the most reliable tool for proving their existence. However, as will be seen from the assessment made earlier, this method required extremely accurate determination of the characteristics of the secondary particles. This is why it is expedient to find other approaches to the solution to this problem. The following method, in particular, can be pointed out. Cases that, because of individual outward signs, can be treated as the consequence of the occurrence of a fireball, are selected from the entire set. Particles belonging to one center

should be discarded in these cases (on a relatively arbitrary basis, perhaps).

γ_M must then be computed through

$$\Sigma(p_{i\parallel} - V_M \varepsilon_i) = 0, \tag{17}$$

where

V_M is the velocity of the fireball in the C-system;

$p_{i\parallel}$ is the component of the momentum of the i^{th} particle in the direction in which the primary is moving.

All particles belonging to one center are summed.

In the M-system, which is established by the condition of Eq. (17), the angular distribution is assumed to be isotropic, and the energy distribution is that corresponding to an a priori distribution (that of a Planckian function, a δ-function, and the like, for example). Let us evaluate the error in fixing γ_M if (in some system of coordinates) the mean error in establishing the momentum of secondary particles equals $\overline{dp}$. Assuming, for purposes of making the evaluations, that $p_\perp = \overline{p}_\perp = \mu \ll \overline{p}_\parallel$, we obtain

$$V_M \sim 1 - \frac{\mu^2}{\bar{p}^2};$$

$$dV_M \sim \frac{2\mu^2}{\bar{p}^3} d\bar{p};$$

$$\frac{d\gamma_M}{\gamma_M} \sim \frac{2\gamma_M^2 \mu^2}{\bar{p}^3} d\bar{p} \sim \frac{d\bar{p}}{\bar{p}}.$$

In this approximation it is easy to evaluate the error $\overline{dp}_{iM}$ in the mean value of the momentum in the M-system if the error in the determination of the momentum in some system with a γ_M value is given

$$\frac{d\bar{p}_{iM}}{\bar{p}_{iM}} \sim \frac{d\bar{p}_i}{\bar{p}_i}. \tag{18}$$

The derivation of this expression assumed additionally that $\gamma_M \gg 1$.

Angular distribution. Let us consider how errors in establishing momenta reflect on the parameter of the distributions attributable to the assumed occurrence of fireballs, assuming that errors in establishing the angles can be ignored. If the velocity of secondary particles is $\beta_M = 1$ for all particles, the summed angular distribution can be attributed to the values γ_{1M}, ..., γ_{kM} /35

and n_{1M}, ..., n_{kM} (γ_{kM}, n_{kM} are the Lorentz factor, and the number of particles in the kth center).

For example, the summed angular distribution of two fireballs is defined by the first three moments of the angular distribution uniquely associated with the magnitudes γ_{1M} [17]. Let us further consider the effect of errors in determining the magnitudes on the characteristic curve for the angular distribution for the following assumptions: (a) the number of fireballs equals one; (b) $\gamma_M = \bar{\gamma}_M = \mu$; (c) $\gamma_M \gg 1$. Now the angular distribution can be found through the mathematical expectation T of the quantity λ [18]

$$T(\lambda) = \frac{1}{4.6}\left[2\ln 2 - \ln(m^2-1) - m\ln\left(\frac{m+1}{m-1}\right)\right] - \ln\gamma_M, \tag{19}$$

where

$m = V_M/\beta_M$; β_M is the velocity of the secondary particles in the M-system.

For our assumptions

$$dm \sim \frac{m^2}{3}\frac{d\gamma_M}{\gamma_M}. \tag{20}$$

When $m \sim 1.4$, we obtain

$$|dT| = \left|\frac{\partial T}{\partial m}dm + \frac{\partial T}{\partial \gamma_M}d\gamma_M\right| \sim 1.1\frac{d\gamma_M}{\gamma_M} \tag{21}$$

Using Eq. (17), we obtain

$$\frac{dT}{T} \sim (0.5 \div 1)\frac{d\bar{p}}{\bar{p}}. \tag{22}$$

Thus, if it is put that the ratio is $dT/T \sim 0.1$, the systematic error must be

$$\frac{d\bar{p}}{\bar{p}} \sim 0.1 - 0.2.$$

Eq. (21) is readily generalized for the case when two fireballs occur. For example, when both bunches in the C-system scatter at different velocities, and $n_{1M} = n_{2M}$, we must use the theorem for the mathematical expectation of a sum of random quantities, and the relationships

$$\gamma_{M_{1,2}} = \gamma_C\bar{\gamma}_M \pm \sqrt{(\gamma_C^2-1)(\bar{\gamma}_M^2-1)}, \tag{23}$$

where

$\bar{\gamma}_M$ is the Lorentz factor for the bunch in the C-system;

$\gamma_{M_{1,2}}$ are the Lorentz factors for both bunches in the L-system.

Energy distribution. By using Eq. (18) one can readily assess the permissible error in the determination of p_i (in the L-system) for the case when all p_{iM} are equal (the order of magnitude of the evaluation is retained for a Planckian distribution). What follows from Eq. (18) is that the relative errors in measuring the momenta in both systems (M and L) are approximately the same. But it is far and away more convenient and simpler to make the measurements for the fireball flying in a direction opposite to that in which a primary particle is moving. For example, if $E_L = 10^{12}$ ev and $\gamma_M = 2$, then $\gamma_{M_1} = 80$, and $\gamma_{M_2} = 7$. Consequently, momenta of particles of a "slow" (in the L-system) fireball are fewer than is the case for a fast one by a factor of approximately 10. /36

REFERENCES

1. Ciok, T., et al., Nuovo cimento., Vol. 8, p. 166; Vol. 18, 1958, p. 741.
2. Cocconi, G., Phys. Rev., Vol. 111, 1958, p. 1699.
3. Dobrotin, N. A., Slavatinskiy, S. A., Izv. AN SSSR. Ser. fiz., Vol. 30, 1966, p. 1566.
4. Dremin, I. M., et al., Zh. eksperim. i teor. fiz., Vol. 48, 1965, p. 952.
5. Slavatinskiy, S. A., Dissertation, FIAN, Moscow, 1968.
6. Grigorov, N. L., et al., Yadernaya fizika, Vol. 9, 1969, p. 597.
7. Yemel'yanov, A. A., Rozental', A. L., Zh. Eksperim. i teor. fiz., Vol. 38, 1960, p. 194.
8. Nikol'skiy, B. A., Mishakova, A. P., Zh. Eksperim. i teor. fiz., Vol. 38, 1960, p. 1508.
9. Ciezewsky, D., Krzywiski, A., Nuovo cimento., Vol. 30, 1963, p. 603.
10. Amati, D., et al., Nuovo cimento, Vol. 22, 1961, p. 569; Vol. 26, 1962, p. 896.
11. Van Hove, L., Nuovo cimento., Vol. 28, 1963, p. 798.
12. Murzin, V. S., Sarycheva, L. I., Kosmicheskiye luchi i ikh vzaimodeystviye, [Cosmic Rays and Their Interaction], Atomizdat, Moscow, 1968.
13. Wallenmeyer, W. A., Phys. Rev., Vol. 105, 1957, p. 1058.
14. Rozental', I. L., Uspekhi fiz. nauk, Vol. 94, 1968, p. 91.
15. Abraham, F., et al., Preprint EFINS, 1965, 65-44; see also Gierula, J., Proc. Internat. Conf. on Cosmic Rays, Ld., Vol. 2, 1965, p. 844.
16. Akimov, V. N., et al., Izv. AN SSSR. Ser. fiz., Vol. 30, 1966, p. 1584.
17. Chernov, G. M. Chudakov, V. M., Zh. eksperim. i teor. fiz., Vol. 47, 1964, p. 1273.
18. Kobavkawa, K., et al., Nuovo cimento., Vol. 38, 1963, p. 992.

THE INVESTIGATION OF CASCADE SHOWERS IN A HORIZONTAL FLUX OF COSMIC RAYS

V. V. Borog, V. G. Kirillov-Ugryumov,
A. A. Petrukhin, V. K. Chernyatin, V. V. Shestakov

ABSTRACT. The investigation of the horizontal flux of cosmic rays is continued using an ionization calorimeter to record cascade showers. The results of the operation of the installation in the spring of 1968 are analyzed.

This paper is a continuation of the investigation of the horizontal flux of /37
cosmic rays conducted by the μ-meson group of the MIFI [Moscow Engineering Physics Institute] [1, 2]. An ionization calorimeter (Figure 1), consisting of six rows of IK-6 ionization chambers, was used to record the cascade showers. The axes of chambers in adjacent rows are mutually perpendicular, and the working surface, with an area of 9 m^2, is vertical. The iron absorber between rows is of the order of 5 rad units thick. The electronic system is such that the passage of 60 and more relativistic electrons through the chamber can be recorded with confidence. The position of the shower axis, encompassing several rows, can be fixed approximately by a coordinate grid formed by the ionization chambers, and /38 more precisely with the help of hodoscopic detectors A and B (see Figure 1). Each detector is a set of 96 cells combining six GS-30 gas discharge counters. Cell dimensions are 20 x 60 cm. Detector C protects the calorimeter against the vertical flux of cosmic rays when the control unit is connected to the anticoincidence channel.

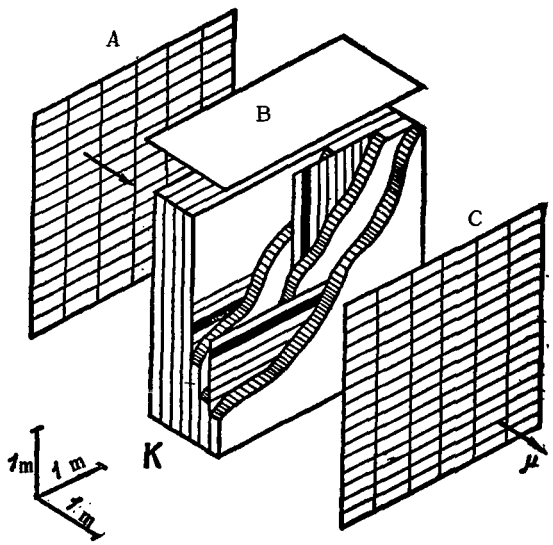

Figure 1. Schematic diagram of the installation (K is the ionization calorimeter; A, B, and C are hodoscopic detectors).

We shall present here an analysis of the results of the operation of the installation in the spring of 1968. The installation was in use in two modes for 850 hours. The control unit, for a large

TABLE 2

Operating mode	Exposure time, h	Accompaniment in detector C		Total
		Yes	No	
$AB\bar{C}K1h$	720	6	7	13
ABK1h	130	4	1	5

multiple showers to select this magnitude as the threshold.

Eighteen multiple events were recorded in 850 hours of exposure. Table 2 shows that at least some of them, accompanied by the functioning of a small number of counters in detector C, owe their occurrence to the vertical flux.

There were eight multiple showers not accompanied by the functioning of detector C. Table 3 lists their characteristics. Yet even they cannot be caused by the practically parallel moving particles in the horizontal flux ($60° \leq \theta \leq 90°$), or those moving at angles of from 0 to 60°. This latter circumstance is associated with the fact that the cells of detector C span but 50% of the area of the horizontal projection of the installation (there is generally no protection for the installation against transverse showers), and the efficiency of recording of strongly interacting high-energy particles is close to unity. The ionization attributable to each of the multiple showers in events 4, 6 and 7 (see Table 3) was observed in a group of three to four chambers, characteristic of showers greatly inclined toward the plane of the installation's working surface. These considerations cast doubt on the connection between the multiple showers recorded and the groups of μ-mesons in the horizontal flux.

A characteristic feature of the majority of the recorded multiple showers /44
in each case is the small magnitude of one of them close to the threshold of sensitivity of the individual channels (60 relativistic electrons). When the results obtained are compared with the data in [4], this difference in the power of multiple showers in both papers must be given special emphasis. If multiple showers nevertheless are caused by electromagnetic interactions of groups of μ-mesons, this can be explained quite readily by the difference in the materials used for the absorbers in the installations (lead and iron). The probability of an electromagnetic interaction is proportional to the ratio

TABLE 3

Event	Frame	Ionization in the rows corresponding to the passage of no more than (relativistic particles)					Distance between axes of showers less than, mm	Number of cells in detector functioning		Interval in zenith angles θ° permitted by geometry of installation
		Rows						A	B	
		2	3	4	5	6				
1	373027	—	—	140	250—340	540	30	11	15	0—85
2	380078	—	—	—	110	330—130	150	4	1	10—85
3	381043	130—240	410	—	—	—	210	2	2	15—75
4	393025	—	—	570—160	—	—	150	5	8	0—75
5	404071	—	—	190	210—1680	110—230	30—270	2	5	0—55
6	440033	—	—	450—150	—	—	180	1	2	0—75
7	446007	—	—	370—210	480	—	60	1	5	0—80
8	450064	—	—	—	—	140—170	30	1	3	10—85

Z^2/A, and the probability of a double interaction to $(Z^2/A)^2$. For lead $(Z^2/A) \approx 32$, and for iron $(Z^2/A) \approx 12$. Thus, the probability of a double interaction in iron is less than it is in lead by a factor of about 7. And if consideration is given to the fact that the number of cascade particles in a shower of specified energy in iron is less than it is in lead by a factor of about 2, and the fall-off of the μ-meson energy spectrum is noted, the probability of a double interaction in iron should decrease further, by a factor of 15. Accordingly, the probability of the appearance of multiple showers with an identical number of cascade particles in iron is less than in lead by at least a factor of 2. Thus, the absence of high-power multiple showers can only be indicative of the fact that there are no mechanisms for the formation of these showers that do not depend on the material.

REFERENCES

1. Borog, V. V., et al., V. sb. Fizika elementaryykh chastits [IN: Physics of Elementary Particles], Atomizdat, Moscow, 1966, p. 59.

2. Borog, V. V., et al., Izv. AN SSSR. Ser. fiz., Vol. 39, 1966. p. 1669.

3. Goryunov, N. N. and Zatsepin, G. T., Zh. eksperim. i teor. fiz., Vol. 39, 1960, p. 271.

4. Vernov, S. N., et al., Proc. IX Internat. Conf. on Cosmic Rays, Vol. 2, 1966, p. 952.

PROSPECTS FOR THE INVESTIGATION OF HIGH-ENERGY COSMIC μ-MESONS

V. G. Kirillov-Ugryumov, A. A. Petrukhin

ABSTRACT. Basic problems involved in future investigations of cosmic μ-mesons are reviewed. Particular attention is given to the possibility of establishing the percentage of K-mesons in terms of angular distribution of μ-mesons, and to the nuclear interaction of μ-mesons. Principal results obtained from investigations made of cosmic μ-mesons up to 1968, are included.

The investigation of high energy μ-mesons is one of the most important tasks /45 of cosmic ray physics. Interest in such investigations is based on the fact that contemporary theory cannot explain the nature of μ-mesons, nor the paradoxical situation wherein two particles, a μ-meson and an electron, differing in mass by a factor of 200, will interact in identical fashion. Investigations of static properties of μ-mesons, and experiments with low energies, cannot point to the road that will solve this particular problem. It is possible that experiments with high energies can solve this problem.

There are two basic trends in these investigations. The first involves the study of the characteristics of the flux of μ-mesons in the atmosphere, for it can provide information on how μ-mesons occur (that is, on the mechanics of their generation). A comparison between these data and the primary cosmic-ray spectrum will make it possible to examine various models of strong interactions in the domain of superhigh energies. The second involves investigation of μ-meson interaction. The purpose is to find unusual interactions and to examine high-energy quantum electrodynamics.

In what follows we shall review the basic problems of future investigations of cosmic μ-mesons. Particular attention has been given to two problems which, today, are of great interest: the possibilities of establishing the percentage of K-mesons in terms of the angular distribution of μ-mesons; and the nuclear interaction of μ-mesons. A provisional summary of principal results obtained from investigations made of cosmic μ-mesons up to 1968 is included.

1. The Origin of μ-mesons

The following characteristics of μ-mesons in the atmosphere can provide information on the origin of cosmic μ-mesons: (a) angular distribution; (b) energy spectrum; (c) charge ratio; (d) degree of polarization; (e) the parameters for groups of μ-mesons.

The angular distribution of μ-mesons can provide information on the mechanics /46 of generation between 10^{11} and 10^{12} ev. For example, if μ-mesons originate right in nuclear interactions, their angular distribution should be isotropic (when energies are sufficiently high, and when absorption and decay in the atmosphere can be ignored). If μ-mesons occur as a result of the decay of certain particles, the spectrum at large zenith angles should be flatter than along the vertical. The energy range depends on particle mass and life. This range is from 10^{11} to 10^{12} ev for π- and K-mesons. The maximum difference between spectra, which provides a means for establishing the channels for μ-meson production is obtained for spectra at angles of 0° and 90°. It should be pointed out that the availability of information on an energy spectrum for one zenith angle will not yield unique information on channels for the generation of μ-mesons because the energy spectrum is dependent to a great extent on the models for strong interaction used in the computation, as well as on the generation mechanism.

An energy spectrum for a horizontal flux was obtained simultaneously in two different papers; on a magnetic spectrometer [1], and with an ionization calorimeter [2]. The results were in good concordance [3]. Reliable experimental data have been obtained up to energies of the order of 10^{12} ev. However, neither of these efforts can provide information on channels for the generation of μ-mesons without drawing on information concerning the vertical spectrum because in the first investigation [1] the range of zenith angles covered is small and the statistics are sparse, and in the second [2] the accuracy with which the zenith angles were measured is poor.

As of this time there have been over fifteen papers written on investigations made of the vertical spectrum in the energy range above 10^{11} ev by various methods. Unfortunately, the results contained in these papers are very divergent indeed, so the resultant spectrum in the 10^{12} ev range can only be obtained when all of the papers are taken into consideration. An analysis made in this manner

[3] shows that the most probable value of the index for the integral spectrum of the vertical flux of μ-mesons is 2.4 (at least up to $2 \cdot 10^{12}$ ev). Since the index for the horizontal spectrum, at least according to available data [1, 2], is 2.0 to 2.1, the conclusion is that the flatter slope of the horizontal spectrum is indicative of the anisotropy of the angular distribution of μ-mesons, that is, of the decaying nature of their generation.

However, there has been a recent paper dealing with the investigation of the absorption curve at various zenith angles [4], from the results of which the authors reached the conclusion that the angular distribution of high-energy cosmic μ-mesons is practically isotropic up to approximately 80°. Although underground measurements always have a certain indeterminacy (see section 2), these results [4] are very interesting, and the question of the nature of the /47
angular distribution (and more precisely, of the degree of isotropy, or anisotropy) is still an open one.

Charge ratio investigations have been going on continuously for many years. Today there are measurements up to energies of 10^{12} ev in vertical, as well as in horizontal fluxes of μ-mesons [5]. But there is no way to establish the uniqueness of the generation mechanism from these experiments because the measurements have not been accurate enough, and because of the indeterminacy of the strong interaction model [6].

Investigation of polarization makes it possible to establish the percentage of K-mesons responsible for the formation of μ-mesons in the 10^{10} ev range. Intensive investigations were made a few years ago. An analysis of the results obtained [7] revealed that the percentage of K-mesons, charged, as well as neutral, is 40 ± 20% up to energies of approximately 20 GeV. There is little future in making polarization investigations at higher energies, so as of today they have pretty much ceased.

Until recently, study of groups of μ-mesons was based on work connected with the investigation of widespread atmospheric showers [8]. The existence of groups was virtually ignored in the work done on investigating the characteristics of fluxes of cosmic μ-mesons. Consideration of their existence is particularly important at high energies, when μ-mesons very seldom put in an appearance, and then only in groups. The use of an installation with an area

of up to tens of square meters is suggested because several μ-mesons can fall on it simultaneously. It is possible that herein is the reason for the sharp divergence in the results of the various experiments conducted in the energy ranges above 10^{12} ev.

2. Interaction of μ-Mesons

The following processes of the interaction of μ-mesons have been studied in cosmic rays: (a) nuclear scattering; (b) electron scattering; (c) the formation of electron-positron pairs; (d) bremsstrahlung; (e) nuclear interaction.

The first process has not yet been investigated in cosmic rays because μ-meson beams have appeared in accelerators where the domain of transmitted pulses attained of some 1 GeV/c is completely unrealistic for experiments in cosmic radiation.

μ-meson-electron scattering is being investigated in cosmic rays, as well as in accelerators. As distinguished from the first process, the particles taking part in it interact only electromagnetically, so the particular process /48 is the only one that can be used to examine the quantum electrodynamics of the μ-meson in pure form. Much of the work done with cosmic radiation has resulted in an experimental value for the cross-section greater than the theoretical (the upper limit for the energy transmitted to the electron of some 20 GeV) [9]. Work on accelerators has agreed with the theory, but has not yet reached the energy domain in which anomalies in cosmic rays have been observed (upper limit 3.4 GeV) [10].

Investigation of the formation of electron-positron pairs in the case of high transmitted energies is made very difficult because of the admixture of pairs from the γ-quanta of bremsstrahlung from the μ-mesons, the cross-section of which is greater than the cross-section for the formation of the pairs by two orders of magnitude. The experiments were conducted using low energy μ-mesons. Results are contradictory, and the use of different theoretical formulas to analyze the data obtained makes a comparison difficult.

The pair formation cross-section is quite large in the case of low transmitted energies, but this domain is of interest for the recording of superhigh-

energy μ-mesons, and not for interaction investigation. This possibility has been under active discussion in recent years and the corresponding installations have been designed, but no results have been published, as yet.

Bremsstrahlung is the fundamental process responsible for the formation of electromagnetic cascade showers of high-energy μ-mesons. Today, cascade showers are used for the restoration of the μ-meson energy spectrum [11]. And the bremsstrahlung cross section is taken as known. If the μ-meson energy spectrum is measured in independent experiments, the possibility of establishing the cross section up to energies of 10^{12} ev develops [12].

Investigation of the nuclear interaction of μ-mesons, something that will make it possible to determine the cross section of the photonuclear process $\sigma_{\gamma N}$ at energies exceeding the capabilities of modern accelerators by two orders of magnitude, is of interest. Estimates of the cross section $\sigma_{\gamma N}$ up to energies of 300 GeV were obtained in experiments carried out in cosmic radiation [13], whereas only energies up to 5 GeV were possible in accelerators [14]. A comparison of all the available data [13] has shown that the results of different efforts may differ from each other over the range of one whole order of magnitude. Three basic reasons for the divergence in the results of the different experiments can be pointed out.

1. The energy transmitted in a particular interaction usually is unknown, and in some of the experiments there is no guarantee at all that all of the secondary particles, particularly the neutral ones, have been recorded.

2. The magnitude of the minimal transmitted energy, something that all /49
computations depend on quite substantially because the cross section is inversely proportional to this energy, is very tentatively estimated.

3. Virtually none of the papers on the subject took into account the probability of recording nuclear interactions in terms of energy.

A few words must be said about underground (or underwater) investigations of the absorption curve, because, at least in principle, these investigations should provide a way to establish the sum of the integral cross sections of the interaction of μ-mesons (loss of energy, more precisely). The results of underground measurements today are used primarily for solving the reverse problem, that is, for obtaining the μ-meson energy spectrum and angular distribution.

This method has at least four drawbacks. First of all, precise information as to the composition of the soil at great depths within a quite wide interval of zenith and azimuth angles is needed for conversion. Second, the precise magnitude of the energy losses in the nuclear interaction is unknown. Third, the experiment must be conducted in such a way that so far as a great percentage of the underground measurements made are concerned, there is no way to separate information on the energy spectrum from that on angular distribution of the μ-mesons. Therefore, if the experimental data are to be used to obtain the energy spectrum, the angular distribution must be given. Finally, the conversion factor for great depths is dependent exponentially on the magnitude of energy losses, so underground measurements should be statistically accurate, as well as free from any fixed errors.

Underwater measurements are free of the first drawback, but the limited depth of the world ocean and the technical difficulties involved prevent any great progress being made in terms of energy. Today, underground measurements have reached a depth of some 8,000 meters of water equivalent, corresponding to approximately $7 \cdot 10^{12}$ ev [15].

3. Tasks of Future Investigations of High-Energy Cosmic μ-Mesons

Determination of the mechanisms involved in the generation of cosmic μ-mesons is the basic task remaining. Naturally enough, if the complete picture of the formation of μ-mesons in the atmosphere is to be obtained, all the characteristics of the μ-meson flux must be investigated, including angular distribution and the other characteristics. Practically speaking, angular distribution is dependent only on the composition of the particles decaying into μ-mesons, and does not depend on the interaction model (given the condition that the model /50
does not depend on the composition of the particles). Thus, investigation of the angular distribution helps establish the channels for μ-meson generation. The first thing that must be done is to establish the presence, or absence, of direct generation of μ-mesons. The next step involves a determination of the percentage of all possible generation mechanisms, including the percentage of K-mesons (see section 4).

A second task for the future is the investigation of the nuclear interaction of μ-mesons. The problem here is disussed in section 5 of this article.

Here, we will simply say that the investigation of nuclear interaction should include measurement of the cross section of the interaction, as well as a study of the structure and form of the nuclear cascades occurring. A comparison of these data with existing cascades from nuclear active particles can provide additional information on the nature of the nuclear interaction of μ-mesons.

Investigation of electromagnetic interactions of μ-mesons in cosmic radiation offers less of a challenge with respect to accelerators than does the study of nuclear interaction. In this case the accuracy required is incomparably greater. Yet there is a constant flow of papers in which divergences from electrodynamics can be noted, as can the absence of μ-meson beams of corresponding energies in accelerators, and this is what serves to stimulate these investigations in cosmic radiation. A detailed analysis of electron-photon showers, caused by the electromagnetic interaction of μ-mesons, is an additional possibility for examining the basic formulas of quantum electrodynamics, and particularly the cascade theory.

It is expedient to solve all of these problems by using the horizontal flux of cosmic μ-mesons. The principal consideration in favor of the use of this selection is as follows. Although the maximum difference between spectra providing for the possibility of determining the channels for the generation of μ-mesons is at 0° and 90°, the energy spectrum in the high-energy domain (greater than 10^{11} ev) is practically independent of the angle in the 0-60° range. Basic changes take place in the spectrum in the interval 60 to 90°, roughly. This is why it is more expedient to investigate the flux of μ-mesons at large zenith angles (60 to 90°) in order to obtain the necessary data with one installation. And it is more advantageous to investigate the interaction of μ-mesons in a horizontal flux of cosmic μ-mesons because the presence of decay channels for the generation of high-energy μ-mesons (and there will always be some percentage of such channels) results in there being more of them in the horizontal flux than in the vertical.

There are additional arguments to be advanced in favor of the horizontal flux. First of all, there is no requirement for an underground vault in which to set up the experiments, so costs are reduced sharply; second, widespread super-high energy air showers at angles larger than 70° were recorded /51 recently, so the investigation of the horizontal flux will make it possible to

enlarge the search for these unique events; and, third, groups of μ-mesons can be investigated in the horizontal flux, something that was confined to the vertical flux alone until recently.

4. Determination of K- and π-Meson Percentages

Let us make the computation for the statistics needed to establish K- and π-meson percentages. At first glance, the results contained in [4] would suggest that there is no need to do so, but in defense of our proposal, we cite two considerations. First, despite the possible emergence of new channels for high energy generation, the decay of π-mesons as a source of μ-mesons should be retained, because there is no doubt regarding the formation of π-mesons of corresponding energies in nuclear interactions. Second, K-decay yields an angular distribution close to isotropic in the energy domain up to 10^{12} ev, so that estimates obtained for K-decay will be the upper limit for direct generation in this domain.

Let there be two channels for the generation of μ-mesons (π- and K-decays) with intensities a_π and a_K, respectively. If we want to show that $a_K/a_\pi \leq \alpha$ [or, and this is the same thing, that $a_\pi/a_K \geq 1/\alpha$], we need to satisfy the inequality

$$\frac{a_K + m\sigma(a_K)}{a_\pi - m\sigma(a_\pi)} \leqslant \alpha, \tag{1}$$

where

$\sigma(a)$ is the root-mean-square error in finding a_π and a_K;

m is the number of standard deviations.

Let us find the minimum for the following functional in order to evaluate the necessary statistics by the least squares method

$$M = \sum_i (a_\pi N_{\pi i} + a_K N_{Ki} - F_i)^2 W_i, \tag{2}$$

where

$N_{\pi i}$ and N_{Ki} are the values of the spectra at the i^{th} point for the π- and K-mesons, respectively;

F_i is the spectrum's measured value;

W_i is the weight of the i^{th} measurement.

Differentiating Eq. (2) with respect to a_π and a_K, and equating the derivatives to zero, we obtain the following system of equations

$$\left.\begin{aligned} a_\pi \sum_i N_{\pi i}^2 W_i + a_K \sum_i N_{\pi i} N_{Ki} W_i &= \sum_i F_i N_{\pi i} W_i; \\ a_K \sum_i N_{\pi i} N_{Ki} W_i + a_K \sum_i N_{Ki}^2 W_i &= \sum_i F_i N_{Ki} W_i. \end{aligned}\right\} \quad (3)$$

The solution for this system is /52

$$a_\pi = \frac{\Delta_\pi}{\Delta} \quad \text{and} \quad a_K = \frac{\Delta_K}{\Delta}, \quad (4)$$

where

$$\Delta_\pi = (\sum_i F_i N_{\pi i} W_i) \sum_i N_{Ki}^2 W_i - (\sum_i F_i N_{Ki} W_i) \sum_i N_{\pi i} N_{Ki} W_i;$$

$$\Delta_K = (\sum_i F_i N_{Ki} W_i) \sum_i N_{\pi i}^2 W_i - (\sum_i F_i N_{\pi i} W_i) \sum_i N_{\pi i} N_{Ki} W_i;$$

$$\Delta = (\sum_i N_{\pi i}^2 W_i) \sum_i N_{Ki}^2 W_i - (\sum_i N_{\pi i} N_{Ki} W_i)^2.$$

The dispersions in the quantities a_π and a_K will be equal to

$$D(a_\pi) = \frac{D(\Delta_\pi)}{\Delta^2} \quad \text{and} \quad D(a_K) = \frac{D(\Delta_K)}{\Delta^2}. \quad (5)$$

After the computation, we obtain

$$D(a_\pi) = \frac{\sum_i N_{Ki}^2 W_i}{\Delta} \quad \text{and} \quad D(a_K) = \frac{\sum_i N_{\pi i}^2 W_i}{\Delta}. \quad (6)$$

We compute the quantity Δ for the following conditions

$$\left.\begin{aligned} N_{\pi i} &= \pi_i N_v \quad \text{and} \quad N_{Ki} = k_i N_v; \\ W_i &= 1/F_i \quad \text{and} \quad F_i \approx N_i = (a_\pi \pi_i + a_K k_i) N_v, \end{aligned}\right\} \quad (7)$$

where

N_v is the intensity of the μ-mesons along the vertical;

π_i and k_i are the coefficients of change in intensity in terms of the angle for the different generation channels.

We than proceed to the computations for the case of measurements at two zenith angles. Then

$$\Delta = N_v^2 \frac{(\pi_1 k_2 - \pi_2 k_1)^2}{(a_\pi \pi_1 + a_K k_1)(a_\pi \pi_2 + a_K k_2)}. \quad (8)$$

Computing $D(a_{\pi, K})$ for these same conditions, and introducing the designations

$$\sigma(a_\pi) = \sqrt{D(a_\pi)} = \sigma_\pi \sqrt{N_v},$$

$$\sigma(a_K) = \sqrt{D(a_K)} = \sigma_K \sqrt{N_v},$$

we obtain the following for the inequality of Eq. (1) /53

$$N_v \geqslant m^2 \left(\frac{\sigma_K + \alpha\sigma_\pi}{\alpha a_\pi - a_K} \right)^2, \quad (9)$$

where

$$\sigma_\pi = \sqrt{\frac{k_1^2(a_\pi \pi_2 + a_K k_2) + k_2^2(a_\pi \pi_1 + a_K k_1)}{(\pi_1 k_2 - \pi_2 k_1)^2}};$$

$$\sigma_K = \sqrt{\frac{\pi_1^2(a_\pi \pi_2 + a_K k_2) + \pi_2^2(a_\pi \pi_1 + a_K k_1)}{(\pi_1 k_2 - \pi_2 k_1)^2}}.$$

Specific computations were made for two intervals of zenith angles; 60-70°, and 80-90°. Reference [17] provided the values for the coefficients π_1, π_2, k_1 and k_2. The statistic needed for certain values of μ-meson energies for various assumptions with respect to the relationship between the channels for the decays of K- and π-mesons for m = 3 are listed in the table. Tabulated data were obtained for the condition that there are two points at the angular distribution. Use of a great many points will result in a reduction in the needed statistic. In this sense, the numbers in the table provide the upper limit.

5. Nuclear Interaction of μ-Mesons

Once George and Evans [18] discovered the nuclear interaction of μ-mesons, a great many attempts were made to obtain the cross section of this process. The usual interpretation reduces to a replacement of a μ-meson by a field of virtual photons, the cross section of interaction of which, it is assumed, is no different than the cross section of real photons

$$\sigma_n(E_\mu, E, q) = A\sigma_{\gamma N} f(E_\mu, E, q), \quad (10)$$

where

E_μ is the μ-meson's primary energy;

a_K	E_μ, Tev*	$\alpha = 0.1$	0.3	0,5	2	5	10
0	0,2	29000	3900	1800	320	180	140
	0,5	14000	1900	800	140	70	50
	1.0	22000	2000	1100	180	100	70
	2.0	17000	2400	1000	200	110	90
	5.0	48000	7000	3200	650	380	290
	10	90000	14000	6000	1400	830	680
0.2	0.2	19000	200000	10000	620	280	210
	0.5	10000	140000	8200	820	500	400
	1.0	12000	130000	8300	370	170	120
	2.0	11000	120000	5700	300	230	120
	5.0	33000	380000	19000	1300	630	480
	10	62000	730000	34000	2800	1400	1100
0.5	0.2	1200	2400	5700	5000	900	560
	0,5	560	950	2700	1800	350	200
	1.0	770	1520	3700	2500	500	300
	2.0	760	1520	3600	2600	550	340
	5.0	2200	4600	11000	9300	2000	1300
	10	4200	9700	23000	20000	5000	3100
0.8	0.2	330	470	640	5800	80000	9000
	0.5	160	210	380	2300	30000	2400
	1,0	290	400	530	4500	60000	5000
	2,0	270	360	510	4600	60000	5000
	5.0	780	1100	1600	16000	230000	20000
	10	1500	2100	3100	34000	500000	46000
1.0	0.2	190	230	290	840	2800	9000
	0,5	90	110	130	330	1000	3000
	1.0	120	150	180	500	1600	4800
	2,0	120	150	190	510	1800	5500
	5.0	400	500	600	2000	7500	24000
	10	800	1000	1400	5000	18000	60000

/54

*1 TeV = 10^{12} eV.

E is energy of the nuclear interaction;

q is the transferred momentum;

$\sigma_{\gamma N}$ is the photonuclear cross section for a nucleon;

A is the number of nucleons in the nucleus.

The functions $f(E_\mu, E, q)$ obtained in various of the theoretical papers on the subject differ greatly from each other, and this, naturally enough, makes interpretation of experiments difficult. But the values of the cross section $\sigma_{\gamma N}$ even for the same function $f(E_\mu, E, q)$, are greatly divergent, as has been pointed out in [13]. Possible experimental reasons were reviewed in section 2. But there can be reasons of yet another order of magnitude. First of all, the cross section $\sigma_{\gamma N}$ is assumed constant when it is computed. If it in fact depends on the energy, this procedure has no validity. Second, a logarithmic dependence on E_μ has been given in all known computations for the function $f(E_\mu, E, q)$. Reference [19], dealing with work done with a μ-meson beam in Brookhaven, estab- /55 lished a linear dependence between the cross section $\sigma_n(E_\mu, E, q)$ and E_μ. A theoretical model of the nuclear interaction of μ-mesons proposed by Hand and Wilson was set up there and provides a linear dependence for $\sigma_n(E_\mu)$. If this dependence is adopted for other efforts concerned with the nuclear interaction of μ-mesons, the values for $\sigma_{\gamma N}$ obtained from them will be changed greatly.

The linear dependence in [19] is established for a narrow band of μ-meson energies; 2.5 to 10.5 GeV. Question. How far does this dependence extend in terms of energy? There is an even more general question. As is known, all other cross sections of the interaction of μ-mesons, beginning at some energy value, become constant. Can this fact be extended to include the nuclear interaction of μ-mesons? The answer to this question is significant for a correct determination of $\sigma_{\gamma N}$ and for its dependence on energy. This question is equally important in interpreting the results of underground measurements. If the nuclear cross section increases up to very high energies, and is still linear, a flatter spectrum than that usually accepted [15] is required in order to explain the results.

Eq. (10) gives the linear dependence of the cross section in terms of A; that is, the cross section of the nuclear interaction of μ-mesons is considered

as proportional to the number of nucleons in the nucleus. This dependence has not been investigated experimentally at high energies. At the same time, according to recent data [20, 21], the cross section of the interaction of protons with nuclei is as $A^{2/3}$. If this dependence proves valid for the nuclear interaction of μ-mesons, this will result in a change in energy losses in nuclear interaction for soil. Actually, virtually all investigations of nuclear interaction were made with lead, so the magnitude b_1 could be computed accordingly. The conversion for b_s can be made through the formula

$$b_s = b_1 (A_s/A_1)^{\beta}. \tag{11}$$

The value of b_s will differ with β. If β is reduced from 1 to 2/3, b_s will increase by a factor of

$$(A_1/A_s)^{1-\beta} = (207/22)^{1/3} = 2.1.$$

Accordingly, we can distinguish three primary tasks in investigating the nuclear interaction of μ-mesons.

1. The nature of $\sigma_n(E_\mu)$ must be established, as must the limits of its increase with energy.

2. The cross section $\sigma_{\gamma N}$ in the domain above 10^{11} ev, and its change with energy, must be estimated. /56

3. The $\sigma_n(A)$ relationship must be investigated.

It goes without saying that the goal is a precise formula for the Eq. (10) cross section.

The problems considered show that there are, in the physics of cosmic μ-mesons, problems of interest to high energy physics. Once the percentages of K- and π-mesons at energies greater than 10^{12} ev are established, certain conclusions can be drawn concerning the role of foreign particles at these energies. The second problem is of greater interest for the physics of μ-mesons. A comparison of cross sections of the inelastic interaction of μ-mesons and electrons, as made in [19], provides hope for a solution for the basic problem; the problem of the difference in the masses of the μ-meson and the electron.

REFERENCES

1. MacKeown, R. K., et al., Proc. IX Internat. Conf. on Cosmic Rays, Vol. 2, London, 1966, p. 964.
2. Borog, V. V., et al., Yadernaya fizika, Vol. 3, 1966, p. 783.
3. Borog, V. V., et al., V sb: Elementarnyye chastitsy i kosmicheskiye luchi [IN: Collection: Elementary Particles and Cosmic Rays], Atomizdat, Moscow, 1967, p. 19.
4. Bergeson, H. E., et al., Phys. Rev., Lett., Vol. 19, 1967, p. 1487.
5. Palmer, N. S. and Hash, W. F., Canad. J. Phys., Vol. 46, 1968, p. 313.
6. MacKeown, P. K., et al., Proc. IX Internat. Conf. on Cosmic Rays, Vol. 2, London, 1966, p. 937.
7. Osborne, J. L., Nuovo cimento, Vol. 32, 1964, p. 816.
8. Vernov, S. N., et al., Izv. AN SSSR. Ser. fiz., Vol. 30, 1966, p. 1694.
9. Deery, R. F. and Neddermeyer, S. H., Phys. Rev., Vol. 121, 1961, p. 1803.
10. Backenstoss, G., et al., Phys. Rev., Vol. 129, 1963, p. 2759.
11. Borog, V. V., et al., Izv AN SSSR. Ser. fiz., Vol. 30, 1966, p. 1669.
12. Ashton, F., et al., Canad. J. Phys., Vol. 46, 1968, p. 361.
13. Borog, V. V., et al., Canad. J. Phys., Vol. 46, 1968, p. 382.
14. Crouch, A., et al., Phys. Rev., Lett., Vol. 13, 1964, p. 636.
15. Miyake, S., et al., Nuovo cimento, Vol. 32, 1964, pp. 1505 and 1524.
16. Matano, T., et al., Canad. J. Phys., Vol. 46, 1968, p. 369.
17. Zatsepin, G. T. and Kuz'min, V. A., Zh. eksperim. i teor. fiz., Vol. 39, 1960, p. 1677.
18. George, E. P. and Evans, J., Proc. Phys. Soc., Vol. A63, 1950, p. 1248.
19. Kirk, J. A., et al., Preprint, University of Washington, USA, September 1968.
20. Belletini, G., et al., Nucl. Phys., Vol. 79, 1966, p. 609.

Denisov, Ye. V., Izv. AN SSSR. Ser. fiz., Vol. 32, 1968, p. 398.

AN EXPERIMENTAL SEARCH FOR HEAVY PARTICLES AT SEA LEVEL

A. M. Gal'per, V. A. Gomozov, V. G. Kirillov-Ugryumov,
Yu. D. Kotov, B. I. Luchkov

ABSTRACT. A method for isolating heavy particles, the experimental installation used, and the first results of a search at sea level for heavy particles with unit charge are described.

There are, at this time, a considerable number of papers dealing with the /57
search for quarks with a fractional charge (1/3 e, 2/3 e and 4/3 e), in accelerators [1-5] and in cosmic rays [6-17]. Results of all these searches have been negative. The upper limit of the flux of quarks in cosmic rays is about 10^{-10} $cm^{-2} \cdot sec^{-1} \cdot ster^{-1}$ at sea level [16, 17]. However, there is the possibility that a theory holding that quarks could have a whole unit charge (1 e) [18] could be built. The search for quarks with unit charge has been much less intensive, and the corresponding upper limit of the flux of these quarks is approximately 10^{-8} $cm^{-2} \cdot sec^{-1} \cdot ster^{-1}$ [19-24].

The search for heavy particles with unit charge in cosmic rays is of interest in and of itself, and regardless of the quark hypothesis. Particles such as these could be new elementary particles, or singly charged nuclei, such as the heavy hydrogen isotope H^5, for example.

The presence of heavy, long-lived particles in cosmic rays was suggested in [25] in order to explain certain experiments in connection with the study of cosmic rays [26]. Reference [27] presented the results of searches for heavy, long-lived particles with mass greater than, or equal to, 5 GeV/c^2 and lifetime $\tau \geq 10^{-6}$ second, with strong and/or electromagnetic interactions. As in the case of quarks with fractional charge, no such particles were found.

This paper describes the method used to isolate heavy particles, the experimental installation used, and the first results of a sea level search for heavy particles with unit charge. The isolation method used resulted in the recording of subrelativistic particles with velocity $\beta < 0.59$, mass $M \geq 3.5$ GeV/c^2, and lifetime $\tau \geq 5 \cdot 10^{-9}$ second. Particles could be recorded by the installation if they traversed it unaccompanied by other ionizing particles.

1. The Isolation Method Used /58

Isolation of heavy particles from the total flux of cosmic rays is based on the dependence of the ionizing path of the particle on its velocity, charge, and mass. The path of a particle with charge Z, mass M, and velocity βc can be expressed in terms of the following relationship

$$R = \frac{M}{Z^2} f(\beta c),$$

where

$f(\beta c)$ is the universal function of βc.

For fixed velocity, the path is directly proportional to the mass of the particle, and inversely proportional to the square of the charge. The longest path will be in the tritium nucleus, at least among the known singly charged particles. If a block of a material, the thickness of which is in excess of the ionizing path of a tritium nucleus with given velocity, is placed in the path of a stream of particles, all the known particles, mesons, protons, deuterons, tritium nuclei, and nuclei with $Z \geq 2$ with the same velocity, will be decelerated and will stop inside the block. Only particles with mass greater than the mass of tritium will traverse the block. By thus making a selection of the particle flux in terms of velocity (something that can be done with a Cerenkov threshold counter) and in terms of path, heavy particles can be isolated from the flux.

2. The Installation

The block diagram of the installation is shown in Figure 1. Two Cerenkov counters, CC_1 and CC_2, with a threshold velocity $\beta_{min} = 0.59$, are used for

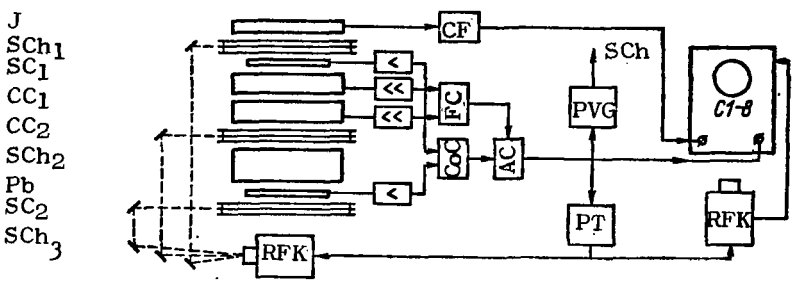

Figure 1. Block diagram of the installation.

velocity selectors. Events are recorded when there is coincidence between pulses from the scintillation counters SC_1 and SC_2, and no pulses from CC_1 and CC_2. At the same time, particles traversing the entire installation, and which have velocities below β_{min} in CC_1 and CC_2, are sorted out. The block of lead, 137 g/cm^2 thick, absorbs singly charged particles with velocity below β_{min} and /59 mass less than 3.8 m_p, where m_p is the proton mass.

The spark chambers isolate cases of singly charged particles traversing the installation without scattering. Scintillation counter J, which measures the ionization produced in it by particles, is used to separate the heavy particles from the μ-mesons, protons, tritium nuclei, and particles with $Z \geq 2$ that can be recorded as a result of the counting losses in the Cerenkov counters.

When a charged particle traverses the installation, pulses with 50 nsec delays are supplied to the coincidence circuit, CoC, which has a resolving time of 16 nanoseconds, through the amplifier. Pulses flow from CC_1 and CC_2 through the amplifier to the pulse shaper, FC, the output of which is a 100 nanosecond pulse if a pulse from just one of the Cerenkov counters is supplied to the input. The pulse then flows from the shaper to the anticoincidence circuit AC, in the inhibit channel. The pulse path is then from counter J through the cathode follower, CF, to the input of the S1-8 oscillograph.

A pulse from the AC output triggers the oscillograph sweep, the high-voltage pulse generator, PVG, and the circuit for triggering the photorecorder, PT. The RFK-5 photorecorders photograph the oscillograph screen and the spark chambers in two projections.

Counters SC_1 and SC_2 set the aperture ratio for the installation, which is 31 cm^2·ster. The counters are plastic scintillators measuring 160 x 160 x 15 mm. Light conductors serve to end-collect the light. FEU-16 photomultipliers, two for each counter, are used in the counters. A cable with a characteristic impedance of 150 ohms is the FEU-16 load.

The Cerenkov counters, CC_1 and CC_2, are designed to disconnect the logic element when particles, the velocities of which are $\beta > 0.59$, traverse the installation. They are made of TF-3 lead glass (specific weight 4.46 g/cm^3) 200 x 200 x 80 mm. Each glass block is edge-scanned by two FEU-52 photomulti-

pliers. The two anticoincidence counters are used to reduce the background of false readings because the counting loss probability is $(1 - \eta_c)^2$, where η_c is the efficiency of each of the Cerenkov counters. When relativistic cosmic μ-mesons were measured counter efficiency was $\eta_c = 0.985 \pm 0.005$.

The ionization counter, J, is designed to measure the ionization produced in it by a particle traversing the installation, and is a plastic scintillator measuring 500 x 500 x 50 mm. It is scanned by five FEU-36 photomultipliers. The counter is shifted 40 mm relative to the axis of the installation and part of the scintillator acts as a light conductor. Amplitude resolution for counter J, measured by cosmic μ-mesons, is approximately 30% (Figure 2).

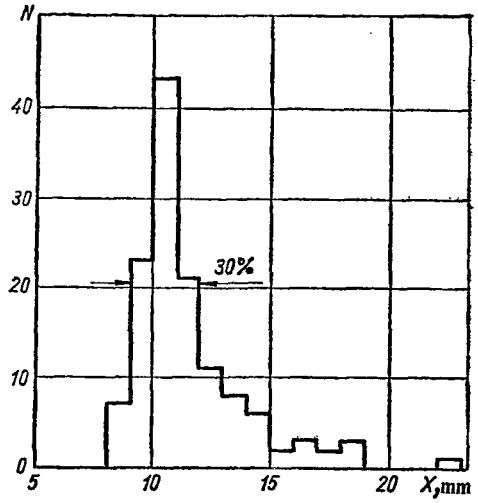

Figure 2. Counter J resolution curve plotted from cosmic μ-mesons. Ionization in millimeters of the oscillograph scale is plotted on the X-axis.

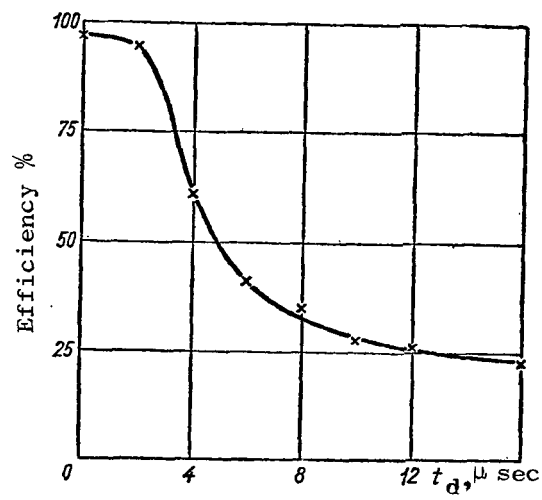

Figure 3. Efficiency of spark chambers in terms of delay time, t_d.

/60

All photomultipliers were selected for signal/noise ratio, and have matching /62 impedances in their supply circuits. Spark chambers SC_1-SC_3 have two 10 mm gaps apiece, and are filled with neon at atmospheric pressure. The gas in the chamber is replaced by purging after each week of operation. The response surface of the chambers measures 400 x 400 mm. Spark chamber electrodes are 4 mm thick sheet aluminum. The side walls are made in the form of plexiglas strips with a cross section of 10 x 10 mm. Figure 3 shows spark chamber efficiency in terms of delay time. A high-voltage pulse, delivered to the SC, and delayed 1.2 μsec with respect to the functioning of the anticoincidence circuit, a delay with

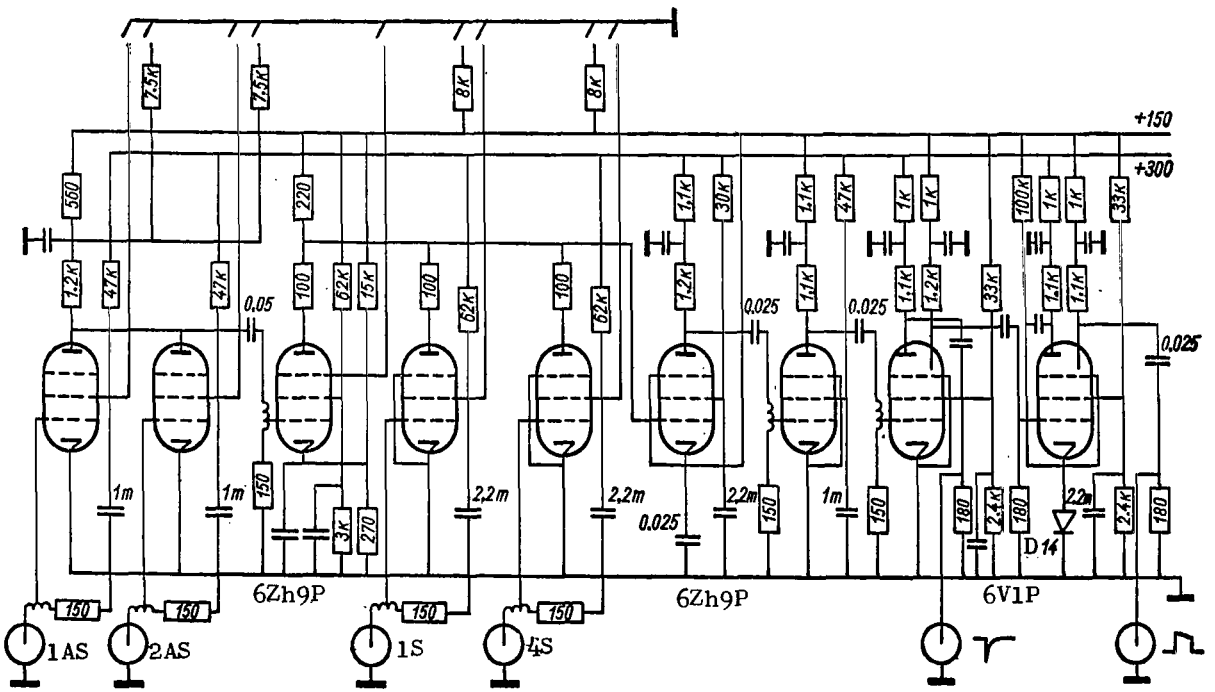

Figure 4. Coincidence-anticoincidence circuit diagram.

practically no effect on chamber efficiency, is used to counter the effect of pickups from the spark chambers on counter J. All chambers are connected in parallel.

Figure 4 is the 4S + 2AS coincidence-anticoincidence circuit diagram. It includes nine 6Zh9P tubes and two 6V1P tubes. The coincidence channel resolution time is 16 nanoseconds. The circuit operates on negative input pulses with an amplitude greater than, or equal to, 1 volt. The input impedances of the circuit channels are 150 ohms, the positive output pulse has a 25 nanosecond front, a duration of 100 nanoseconds, and an amplitude of 10 volts. The anticoincidence channels can operate in the addition mode, as well as in the coincidence mode. The 300 volt supply circuit draws 50 milliamperes, the 150 volt supply circuit 140 milliamperes.

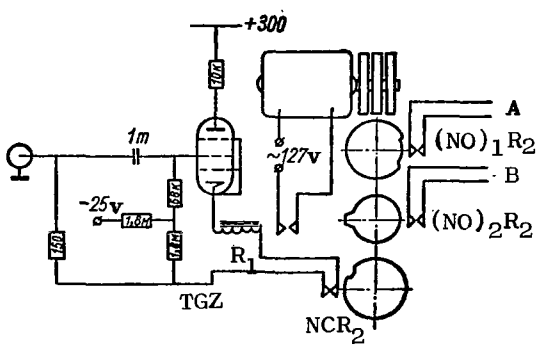

Figure 5. RFK trigger circuit.
A - RFK motor circuit;
B - RFK film transport circuit.

Figure 5 is the RFK trigger circuit. When a signal is supplied to the input to this circuit thyratron TGZ is triggered. The thyratron cathode circuit includes relay R_1. /63 The pair of contacts of this relay closes the circuit supplying the motor and its reduction gear. The motor shaft speed is 24 rpm. This shaft also carries cams for closing associated contacts. The RFK motor is energized when normally open contacts $(NO)_1R_2$ are closed, and when contacts $(NO)_2R_2$ are closed the RFK is supplied with a pulse that energizes the film transport circuit. Finally, the normally closed contacts, NCR_2, open and quench the thyratron. Motor inertia is such that the contacts return to their original positions. The film transport cycle lasts for 2.5 seconds.

3. Experimental Results

The installation was used on the ground floor of the building, and was covered by material equivalent to 80 cm of concrete. Counter J was calibrated on cosmic μ-mesons systematically during installation operation, and this was done with counters CC_1 and CC_2 disconnected. 777 cases of installation operation were recorded in 531 hours of use, during which the pulse from counter J

was recorded and measured. Most of these events were rejected on the basis of spark chamber selection criteria, in accordance with which only those cases were selected when:

(a) only one primary particle traversed the installation;

(b) the continuation of the particle trace upward entered the coincidence counter and the working part of counter J;

(c) the scattering angle in the lead block did not exceed 5°.

The selection criteria adopted avoided cases caused by particle showers. The result of the selection left 14 events. Thus, use of spark chambers in the installation resulted in a reduction in the background by a factor of approximately 50. Figure 6 shows the ionization distribution, as measured by counter J:

(a) for all events with counters CC_1 and CC_2 disconnected;

(b) for events with counters CC_1 and CC_2 disconnected, and satisfying the spark chamber selection criteria (calibration μ-mesons);

(c) for 777 events recorded by the installation with counters CC_1 and CC_2 connected;

(d) for 14 of the 777 events satisfying the spark chamber selection criteria.

Most of the cases of distribution in Figure 6d are, evidently, μ-mesons recorded by the installation as a result of counting losses for counters CC_1 and CC_2. The heavy, singly charged particles recorded by the installation are the result of ionization in excess of the double ionization of a relativistic particle; that is, they should fall in the right-hand side of the distribution in /64
Figure 6d. The μ-meson distribution (Figure 6b) is compared in what follows with the distribution of the selected events (Figure 6d). Cited here are the percentages of cases, p_μ, in μ-mesons of distribution with pulse amplitude greater than some magnitude X, the expected number of μ-mesons with similar ionization from the selection in 14 events, N_μ, and the observed number N, of cases with such ionization among the 14 selected events:

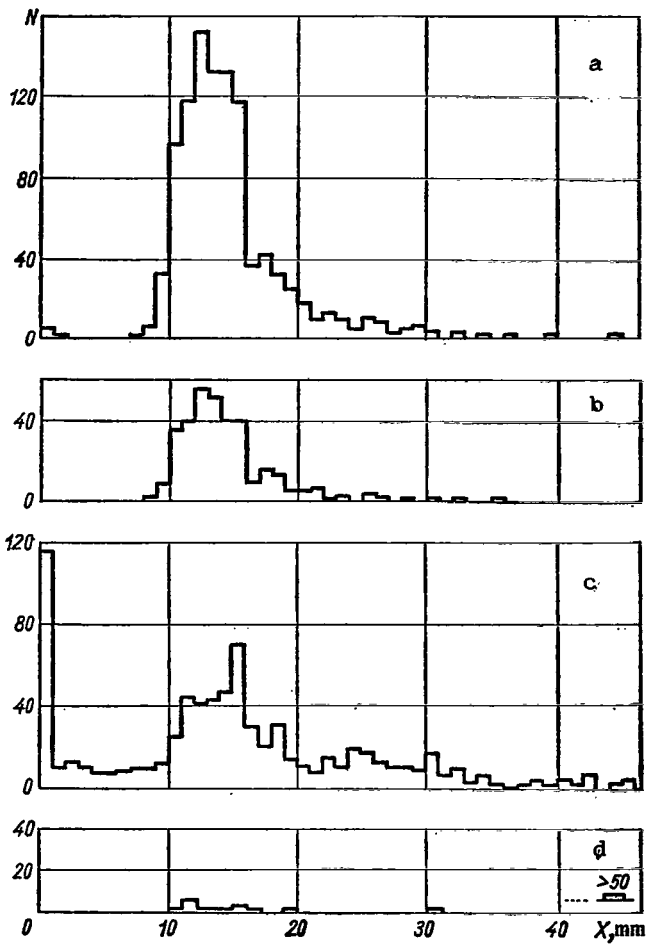

Figure 6. Experimental distributions.

a and b - events with counters CC_1 and CC_2 disconnected;

c and d - events with counters CC_1 and CC_2 connected.

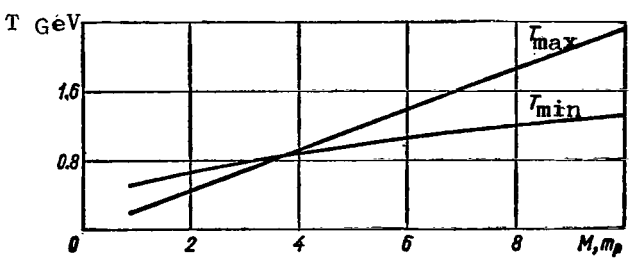

Figure 7. Energy domain for particles recorded by the installation.

On the Oscillograph scale $\geq X$, mm	p_μ	N_μ	N
18	0.08±0.015	1.1	3
24	0,024±0.009	0.4	2
27	0,012±0.006	0.2	2

/65

The observed number exceeds the expected number of μ-mesons with increased ionization, as will be seen. The probability that this came about as a result of a random fluctuation can be established through a Poisson distribution and proves to be quite small; about 7.5% for $X \geq 18$ mm, and approximately 2% for $X \geq 27$ mm.

The estimates we made of the background attributable to nuclear interaction of μ-mesons and to protons of cosmic rays scattered in the rear hemisphere showed that the expected number of such events is considerably less than one. Thus, the two particles with increased ionization observed among the 14 cases cannot be reliably explained by statistical errors, nor by the fixed counting losses in the installation that we know about. However, because of the very meager statistics it is too early to draw any conclusions with respect to an interpretation of the result obtained, the more so because these two events could even be the result of certain methodological errors that were not even considered. A new, improved, installation is now being built, one that will enable us to verify and refine the results obtained.

We can establish the upper limit for the flux of heavy particles with unit charge by taking into consideration all recorded μ-meson events. It is equal to $3.4 \cdot 10^{-8}$ $(cm^2\text{-s-ster})^{-1}$. Figure 7, in which particle mass in units of proton mass is plotted on the X-axis, and kinetic energies on the Y-axis, shows the energy domain for particles recorded by the installation.

/66

REFERENCES

1. Morrison, D. R. O., Phys. Lett., Vol. 9, 1964, p. 199.
2. Leipuner, L. B., et al., Phys. Rev., Lett., Vol. 12, 1964, p. 423.
3. Hagopian, V., et al., Phys. Rev., Lett., Vol. 13, 1964, p. 280.
4. Blum, W., et al., Phys. Rev., Lett., Vol. 13, 1964, p. 353a.
5. Bingham, H. H., et al., Phys. Lett., Vol. 9, 1964, p. 201.
6. Sunyar, A. W., Phys. Rev., Vol. 136B, 1964, p. 1157.
7. Bowen, T., et al., Phys. Rev., Lett., Vol. 13, 1964, p. 728.
8. Delisse, D. A. and Bowen, T., Phys. Rev., Vol. 140B, 1965, p. 458.
9. Massam, T., et al., Nuovo cimento, Vol. 40A, 1965, p. 589.
10. Buhler-Broglin, A., et al., Nuovo cimento, Vol. 45A, 1966, p. 520.
11. Buhler-Broglin, A., et al., Nuovo cimento, Vol. 49A, 1966, p. 209; Vol. 51A, 1966, p. 837.
12. Barton, J. C. and Stockel, C. T., Phys. Lett, Vol. 21, 1966, p. 360.
13. Kasha, H., et al., Phys. Rev., Vol. 150, 1966, p. 1140.
14. Lemb, R. C., et al., Phys. Rev., Lett., Vol. 17, 1966, p. 1068.
15. Kasha, H., et al., Phys. Rev. Vol. 154, 1967, p. 1263.
16. Gomez, R., et al., Phys. Rev., Lett, Vol. 18, 1967, p. 1022.
17. Kasha, H., et al., Phys. Rev., Lett., Vol. 20, 1968, p. 217.
18. Gürsey, F., et al., Phys. Rev., Vol. 135B, 1964, p. 467.
19. Khrimyan, A. V., et al., Izv. AN SSSR. Ser. fiz., Vol. 30, 1966, p. 1648.
20. Fransini, P., et al., Phys. Rev., Lett., Vol. 14, 1965, p. 196.
21. Dorfan, D. E., et al., Phys. Rev., Lett., Vol. 14, 1965, p. 699.
22. Franzini, P. and Shulman, S., Phys. Rev., Lett., Vol. 21, 1968 p. 1013.
23. Ashton, F., et al., Phys. Rev., Lett., Vol. 21, 1968, p. 303.
24. Kasha, H., and Stefanski, R. J., Phys. Rev., Lett., Vol. 20, 1968, p. 1256.
25. Callan, C. G. and Glashow, S. L., Phys. Rev., Lett., Vol. 20, 1968, p. 779.

26. Bergeson, H. E., et al., Phys. Rev., Lett., Vol. 19, 1967, p. 1487.

27. Bjørnboe, J., et al., Nuovo cimento, Vol. 53B, 1968, p. 241.

RESONANCES IN $K\bar{K}$- AND $K\Lambda$-SYSTEMS

V. S. Demidov, V. G. Kirillov-Ugryumov,
A. K. Ponosov, V. P. Protasov, F. M. Sergeyev

ABSTRACT. Investigations made of the decay of baryonic and mesonic resonances with zero strangeness to a pair of strange particles ($K^0\Lambda$ or $K_1^0 K_1^0$) are discussed. The effective mass of the baryonic system is between 1.6 and 2.4 GeV, that of the mesonic system between 1.0 and 1.5 GeV.

Investigation of the resonance states of elementary particles today is one /67
of the fastest developing branches of physics. The progress in the field toward increasingly higher energies, together with improvements in experimental techniques, make it possible to study resonances with large mass and to observe the rare channels of decay of known resonances. This paper is devoted to the investigation of decays of baryonic and mesonic resonances with zero strangeness to a pair of strange particles ($K^0\Lambda$ or $K_1^0 K_1^0$). The effective mass of the baryonic system is between 1.6 and 2.4 GeV, that of the mesonic system between 1.0 and 1.5 GeV.

1. $K\Lambda$-System. Phenomenological Analysis.

Initially, the experimental investigation of reactions with K-mesons and Λ-hyperons in the final state was the result of interest in threshold anomalies, so-called cusps. A. I. Baz' and L. B. Okun' [1] used the unitarity ratio for a scattering matrix to demonstrate that the amplitudes of those channels already discovered undergo a sharp change near the threshold of a new channel. This effect appears in the form of narrow anomalies (width $\Delta E \sim 1$ MeV) in the energy relationships for the total and differential cross sections, polarization, and the like. In addition to the independent value of these anomalies (cusps), of interest as well is the fact that the relative parity of secondary particles in the different channels can be determined, in principle. The cusp anomalies in the channel

$$\pi^- + p \to K^0 + \Lambda \qquad (1)$$

near the threshold of reaction $\pi^- p \to K\Sigma$ for finding the relative parity of the Λ- and Σ-hyperons, has been suggested as being applicable to reactions with strange particle production.

There was no success in discovering cusps in the experiments connected with the investigation of the Eq. (1) reaction because of the extraordinarily rigid requirements with respect to the energy resolution, but these experiments did provide many other important and interesting characteristics of the reaction.

/68

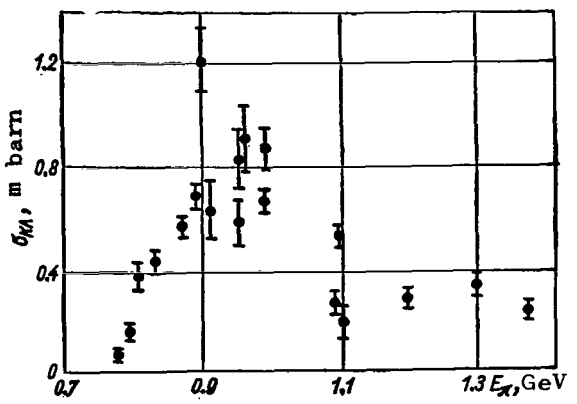

Figure 1. Total cross section of the Eq. (1) reaction in terms of π-meson kinetic energy [4].

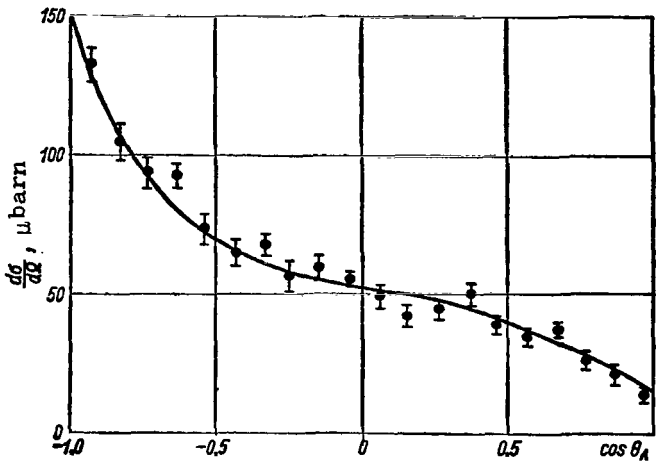

Figure 2. Characteristic shape of the angular distribution of Λ-hyperons in a CM-system for the Eq. (1) reaction; E_π = 905 MeV.

It developed that E_π has a clearly defined maximum when E_π = 925 MeV, and a small "shoulder" when E_π = 829 MeV (Figure 1), when the total reaction cross section is plotted in terms of primary π-meson energy. The principal movement of the Λ-hyperons (K-mesons) in the CM-system for the reaction is backward (forward) relative to the movement of the primary meson (Figure 2). The terms with n = 3; 4 in the polynomial $d\sigma/d\Omega = \Sigma C_n \cos^n \theta$, where θ is the angle of emission in a /69 CM-system, made an unexpectedly great contribution near the threshold in the approximation of the angular distribution of the secondary particles. The dependence of polarization on θ becomes zero twice (Figure 3) in the region of the shoulder (E_π = 829 MeV), and once in the region of the peak (Figure 4).

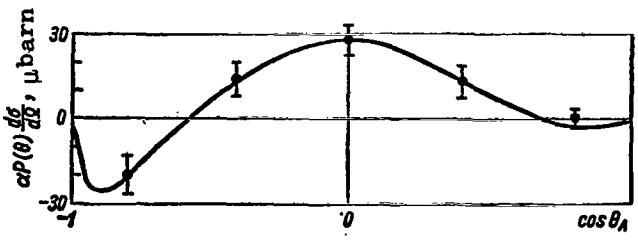

Figure 3. The $\alpha P(\theta)$ $(d\sigma/d\Omega)$ relationship for Λ-hyperons in the Eq. (1) reaction. $E_{\pi} = 829$ MeV; α is the parameter for the asymmetry of the Λ-decay ($\alpha < 0$); $P(\theta)$ is the polarization [2].

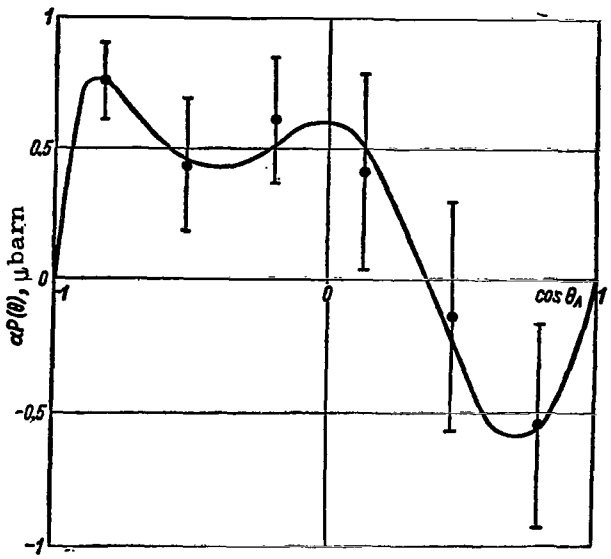

Figure 4. The $\alpha P(\theta)$ relationship when $E_{\pi} = 990$ MeV [2].

Let us consider the kinematics of the Eq. (1) reaction. The differential cross section can be written in general form as follows:

$$\frac{d\sigma}{d\Omega} = \frac{k_1}{k_2} \cdot \frac{1}{(8\pi W)^2} \mid T_{if} \mid^2 = A^2.$$

where

k_1 and k_2 are proton and hyperon momenta, respectively; /70

W is the total energy in the CM-system;

T_{if} is the matrix element for the transition from the initial to the final condition;

A is the reaction amplitude.

The expansion of the amplitude in eigenfunctions of the total momentum when the proton target is not polarized can be represented in the form

$$A^{\pm} \sim \sum_{l>1} [f_{l-1}^{+}(W) - f_{l+1}^{-}(W)] P_l'(\cos\theta) - \sum_{l>1} [f_l^{+}(W) -$$

$$- f_l^{-}(W)] P_l'(\cos\theta)\cos\theta \pm i \sum_{l>1} [f_l^{+}(W) - f_l^{-}(W)] P_l'(\cos\theta)\sin\theta,$$

where

θ is the angle of emission of a hyperon relative to the direction in which a primary meson is moving;

$f_l^{\pm}$ are partial amplitudes for the orbital momentum, l, and for the total momentum $j = l + 1/2$ and $j = l - 1/2$;

$P_l'(\cos\theta)$ is a derivative of the Legendre polynomial.

The amplitude A^+ corresponds to the projection of hyperon spin in the direction $n = k_1 \times k_2 / |k_1 \times k_2|$, equal to $+1/2$; A^- is the amplitude for the projection equal to $-1/2$. Using the expansion of A, the differential cross section can be written in the form

$$\frac{d\sigma}{d\Omega} = |f_1|^2 + |f_2|^2 - 2\cos\theta \operatorname{Re}(f_1 f_2^*). \tag{2}$$

Here

$$f_1 = \sum_{l>1} [f_{l-1}^+(W) - f_{l+1}^-(W)] P_l'(\cos\theta);$$

$$f_2 = \sum_{l>1} [f_l^+(W) - f_l^-(W)] P_l'(\cos\theta).$$

The expression for polarization too is readily obtainable as

$$P(\theta) = \frac{|A^+|^2 - |A^-|^2}{|A^+|^2 + |A^-|^2} = \frac{2\sin\theta \operatorname{Im}(f_1 f_2^*)}{d\sigma/d\Omega}. \tag{3}$$

The more natural approach, from the experimental point of view, and after adapting Eqs. (2) and (3) to the angular distributions and to the polarization distribution obtained, is to attempt to find the magnitudes of the partial amplitudes, f_l. Rimpault used this procedure [2]. The range of energies from the threshold of reaction $\pi p \to K\Lambda$ (768 MeV) to 1000 MeV was used in his work for purposes of analysis. This was the basis for taking into consideration only a limited number of complex amplitudes of f_l. Used in the computations /71 were f_0^+, $f_1^{\pm}$, $f_2^{\pm}$, f_3^-, 12 unknowns in all. The solution was found by minimizing the expression

$$H^2 = \sum_{i=1}^{k} (A_i^+ - \sqrt{n_i^+})^2 + (A_i^- - \sqrt{n_i^-})^2, \tag{4}$$

where

k is the number of intervals in the angular distributions;

$$n_i^+ = \frac{1}{2} \cdot \frac{d\sigma}{d\Omega_{ie}} [1 + P(\theta)_{ie}];$$

$$n_i^- = \frac{1}{2} \cdot \frac{d\sigma}{d\Omega_{ie}} [1 - P(\theta)_{ie}];$$

$d\sigma/d\Omega_{ie}$, $P(\theta)_{ie}$ are the experimental values for the differential cross section and for the polarization in the i^{th} angular interval, respectively.

As will be seen, the method used is an ingenious modification of the least squares method so as to reduce the degree of the equations for determining the amplitudes. The computations showed that amplitudes f_0^+, f_1^-, f_2^-, f_3^-, played a dominant role in the energy range investigated, and that their squares can reach magnitudes of the order of 20 μbarns (depending on the energy of E_π). Figures 2 through 4 show the distributions corresponding to the solutions obtained.

If the amplitude f_3^- is represented in the form of a Breit-Wigner distribution

$$f_3^- \approx \frac{C}{W_r^2 - W^2 - i\Gamma/2} ,$$

(C is a normalizing constant), the values obtained for this amplitude will correspond to the parameters $E_\pi \approx 890$ MeV ($W_r \approx 1685$ MeV), with $\Gamma \approx 180$ MeV. These magnitudes coincide with the parameters for the $F_{5/2}$ -resonance for elastic πN-scattering (the isotopic spin state is T=1/2). The behavior of f_3^- with respect to the energy also is confirmation of the presence of resonance.

Since magnitude values were sought by adapting to angular distributions and polarization it is only natural that the computed curves describe the experimental results very well in these cases (see Figures 2 through 4). The situation was demonstrably considerably worse for total cross sections. In the region of the peak for $\sigma_{K\Lambda}$ in terms of the energy ($E_\pi \approx 925$ MeV), the computed cross section was obtained as half the experimental cross section. This means that the situation is incomparably more complex than it would be if it were evaluated from a common sense standpoint. One possible way to overcome the divergence thus appearing is to use different variants of the set of partial amplitudes, and even to include greater momenta. However, it is quite clear that the participation of resonance states is necessary in order to explain the

behavior of the total cross section. /72

Another direction in the theoretical analysis of the data on the Eq. (1) reaction is based on definite assumptions concerning the dynamics of the process. It is believed that the principal experimental characteristics, such as the total cross section in terms of the energy, the angular distributions of the hyperons (K-mesons), and polarizations, provide a means for considering the amplitude of the reaction in the form of a sum of Born amplitudes and the contribution from the resonance conditions in the straight and intersecting channels. The position and width of the resonances are considered to be additional parameters.

As is known, the kinematics of a two-particle reaction can be described most simply by Mandel'stam [sic] variables

$$s = (p_1 + q_1)^2 = (p_2 + q_2)^2 \quad \text{(s-channel)}; \tag{5}$$

$$t = (p_1 + p_2)^2 = (q_1 + q_2)^2 \quad \text{(t-channel)}; \tag{6}$$

$$u = (p_1 + q_2)^2 = (p_2 + q_1)^2 \quad \text{(u-channel)}. \tag{7}$$

Here $p_{1(2)}$ and $q_{1(2)}$ are four-dimensional nucleon (hyperon) and π-meson (K-meson) momenta, respectively, and $p_1^2 = m_1^2$. The Born term in the s-channel corresponds to the single-nucleon intermediate state (Figure 5a). The Born term in the u-channel can be described by a single-particle diagram with exchange of a strange baryon (Σ^+) (Figure 5b). Finally, the term with the K*-meson in the intermediate state (Figure 5c) is considered in the t-channel.

Various combinations of Born poles and resonance terms have been investigated. Kanazawa [3] attempted to explain the experimental data by considering the amplitude of the reaction in the form of the sum of three terms, the nucleon pole, the Σ-pole, and a resonance term, the parameters of which were determined by adaptation to the experiment. There was success in obtaining agreement with the experiment in the region of the total cross section peak for the condition that $P_{1/2}$- or $P_{3/2}$-resonance was included. However, the model /73 yielded an increase in the percentage

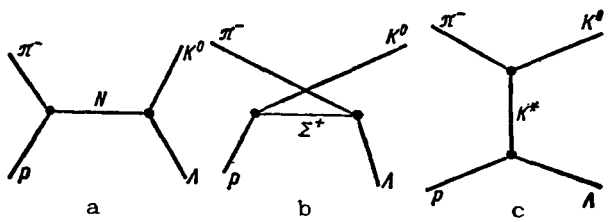

Figure 5. Diagrams corresponding to the Eq. (1) reaction.

of K-mesons moving in the rear hemisphere with increase in energy. This was not confirmed experimentally.

Hoff [4] considered a model with two resonances; one in the region of the reaction's total cross section peak, the other in the region of the "shoulder" when E_π = 829 MeV. A term, corresponding to the K*-meson exchange, was introduced in order to explain the angular distribution of hyperons. It should be pointed out that this term most naturally describes the backward movement of hyperons in the CM-system for the reaction, whereas the nucleon pole provides a symmetrical divergence, with the Σ-exchange leading primarily to the forward movement of hyperons in the CM-system. The last two terms must be combined with definite weights and with opposite signs, in order to adapt the data from the experiment based on these terms.

Analysis revealed that polarization in the basic data can be described by the interference of the K*-exchange term and of the resonant $P_{1/2}$-wave. The $P_{3/2}$ variant is rejected on the ground that it yields a forward peak for hyperon divergence at energies above resonant. It was possible to describe polarization near E_π = 829 MeV by including the resonant $F_{5/2}$-wave.

The resonance parameter values listed in Table 1 can be obtained by representing the resonance amplitudes in Breit-Wigner form. Analogs for these resonances were not found in elastic πN-scattering.

TABLE 1

j	l	W_r, MeV	Γ_l, MeV
1/2	1	1704	64
5/2	3	1647	~10

TABLE 2

Wave	W_r, MeV	Γ, MeV
$P_{1/2}$	1497	89
$D_{3/2}$	1534	105
$F_{5/2}$	1690	100

The Hoff model satisfactorily describes the entire set of experimental data up to the threshold of the reaction $\pi p \to K\Sigma$. After that, however, there is a sharp deterioration in concordance with the experiment. First of all, the computed total cross section becomes larger than the experimental one by a factor of 2. Second, the shape of the angular distribution changes with increase in energy. The Λ-hyperons begin to move forward in the CM-system. The simplest way to attempt to explain the unsoundness of the model at these energies requires the inclusion of other partial waves.

As distinguished from the analysis made by Hoff, reference [5] considered /74 the amplitude of the reaction in the form of sums of the K*-exchange term and the resonances corresponding to the established resonances of the πN-scattering with isotopic spin T = 1/2. Resonances used are listed in Table 2.

What follows from the computation is that the total cross section cannot be described satisfactorily by any pair of resonances from Table 2. Nevertheless, the variant with a combination of P- and F-waves comes closest to the experimental points. It should be pointed out that the angular distributions and polarization are described better by combinations of P- and D-waves than by other possible pairs. A computation was made for three resonances as well. Only angular distributions were described satisfactorily, however. In this variant the total cross section can be described only qualitatively, and generally speaking there was no success in obtaining concordance with the experiment for polarization distributions.

The above-considered papers discussed the singularities of the amplitude of the reaction closest to the physical region; the contribution of long-range singularities was assumed small. An attempt can be made to take this contribution into consideration in some fashion, at least in principle. An attempt such as this was made in [6]. The authors considered the amplitude in the form of the sum of the nucleon pole, the Σ-exchange term, the K*-exchange, and the resonance $F_{5/2}$ in the channel with isospin T = 1/2 (1688 MeV). The remainder of the amplitude was represented in the form of a polynomial in s and t variables. The coefficients of this polynomial, as well as the statistical weights of the resonance terms were considered as parameters. The numerical results were obtained by adapting the general computational expressions to the experimental angular distributions for primary π-meson energies E = 791, 829, and 870 MeV. It was shown that partial waves up to $F_{7/2}$, inclusive, took part in the reaction, but that conditions $S_{1/2}$ and $P_{3/2}$ played the principal role in the region considered. It is very interesting to find out that the amplitude $P_{3/2}$ acted like the real part of the resonance amplitude corresponding to $W_r \approx 1660$ MeV, depending on the energy.

The set of parameters in this paper could only describe the total cross section of the reaction from the threshold to an energy E_π = 830 MeV. Polarization distributions were not at all in concordance with the experiment, even in this interval. Hence, it is apparent that the situation in the channel with T = 1/2 is extremely complex, and far from exhausts the store of data obtained in the πN-scattering. A detailed analysis of the theoretical work done reveals

that the lack of success in explaining the Eq. 1 reaction is attributable to a number of circumstances, particularly to the inadequate consideration given to the unitarity ratio, to neglect, without specific bases, of the imaginary parts of certain partial amplitudes, and others. A detailed analysis is beyond the /75 scope of this paper.

What follows is important, and must be pointed out. It is completely clear at this point that the explanation for the Eq. (1) reaction requires the use of the resonance conditions with the K-meson and Λ-hyperon decay channel. The possibility of the existence, in this channel, of resonance conditions that were not discovered in the elastic πN-scattering, for whatever reason, cannot be excluded. A. I. Baz', et al., pointed to the possibility of the existence of this resonance [7]. Analyzing the data on the behavior of the cross section of the $\pi p \to K\Sigma$ and $\pi p \to K\Lambda$ reactions, they concluded that the existence of a level in the $K\Sigma$-system with isospin $T = 1/2$ and binding energy $Q \sim 30$ MeV, was possible. This level should result in resonance in the $K\Lambda$-system below the threshold of Σ-hyperon production. The authors emphasized the fact that $K\Lambda$-resonance is a secondary phenomenon attributable to the peripheral interactions of near-threshold particles.

2. $K\Lambda$-Resonances. Survey of the Experimental Data

Ye. V. Kuznetsov, et al. [8], made the first attempt at a direct experimental finding of resonances in the $K\Lambda$-system. Heavy-liquid bubble chambers were used to study the production of Λ-hyperons and K-mesons by π-mesons with $p_\pi = 2.8$ Gev/c. Investigating the binding energy distribution for the system

$$Q_{K\Lambda} = \sqrt{(E_K + E_\Lambda)^2 - (\mathbf{P}_K + \mathbf{P}_\Lambda)^2} - (M_\Lambda + M_K)$$

where

E_i is particle energy;

P_i is a three-dimensional pulse;

M_Λ and M_K are the Λ-hyperon and K-meson masses, respectively,

the authors found a concentration of events near the low $Q_{K\Lambda}$ values. Also found was a notable percentage of cases when a meson and a hyperon move in the same direction. Meson-hyperon pairs of these events had a low $Q_{K\Lambda}$ value. These

facts were the basis for the conclusion that resonance in the $K\Lambda$-system with a mass of 1650 MeV exists. This result, it would appear, confirmed Hoff's prognosis and, in addition, agreed with the conclusion drawn by Bertenza, et al. [9], who explained the anomalous behavior of the polarization of the Λ-hyperon in the Eq. (1) reaction for energy E_{π} = 829 MeV by the resonance with this mass value.

However, reference [10], which is a continuation of the research reported in [8], used a much more detailed analysis, and incomparably greater statistical materials, to prove that the experimental accuracies obtained were such that they did not permit making a judgment as to the appearance of $K\Lambda$-resonances against a background of random processes. /76

Reference [11] used spark chambers to study the generation of the $K^0\Lambda$-system in the $\pi^- p \to K^0\Lambda\pi^0$ reaction for a primary energy of 1.508 GeV. Hyperons and K-mesons were identified from the photographed geometry of the divergence and from the ionization of the decay products. Ionization was estimated from spark brilliance. Analysis revealed that in approximately 84% of the cases the reaction took place as a two-particle reaction with the participation of Y*(1380)-resonance: $\pi^- p \to K^0 Y^{*0}$.

A simple statistical curve cannot be used to describe the distribution in terms of the effective mass of the $K^0\Lambda$-system. Consideration of the Y* reflection in this spectrum will improve concordance of the computation with the experiment, but the experimental results have a 3% probability of compatibility with the existence of resonance in the $K\Lambda$-system ($M_{K\Lambda} \approx 1680$ MeV).

The $K^+\Lambda$-system, isotopically bound to the $K^0\Lambda$-system, was studied in π^+ p-interactions for energy E_{π} = 1.95 GeV. The following reactions were investigated in a 20" liquid-hydrogen bubble chamber [12]

$$\pi^+ + p \to \begin{cases} K^+ + \Lambda + \pi^+; & (8) \\ K^0 + \Lambda + \pi^+ + \pi^+; & (9) \\ K^+ + \Lambda + \pi^+ + \pi^0. & (10) \end{cases}$$

A concentration of events close to the mean value for the mass of the $\Lambda\pi$-system 1380 MeV, and close to the mean value for the mass of the $K^+\Lambda$-system 1688 MeV, was found on the Dalits graphic for the Eq. (8) channel. The authors

explain this by the appearance of decays in the resonance $Y^*(1380) \to \Lambda\pi^+$, and in the isobar $N^{*+}(1688) \to K^+\Lambda$. It seems that Y* is missing in the reactions in which the isobar participates, and vice versa.

A 30" propane chamber was used to study the $\pi^-p \to K^+\Lambda\pi^-$ and $\pi^-p \to K^0\Lambda\pi^0$ reactions [13]. The primary momentum was 2.0 GeV/c. Mass distributions for the $K\pi$, $\Lambda\pi$ and $K\Lambda$ systems were obtained. The experimental distributions were compared with the computed distribution, taken in the form

$$F(m_{ij}) = \alpha F_{ph} + \beta F(Y^*) + \gamma F(K^*),$$

where

m_{ij} is the mass for the combination of the i^{th} and j^{th} particles;

F_{ph} is the phase distribution;

F(Y*) and F(K*) are distributions that take into consideration the contribution of resonances Y*(1385) and K*(888). These distributions were written in the Breit-Wigner form.

It was found that all three experimental histograms can be adequately well written using the following values for the partial weights: $\alpha = 0.18$, $\beta = 0.45$; $\gamma = 0.37$. However, there are definitely more observed cases than there are cases on the computed curve near 1.86 GeV in the $K\Lambda$-system mass distribution. /77

Wangler, et al., used a 20" liquid-hydrogen chamber to investigate the production of strange particles in π^-p-collisions with momentum of 3 GeV/c [14]. The distribution in terms of effective mass $M_{K\Lambda}$ was close to the curve for the phase volume in shape in channels with three particles in the final state ($K^+\Lambda\pi^-$ and $K^0\Lambda\pi^0$). There are no statistically guaranteed anomalies here. Channels with four particles in the final state ($\pi^+\pi^-\Lambda K^0$ and $\pi^-\pi^0\Lambda K^+$) yield effective mass distributions with a characteristic concentration of events near the left limit for both combinations of signs for the $K\Lambda$-system, something that is peculiar to multiparticle phase volumes, but narrow spikes near $M_{K\Lambda}$ = 1.675 GeV and $M_{K\Lambda}$ = 1.95 GeV can be observed. While the first anomaly may correspond to an $N^*_{1/2}(1688) \to K\Lambda$ decay, the second (if it is authentic), corresponds to an unknown resonance.

The authors analyzed their data and concluded that there is a strong correlation between the Y^{*0} and K^{*0} productions in the $\pi^-p \to \Lambda\pi^0K^+\pi^-$ reaction, that is; the reaction has the quasi-two-particle form $\pi^-p \to Y^{*0}K^{*0}$. There is

no such correlation in the $\pi^- p \to \pi^- \pi^+ K\Lambda$ reaction. This can be understood on the basis of the one-meson exchange representation. A K^{*+}, K^{*+} Y^{*-}-system can occur at the same time as K^{*0} and Y^{*0} are produced in a reaction with a K or a K^{*+} exchange only during an exchange with a positive meson with a dual charge and comparatively small mass. No such meson has ever been found. K* production plays a significant role in a three-particle channel ($\Lambda^0 K^+ \pi^-$), with the role of Y* a small one.

The mass spectrum of the $K^0\Lambda$-system generated by π^--mesons with momentum of 3.86 GeV/c on light nuclei (C, F, Cl) was studied by a group from the MIFI [Moscow Engineering Physics Institute) in a 105 cm bubble chamber filled with a mixture of light freons [15]. The effective mass distribution $M_{K\Lambda}$ has the form characteristic of multiparticle final states. Events are grouped near small mass values for $M_{K\Lambda}$, for the most part. Peaks are found in the intervals 1.65 GeV < $M_{K\Lambda}$ < 1.8 GeV and 1.9 GeV < $M_{K\Lambda}$ < 2.0 GeV. A conclusion is drawn concerning the appearance of resonance in a KΛ-system with parameters $M_{K\Lambda} \tilde{=} 1.94$ GeV and $\Gamma \sim 100$ MeV. Bertanza, et al., [16], studying the $\pi^- + p \to \Lambda + K +$ (accompaniment) reaction, observed the appearance of Λ-hyperons, emitted together with K-mesons in the front hemisphere when there is an increase in the multiplicity of π-meson accom- /78 paniment. Hyperons fly straight backward when multiplicity is small. The authors explain this by saying that when multiplicity is small the KΛ-system is produced in the peripherial interaction, and that the role of central collisions increases with increase in multiplicity. No direct observations of resonances in the KΛ-system were made.

Reference [17] is an extremely detailed investigation of the joint production of Λ and K in the interval of momenta of π-mesons from 1.8 to 4.2 GeV/c. There were no indications of the existence of KΛ-resonances, despite the fact that a very detailed mass analysis of final states was made. Of interest here are the results pertaining to the formation of Y* and K* resonances. These can be discussed in some detail.

Resonances Y^{*0}_1 and Y^{*-}_1 make a significant contribution in the state with three particles at the end up to energies of the order of 2.5 GeV. Their weight decreases with increase in energy, but for $E_\pi = 3.3$ GeV the contribution Y^{*0} to the $\Lambda K^0 \pi^0$ state is still some 30%; the weight of Y^{*-} drops off more rapidly. The role of K* resonance exists over the entire interval of energies investigated.

Even in this case the resonance production cross section falls with increase in energy, with K^{*+} subsiding more rapidly than K^{*0}.

The combined production of Y^*_1 (1385) and K* (890) predominates for four- and five-particle final states from 1.8 to 2.2 GeV, to the extent that the majority of the reactions can be explained by quasi-two-particle arrangements: $\pi^- p \to Y^*K^*$. However, the Y* and K* resonance production cross sections decrease with increase in primary energy.

Resonance in a $K^+\Lambda$-system with a mass of some 1.7 GeV was found [18] in the reaction

$$\pi^- + p \to \Lambda + K^+ + \pi^- \tag{11}$$

upon irradiation by π-mesons with momentum of 6 GeV/c in an 80" liquid-hydrogen bubble chamber. It is interesting to note that the authors failed to find amplifications in the $K^0\Lambda$ and $K^+\Lambda$ mass spectrum in channels

$$\pi^- + p \to \Lambda + K^0 + \pi^0 \tag{12}$$

and

$$\pi^+ + p \to \Lambda + K^+ + \pi^+ \tag{13}$$

They see the explanation of the effect in the possibility of describing the reactions on the bases of exchange diagrams with the production of a $K\Lambda$-system at one apex.

Associated with the Eq. (11) and Eq. (12) reactions in a straight s-channel /79 are two amplitudes $A_{1/2}$ and $A_{3/2}$, corresponding to the possible isotopic spin states with unknown phase difference. Only one amplitude, $A_{3/2}$, takes part in the Eq. (13) reaction. Reactions in the crossed t-channel can be described in terms of the isospin exchange amplitudes B_0 and B_1 (I = 0, I = 1), establishing the G-parity exchange (f^0 or ρ). Then the cross sections in the t-channel can be written in the form

$$\sigma_1 = C(2/3)^{1/2} \mid \mid B_0 \mid + \mid B_1 \mid e^{i\varphi} \mid^2;$$
$$\sigma_2 = C \mid 2^{1/2} B_1 \mid^2;$$
$$\sigma_3 = C(2/3)^{1/2} \mid \mid B_0 \mid - \mid B_1 \mid e^{i\varphi} \mid^2,$$

where

φ is the difference in phases between B_0 and B_1.

Pointing out the fact that the amplitudes B_0 and B_1 have opposite signs, the authors came to the conclusion that the suppression of the ΛK-anomaly in the Eq. (12) and Eq. (13) reactions takes place as a result of the interference of small B_1 with B_0, which is large in magnitude (or of small $A_{3/2}$ with large $A_{1/2}$ in the s-channel). Reference [18] contains the conclusion that the anomaly that does appear can be the reflection of the isobar N* (1688), but the experimental data are compatible with direct proton dissociation to ΛK^+.

Associative Λ and K production in a heavy-liquid chamber (86% propane by volume, 14% CF_3Br by volume) by π^--mesons with momenta of 6.1, 11.6, and 18.1 GeV/c were studied [19]. It was found that in a reaction with little π-meson accompaniment, the Λ-hyperons will fly straight backward (the K-mesons will fly forward). The sharpness of the angular distributions diminishes with increase in multiplicity. The four-dimensional momentum transferred to the hyperon is quite large. Resonances in the $K^0\pi^+$ [K* (888)] and $\Lambda\pi^+$, $\Lambda\pi^-$[Y^*_1 (1385)] systems were clearly noted in the experiment, so results could be explained by polar diagrams.

So far as the $K\Lambda$ mass distributions are concerned, it is the contention of the authors that since a strict correlation was noted between the values of the binding energy $Q_{K\Lambda}$ and the multiplicity of the π-meson accompaniment (small $Q_{K\Lambda}$ - large multiplicity; large $Q_{K\Lambda}$ - small multiplicity), the groupings of events near the small binding energy values can be explained by the faster kinematic, and not resonance, effects.

Three-, four- and five-particle states with a Λ-hyperon and K-meson were studied in an 80" liquid-hydrogen chamber in π^-p-collisions with momentum of 7.91 GeV/c [20]. Noted in the mass spectrum of the ΛK^0 and ΛK^+-systems was an intensification with a mean mass value $M_{K\Lambda} \sim 1.7$ GeV and a width of 75 to 100 MeV. Narrow spikes with $\sim$ 1.9 to 1.95 GeV for $M_{K\Lambda}$ and $\sim$ 1.8 to 1.85 GeV for $M_{K\Lambda}$, /80 also were noted. The authors are of the opinion that the anomaly with the value $M_{K\Lambda} \sim 1.7$ GeV is the result of the decay of the N* (1688) isobar. The authors evidently attach no significance to the other irregularities.

The associative production of K-mesons and of hyperons too has been quite widely studied as related to NN-collisions, but the conclusions as to the nature of the interaction of a hyperon and a K-meson in these reactions also are ambiguous.

The Bierman group [21] used an 80" hydrogen chamber to study pp-collisions in the case of a 5.0 GeV/c momentum. Intensification in the mass spectrum of a $K^+\Lambda$-system ($pp \rightarrow p\Lambda K^+$) reaction) for a value $M_{K\Lambda} \sim 1.7$ GeV was observed. As the authors say, this can be explained by the overlapping of the effects of peripheral interaction and the decay of the N* (1688) isobar. The diagram with π-meson exchange can be the basis for a complete explanation of the results of the investigation of the $p + p \rightarrow p + \pi^+ + \Lambda + K^0$ reaction.

pp-Collisions with momentum of 5.5 GeV/c also were studied in an 81 cm liquid-hydrogen chamber [22]. The

$$p + p \rightarrow \begin{cases} p + \Lambda + K^+; \\ p + \Lambda + K^0 + \pi^+; \\ p + \Lambda + K^+ + \pi^0; \\ n + \Lambda + K^+ + \pi^+. \end{cases}$$

reaction was investigated. The authors claim that a peak appeared at the value $M_{K\Lambda} \sim 1.7$ to 1.8 GeV in all mass distributions for a $K\Lambda$-system. It is the opinion of these authors that the results of the experiment can be explained by a peripheral diagram with production of a K-meson and Y_1^* at a single apex.

Reference [23], which investigated this same reaction, contains a $\Lambda K^{+(0)}$ mass spectrum. The primary momentum was 6.92 GeV/c. A concentration of events with small masses was obtained in the mass spectrum for a three-particle product state, and this can be explained by the $p + p \rightarrow N^*_{1/2}$ (1688) $+ p \rightarrow \Lambda + K^+ + p$ reaction, or by the peripheral interaction in terms of a single meson exchange in which Λ and K occur at the same apex. When the authors analyzed the pp-interaction data at lower energies they found a shift of the mass distribution peak from $M_{K\Lambda} \sim 1.7$ GeV to $M_{K\Lambda} \sim 1.8$ GeV, with increase in the energy of the incident /81 proton, and this tends to favor the peripheral interactions explanation. Only the single meson exchange is used to explain four-particle states in this reference.

Reference [24] studied pp-collisions with momentum of 10 GeV/c. States with four and five particles at the end, $\Lambda NK\pi$ and $\Lambda NK\pi\pi$, were reviewed. This reference cites the intensive production of Y* (1380) and Y* (1650). The authors estimate the formation of the N* (1688) isobar with a probability of about 18 $\pm$ 9% in these reactions.

So far as the KΛ-system is concerned, there is an excess of the experimental number of events over the phase curve in the mass domain from 1.7 to 2.0 GeV in the mass distribution, $M_{K\Lambda}$, in the reaction $p + p \to \Lambda + K + N + \pi$. Although concordance with the phase distribution is not very good, the statistics were too meager for the authors to draw any conclusions as to the presence of resonances of any sort in the KΛ-system. Additional information on the experimental investigation of resonances in the KΛ-system can be found in [25, 26].

Table 3 lists "resonances" observed by different authors in the KΛ-system. It must be emphasized that not one of the resonances listed in the table has been established uniquely, and conclusively.

TABLE 3

Effective mass, M, MeV	Width Γ, MeV	Decay channel	Literature
~1650	—	ΛK^0	[8, 9]
~1700	~100	ΛK^+ (ΛK^0)	[12, 18]
1820	≤60	ΛK^0	[25]
~1950	~100	ΛK^0(ΛK^+)	[14, 15]

The foregoing shows that today problems connected with the properties of the reactions of the combined production of K-mesons and Λ-hyperons, and particularly the question of the existence of resonance states in this system, have not been solved. The mutual effect of the various channels with the participation of Λ and K in the product state has not been investigated. There are a great many other questions that remain unclear, but they are beyond the scope of this survey.

Only the following considerations can be incorporated here. The two-particle reaction $\pi p \to K\Lambda$ is the best studied one at this time. The characteristics of this reaction in the energy domain near the Σ-hyperon production threshold can be understood if the explanation of resonance in a KΛ-system with effective masses of 1.6 to 1.7 GeV is used. This reaction has not been analyzed theoretically at higher energies, but the experimental data are extremely interesting. Measurement of the angular distributions of Λ-hyperons has shown that the ratio of the number of particles flying backward in a CM-system to the particles flying forward as a function of the energy has a minimum in the case of a primary meson momentum p = 1.35 GeV/c, after which it once again increases. /82

This ratio reaches a maximum when p = 2.0 GeV/c. A second maximum also has been observed at p = 1.42 GeV/c on the curve for the total cross-section of the reaction as a function of the energy [27]. This behavior of the total and differential cross sections can be explained, in principle, by postulating the existence of resonance with mass $M_{K\Lambda} \sim 1.9$ GeV in the $K\Lambda$-system. Still unclear is whether this is a reflection of the decay of the N* (1920) isobar with isotopic spin of 3/2 in the $N^* \to K + \Sigma$ channel, or a new resonance. The problem of $K\Lambda$ resonances is in need of careful study.

$\Sigma \to \Lambda + \gamma$

3. Resonances in the $K\bar{K}$-System

The investigation of the $K\bar{K}$-system was more successful. Study of this system made it possible to observe (φ, f') resonances, for which this decay channel is the main channel, and helped to establish the characteristics of the known (A_2) resonances. The study made of the $K\bar{K}$-system provided indications of the existence of new, as yet not finally established, (S*, G) resonances.

The $K^0\bar{K}^0$ pair can be characterized by a definite charge and space parity, with $C = P = (-1)^l$, where l is the moment of the relative momentum of K and $\bar{K}$. As we know, it is not K^0 and $\bar{K}^0$ that take part in the reactions, but their linear combinations K_1^0 and K_2^0. The charge parity is positive for the $K_1^0K_1^0$- and $K_2^0K_2^0$-systems, and negative for the $K_1^0K_2^0$-system. Therefore, resonances with positive parity decay into $K_1^0K_1^0$- and $K_2^0K_2^0$-systems, those with negative into $K_1^0K_2^0$. Of all the resonances observed in the KK-system, only the φ-meson with mass M = 1019.3 ± 0.6 MeV and half-width Γ = 3.4 ± 0.8 MeV, one of nine known vector mesons with 1^- spin and parity, has negative parity. It can be observed quite distinctly in π^-p-and K^-p-interactions, as well as during the annihilation of /83
antiprotons.

An anomaly also can be observed near the threshold in the $K_1^0K_1^0$-system. However, it can be explained by S* resonance [28, 29], as well as by the long length of the scattering of a K-meson by a K-meson [30, 31]. Resonance in the $K_1^0K_1^0$-system with mass of about 1.3 GeV, which can be interpreted as $A_2^0 \to K_1^0K_1^0$, decay, was observed for the first time by V. V. Barmin, et al., [32]. Today this has been confirmed by the great amount of work that has been done using heavy-liquid [33] and hydrogen [34, 35] bubble chambers, as well as spark chambers [29, 31]. Most studied the $\pi^-p \to K_1^0K_1^0n$ or $\pi^-p \to K_1^0K_1^0$ + neutral particles

reactions with various π-meson momenta (from reaction threshold to 12 GeV/c). Several resonances can be observed simultaneously at high π-meson energies. The authors of reference [29] introduce four resonances (S*, f^0, A_2^0, G), to explain the spectra of effective masses for the $K_1^0K_1^0$-system observed.

An interesting situation has arisen in connection with the possible splitting of the A_2 resonance into two maxima. This effect was found with the aid of a deficient mass spectrometer by G. Chikovani, et al., [36]. Crennell, et al., [35], found this same splitting with a hydrogen bubble chamber. A significant argument in favor of the existence of two resonances is that these people observed only one of the two maxima in the $K_1^0K_1^0$-system in the A_2-meson domain. This led the authors to conclude that two resonances, A_{2L} and A_{2H}, with different quantum numbers, did in fact exist. The difference in masses is 40 MeV. The presence of two resonances with different quantum numbers explains the difficulties that arose in establishing the quantum numbers of the A_2-meson [37]. Other, circumstantial, evidence also is available. Morrison [38], for example, arrived at his conclusion as to the presence of two resonances in the A_2-meson on the basis of an analysis of the dependence of the cross section of the production of resonances on the primary energy. Nine mesons with 2^+ spin and parity are known. These are the A_2 (three isotopic states), the K^*_{1405} (four states), f^0, and $f^{0'}$. It is difficult to explain the existence of two A_2 resonances with identical quantum numbers [39], within the context of SU_3-symmetry. It should also be pointed out that one sees a single broad maximum in the $\rho\pi$-, as well as in the $K\bar{K}$-system, in most of the experimental work in the 1300 MeV range. Moreover, one finds a maximum with a mass of some 1200 MeV (the so-called $A_{1.5}$-resonance) with width $\Gamma \sim 20$ MeV [40, 41] in the $\rho\pi$-system. Further experiments are needed in this domain.

4. Results of the Experiment /84

MIFI* studied the spectrum of effective masses of the $K^0\Lambda$ and $K_1^0K_1^0$-systems generated by π^--mesons with a 3.86 GeV/c momentum in a 105 cm freon bubble chamber. The preliminary results have been published in [15, 33, 42]. 190,000 stereo photographs were processed. Figure 6a shows the effective mass distribution (250 recorded $K_1^0K_1^0$ pairs for all stars). The concentration of events in the 1200 to 1300 MeV range, as well as at small effective mass values, can be seen. Figure 6b shows the analogous distribution (27 cases) for unrayed events.

*MIFI = Moscow Engineering Physics Institute.

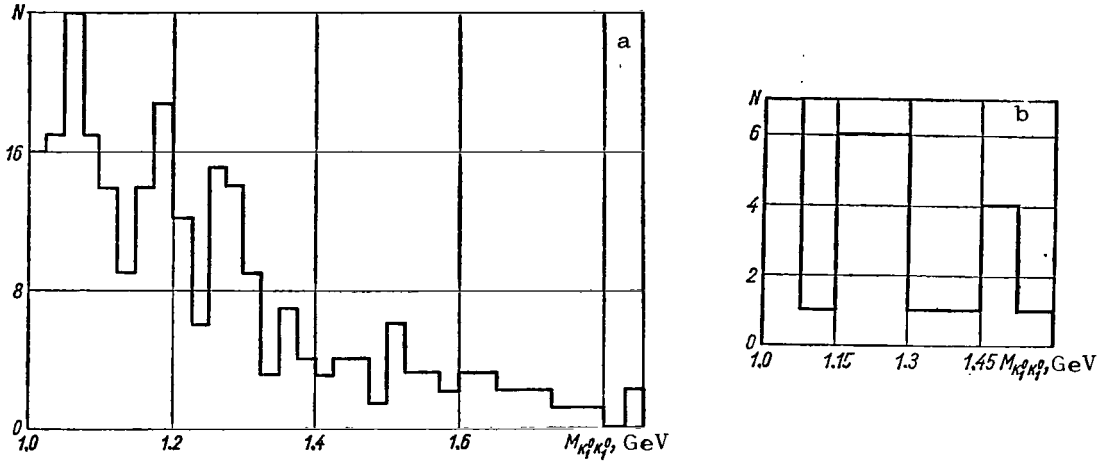

Figure 6. Effective mass distribution for the $K_1^0K_1^0$-system.

Investigation of the $K^0\Lambda$-system also was continued. Figure 7 shows the effective mass, $M_{K_0\Lambda}$, distribution for 536 reactions. The "random stars" method was used to compare the experimental distribution with that computed. It developed that the computed distribution can only describe the most general outlines of $\Delta N\ (M_{K\Lambda})$. The computation does not reflect the irregularity in the experimental distribution. /85

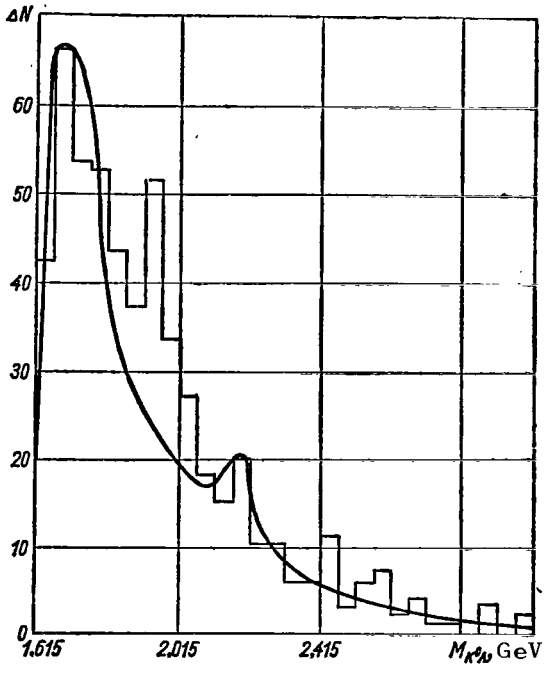

Figure 7. Effective mass distribution for the $K^0\Lambda$-system.

Estimates in terms of the χ^2 criterion were made in order to explain whether or not the shape of $\Delta N\ (M_{K\Lambda})$ can be established by a selection from the original distribution as represented by the "random stars" curve. It developed that the probability of such selection, p, is less than 5% (p = 2.5%). The observed anomalies of the mass spectrum thus cannot be recognized as random when the original significance level is p = 5%.

Since it has been established that an appreciable number of Y* (1385)- and K* (888)-resonances are generated in the reactions of the associated production of /86

Λ-hyperons and K-mesons with π-meson accompaniment, their effect on the distribution of $K_{K\Lambda}$, was investigated. It developed that the reactions

$$\pi + N \rightarrow \begin{cases} K + \Lambda + n\pi & (n = 1, 2, 3); \\ K^* + \Lambda + n\pi & (n = 0, 1, 2); \\ K + Y^* + n\pi & (n = 0, 1, 2) \end{cases}$$

could not imitate the experimental mass spectrum, individually, or in combinations.

The effect of decays of an isobar with isotopic spin T = 1/2 in $N^* \rightarrow K + \Lambda$ channels on $\Delta N(M_{K\Lambda})$ can be analyzed, at least in principle. The mass distribution, resonances taken into consideration, can be written in the form,

$$\frac{dN}{dM} \sim M\sigma \left| A + \frac{B}{M^2 - M_0^2 - i\Gamma M_0} + \ldots \right|^2,$$

where

M is system mass;

M_0 is resonance mass;

Γ is resonance width;

σ is the phase factor.

Since the nucleus is the target in our case, dN/dM must be summed over all possible reaction channels and energies occurring in the cascade process. We do not know how the process develops in the nucleus, but if the fact that the resonance term decreases rapidly with displacement from the resonance mass, is used, the result of the summing can be approximated in the form

$$\frac{dN}{dM} \sim A\sigma_\Sigma + \frac{B}{(M_0^2 - M^2)^2 + \Gamma^2 M^2},$$

where

σ_Σ is the sum of the phase distributions that we identify with the distribution of random stars. This latter formula has been used to compute the mass distribution with resonances N (1688) $F^+_{5/2}$ and N (2190) $G^-_{7/2}$ taken into consideration. Figure 7 (the smooth curve) shows the results. Clearly, the spike in the $M_{K\Lambda} \sim 1.9$ GeV area requires the introduction of yet another resonance term to describe it.

The dependence of the asymmetry parameter, α, on the effective mass, also was studied:

$$\alpha = \frac{N_b - N_f}{N_b + N_f},$$

where /87

N_b and N_f are the numbers of Λ-hyperons flying backward, and forward, respectively, relative to the direction of motion of $K\Lambda$ in its system of rest.

This relationship is upset by a tendency to become symmetrical in the 1.65 GeV < $M_{K\Lambda}$ < 2.00 GeV range, indicating the presence of resonances in this range.

Thus, the anomaly in the $M_{K\Lambda} \sim 1.9$ GeV range observed in the mass spectrum for the $K^0\Lambda$-system, and the behavior of α, can explain the existence of resonance for this system. The estimates of the parameters of the resonance are $M \sim 1.94$ GeV, $\Gamma \sim 100$ MeV.

REFERENCES

1. Baz', A. I. and Okun', L. B., Zh. eksperim. i. teor. fiz., Vol. 35, 1958, p. 757.
2. Rimpault, M., Nuovo cimento, Vol. 31, 1964, p. 56.
3. Kanazawa, A., Phys. Rev., Vol. 123, 1961, p. 997.
4. Hoff, G. T., Phys. Rev., Vol. 139, 1965, p. 671.
5. Rush, J. E. and Holladay, W. G., Phys. Rev., Vol. 148, 1966, p. 1444.
6. Hoffman, H. S. and Schnitzer, H. J., Nucl. Phys., Vol. 76, 1966, p. 481.
7. Baz', A. I., et al., Zh. eksperim. i. teor. fiz., Vol. 43, 1962, p. 166.
8. Kuznetsov, Ye. V., et al., Zh. eksperim i. teor. fiz., Vol. 42, 1962, p. 1675.
9. Bertanza, L., et al., Phys. Rev., Lett., Vol. 8, 1962, p. 332.
10. Barman, V. V., et al., Yadernaya fizika, Vol. 3, 1966, p. 342.
11. Curtis, L. J., et al., Phys. Rev., Vol. 132, 1963, p. 1771.
12. Dagan, S., et al., Phys. Rev., Vol. 161, 1967, p. 1384.
13. Colley, P., et al., Phys. Rev., Vol. 128, 1962, p. 1930.
14. Wangler, T. P., et al., Phys. Rev., Vol. 137, 1965, p. 414.
15. Demidov, V. S., et al., Yadernaya fizika, Vol. 9, 1969, p. 587.
16. Bertanza, L., et al., Phys. Rev., Vol. 130, 1963, p. 786.
17. Dahl, O. I., et al., Phys. Rev., Vol. 163, 1967, p. 1377.
18. Crennell, D. J., et al., Phys. Rev., Lett., Vol. 19, 1967, p. 1212.
19. Belliere, J., et al., Nuovo cimento, Vol. 29, 1963, p. 339.
20. Ehrlich, R., et al., Phys. Rev., Vol. 152, 1966, p. 1194.
21. Bierman, E., et al., Phys. Rev., Vol. 147, 1966, p. 922.
22. Alexander, G., et al., Phys. Rev., Vol. 154, 1967, p. 1284.
23. Alexander, G., et al., Nuovo cimento, Vol. 53A, 1968, p. 455.
24. Holmgren, S. O., et al., Nuovo cimento, Vol. 51A, 1967, p. 305.
25. Materialy XII Mezhdunarodnoy konferentsii po fizike vysokikh energiy, [Materials from the XIIth International Conference on High Energy Physics], Dubna, 1964, Vol. I, Atomizdat, Moscow, 1965.
26. Barashenkov, V. S., Secheniya vzaimodeystviya elementarnykh chastits, [Interaction Cross Sections for Elementary Particles], Nauka Press, Moscow, 1966.

27. Goussu, O., et al., Nuovo cimento, Vol. 42A, 1966, p. 606.

28. Crennell, D. J., et al., Phys. Rev., Lett., Vol. 16, 1966, p. 1025.

29. Beusch, W., et al., Phys. Lett., Vol. 25B, 1967, p. 357.

30. Hess, R. I., et al., Phys. Rev., Lett., Vol. 17, 1966, p. 1109.

31. Hoang, T. F., et al., Phys. Rev., Lett., Vol. 21, 1968, p. 316.

32. Barmin, V. V., et al., Zh. Eksperim. i. teor. fiz., Vol. 43, 1962, p. 1564; Barmin, V. V., et al., Yadernaya fizika, Vol. 1, 1965, p. 870. /88

33. Demidov, V. S., et al., Yadernaya fizika, Vol. 4, 1968, p. 470.

34. Chung, S. U., et al., Phys. Rev., Lett., Vol. 18, 1967, p. 100.

35. Crennell, D. J., et al., Phys. Rev., Lett, Vol. 20, 1968, p. 1318.

36. Chikovani, G., et al., Phys. Lett., Vol. 25B, 1967, p. 44.

37. Vetlitskiy, I. A., et al., Yadernaya fizika, Vol. 6, 1967, p. 795.

38. Morrison, D. R. O., Phys. Lett., Vol. 25B, 1967, p. 238.

39. Coulter, P. W. and Shaw, G. L., Phys. Rev., Lett., Vol. 21, 1968, p. 634.

40. Cason, N. M., et al., Phys. Rev., Lett., Vol. 18, 1967, p. 880.

41. Von Krogh, J., Phys. Lett., Vol. 27B, 1968, p. 253.

42. Demidov, V. S., et al., V sb. Elementarnyye chastitsy i kosmicheskiye luchi, In collection; [Elementary Particles and Cosmic Rays], Atomizdat, Moscow, 1967, p. 40.

THE PRODUCTION OF AN OCTET OF PSEUDOSCALAR MESONS IN THE COULOMB FIELD OF A NUCLEUS AND THE CROSS-SECTION OF THE PHOTOPRODUCTION OF MESONS BY MESONS

G. S. Iroshnikov, Yu. P. Nikitin

ABSTRACT. The possibility of using information on the photoproduction of mesons by mesons based on data on the production of mesons in the Coulomb field of the nucleus is analyzed. The conclusion is that there is a real possibility of so doing if the model of the strong interactions used is valid within one order of magnitude.

The process involved in the photoproduction of a psuedoscalar meson, P, by a meson (Figure 1) /89

$$\gamma + P \to P + P \tag{1}$$

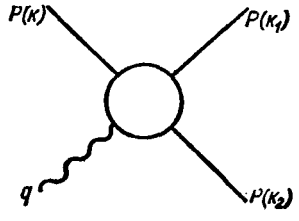

Figure 1. Photoproduction of a pseudoscalar meson by a meson.

cannot be observed directly today because of a lack of meson targets or counter meson and γ-beams. This process is still unrealizable by a laser light beam because π-mesons with energies $E \geq 10^6$ GeV would be required within the laboratory system. But as has been pointed out [1, 2], it is possible, in principle, to measure the cross section of the Eq. (1) process by studying the reaction of the interaction between the mesons and the nuclei

$$P + Z \to P + P + Z \tag{2}$$

when small momenta, Δ, are transmitted to the nucleus. The Eq. (2) process is attributable to strong and electromagnetic interactions. If the cross section of the Eq. (2) reaction is known when $\Delta^2 \to 0$, the cross section of the Eq. (1) photoproduction can be derived, providing that the contribution of the interactions predominates when momentum transfers to the nucleus are small. At the same time, it is desirable to study the Eq. (2) reaction when conditions are such that the nucleus is not excited and the nucleons of the nucleus act coherently. There is then no need to take details concerned with the structure of the nucleus into consideration.

The nuclear matrix element for the transition is definitely different from zero for states with energy differences $\Delta E \sim E_F A^{-1/3}$ [3] (here A is the number

of nucleons in the nucleus; E_F is the Fermi energy). The nucleus should not be excited, therefore, when momenta $\Delta^2 \ll 2mE_F A^{-1/3}$ are transmitted to the nucleus (m is the mass of a nucleon). What this means in the case of xenon (A = 131, Z = 54), for example, is that Δ should be small compared with the mass of a π-meson, μ, or, more precisely, $\Delta^2 \ll 0.7\ \mu^2$.

The momenta transferred during the interaction must be small compared with the inverse radius of the nucleus, R^{-1} in order to have coherent action on the part of the nucleons of the nucleus; that is, $\Delta^2 < 0.05\ \mu^2$ for xenon. The nucleus can thus be considered as an object that receives only recoil when the momenta transferred are small enough. At the same time, the computation for the cross section of the Eq. (2) reaction can be greatly simplified, and it is easy to establish that domain of kinematic variables in which the Coulomb interaction is dominant. /90

As will become clear in what follows, the most convenient range of initial energies, E_L, will be between 10 and 30 GeV, where the results are only slightly dependent on the coupling constants. We can, therefore, assume that they are equal for different reactions, right from the beginning. This confirms the computation made for the relationships between the amplitudes of the reactions within the framework of the SU_3 symmetry. This will be discussed in what follows because these relationships are of independent theoretical interest.

1. Production of an Octet of 0^- Mesons in the Field of the Nucleus and the Cross Section of the Photoproduction of Mesons by Mesons

The Eq. (2) reaction can be described by the diagram shown in Figure 2, in the lowest order of the perturbation theory concerned with electromagnetic interaction. The differential cross section corresponding to it is equal to

$$\frac{\partial^3 \sigma_c}{\partial(\Delta^2)\,\partial s\,\partial u} = \frac{\alpha Z^2 |F(\Delta^2)|^2}{\pi} \cdot \frac{\Delta^2 - \Delta^2_{\min}}{(s-m^2)\,\Delta^4} \cdot \frac{\partial \sigma(P\gamma \to PP)}{\partial u}, \qquad (3)$$

where

$s = (k_1 + k_2)^2$;

$\Delta^2 = -q^2$;

$u = (k - k_1)^2$;

$m^2 = k^2$;

$k_1^2 = m_1^2$;

$k_2^2 = m_2^2$;

$\alpha = 1/137$;

$F(\Delta^2)$ is the charge form factor for the nucleus;

$\Delta_{min} = (s - m^2)/2E_L$ when $s \ll E_L^2$;

E_L is the laboratory energy of the bombarding meson; /91

$\partial\sigma(P_\gamma \to PP)/\partial u$ is the cross section of the photoproduction of mesons by mesons when $\Delta^2 \to 0$.

The magnetic form factor for the nucleus can be ignored [1].

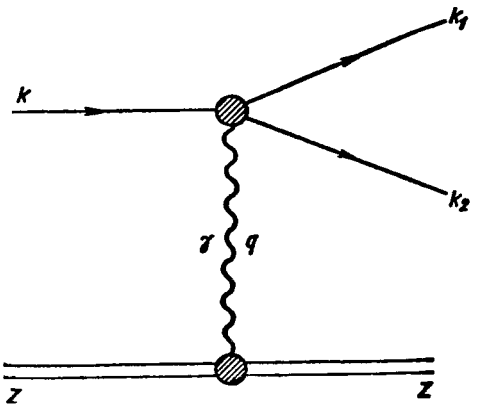

Figure 2. Diagram of the production of a meson in the Coulomb field of the nucleus, Z.

As we know, in unitary symmetry theory the electromagnetic current is a component of the vector octet (see [4], for example)

$$I_\mu^e = (V_\mu)_1^1,$$

so the matrix element of the Eq. (1) process satisfying the requirements for gage, charge, and Lorentz invariance, has the form

$$T(P_\gamma \to PP) = i(2\pi)^4 \delta^4(k + q - k_1 - k_2)\varepsilon_{iklm} l_i(q) k_k \times$$
$$\times k_{1_e} k_{2_m} \{A(S, u, t)[P_1^\gamma(k)\overline{P}_\gamma^\delta(k_1)\overline{P}_\delta^1(k_2) - P_\gamma^1(k)\overline{P}_\delta^\gamma(k_1) \times$$
$$\times \overline{P}_1^\delta(k_2)] + B(s, u, t)[P_\gamma^1(k)\overline{P}_1^\delta(k_1)\overline{P}_\delta^\gamma(k_2) -$$
$$- P_1^\gamma(k)\overline{P}_\delta^1(k)\overline{P}_\gamma^\delta(k_2)] + C(s, u, t)[P_\gamma^\delta(k)\overline{P}_\delta^1(k_1)\overline{P}_1^\gamma(k_2) -$$
$$- P_\delta^\gamma(k)\overline{P}_1^\delta(k_1)\overline{P}_\gamma^1(k_2)]\},$$

where

P_α^β is the wave function of a meson in the 0^- octet;

$\overline{P}_\alpha^\beta$ is the adjoint function;

α and β are unitary indices;

l_μ is photon polarization;

$t = (k - k_2)^2$.

The functions A, B, and C are associated by the crossing symmetry relationships:

$$A(s, u, t) = B(s, t, u); \qquad C(s, u, t) = C(s, t, u);$$
$$A(s, u, t) = C(t, u, s); \qquad B(s, u, t) = B(t, u, s);$$
$$A(s, u, t) = A(u, s, t); \qquad B(s, u, t) = C(u, s, t).$$

Since the kinematic factor $\epsilon_{iklm}\, t_i\, k_k\, k_{1_l}\, k_{2_m}$, is present in the Eq. (4) matrix element, the amplitudes of A, B, and C must tend to a constant when momenta are low in order to ensure the correct threshold relationship for the cross section of the photoproduction. The following equality occurs at the point $s = u = t = (1/3) \sum_i m_i^2$

$$A = B = C = f. \tag{4'}$$

If we assume that during the transition from the threshold to this point the magnitudes of A, B, and C remain constant, or are constants that change slightly, we will have the equality of Eq. (4') near the threshold as well, and this, together with Eq. (4), result in the obtaining of a relationship between the apexes of the various processes when momenta are low. /92

The cross section of the photoproduction in the CM-system ($k_1 + k_2 = 0$), averaged with respect to photon polarization, equals

$$\frac{\partial\sigma(P_\gamma \to PP)}{\partial u} = \frac{|f_{3P_\gamma}|^2}{2^9\pi} \cdot \frac{\lambda(s, m_1^2, m_2^2)}{s} \sin^2\vartheta_{CM} \tag{5}$$

where

ϑ_{CM} is the angle between impulses k and k_1 in the CM-system.

The quadratic form $\lambda(x, y, z) = x^2 + y^2 + z^2 - 2xy - 2xz - 2yz$ is associated with the momentum k_1 in this same system by $|\mathbf{k}_1| = (2\sqrt{s})^{-1}\sqrt{\lambda(s, m_1^2, m_2^2)}$. As will be seen from Eq. (5), the Eq. (3) cross section tends to zero in the direction of the momentum of the incident beam of mesons. Since this result is the consequence of the retention of the projection of the total momentum at the $3P_\gamma$ apex, the vanishing of the Eq. (3) cross section with forward scattering does not depend on the concrete form of the function f. This property is retained in the L-system as well, so the cross section of reaction (2) can be measured with adequate reliability because its maximum does not lie in a strictly forward direction.

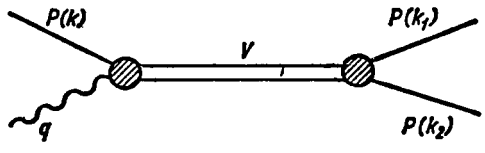

Figure 3. Resonance photoproduction of a meson by a meson.

Integrating Eq. (3) with respect to the variable u (or with respect to v_{CM}), we obtain

$$\frac{\partial^2\sigma_c}{\partial(\Delta^2)\partial s} = \frac{\alpha Z^2 \mid F(\Delta^2)\mid^2}{\pi} \frac{(\Delta^2-\Delta^2_{\min})}{\Delta^4} \cdot \frac{\sigma^{(s)}_{P\gamma\to PP}}{s-m^2} =$$

$$= \frac{\alpha Z^2 \mid F(\Delta^2)\mid^2 \mid f^{(s)}_{P\gamma\to PP}\mid^2}{3\cdot 2^8\pi} \cdot \frac{(\Delta^2-\Delta^2_{\min})}{\Delta^4} \cdot \frac{\lambda^{3/2}(s, m_1^2, m_2^2)}{s^2} \qquad (6)$$

Here the magnitude $f^{(s)}_{P\gamma} \to PP$ is the averaged vertex function $f^{(s,\,u)}_{P\gamma\to PP}$, averaged with respect to $u(\vartheta_{CM})$, if its dependence on $u(\vartheta_{CM})$ is significant.

The Eq. (1) reaction can also result in resonance and the subsequent decay into two mesons (Figure 3). Now, when this resonance belongs to the octet of vector mesons, 1^-, the corresponding cross-section has the form /93

$$\frac{\partial^2\sigma_c}{\partial(\Delta^2)\partial s} = \frac{\alpha Z^2 \mid F(\Delta^2)\mid^2 \mid f_{P\gamma\to V}\mid^2 \mid f_{V\to PP}\mid^2}{3\cdot 2^6\pi} \cdot \frac{(\Delta^2-\Delta^2_{\min})}{\Delta^4} \times$$

$$\times \frac{\lambda^{3/2}(s, m_1^2, m_2^2)}{s^2[(s-m_V^2)^2+\Gamma^2]}, \qquad (7)$$

where

$\Gamma = m_V/\tau_V$, τ_V, m_V, are the width, lifetime, and mass of a vector meson, respectively.

Eq. (7) can be used to find the constants for the radiation decay of vector mesons into pseudoscalar mesons.

2. Evaluation of the Contribution of Strong Interactions

Since we are interested in low transferred momenta Δ, the evaluation of the contribution of strong interactions can be made within the framework of the one-boson exchange model. The Eq. (2) process can yield the contribution of the exchange of pseudoscalar and vector mesons. Of these, as the evaluations show, the greatest is attributable to the ω-meson exchange (Figure 4). The exchange by the octet of vector mesons, 1^-,[10] is forbidden within the limits of precision up to the violation of unitary symmetry as a consequence of conservation of

10. $G' = RC$, where R is the operation of reflection relative to the coordinate origin on the weight diagram for the representation of the SU_3 group: C is the operation charge conjugation. We have $G'_P = -1$, and $G'_V = +1$, for the pseudoscalar and vector mesons.

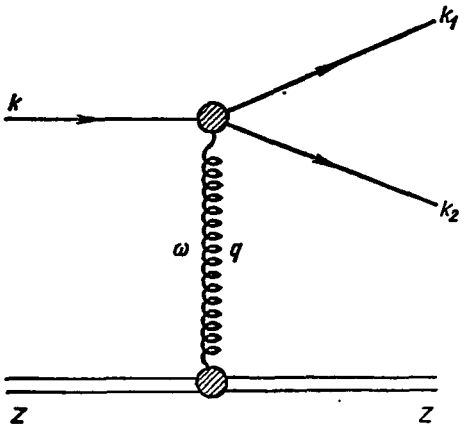

Figure 4. Diagram of the production of a meson as a result of the exchange of an ω-particle with the nucleus.

of G'-parity (for which see reference [4], for example). In concordance with this is the fact that the contribution from the φ-meson, computed in the model under consideration, proves to be less than the contribution of the ω-meson by two orders of magnitude due to large mass of φ and the narrow decay width $\varphi \to 3\pi$. The exchange of π and η-mesons is even more suppressed because the PNN apex in the pseucoscalar coupling diagram is proportional /94 to the transferred momentum Δ, and this, in our problem, is small in magnitude. Leroy [5], computing the contribution from a one-π meson exchange with the help of a modified π-meson propagator in a nuclear substance, also came to the conclusion that the π-meson contribution is small compared with the Coulomb contribution. The rest of the hadrons either have large masses, or their exchange is forbidden by the quantum numbers. This is why we have limited ourselves to the ω-exchange in evaluating the role of strong interactions. The corresponding contribution to the Eq. (2) process cross section can be obtained quite readily from the Eq. (6) Coulomb process by replacement of the propagator and apex functions

$$\frac{\partial^2 \sigma_N}{\partial(\Delta^2)\partial s} = \frac{g_{\omega NN} A^2 |F(\Delta^2)|^2 \left| f^{(s)}_{P\omega \to PP} \right|^2}{3 \cdot 2^8 \pi} \cdot \frac{(\Delta^2 - \Delta^2_{min})}{(\Delta^2 + m_\omega^2)^2} \times$$

$$\times \frac{\lambda^{3/2}(s, m_1^2, m_2^2)}{s^2}, \qquad (8)$$

where

$g_{\omega NN} = f^2_{\omega NN}/4\pi$ is the constant for the coupling of the ω-meson with the nucleon;

m_ω is the mass of the ω-meson.

The ratio of the Eq. (6) and Eq. (8) cross sections, for fixed s, equals

$$\frac{\partial \sigma_c}{\partial \sigma_N} = \left(\frac{Z}{A}\right)^2 \frac{\alpha |f_{3P_\gamma}|^2}{g_{\omega NN} |f_{3P_\omega}|^2} \left(\frac{m_\omega}{\Delta}\right)^4, \quad \Delta^2 \ll \mu^2 \qquad (9)$$

and is determined by the transferred momentum Δ. This relationship has the following, similar, form in the case of resonance in an intermediate state

$$\left.\frac{\partial\sigma_c}{\partial\sigma_N}\right|_{S\approx m_V^2} = \left(\frac{Z}{A}\right)^2 \frac{\alpha\,|f_{VP\gamma}|^2}{g_{\omega NN}\,|f_{VP\omega}|^2}\left(\frac{m_\omega}{\Delta}\right)^4. \qquad (10)$$

3. Study of the Domain of Kinematic Variables Inside Which the Coulomb Mechanism is Dominant, and its Dependence on the Energy of the Incident Particles

If there is to be a reliable determination of the cross section of photoproduction

$$\sigma_{P\gamma\to PP} = \frac{|f_{3P\gamma}|^2}{3\cdot 2^8\pi}\cdot\frac{(s-m^2)\lambda^{3/2}(s,\,m_1^2,\,m_2^2)}{s^2} \qquad (11)$$

the contribution of the strong interactions in the Eq. (2) reaction cross section must be small compared with the contribution from the electromagnetic interactions. This can be achieved in the domain of small Δ, small such that the relations of the Eq. (9) cross sections be of the order of ten. Now the effect of the strong interactions can be ignored. Moreover, what must be pointed out in particular is that the Coulomb cross section $d\sigma_c$ of Eqs. (6) and (7) has a maximum when $\Delta_0^2 \approx 2\Delta_{min}^2 = (s - m^2)^2/2E_L^2$. From whence the value of the variable s corresponding to this maximum is equal to /95

$$s = \sqrt{2}\,\Delta_0 E_L + m^2. \qquad (12)$$

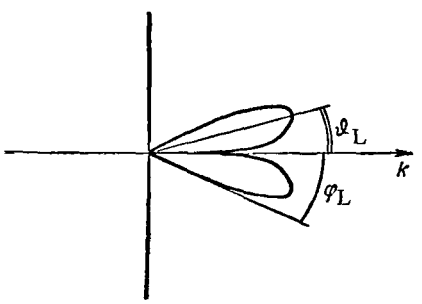

Figure 5. Determination of the angles of escape of the Eq. (2) reaction products in the L-system.

The angle ϑ_L corresponds to a maximum for the Eq. (2) reaction cross section; φ_L is the maximum angle of escape of the particles.

Let us now explain the nature of the region of angles in the L-system in which the Coulomb mechanism prevails over the nuclear (corresponds to adequately small Δ_0), and how the dimensions of this region depend on the initial energy, E_L, of the incident particles.

Let us introduce the angle ϑ_L^{11} at which the Eq. (3) cross section has a maximum and the maximum angle φ_L of escape of secondary particles. Both angles are in the L-system (Figure 5). The Eqs. (3) and (5) cross sections in the CM-system have maxima in terms of the variable $u(\vartheta_{CM})$ when $\vartheta_{CM} = \pi/2$, and are symmetrical with respect to the exit angles of

both particles in the final state[12] regardless of whether they are of the same type, or different. No such symmetry exists in the L-system, and different angles correspond to different types. The angles in the L and CM systems can be associated by using well known formulas

$$\tan\vartheta_L = \frac{v\sqrt{1-V^2}\sin\vartheta_{CM}}{v\cos\vartheta_{CM}+V};$$

$$\sin\varphi_L = \frac{p\sqrt{1-V^2}}{mV},$$

where

v and p are the velocity and momentum of a particle in the CM-system;

V is the velocity at which the CM-system moves with respect to the L-system for fixed $s(s \ll E_L^2)$.

The following expressions are obtained for the angles characterizing the region of kinematic variables considered for the general case of various particles in the final state /96

$$\tan\vartheta_L^1 = \frac{\sqrt{s}\,\lambda^{1/2}(s, m_1^2, m_2^2)}{E_L(s+m_1^2-m_2^2)}; \quad \tan\vartheta_L^2 = \frac{\sqrt{s}\,\lambda^{1/2}(s, m_1^2, m_2^2)}{E_L(s+m_2^2-m_1^2)}; \tag{13}$$

$$\sin\varphi_L^1 = \frac{\lambda^{1/2}(s, m_1^2, m_2^2)}{2m_1 E_L}; \quad \sin\varphi_L^2 = \frac{\lambda^{1/2}(s, m_1^2, m_2^2)}{2m_2 E_L}. \tag{14}$$

But we have ignored the angle ψ at which the CM-system of secondary particles is moving because

$$\psi \approx \frac{\sqrt{\Delta^2-\Delta_{min}^2}}{E_L} \tag{15}$$

because at energies of the order of several billion electron volts, and higher, and at small Δ, this angle will not be larger than a few minutes.

Eqs. (13) and (14) convert to the following in the case of the production of identical particles ($m_1 = m_2 = m$)

---

11. The angle ϑ_L corresponds to the maximum for the Eq. (3) cross section in the energy range $E_L < 30$ GeV, where the p-wave is dominant. At higher energies the contribution of succeeding waves must be taken into consideration, and as a result the cross section maximum can shift.

12. Strictly speaking, this is valid only for the p-wave.

$$\tan\vartheta_L' = \frac{\sqrt{s-4m^2}}{E_L}. \tag{16}$$

Let us consider concrete reactions in order to obtain numerical values for the angles ϑ_L and φ_L.

a. Production of π-mesons in the field of the nucleus. The Eq. (2) reaction will take the form

$$\pi^\pm + Z \to \pi^\pm + \pi^0 + Z. \tag{18}$$

two photoproduction processes are associated with it: the potential

$$\pi^\pm + \gamma \to \pi^\pm + \pi^0 \tag{19}$$

and the resonance

$$\pi^\pm + \gamma \to \rho^\pm \to \pi^\pm + \pi^0. \tag{20}$$

What follows from isotopic invariance is that the Eq. (18 to 20) reaction cross sections are identical for positive and negative π-mesons, that the particles in the final state have isospin T = 1, and odd orbital moments. The magnitude $f_{3\pi\gamma}$ associated with the Eq. (19) reaction is unknown because this is the magnitude under study during the experimental investigation of this Eq. (19) reaction. Dimensionality considerations will yield $f_{3\pi\gamma} \sim \sqrt{\alpha}\mu^{-3}$. The relationship between the magnitudes $f_{3\pi\gamma}$ and $f_{3\pi\omega}$ we need can be evaluated on the basis of the following considerations. Since only the isoscalar photons take part in /97 the Eq. (19) and Eq. (20) reactions, the quantum numbers of the ω-meson and photons coincide. Therefore, apexes in which the ω-meson $f_{3\pi\omega}$ and γ-quanta $f_{3\pi\gamma}$ participate have identical spin and isotopic structures (what this means in terms of perturbation theory is that all the virtual loops of these apexes are the same). The following equality should result

$$\frac{f_{3\pi\gamma}}{f_{\pi\rho\gamma}} = \frac{f_{3\pi\omega}}{f_{\pi\rho\omega}}. \tag{21}$$

Substituting the value of the magnitudes

$$f_{\pi\rho\gamma} \approx \sqrt{\alpha}\,\frac{1.2}{\mu}\ [6], \quad f_{\pi\rho\omega} \approx \frac{2.3}{\mu}$$

we obtain the following relationship

$$\frac{f_{3\pi\gamma}^2}{f_{3\pi\omega}^2} = \frac{f_{\pi\rho\gamma}^2}{f_{\pi\rho\omega}^2} \approx 0.27\alpha. \tag{22}$$

If the decay constant $\omega \to 3\pi$ ($f_{\omega \to 3\pi} \approx (1.6/\mu)^3$ [8] is substituted for $f_{3\pi\omega}$ in Eq. (21), we find $f_{3\pi\gamma} \approx \sqrt{\alpha}\,(1.3/\mu)^3$. Taking Eq. (22) into consideration, and using Eqs. (9) and (10), ($g_{\omega NN} \approx 3$), we obtain the fact that when $\Delta = 0.18\mu$, the Coulomb cross section $d\sigma_c$ is equal in order of magnitude to the nuclear cross section $d\sigma_N$, but that when $\Delta = 0.10\mu$ the Coulomb cross section exceeds the nuclear by one order of magnitude. Assuming that $\Delta_0 = 0.10\mu$ in Eq. (12), and finding the corresponding s for fixed energy E_L for the incident particles, we now find that in the case of the Eq. (18) reaction, the region of kinetic variables in which the Coulomb cross section is greater than the nuclear by one order of magnitude can be characterized by the angles $\vartheta_L \approx 1 - 3°$, $\varphi_L \approx 4°$. Figure 6 shows the concrete dependence of these angles on energy E_L. Also shown are $\hat{s}$ values corresponding to the $d\sigma_c$ maximum in terms of the transferred momentum at the specified energy. γ-quanta developing during the decay of neutral π-mesons incident at angles $\varphi_L \geq \vartheta \geq \vartheta_L$ when $E_L = 10$ GeV, will have minimal angles of divergence χ_L in the interval $16° \geq \chi_L \geq 4.5°$, and $14.5° \geq \chi_L \geq 1.15°$ when $E_L = 40$ GeV. The upper limit of χ_L tends to 11.4°, the lower to zero, with increase in the original energy. As will be seen from Figure 6, when the energies are less than some $(E_L)_{min}$, the Coulomb cross section cannot exceed the nuclear by a factor of more than 10, and when $(E_L)_{min} \leq E_L \leq 10$ GeV, there is a sharp dependence of both angles on the energy. When $E_L \gtrsim 10$ GeV, the /98 maximum exit angle for the π-mesons, φ_L is practically constant, with the angle ϑ_L decreasing slowly with increase in energy as $\sqrt{\Delta_0/E_L}$. When $E_L = 60$ GeV, $\nu_L \approx 1°$. The magnitude of these angles is large enough to permit the cross section $\sigma_{\pi^\pm\gamma \to \pi^\pm\pi^0}$ to be studied experimentally over a broad range of energies.

b. Reactions with the participation of K-mesons. Let us consider the following reactions

$$\gamma + K^\pm \to K^\pm + \pi^0; \tag{23}$$

$$\gamma + K^\pm \to \pi^\pm + K^0,\ \tilde{K}^0; \tag{24}$$

$$\gamma + \pi^\pm \to K^\pm + \tilde{K}^0,\ K^0. \tag{25}$$

The following relationships flow from Eqs. (4) and (4') for the apexes of these reactions near the threshold

$$f_{\gamma K^+ \to K^+ \pi^0} = \sqrt{2} f; \qquad f_{\gamma \pi^+ \to K^+ \tilde{K}^0} = f;$$
$$f_{\gamma K^+ \to K^0 \pi^+} = f; \qquad f_{\gamma \pi^+ \to \pi^+ \pi^0} = \frac{3}{\sqrt{2}} f, \tag{26}$$

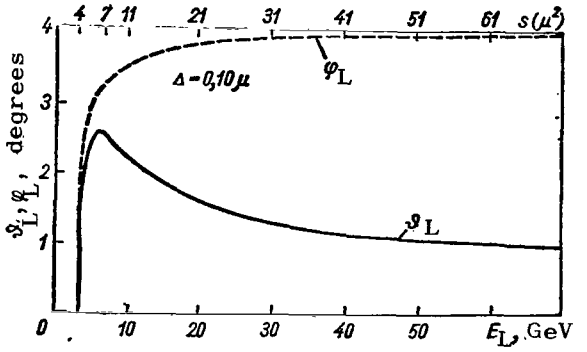

Figure 6. Energy dependence exit angles for secondary particles for the reaction $\pi^{\pm} + Xe \to \pi^{\pm} + \pi^0 + Xe$. The values selected for the kinematic variables Δ and s should provide for the dominance of the Coulomb mechanism of the reaction (μ is the mass of the charged π-meson).

where

f is a function from Eq. (4'). The relationships for the processes with antiparticles are obtained from Eq. (26) by changing the signs in all four equalities.

Relationships similar to those of Eq. /99 (26) are needed for the reactions in which the ω-meson takes part in order to use Eq. (9), which establishes the necessary momentum transfer Δ. Only the type F coupling contributes to a matrix element for these processes that is invariant with respect to the SU_3 group (because of C-invariance)

$$M(P\omega^0 \to PP) = i(2\pi)^4 \delta^4(k + q - k_1 - k_2)\, g \varepsilon_{lklm} \times$$
$$\times \omega_i^0(q)\, k_k (k_1)_l (k_2)_m \operatorname{Sp}\{P(k)[\bar{P}(k_1)\bar{P}(k_2) - \bar{P}(k_2)\bar{P}(k_1)]\}, \tag{27}$$

where

$\omega_i^0(q)$ is the ω-meson wave function[13]. The following system of equalities can now be found

$$f_{\omega K^+ \to K^+ \pi^0} = \frac{g}{\sqrt{2}}; \qquad f_{\omega \pi^+ \to K^+ \tilde{K}^0} = g; \tag{28}$$

$$f_{\omega K^+ \to K^0 \pi^+} = g; \qquad f_{\omega \pi^+ \to \pi^+ \pi^0} = \sqrt{2} g. \tag{29}$$

Now, by combining Eqs. (26), (28, and (29) with Eq. (22), we readily find the ratios of the corresponding apex functions of the reactions under consideration contained in Eq. (9). Further, carrying out a procedure similar to that outlined in section "a", we obtain the characteristic exit angles for the secondary π- and K-mesons in terms of the energy of the original K-mesons

13. Accounting for the φ - ω-mixing is insignificant in this case because, as has already been pointed out, the exchange of the vector meson is forbidden by conservation of G'-parity.

[Figures 7 to 9, respectively, for the Eqs. (23 to 25) reactions; also indicated here are the transferred momenta Δ in the vicinity of which the cross sections of these reactions must be measured].

Then too, the Eqs. (23 and 24) reactions can go through an intermediate charged resonance $K^*(892)$ when the variable $s \approx 43\mu^2$, corresponding to energy $E_L \approx 30$ GeV

$$\gamma + K^{\pm} \to K^{*\pm} \to K^{\pm} + \pi^0; \tag{30}$$

$$\gamma + K^{\pm} \to K^{*\pm} \to K^0(\tilde{K}^0) + \pi^{\pm}. \tag{31}$$

What follows from the isotopic invariance is that the cross section of the Eq. (31) process is larger than the Eq. (30) reaction cross section by a factor of 2. Known experimentally is the coupling constant K^* with a neutral vector meson $|f_{K^{*+}\,K^+\,V^0}| = 2.6\,\mu$ [12], $1.96\,\mu$ [13]. If this meson is identified as ω, the average of the two sets of data cited are in good concordance with the SU_3-prediction $f_{K^{*+}\,K^+\,\omega} = f_{\omega\rho\pi} \approx 2.3/\mu$. Further, using the fact that $f_{K^* \to K\gamma} = f_{\rho \to \pi\gamma}$, from SU_3-symmetry we obtain the following values for the exit angles for the π and K-mesons for the Eqs. (30 and 31) reactions in a manner similar to that explained above: $\vartheta_L^{\pi} = 1.5°$; $\varphi_L^{\pi} = 3{,}8°$; $\vartheta_L^{K} = 0.9°$; $\varphi_L^{K} = 1.1°$. Also possible, in addition to the processes considered, are reactions in which, in addition to the π- and K-mesons, there is participation by η-mesons contained in this same 0^- octet. The distribution in terms of the exit angles for the η-mesons will be approximately that for the K-mesons. /101

As will be seen from the graphics included here, the most convenient for the experimental study (angles large enough, yet energies not too high) are the Eqs. (19), (20), and (23) reactions. The Eq. (25) reaction is the most unfavorable of the other reactions from this point of view.[14]

---

14. In order that interference between strong and electromagnetic interactions not be taken into consideration, the ratio of the Eqs. (9) and (10) cross sections must be taken as of the order of 10^2. Now the values of the angles in Figures 6 to 8 must be reduced (when $E_L > 10$ GeV) by a factor of 1.3 for ϑ_L and by a factor of 1.8 for φ_L, respectively.

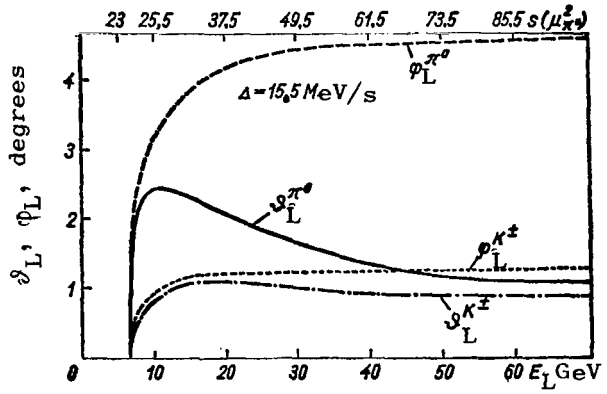

Figure 7. The $K^{\pm} + Xe \rightarrow K^{\pm} + \pi^0 + Xe$ reaction. (See Figure 6).

$\mu_{\pi O}$ is the neutral π-meson mass.

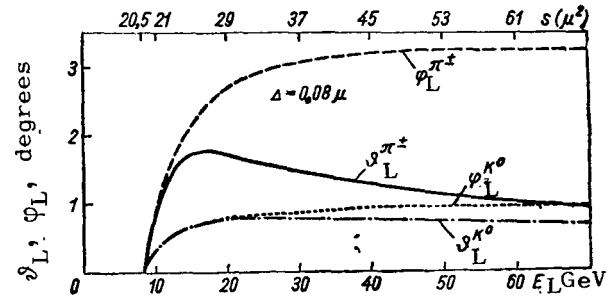

Figure 8. The $K^{\pm} + Xe \rightarrow K^0 (\widetilde{K}^0) + \pi^{\pm} + Xe$ reaction. (See Figure 6).

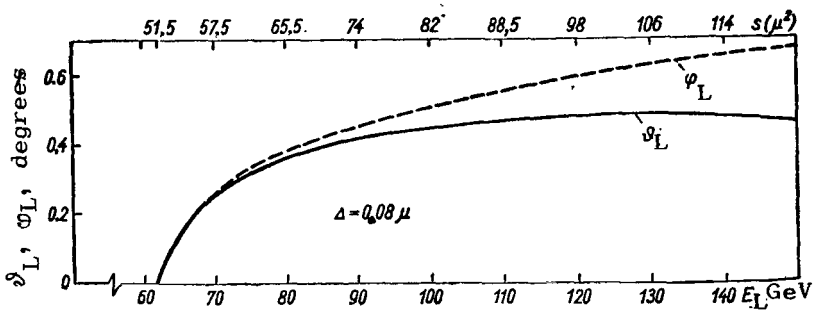

Figure 9. The $\pi^{\pm} + Xe \rightarrow K^{\pm} + \widetilde{K}^0 (K^0) + Xe$ reaction. (See Figure 6).

4. The Range of Kinematic Variables in Terms of Inaccuracy in Finding the Ratio of the Apex Functions

Eq. (9) tells us that the magnitude of the momentum Δ, transmitted to the nucleus for a specified cross sectional ratio depends on the parameter $\beta = |f_{3P_\gamma}|^2/g_{\omega NN}|f_{3P_\omega}|^2$, which we know only in terms of the order of magnitude: $\Delta \sim \beta^{1/4}$. Moreover, since the magnitudes f_{3P_γ} and f_{3P_ω} are functions of s, the β values in point of fact can change for various s, so measurement results will be reliable only for values of s, and hence E_L, such that the exit angles for the particles are fairly weakly dependent on β.

It is the quantity β which determines $(E_L)_{min}$, according to Eq. (12). As we see from Figure 6, for example [the Eq. (19) reaction], when $E_L < 10$ GeV, angles φ_L and ϑ_L will change very sharply with small variation in the magnitude of $(E_L)_{min}$. At the same time, the dependence on $(E_L)_{min}$ and, as a result, on β, is slight for energies in excess of 10 GeV: $\varphi_L \sim \beta^{1/4}$, $\vartheta_L \sim \beta^{1/8}$. Therefore, in order to obtain reliable experimental data on the cross section of the Eq. (19) photoprocess, it is advantageous to use π-meson beams with energies of the order of 10 GeV and higher. At lower energies the results are heavily dependent on the magnitude of β, so are unreliable. The same is true of the other reactions con- /102
sidered in the foregoing.

Measurements of the Eq. (19) cross section at $E_L = 2.8$ GeV had been made earlier in [14]. But secondary π-mesons with exit angles $3° \leq \vartheta \leq 30°$ and $4\mu^2 \leq s \leq 21\mu^2$, $\Delta < 0.5\mu$ had been selected, that is in the range of kinematic variables in which strong interactions can make a significant contribution. This is why making new measurements of the Eq. (19) photoproduction cross section in the field of the nucleus is extremely desirable. Let us note as well the existence of the possibility of refining the values of β for various s. This is so because the contributions from the electromagnetic and strong interactions in the Eq. (2) reaction cross section depend on Δ^2 in different ways

$$\Delta^4 \frac{\partial^2\sigma_c}{\partial(\Delta^2)\partial s} \sim \Delta^2 - \Delta^2_{min}$$

at the same time that

$$\Delta^4 \frac{\partial^2\sigma_N}{\partial(\Delta^2)\partial s} \sim \frac{\Delta^4(\Delta^2 - \Delta^2_{min})}{m_\omega^4}.$$

An experimental determination of the boundary of the region of Δ values within

which the magnitude $\Delta^4 [\partial^2\sigma/\partial(\Delta^2)\partial s]$ remains a linear function of Δ^2 is necessary for this refinement. Then, using Eq. (9), when $\partial\sigma_c/\partial\sigma_N = 1$, we can compute the value of β corresponding to assigned s.

Thus, the analysis made of the possibility of using the information on the photoproduction of mesons by mesons that incorporates data on the production of mesons in a Coulomb field of a nucleus shows that this possibility is a very real one if the model of the strong interactions we have used is correct to within one order of magnitude.

REFERENCES

1. Pomeranchuk, I. Ya. and Shmushkevich, I. M., Nucl. Phys., Vol. 23, 1961, p. 452.
2. Good, M. L. and Walker, W. D., Phys. Rev., Vol. 120, 1960, p. 1857.
3. Migdal, A. G. and Kraynov, V. P., Priblizhennyye metody kvantovoy mekhaniki, [Approximate Quantum Mechanics Methods], Nauka Press, Moscow, 1966.
4. NguyenVan Kh'yey, Lektsii po teorii unitarnoy simmetrii elementarnykh chastits, [Lectures on the Theory of Unitary Symmetry of Elementary Particles], Atomizdat, Moscow, 1967.
5. Leroy, J. P. Nuovo cimento, Vol. A-49, No. 2, 1967, p. 213.
6. Alles, W. and Boccaletti, D., Nuovo cimento, Vol. 27, 1963, p. 306. /103
7. Geoo-Mann, M., et al., Phys. Rev., Lett., Vol. 8, 1962, p. 261.
8. Shekhter, V. M., Rezonansnyye sostoyaniya elementarynkh chastits, [Resonance States in Elementary Particles], Science Reviews, Moscow, 1965, (VINITI).
9. Hori, S., et al., Phys. Lett., Vol. 1, 1962, p. 81.
10. Scotti, A. and Wong, D., Proceedings Athens Topical Conference on Recently Discovered Resonant Particles, Athens, Ohio, (April 26-27). 1963, p. 173.
11. Köpp, G. and Söding, P., Phys. Lett., Vol. 23, 1966, p. 494.
12. Sällström, P., et al., Nuovo cimento, Vol. A-49, No. 3, 1967, p. 348.
13. Jackson, J. D., et al., Phys. Rev., Vol. 139 B, 1965, p. 428.
14. Varmin, V. V., et al., Zh. eksperim. i teor. fiz., Vol. 43, 1962, p. 1223; Vol. 44, 1963, p. 748.

DETERMINATION OF THE LENGTH OF nn-SCATTERING IN EXPERIMENTS IN CAPTURING μ^--MESONS WITH DEUTERONS

Yu. P. Nikitin

ABSTRACT. The influence of the interaction of neutrons in the final state on the nature of the nuclear reaction is investigated.

One of the consequences of the hypothesis with respect to the charge independence of strong interactions at low energies is equality of the lengths of the nucleon-nucleon (nn-) scattering in a state with isotopic spin T = 1 and spin S = 0 /104

$$^1a_{pp} = {}^1a_{np} = {}^1a_{nn},$$

where

$^1a_{pp}$ is that part of the length of the pp-scattering that is associated solely with a strong interaction.

The following values have been found experimentally [1]

$$^1a_{pp} = (-17 \pm 3)f; \quad ^1a_{np} = -23.7f.$$

Determination of the length of the nn-scattering is of great interest because of the substantial difference in the values of $^1a_{pp}$ and $^1a_{np}$. There has been no success in making direct observation of nn-scattering. However, it is possible to use nuclear reactions in which several neutrons are formed for this purpose and to investigate the influence of the interaction of neutrons in the final state on the nature of the nuclear reaction. Processes of the following type are the most attractive in this regard

$$\pi^- + d \to 2n + \gamma; \tag{1}$$

$$\mu^- + d \to 2n + \nu, \tag{2}$$

when, in the final state, there are no strongly interacting particles other than the two neutrons. However, strong interactions in the intermediate states of the Eq. (1) reaction introduce considerable indeterminacy in the theoretical computations, and it is difficult to interpret the experimental data. This is why it is of interest to check the value $^1a_{nn} = (-16.4 \pm 1.9)$f, obtained in experiments on π-meson capture [1], in research on weak capture of μ^--mesons by deuterons, which latter permits making a more reliable theoretical

interpretation. Actually, in the Eq. (2) reaction the capture of a μ-meson by a deuteron proton can be attributed to a weak interaction, and this permits the computation of this process in the first order of the perturbation theory.

Reference [2] suggested finding a_{nn} by ascertaining the distribution in the Eq. (2) reaction in terms of the angle of divergence of the two neutrons (for specified neutron energy) in the domain of small angles, or the neutron energy spectrum for fixed angle of divergence. Experiments to determine the shape of the energy spectrum for the neutrons in the Eq. (2) reaction for energies $\varepsilon_n \sim$ 1 - 2 MeV would be simpler, obviously. The energy spectrum for the neutrons is sensitive to the magnitude of a_{nn} in this energy domain, as is pointed out in this paper. We should point out that a detailed study of the Eq. (2) process is even now within the realm of experimental feasibility and can become available in the near future. /105

We already know [3] that the capture of μ-mesons in liquid deuterium takes place on the basis of the state of the hyperfine structure of the mesic atom with F = 1/2, because the transitions of mesic atoms from the F = 3/2 to the F = 1/2 state are intensive, thanks to the atomic collisions. This is why we have considered capture from the F = 1/2 state only. The neutron spectrum was computed on the basis of standard Hamiltonian for μ-capture [4]. The matrix element for the Eq. (2) reaction is in the form

$$M_{if} = \frac{G}{2^{3/2}} \int d\mathbf{p} \chi^+_{s_1} \chi^+_{s_n} \chi^+_{s_\nu} (1 - \sigma\hat{\nu}) \times$$
$$\times \left[\psi^{(-)*}_{2n}\left(\mathbf{p} - \frac{\nu}{2}, \mathbf{n}_{12}\right) \left(G_V + G_A \sigma_1\sigma + G_P \sigma_1\nu + \right.\right.$$
$$+ g_V \frac{\sigma\mathbf{p}}{m} + g_A \frac{\sigma_1\mathbf{p}}{m}\Big) - \psi^{(+)*}_{2n}\left(\mathbf{p} + \frac{\vec{\nu}}{2}, \mathbf{n}_{12}\right) \left(G_V + G_A \sigma_2\sigma + \right.$$
$$\left.\left. + G_P \sigma_2\hat{\nu} - g_V \frac{\sigma_2\mathbf{p}}{m} - g_A \frac{\sigma_2\mathbf{p}}{m}\right)\right] \psi_d(\mathbf{p}, \sigma_1, \sigma_2) \psi_\mu(0) \chi_{sd} \chi_{s\mu}. \quad (3)$$

where

G is the weak interaction constant;

χ_s are the spin functions for the fermions in the Eq. (2) reaction;

χ_{sd} is the deuteron spin function;

$\psi_\mu(0)$ is the wave function for the μ-meson in the atom of deuterium, taking

it that r = 0 because of the smallness of the radius of the deuteron as compared with the dimensions of the mesic deuterium;

ν is the neutrino momentum;

$\nu/\nu = \hat{\nu}$;

n_{12} is the relative momentum of the neutrons;

m is the nucleon mass.

The deuteron wave function in coordinate representation was selected in the form [5]

$$\psi_d(\mathbf{r}, \sigma_1, \sigma_2) = \left(\frac{N}{\sqrt{4\pi}}\right)\left\{\frac{U(r)}{r} + \frac{\rho}{2\sqrt{2}} \cdot \frac{W(r)}{r} \times \left(\frac{3(\sigma_1 r)(\sigma_2 r)}{r^2} - \sigma_1\sigma_2\right)\right\}; \quad (4)$$

$$U(r) = \sum_{i=1}^{4} C_i e^{-\alpha_i r}; \quad /106$$

$$W(r) = \frac{1}{\alpha_1^2}\sum_{i=1}^{4} C_i \alpha_i^2 \sqrt{\frac{2\alpha_i r}{\pi}} \times K_{s/2}(\alpha_i r),$$

where

$K_\nu(x)$ is the McDonald function, the parameters $N^2 = 3.41\ \alpha_1$, $C_1 = -C_4 = 1$, $C_3 = C_2 = 3.84$, $\alpha_1 = 0.432\ \mu$, $\alpha_2 = 3.69\ \mu$, $\alpha_3 = 4.81\ \mu$, $\alpha_4 = 6.05\ \mu$, $\rho = 0.0265$;

μ = the μ-meson mass.

In the momentum representation

$$\psi_d(\mathbf{p}, \sigma_1, \sigma_2) = \frac{N}{\pi\sqrt{2}}\left\{1 - \frac{\rho}{2\sqrt{2}} \cdot \frac{p^2}{\alpha_1^2} \times \left(\frac{3(\sigma_1 p)\sigma_2 p}{p^2} - \sigma_1\sigma_2\right)\right\} \sum_{i=1}^{4} \frac{C_i}{\alpha_1^2 + p^2} \cdot \quad (5)$$

The selection of the deuteron wave function in the Eqs. (4), (5) form with the parameters indicated is attributable to the fact that this wave function provides the correct values for the coupling energy and the deuteron quadrupole moment. It is also a good description of the experiments in connection with the photodisintegration of the deuteron when the energies of the γ-quanta are $E_\gamma \leq 150$ MeV [5]. The 2n-system wave function was selected in the form

$$\psi_{2n}^{(-)}(\mathbf{r}, \mathbf{n}_{12}) = e^{in_{12}r} + \frac{f_0}{n_{12}r}(e^{-in_{12}r} - e^{-\lambda r}), \quad (6)$$

where

$f_0 = e^{i\delta_0} \sin \delta_0$;

δ_0 is the phase of the nn-scattering in the s-state;

and the parameter λ is associated with the length of the s-scattering of a_{nn} with the effective radius, r_0, by the relationship

$$\lambda = \frac{3}{2r_0}\left(1 + \sqrt{1 - \frac{16r_0}{9a_{nn}}}\right); \qquad (7)$$

nn-scattering is ignored in states with moments $l \geq 1$. The conjugate wave function of the 2n system in the momentum representation is in the following form when the s-scattering is taken into consideration

$$\psi_{2n}^{(-)*}(\mathbf{p}, \mathbf{n}_{12}) = (2\pi)^{3/2}\delta(\mathbf{p} - \mathbf{n}_{12}) + \frac{f_0}{n_{12}}\sqrt{\frac{2}{\pi}} \times \times\left(\frac{1}{p^2 - n_{12}^2 - i\varepsilon} - \frac{1}{p^2 + \lambda^2}\right). \qquad (8)$$

The Eq. (3) matrix element was used to make the numerical computation for the energy spectrum for the neutrons in the Eq. (2) reaction for five sets of parameter values, as listed in the table (see figure). /107

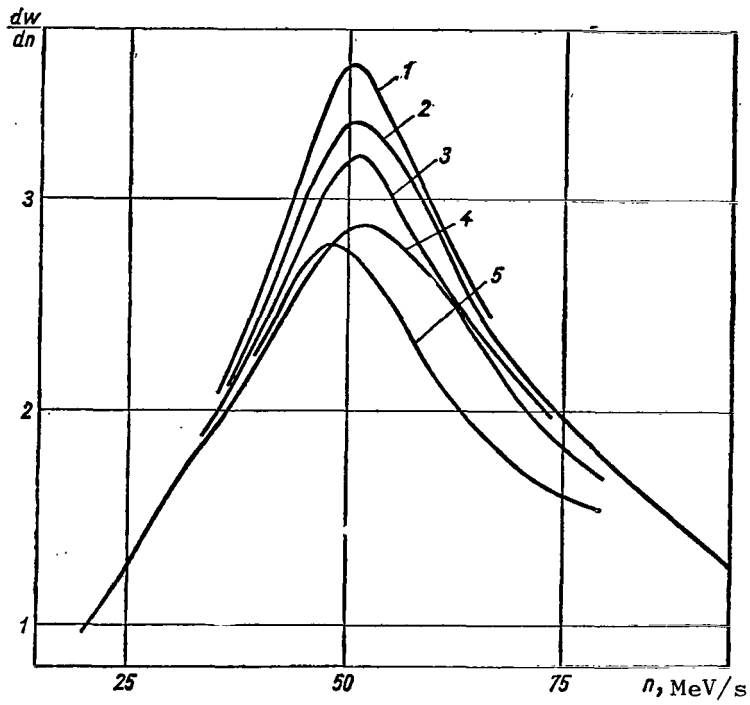

Spectrum of Neutron Bursts

Parameter	Set				
	1	2	3	4	5
$a_{nn}\left(\frac{1}{\mu}\right)$	−16	−12,8	−12,8	−8	−12,8
$r_0\left(\frac{1}{\mu}\right)$	1.44	1.44	1.44	1,44	3
G_P/G_A	8	8	16	8	8

The neutron spectrum, dw/dn, normalized to unity for a 22 MeV/c neutron momentum is shown in the figure. Let us note that the interference of the S- and D-waves of the deuteron wave function make less than a 1% contribution to the spectrum. The sensitivity of the shape of the spectrum to the parameters for the interaction in the final state, a_{nn} and r_0, and the pseudoscalar G_P, can be characterized by the relationships /108

$$\frac{\Delta w_m}{w_m} \approx 0{,}35 \frac{\Delta a_{nn}}{a_{nn}} \approx 0{,}15 \frac{\Delta r_0}{r_0} \approx 0{,}06 \frac{\Delta G_P}{G_P}.$$

Here w_m is the magnitude of the spectrum presented at the maximum. Thus, measurement of a_{nn} with 10% accuracy requires establishment of the spectrum with 3% accuracy. A 10% indeterminacy in the radius of the interaction will result in a 5% indeterminacy in the magnitude of a_{nn}. Spectrum shape is only mildly dependent on the magnitude of the effective pseudoscalar, G_P.

REFERENCES

1. Haddock, R. P., et al., Phys. Rev., Lett., Vol. 14, 1965, p. 318.
2. Dasch, H. G., Nuovo cimento, Vol. 39, 1965, p. 731.
3. Gershteyn, S. S., Zh. Eksperim. i. teor. fiz., Vol. 40, 1961, p. 698.
4. Fujii, A. and Primakoff, H., Nuovo cimento, Vol. 12, 1959, p. 327.
5. Gordin, M., et al., Nuovo cimento, Vol. 37, 1965, p. 524.

THE ABSORPTION OF $\pi^{\pm}$-MESONS BY COMPLEX NUCLEI

A. I. Fesenko

ABSTRACT. The theoretical and experimental work already done in connection with the mechanism involved in the capture of $\pi^{\pm}$-mesons by nuclei is reviewed. It is concluded that pertinent questions have not been answered and that further investigation is required.

Nuclear reactions have been broken down into two classes: /109

(1) reactions in which the energy and the momentum transferred to the nucleus by the particle are distributed among the many degrees of freedom of the nucleus;

(2) direct reactions, in which the energy and the momentum of the incident particle are transferred by a small group of nucleons of the nucleus.

The compound nucleus forms and decays in the case of low and medium energies in the first of these reactions. At high energies a great many particles that have no correlation with the direction in which an incident particle is moving (in a CM-system) escape. These reactions are accompanied by strong momentum transfer to the residual nucleus. There are three groups of rather crude models to describe this type of reaction: a simple statistical model; thermodynamic models; and the cascade mechanism [1].

In direct nuclear reactions one, or several fast particles are formed, and these carry almost all of the energy and momentum transferred to the nucleus by the incident particle. Little momentum is transferred to the residual nucleus, and the nucleus remains in its ground, or slightly excited, state.

Fast secondary particles are correlated with the direction in which the incident particle is moving. Reactions of the (p, 2p), (p, dp), (p, d), (n, d), (d, p), (π^+2p), (π, πp), etc., types are included in direct nuclear reactions. Direct reactions comprise approximately 20 to 30% of all inelastic processes (in the energy range near 10 MeV).

Butler advanced a theory [2] that explained the special features of the (d, p), (d, n), (p, d), (n, d) reactions qualitatively (anisotropy

in the angular distribution, excesses of high energy particles, and the like), in order to describe these reactions of stripping and pickup.

Butler's theory considers the interaction of plane waves (of incident and outgoing particles) with the absorbing sphere (the nucleus target). Plane waves are a poor approximation, however. Today a great many of the experimental facts can be explained by the distorted waves method, which takes into consideration the d and p interaction with the optical potential of the nucleus, the latter selected so as to describe satisfactorily the elastic scattering of these particles for the corresponding energies. There is no theoretical basis for this method because the perturbation theory [3] is applied to the strong interaction Hamiltonian. /110

Serber's hypothesis with respect to the quasielastic scattering of an incident nucleon by a separately moving nucleon inside the nucleus has been used to describe the (p, 2p) reaction [4]. The development of this hypothesis made it possible to explain quite a good many of the experimental factors in the (p, 2p), (p, d), (d, p), etc., type reactions from a unified point of view.

Chew and Low [5] were the first to use the diagram technique to review quasielastic nuclear reactions. Figure 1 is a diagram of quasielastic scattering. Subsequent development of this apparatus by I. S. Shapiro [6] led to the dispersion theory of nuclear reactions. The dispersion theory is concerned with the amplitude reaction, and not with wave functions. This is particularly important in studying reactions in which complex particles, such as d, t, and α-particles, as well as others, participate.

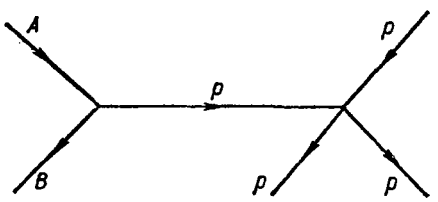

Figure 1. Diagram of quasielastic scattering.

The complex magnitude M, which is associated with the differential cross section in the CM-system by the following formula, can be designated by the amplitude of the reaction A + x → B + y

$$\frac{d\sigma}{d\Omega} = \frac{m_{xA}\, m_{yB}}{4\pi^2} \cdot \frac{p_y}{p_x} \mid M \mid^2.$$

In this reaction the amplitude of M is a function of two variables; the square of the transferred momentum q, and the summed kinetic energy, E, of the colliding particles in the CM-system:

$$q^2 = (\mathbf{P}_x - \mathbf{P}_y)^2;$$
$$E = E_x + E_A .$$

The amplitude of the reaction is the sum of an infinite series of Feynman diagrams. And the direct processes can be described by diagrams with a small number of internal lines, that is, of virtual particles (polar, triangular, and other diagrams).

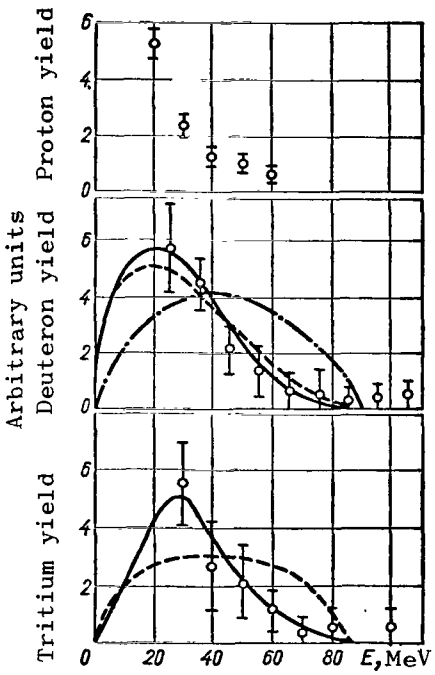

Figure 2. The energy distribution of singly charged particles emitted when the light nuclei of an emulsion are split.

The curves describe the energy spectra corresponding to the phase volume (the dashed curve) and to the He^3 (the dash-dot curve) and He^4 (the solid curve) polar particles.

The dispersion theory of direct nuclear reactions predicts the mechanism that should be evident in each concrete reaction. This means the dominating contribution of the corresponding Feynman diagram to the amplitude of the reaction can be determined. Only two diagrams, the polar and the triangular, have been used to describe three-particle reactions of the (π^+, 2p) (π^-, nn) type. /111

V. M. Kolybasov [7, 8] provides computations made for processes in which a slow π^--meson is absorbed by light nuclei of the α-particle type (C^{12}, O^{16}). The computations are made for a polar diagram with a virtual α-particle and no hypothesis of any type is forthcoming concerning the structure of the nuclei. The emission and energy spectra for protons, deuterons, and tritium nuclei are obtained, as are the angular correlations of these particles. The computed and experimental spectra are shown in Figure 2, where the spectra of the nuclei of tritium and of the deuterons, computed on the basis of the diagrams (Figure 3), are in quite good concordance with the data contained in [9]. The distribution of nucleon pairs in terms of the energy of relative motion is sensitive to the π^--meson capture mechanism. Figure 4 shows the distributions of nn-pairs in terms of energy of relative motion, computed for various mechanisms involved in the capture of

π^0-mesons by C^{32} nuclei. Curves 1 and 2 were plotted in terms of the deuteron polar diagram, with curves 3 and 4 plotted in terms of the α-particle. The lack of experimental data makes it impossible to give preference to any particular polar diagram. These same distributions will be found in the paper by R. I. Dzhibuti and T. I. Kopaleyshvili [10]. Their basis was a two-nucleon absorption mechanism. A model of the two-nucleon absorption mechanism for /112
π-mesons is used in other theoretical papers as well (see [1-17] in [11]).

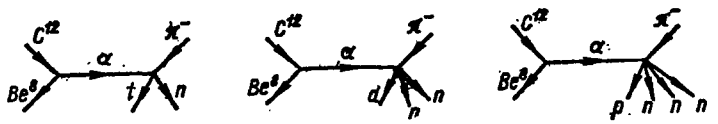

Figure 3. Polar diagrams corresponding to the α-particle capture mechanism.

T. I. Kopaleyshvili [12] has made a theoretical investigation of the absorption of moving π-mesons by C^{12} and O^{16} nuclei in $(\pi^+, 2p)$, $(\pi^-, 2n)$, $(\pi^{\mp}, np)$ reactions for π-meson energy values of 20 and 60 MeV. The basis for the computation is the assumption of a two-nucleon mechanism for the absorption of π-mesons, and that the principal contribution to the reaction cross section is made by the emission of two nucleons from the P-shell. Evaluations of the contribution from the S-shell show that this contribution is approximately 1/20th that made by the P-shell, and that the knock-on of one nucleon from the S-, and the other from the P-shell, is about 15%. Only the contribution from the P-shell (Figure 5) was taken into consideration in the distribution of the escaping pairs of nucleons in the $(\pi^+, 2p)$, (π^+, np), processes in the O^{16} nucleus obtained in terms of their relative energies ($t = E_r/E_t$, where E_r is the relative energy, and E_t is the total released energy). Curves 1 and 3 are for /113 the $(\pi^+, 2p)$ reaction, and curves 2 and 4 are for the (π^+, pn) reaction. The paired correlation of the nucleons in the

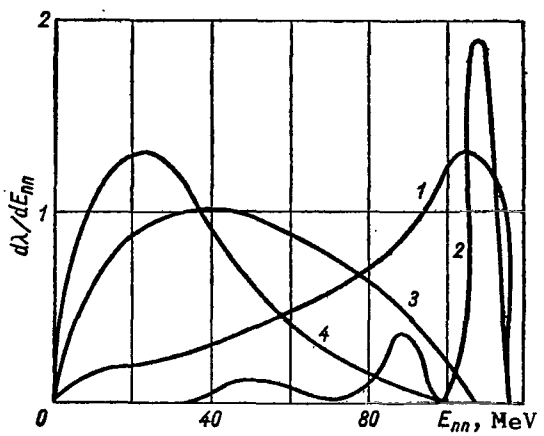

Figure 4. Distribution of pairs of neutrons in terms of energy of relative motion during the capture of π^--mesons by C^{12} nuclei.

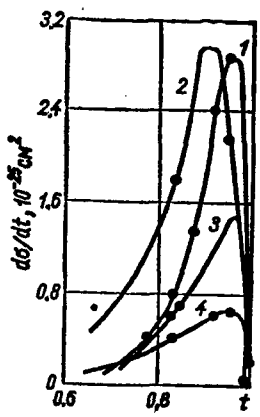

Figure 5. Distribution of nucleons in terms of their relative energies.

nucleus was taken into consideration in the 1, 2 distribution, but was not in the 3, 4 distributions.

Reference [13] considers the $(\pi^+, 2p)$ reaction within the framework of the direct mechanism of the absorption of the π-meson by two nucleons. Nuclei states corresponding to the configurations $|s^4p^8>$, $|s^3p^9>$, $|s^2p^{10}>$ (for the C^{12} nucleus) are considered in the analysis of energy spectra for product nuclei. The highly excited state of the nucleus with inner S-shell destroyed is in the $|s^2p^{10}>$ configuration. The $N^{14}(\pi^+, 2p)C^{12}$ reaction in particular was reviewed. The computed spectrum of the C^{12} nucleus is shown in Figure 6 (the experimental data were taken from [14]). As will be seen from this figure, the concordance between the experimental and theoretical curves is encouraging. This tells us that low π-meson energies (about 100 MeV) allow us to discover the excited state of nuclei with one, and even two holes in the S-shell. The reference cited shows that the development of a model for the direct mechanism involved in the absorption of π-mesons (as well as of nucleons and of compound particles) is the best way to analyze experimental data and to obtain even more information concerning the mechanism involved in direct nuclear reactions. However, the difficulties involved in the identification of the mechanism involved in direct processes are still great. There is a need for the theory to point out the criteria for recognizing the mechanism from the experimental data.

A detailed review of the criteria needed to determine the polar mechanism is provided in [15]. Let us list these criteria once again.

1. The Treyman-Yang [sic] criterion.

2. Measurement of $|\overline{M}|^2$ in terms of the energy, E, of the colliding particles in a CM-system of reaction with values of the other kinematic invariants fixed. If the reaction mechanism is polar, $|\overline{M}|^2$ should not depend on E.

3. Obtaining the differential cross section in terms of the momentum, q, of the residual nucleus in the L-system.

4. Measurement of the absolute value of the magnitude of the differential cross section, and its comparison with the theoretical prediction. /114

5. Measurement of the A + x → B + y + z reaction cross section as a function of the independent kinematic invariants of the y' + x → y + z reactions (y' is a virtual particle).

6. Check of the feasibility of isotopic relationships between the different channels at the vertices.

7. Measurement of the polarization of the residual nuclei.

π^--mesons. Despite the fact that a great many experiments have been made (see [20-37] in [12]) in which the interaction between slow π^--mesons and nuclei has been studied, the π-meson absorption mechanism is still not very well understood. The targets used in the experiments were light nuclei with $A < 40$, for the most part. The experiments conducted by A. O. Vaysenberg, et al., [9] utilized the photoemulsion method and revealed that the absorption of slow π^--mesons by C^{12} and O^{16} nuclei is accompanied by the escape of fast protons, deuterons, and tritium nuclei. The escape of the deuterons and of the tritium nuclei with energies greater than 10 MeV is approximately 40% and 15%, respectively. The energy spectra of protons, deuterons, and tritium nuclei (see Figure 2) obtained led the authors to conclude that the main contribution to the amplitude of the reaction of absorption of π^--mesons by nuclei is made by the polar diagram with a virtual α-particle.

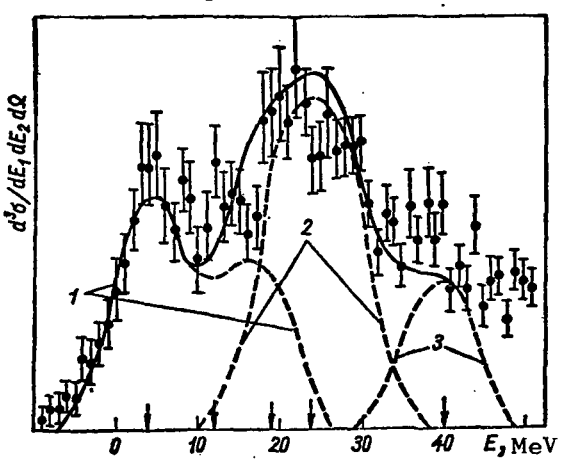

Figure 6. The curve of C^{12} excitation in the $N^{14}(\pi^+, 2p)C^{12}$ reaction as a function of E^*, the nuclei-residues excitation energy.

The solid curve is the theoretical spectrum, obtained from a model of shells with intermediate coupling. The dashed maxima, 1, 2, and 3, correspond to the configurations of the nuclei-residues $|s^4p^8>$, $|s^3p^9>$, $|s^3p^{10}>$.

P. I. Fedotov [16] also investigated /115 the absorption of slow π^--mesons by carbon nuclei. Based on the energy spectrum of fast secondary particles, as well as on the mean excitation energy available for

the residual nuclei, $\overline{U}_{exp}$ = (52 ± 7) MeV ($\overline{U}_{comp}$ = 48 MeV). The author concluded that π^--mesons can be captured by a pair of nucleons in the nucleus, and that the ratio, R, of the probability of the absorption of π-mesons by pairs of nucleons, n - p(W_{np}) and p - p(W_{pp}), is 4 ± 1.3. Reference [11] measured the angular distributions of nucleon pairs emitted during the absorption of π^--mesons by nuclei, as well as the energy spectra of fast protons.

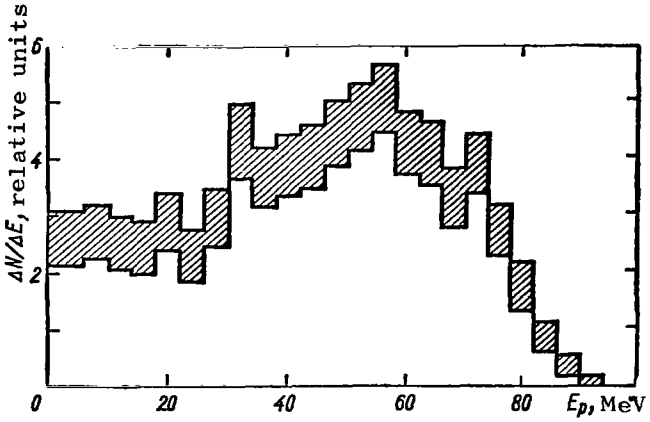

Figure 7. The energy spectrum of protons formed in the $C^{12}(\pi^-, 2p)B^{10}$ reaction.

Figure 7 shows the energy spectrum of protons formed during the absorption of π^--mesons by C^{12} nuclei (the hatched part shows the statistical errors). A similar spectrum was obtained for the O^{16} nuclei. A comparison between spectra and computations made on the assumption of a two-nucleon π^--meson capture mechanism favors this mechanism. A particularly careful study was made of the angular correlation of the two nucleons formed during π^--meson capture by np- and pp-pairs (Figure 8).

The authors feel that the angular distribution of the nucleons points to the predominance of the two-nucleon mechanism. The ratio R = W_{np}/W_{pp}, which is quite sensitive to the two-nucleon correlation inside the nucleus, was measured. The mean value for P-shell nuclei was R = 3.3 ± 0.9. Computation of pp- and np-pairs inside the nuclei, with the Pauli principle taken into consideration, yielded R = 3, which is in concordance with the data in the paper.

<u>π^+-mesons</u>. The absorption of π^+-mesons by nuclei can also be studied in order to establish the π-meson absorption mechanism. The energy of π^+-mesons in a beam differs in different references, but is between 70 and 200 MeV. The photoemulsion method was used in [17, 18] to investigate the absorption of π^+-mesons with an energy of 70 MeV. The yield of fast protons (about 90%) and of deuterons (approximately 10%) in reactions of the (π^+, 2p) type was established. The nature of the angular and momentum spectra indicates the absence of any significant percentage of captures of π^+-mesons by pairs of nucleons in the low-energy states. /116

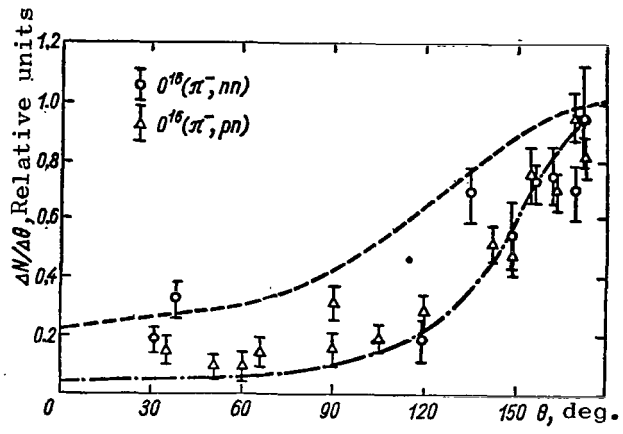

Figure 8. Angular distribution of the nucleon-nucleon pairs formed in the O^{16} reaction.

All data normalized to unity at 180°. The dashed curve was computed in terms of the α-particle for the model, while the dash-dot curve was computed for the two-nucleon mechanism. The theoretical curves were taken from V. M. Kolybasov [8].

Reference [19] studied the N^{14} (π^+, 2p)3α reaction for π^+-meson energy of 20 MeV. The authors concluded that the absorption of π^+-mesons in a reaction of this type is attributable primarily to quasideuteron pairs of nucleons from the P-shell of the N^{14} nucleus.

V. F. Kosmach, et al., [20], investigated the $C^{12}(\pi^+, 2p)d2\alpha$ reaction, the cross section of which is about 10% of the total cross section of the absorbtion of π^+-mesons by C^{12} nuclei. Analysis of energy and angular distributions of α-particles and deuterons shows that the reaction is attributable to a more complex mechanism than that involved in the $N^{14}(\pi^+, 2p)3\alpha$ reaction. The authors assume the capture of the π^+-meson by an α-particle in the $C^{12}(\pi^+, 2p)d2\alpha$ reaction, with the result that the α-particle /117 splits into d and 2p. The Charpak team [14, 21, 22] did some interesting experiments in CERN, where the Treyman-Yang criterion for explaining the mechanism of the direct reaction (π^+, 2p) was tested for the first time. The initial π^+-meson energy was 80 MeV. The nuclei of D, He^4, Li^6, Be^9, B, C^{12}, N, O^{16}, F^{19}, Al^{27}, S, Cl, Ca^{40}, Fe, Pb were selected as targets. Spectra of the summed proton energy were obtained for these nuclei. The experimental data for carbon, nitrogen, and oxygen were compared with the computations made by T. I. Kopaleyshvili (Figure 9). There is qualitative concordance between experiment and theory. The $Li^6(\pi^+, 2p)He^4$ reaction was analyzed in more detail [23]. Figure 10 shows the experimental spectrum of summed proton energy, converted to the He^4 nucleus excitation energy. As will be seen, the spectrum has three separate regions. Region I is that for the ground state of He^4, while II and III are for He^4 in the excited state. The distribution in terms of the Treyman-Yang angle was plotted for each region (Figure 11). The Treyman-Yang criterion is satisfied if He^4 forms in the ground state. The angular and momentum distributions of the He^4

recoil nucleus in Range I is well explained by the mechanism involved in the absorption of a π^+-meson by a peripheral deuteron, that is, the polar nature of the process prevails. Range II corresponds to the state of He^4 excited by energy between $10 < E_{ex} < 40$ MeV. The analysis made of the data in this region assumed that the π-meson is absorbed by an α-particle in the Li^6 nucleus. This energy

/118

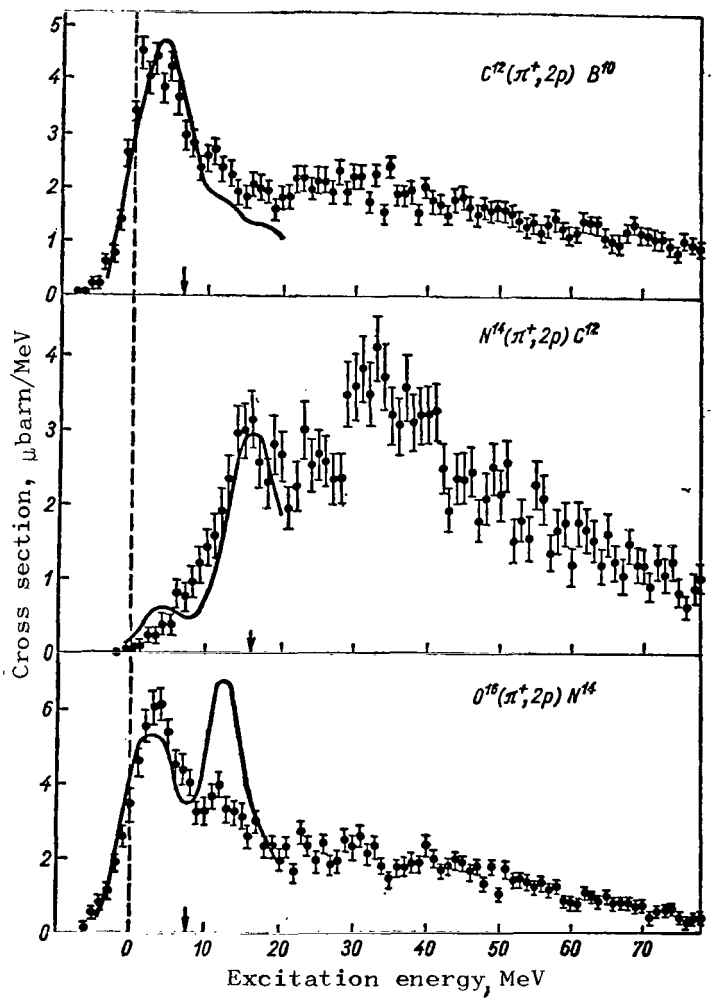

Figure 9. Spectrum of nucleus-residue excitation energy in the $(\pi^+, 2p)$ reactions in C^{12}, N^{14} and O^{16}.

The spectra were obtained from the spectra of the summed proton energy and photon kinematics. The solid curves were computed in [12].

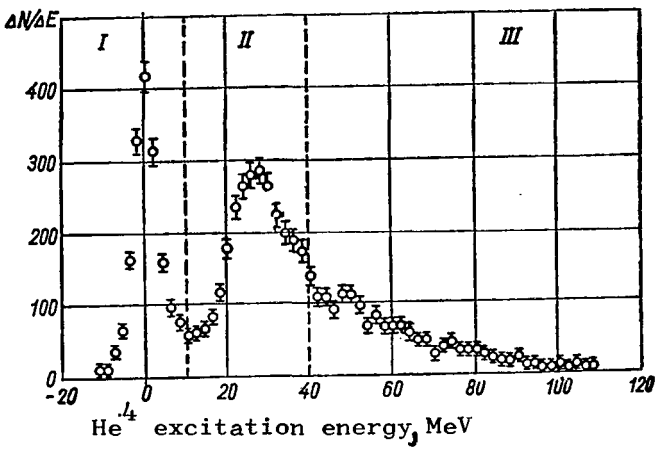

Figure 10. He^4 excitation energy in the $Li^6(\pi^+, 2p)He^4$ reaction.

region also indicates the peripheral model for the description of the $Li^6(\pi^+, 2p)He^4$ reaction. Moreover, direct nuclear reactions provide information on the location and magnitude of the energy levels of the nucleus, on the reduced widths of deuterons, of tritium nuclei, of π-particles, and the like. However, it is difficult to make a quantitative study of nucleon association levels. It is necessary to select those reactions in which these levels would be excited with the same selectivity as single particle levels [in the (d, p) reaction], for example. /119

This brief survey of the theoretical and experimental work already done makes it apparent that the question concerned with the mechanism involved in the capture of $\pi^{\pm}$-mesons by nuclei has not been answered, and requires further investigation.

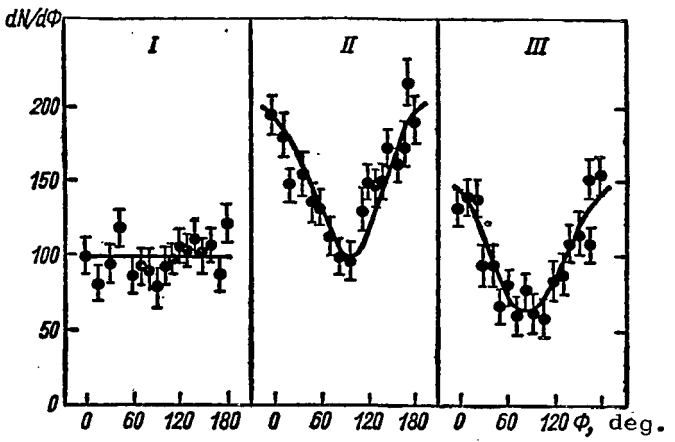

Figure 11. Distribution in terms of the Treyman-Yang angle in the $Li^6(\pi^+, 2p)He^4$ reaction.

REFERENCES

1. Shapiro, I. S. Uspekhi fiz. nauk, Vol. 92, 1967, p. 549.
2. Butler, S. T. Proc. Roy. Soc., Vol. A-208, 1961, p. 559.
3. Ogloblin, A. A, B kn., Trudy problemnogo simpoziuma po fizike yadra, [IN Book: Proceedings of the Problem Symposium on Physics of the Nucleus], Vol. 2, Tbilisi, 1967, p. 169.
4. Serber, R., Phys. Rev., Vol. 72, 1947, p. 1114.
5. Chew, G. F. and Low,FF. E., Phys. Rev., Vol. 113, 1959, p. 1640.
6. Shapiro, I. S., Teoriya pryamykh yadernykh reaktsiy, [Theory of Direct Nuclear Reactions], Gosatomizdat, Moscow, 1963.
7. Kolybasov, V. M., Yadernaya fizika, Vol. 3, 1966, p. 729.
8. Kolybasov, V. M., Ibid., p. 965.
9. Vaysenberg, A. O., et al., Zh. eksperim. i teor. fiz., Vol. 47, 1964, p. 1262.
10. Dzhibuti, R. I. and Kopaleyshvili, T. I., Nucl. Phys., Vol. 55, 1964, p. 337. /120
11. Nordberg, M. E., et al., Phys. Rev., Vol. 165, 1968, p. 1096.
12. Kopaleyshvili, T. I., Yadernaya fizika, Vol. 4, 1966, p. 538.
13. Golovanova, N. F. and Zelenskaya, N. S., Yadernaya fizika, Vol. 8, 1968, p. 274.
14. Charpak, G., Phys. Lett., Vol. 16, 1965, p. 54.
15. Shapiro, I. S. and Kolybasov, V. M., Preprint ITEF, 1968, p. 591.
16. Fedotov, P. I., Yadernaya fizika, Vol. 2, 1965, p. 466.
17. Kirillov-Ugryumov, V. G., et al., Yadernaya fizika, Vol. 5, 1967, p. 851.
18. Kirillov-Ugryumov, V. G., et al., V sb. Elementarnyye chastitsy i kosmicheskiye luchi,[IN Collection: Elementary Particles and Cosmic Rays], Atomizdat, Moscow, 1967, p. 121.
19. Afanas'yev, B. P. and Ostroumov, V. I., Yadernaya fizika, Vol. 1, 1965, p. 647.
20. Kosmach, V. F., et al., Ibid., Vol. 8, 1968, p. 32.
21. Favier, J., et al., Phys. Lett., Vol 25B, 1967, p. 409.
22. Meyerhof, W. E., B. kn. Trudy problemnogo simpoziuma po fizike yadra, [IN Book: Proceedings of the Problem Symposium on Physics of the Nucleus], Vol. 2, Tbilisi, 1967, p. 169.
23. Zupancic, C., Invited paper to the Second International Conference on High-Energy Physics and Nuclear Structure, Rehovolt, 1967.

MEASUREMENT OF ELECTRON AND γ-QUANTA ENERGIES IN HEAVY-LIQUID BUBBLE CHAMBERS

A. T. Bederkin, V. S. Demidov, A. I. Ponosov,
V. P. Protasov, F. M. Sergeyev

ABSTRACT. The various methods used to measure electron and γ-quanta energies in heavy-liquid bubble chambers are analyzed. The experimental results obtained from these measurements are tabulated.

Reactions in which π^0-mesons and γ-quanta participate are of great interest /121 in the study of strong and electromagnetic interactions. This has produced a need to use instruments that can record these reactions during experiments with quite high efficiency. One such instrument is the heavy-liquid bubble chamber. But when recording efficiency is good it is difficult to obtain highly accurate measurements of the energies of γ-quanta and electrons. This contradiction can be eliminated by selecting the instrument dimensions and the density of the working liquid for each concrete problem. Thus, we can obtain the necessary optimum for "photon" characteristics for the chamber, giving preference to detection, of course. Figure 1 is a photograph of the electron tracks made in a 105 cm freon chamber in the MIFI [Moscow Engineering Physics Institute].

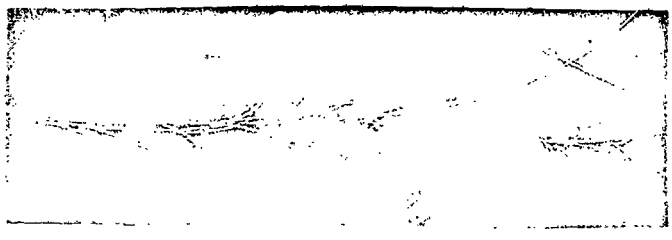

Figure 1. Photograph of electron and positron tracks in a bubble chamber. Magnetic field 16,000 oersteds.

A further problem is that of using a qualitative technique for processing and applying sufficiently precise measurement methods. Important results have been obtained along these lines in recent years, and because the processes in which γ-quanta and π^0-mesons take part are attracting the attention of an ever-widening circle of experimenters, it has become necessary to bring together the most significant of these results. It should be pointed out that Morellet recently compiled quite a detailed survey [1], and that we do not yet /122 have similar surveys in our literature.

1. The Interaction of γ-quanta and Electrons with Matter

An electron loses its energy as a result of the interaction with the atoms of the medium as it passes through a substance. An electron can undergo inelastic collision with an atom, resulting in its excitation, or ionization, or to deflection into the field of the nucleus. Soft quanta emissions occur with each deflection, and it is rare to have the emission of a single quantum with energy comparable to electron energy.

a. Ionization deceleration. Ionization losses of electrons in a medium can be computed through the Bethe-Block formula

$$-\frac{1}{\rho}\cdot\frac{dE}{dx}=\frac{2\pi n_e e^4}{m_e v^2}\left\{\ln\frac{2m_e v^2 W_{max}}{I^2(1-\beta^2)}-2\beta^2-2\frac{c}{Z}-\delta\right\}, \tag{1}$$

where

I is the mean ionization potential of the atom;

$W_{max} = T_e/2$;

v, T_e are the velocity and the kinetic energy of the bombarding electron;

m_e, e are electron mass and charge, respectively;

n_e is the number of electrons in 1 gram of the substance;

δ is the density effect of the medium.

The magnitude of c/Z takes the shell structure of the atom into consideration.

When there is a nuclei mixture

$$\left(-\frac{1}{\rho}\cdot\frac{dE}{dx}\right)_{mix}=\sum_i\left(-\frac{1}{\rho}\cdot\frac{dE}{dx}\right)_i P_i, \tag{1a}$$

where

ρ, P are density and statistical weight of a component of the mixture, respectively.

The ionization characteristics of the components of the most widely used chamber mixtures are listed in Table 1.

TABLE 1

Components	Z	A	I, ev	c/Z	δ
H	1	1	19.5	0	—
C	6	12	78	0.001	1
F	9	19	117.2	0.0014	1.5
Cl	17	35.5	217.6	0.0037	3
Br	35	80	430	0.0104	3

b. Bremsstrahlung. The emission of energy quanta plays an important role /123 in the energy losses of electrons in a medium. Fluctuations in mean radiation losses are slight if soft quanta are emitted as a result of collisions. The spread is great in the case of the emission of a hard quantum.

Computations made on the basis of the Thomas-Fermi model yield the following formula for the distribution of radiated frequencies [2]

$$\varphi_q d\frac{k}{E_0-\mu} = 2\langle\varphi_1^r\rangle\frac{dk}{k}\cdot\frac{E}{E_0}\left\{2\left[\frac{E_0^2+E^2}{E_0E}-\frac{2}{3}\right]\times\right.$$
$$\left.\times\ln(183Z^{-1/3})+\frac{2}{9}\right\} \qquad (2)$$

(the case of total shielding). Here φ_q is the cross section of the radiation of a quantum in the energy interval from $k/(E_0 - \mu)$ to $(k + dk) / (E_0 - \mu)$; E_0, μ are total energy and mass of the electron, respectively; and $\langle\varphi\rangle = Zr_e^2/137$. The following formula represents the distributions of bremsstrahlung intensity

$$\frac{k\varphi_q}{E_0\langle\varphi\rangle} = \frac{k}{E_0}\cdot\frac{a}{\ln\{E_0/(E_0-k)\}} \quad (a\sim 20\div 23), \qquad (3)$$

and describes those distributions quite well for energies $E \geq 50m_e c^2$ [2].

It is probable that an electron moving a distance dl in a substance containing N atoms per cm^3 will lose energy k equal to

$$W(k)\,dk = \frac{a\langle\varphi\rangle N}{E_0}\cdot\frac{dk\,dl}{\ln\{E_0/(E_0-k)\}} \qquad (4)$$

or, if new variables are introduced

$$y = \ln\frac{E_0}{E_0-k}\ ; \qquad E = E_0 - k = E_0 e^{-y}\ ; \qquad (5)$$

$$w(y)\,dy = bdl\,\frac{e^{-y}\,dy}{y}\,, \tag{6}$$

where

$b = a < \varphi > N$.

The probability that electron energy will be reduced by a factor of e^y over path dt can be written in the form

$$w(y)\,dy = \frac{e^{-y}\,y^{bdl-1}}{\Gamma(bdl)}\,dy. \tag{6a}$$

This probability is normalized to unity

$$\int_0^\infty w(y)\,dy = 1.$$

Eq. (6a) is valid as well for finite t; that is /124

$$w(y,\ l)\,dy = \frac{e^{-y}\,y^{bl-1}}{\Gamma(bl)}\,dy, \tag{7}$$

where

Γ (bt) is the gamma function.

X_0, the radiation length, can be found through the expression

$$b = (X_0 \ln 2)^{-1} \tag{8}$$

or

$$X_0^{-1} = \frac{4}{137}\,\frac{N}{A}\,Z(Z+\xi)r_e^2 \ln(183\,Z^{-1/3}). \tag{9}$$

Here N, Z, and A are the number of atoms per cm^3, charge, and atomic weight, respectively. The magnitude of ξ takes into consideration the shielding effect of atomic electrons. For a nuclei mixture

$$\frac{1}{X_0} = \sum_i \left(\frac{P_i}{X_{0i}}\right), \tag{9a}$$

where

P_i is the statistical weight of the mixture component.

X_0 and ξ values are listed in Table 2.

TABLE 2

Components	Z	A	ρ, g/cm^3	X_0, cm	ξ
H	1	1	0.0628	915	1.39
C	6	12	1.55	27.3	1.32
F	9	19	1.11	29.5	1.30
Cl	17	35.5	1.56	12.3	1.26
Br	35	80	3.1	3.61	1.22
Xe	54	131	2.2	3.5	—
C_3H_8	—	—	0.41	112	—
C_2F_5Cl	—	—	1.2	24.2	—
CF_3Br	—	—	1.5	10.6	—
$C_2F_5Cl_3$	—	—	1.1	22.8	—

c. Photoelectric effect. The passage of γ-quanta into matter is accompanied by a photoelectric effect, the Compton effect, pair production, and selective absorption processes. In the latter case radiation at some one frequency can be absorbed and the discrete level of the atom can be excited. /125

The conservation of energy and momentum laws prohibit the photoelectric effect by a free electron, that is, the bond between the electron and the atom to which some of the photon momentum is imparted is extremely significant for the photoelectric effect. The stronger this bond, the greater the probability of the photoelectric effect. The cross section in the nonrelativistic case is in the form

$$\sigma = \frac{32\sqrt{2}\pi}{3} \cdot \frac{Z^5}{137^4} r_e^2 \left(\frac{m_e c^2}{k}\right)^{7/2}$$

and in the extreme relativistic case is in the form

$$\sigma = 4\pi r_e^2 \frac{Z^5}{137^4} \cdot \frac{m_e c^2}{k} .$$

The intensity of radiation of photoelectric energy is zero in the direction of photon propagation.

d. The Compton effect. The process involved in the scattering of γ-quanta by electrons of the medium can occur with, and without, change in the frequency of the incident radiation. The wavelength remains unchanged when the energy of the quanta is less than the ionization potential. The sources of scattered radiation are the bound electrons of the atom that resonate as a result of the effect of the incident radiation and thus themselves

become radiators of γ-quanta at the same frequency as that of the incident radiation. This type of scattering has been named Thomson scattering. The cross section per electron does not depend on the frequency

$$\sigma_T = \frac{8}{3}\pi r_e^2 = 0.66 \cdot 10^{-24}\ \text{cm}^2$$

The frequency of the incident radiation will change when γ-quanta are scattered by free electrons (the Compton effect). The cross section of this process can be described by the Klein-Nishina-Tamm formula [2].

The angular distribution is in the form ($Q = kc/m_e c^2 \gg 1$)

$$\frac{d\Phi}{r_e^2 d\Omega_{\theta_e}} = \frac{Q}{Q^2\theta_e^2 + 1}, \quad \text{if } \theta_e^2 Q \ll 1;$$

$$\frac{d\Phi}{r_e^2 d\Omega_{\theta_e}} = \frac{4\cos\theta_e}{Q^2 \sin^4\theta_e}, \quad \text{if } Q\sin^2\theta_e \gg 1,$$

where

θ_e is angle of emission of the electron.

The higher the energy, the greater the angular distribution. The probability of the scattering of a γ-quantum as a function of the energy is given by the expression

$$W = \pi r_e^2 \frac{1}{Q}\left(\ln 2Q + \frac{1}{2}\right), \quad Q \gg 1.$$

e. Pair formation. A photon will produce a e^+ e^- pair in the electromagnetic field of the nucleus. For γ-quanta with $E_\gamma > 50$ MeV, the pair production cross section is in the form /126

$$\sigma = \frac{Z^2}{137} r_e^2 \left\{\frac{28}{9}\ln(183 Z^{-1/3}) - \frac{2}{27}\right\}$$

(total shielding, extreme relativistic case). The attenuation in the beam of photons attributable to the pair formation conforms to the ratio $dn/n = -dx/C_0$, from whence

$$n = n_0 e^{-x/C_0},$$

where

$$C_0 = \left[\frac{28}{9}\ln(183 Z^{-1/3})\frac{Z^2 N}{137}\cdot\frac{r_e^2}{A}\right]^{-1} \qquad (10)$$

(C_0 is the conversion length).

Comparing Eqs. (9) and (10), we obtain

$$C_0 \approx \frac{9}{7} X_0. \tag{11}$$

The empirical energy dependence C_0 has the form [3]

$$C_0 = 5.2(1 + 13E_\gamma^{-0,7706}), \tag{12}$$

where

$[C_0]$ = [cm]; $[E_\gamma]$ = [MeV].

f. Total absorption. The total effect of the absorption of γ-quanta in a substance is the sum of the processes reviewed, and can be expressed by the exponential law

$$N(x) = N(0)\ e^{-\mu(h\nu)x}$$

Table 3 lists the values for μ (g/cm^2) without taking the photoelectric effect into consideration.

TABLE 3

Components	Energy, MeV							
	10	40	100	200	600	10^3	$5 \cdot 10^3$	10^4
H	3,18	1.6	1.23	1.1	1.1	1,1	1,12	1.12
C	1.92	1.31	1,33	1,66	1.66	1.68	1.73	1.73
F	2.08	1,7	1,8	1,97	2.2	2,24	2,36	2.37
Cl	2,56	2.8	3.22	3,45	3,8	3,9	4.0	4.0
Br	3,38	4.65	5,43	5,92	6,45	6.6	6,84	6.85

2. Methods Used To Measure E_e and E_γ. /127

γ-quanta can be recorded in photo- or Compton-electrons, and in electron-positron pairs. E_γ can be evaluated in terms of the apex angle for the pair, δ [4]:

$$\delta = \frac{4m_e c^2}{E_\gamma} \varphi(E'/E_\gamma).$$

Here $\varphi(E'/E_\gamma) \approx 1$ is a function that is only slightly dependent on the distribution of the energy of the quantum between the components of the pair. E_γ can also be found by measuring the relative scattering of e^+ and e^- [5], as well as by measuring the ionization density over the section where the components of the air do not split [6]. These methods can be used when working with photoemulsions.

If the energy of the electron and of the positron of a conversion pair, E_+ and E_-, is measured, the energy of the γ-quantum will be found as $E_\gamma = E_+ + E_- + 2m_e c^2$.

Finding the electron energy is a complex problem. First of all, the chamber medium is needed as the measurement means, yet so far as the electron is concerned, the medium makes it very difficult to solve the particle motion problem. This is so because the errors attributable to scattering, ionization, and radiation often are large compared with measurement errors. Losses of energy to ionization of the medium, to radiation, and to Coulomb scattering, result in the electron trajectory in the medium no longer being an ideal helicoid when a magnetic field is present. These factors must be taken into consideration, therefore, in order to increase the accuracy with which the kinematic parameters of tracks are measured.

The energy of an electron can be found with respect to the mean free path if rough approximations are desired. The mean free path of the electron generally is not fixed precisely, but one can obtain the mean free path, r, of the electron, and its root-mean-square deviation, s, in terms of the original energy [7] through

$$r = \lg(E_0 + 1); \quad \frac{s}{r} = \left(1 - \frac{r}{E_0}\right) r^{-1/2}.$$

Multiple scattering [8], because of the correlations between the individual sections of the track, results in a track shape that is closest to a circle with radius R_m. We can write the following approximation for a projection on a plane in which the track lies

$$R_m = l / \langle \theta_m \rangle;$$

$$\langle \theta_m \rangle = \frac{E_s}{p\beta c} \left(\frac{l}{X_0}\right)^{1/2}; \quad E_s = 21 \text{ MeV}$$

Here $\langle \theta_m \rangle$ is the root-mean-square angle between the initial direction of the track and a tangent to the end of the track with length l for an electron with momentum p in a medium with radiation length X_0. Electron energy thus can be evaluated in terms of multiple scattering. /128

If the bubble chamber is operating in a magnetic field (B), it is convenient to find the energy and the momentum in terms of curvature of the trajectory, R

$$pc\ [\text{MeV}] = 0.3BR[\text{kg}\cdot\text{cm}],$$

$$E_{\text{kin}} = m_e c^2 \left\{ \sqrt{\left(\frac{e}{m_e} \cdot \frac{BR}{c} \right)^2 + 1} - 1 \right\}.$$

Precision methods for processing electron tracks, taking the effect of the medium into consideration, have been developed in recent years. The development of the methodology is proceeding in three directions.

1. Methods in which heavy particle formulas are used. Radiation effects, ionization, and scattering are included in the momentum error. In this type of procedure, the track length must be fairly short to find kinematic parameters with high precision (the Behr-Mittner method).

2. Methods, the development of which takes into consideration (as a reflection of reality) the fact that electron tracks have specific anomalies, and that completely new formulas must be used for them.

3. Methods using the conclusions of the cascade theory.

These include methods used to find the energy of γ-quanta by summing the free paths of all electrons in a shower, as well as those which measure E in terms of the number of particles at its maximum.

The Behr-Mittner method. It is very important to take into consideration energy losses attributable to bremsstrahlung when measuring the energy of electrons in heavy-liquid bubble chambers. These losses differ from losses attributable to multiple scattering, or to ionization losses, primarily because of the considerable fluctuations that occur relative to mean magnitudes.

There is the finite probability thatn an electron can lose all its energy as a result of single radiation.

However, it is possible to find sections of electron trajectories over which radiation losses are much lower than the total energy E_0, and these can be considered simply as a correction. Herein lies the essence of the Behr-Mittner method. The main part of the electron's energy is found in terms of the geometric characteristics of the track, in terms of the radius of curvature of the section of the trajectory (of length L), used for the measurement, for example. But, naturally, it is necessary to discard the case when the percentage of energy carried off by a single photon of emission over length L exceeds the /129 value $h\nu_{max}/E_0$, specified in advance on predetermined physical bases. This

includes the cutoff for the spectrum of radiation losses.

The computations for mean radiation losses are based on the following assumptions: scattering is slight, so slight that the trajectories all lie in one plane; there are no ionization losses.

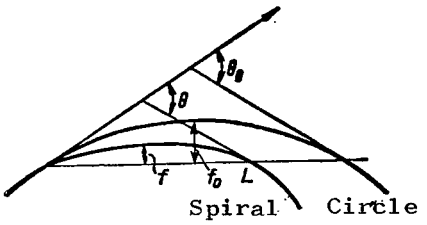

Figure 2. Track of a particle in a magnetic field in a vacuum (circle) and in matter (spiral).

Let f_0 be the deflection of the electron trajectory over length L in a vacuum (no losses); f the deflection of the real trajectory; and θ_0 and θ the angles of rotation, respectively (Figure 2). Then

$$U_L = \frac{f_L}{f_0} = \frac{\theta_L}{\theta_0} = \frac{1}{L}\int_0^L \frac{p_0}{p(l)}\,dl, \tag{13}$$

where

p_0, p are the momenta corresponding to f_0 and f.

Since

$$E_0/E(l) = p_0/p(l) = e^y, \qquad \text{then} \qquad U = \frac{1}{L}\int_0^L e^{y(l)}\,dl.$$

Spectrum cutoff can be expressed mathematically by the inequality
$p(l+dl) > p(l)\,e^{y_0}$ $(l < L)$

There should be a length L for each y_0. For length L + dL we have

$$U_{L+dL} = \frac{1}{L+dL}\int_0^{L+dL} e^{y(l)}\,dl = e^{y(dL)}\left[\frac{dL}{L} + \left(1 - \frac{dL}{L}\right)U_L\right], \tag{14}$$

$$\langle U_{L+dL}\rangle = \langle e^{y(dL)}\rangle\left[\frac{dL}{L} + \left(1 - \frac{dL}{L}\right)\langle U_L\rangle\right]. \tag{14a}$$

In precisely the same way /130

$$\langle U^n_{L+dL}\rangle = \langle e^{ny(dL)}\rangle\left[\langle U^n_L\rangle + n\,\frac{dL}{L}\langle 1-(n-1)\,U^{n-1}_L\rangle\right]. \tag{15}$$

By definition

$$\langle e^{ny(dL)}\rangle = \frac{\int_0^{y_0} e^{(n-1)y}\,y^{bdL-1}\,dy}{\int_0^{y_0} e^{-y}\,y^{bdL-1}\,dy}$$

We write

$$\int_0^{y_0} e^{(n-1)y}\, y^{bdL-1}\, dy = \sum_{k=0}^{\infty} \frac{(n-1)^k}{k!} \int_0^{y_0} y^{k+bdL-1}\, dy =$$

$$= \sum_0^{\infty} \frac{(n-1)^k}{k!}\, \frac{y_0^{bdL+k}}{k+bdL} = \left[\frac{1}{bdL} + \sum_1^{\infty} \frac{(n-1)^k}{k!}\, \frac{y_0^k}{k+bdL}\right] y_0^{bdL};$$

$$\int_0^{y_0} e^{-y}\, y^{bdL-1}\, dy = \left[\frac{1}{bdL} + \sum_1^{\infty} \frac{(-1)^k}{k!}\, \frac{y_0^k}{k+bdL}\right] y_0^{bdL}.$$

If bdL $\ll$ 1, we can write

$$\frac{bdL}{k+bdL} \approx \frac{bdL}{k}.$$

Therefore

$$< e^{ny(bdL)} > = \left[1 + \sum_1^{\infty} \frac{(n-1)^k}{k \cdot k!}\, y_0^k\, bdL\right] \times$$

$$\times \left[1 - \sum_1^{\infty} \frac{(-1)^k}{k \cdot k!}\, y_0^k\, bdL\right] = 1 + bdL \left\{\sum_1^{\infty} [(n-1)^k + \right.$$

$$\left. + (-1)^{k+1}] \frac{y_0^k}{k \cdot k!}\right\} = 1 + A_n\, bdL. \qquad (16)$$

For n = 1; 2

$$\left.\begin{aligned} A_1 &= y_0 - \frac{1}{4} y_0^2 + \frac{1}{18} y_0^3 - \frac{1}{4 \cdot 4!} y_0^4 + \ldots; \\ A_2 &= 2y_0 + \frac{1}{9} y_0^3 + \frac{2}{5 \cdot 5!} y_0^5 + \ldots; \\ A_2 - 2A_1 &= \frac{1}{2} y_0^2 + \ldots \end{aligned}\right\} \qquad (17)$$

From Eqs. (14a) through (16), we obtain /131

$$< U_L >^2 = \frac{1}{2} A_1 bL + 1; \quad < U_L^2 > = 1 + \frac{1}{3} (A_2 + A_1)\, bL.$$

By the definition for dispersion

$$\sigma_{U_L}^2 = < U_L^2 > - < U_L >^2 = \frac{1}{3} (A_2 - 2A_1)\, bL = \frac{1}{6} y_0^2\, bL.$$

Let us introduce the radius of curvature for the trajectory R. The following can be written for it

$$< \frac{\Delta R}{R} > = < \frac{\Delta U}{U} > = < U_L > - 1 = \frac{1}{2} A_1 bL = \frac{1}{2} y_0\, bL.$$

We obtain the following expression for the radiative correction to the magnitude of radius R

$$\Delta R_{\text{rad}} = \frac{1}{2} bL y_0 R. \tag{18}$$

The root-mean-square error is equal to

$$\left\langle \left(\frac{\Delta R}{R}\right)^2 \right\rangle = \langle U_L^2 \rangle - \langle U_L^2 \rangle^2 = \frac{1}{6} y_0^2 bL \tag{19}$$

and

$$\sigma_R^2 = R^2 \left[\left\langle \left(\frac{\Delta R}{R}\right)^2 \right\rangle - \left\langle \frac{\Delta R}{R} \right\rangle^2 \right] =$$
$$= R^2 \left[\frac{1}{6} y_0^2 bL - \left(\frac{1}{2} A_1 bL \right)^2 \right].$$

Since $bL \ll 1$,

$$\sigma_R^2 = \frac{1}{6} bL y_0^2 R^2. \tag{20}$$

Now let us consider the errors attributable to scattering. The error due to scattering in finding the track curvature is equal to

$$\sigma_R^2 = \frac{2}{3} \Phi_0^2 \frac{R^4}{L}. \tag{21}$$

The total error, based on the error summation rule, is

$$\sigma^2 = \sigma_R^2 \text{ (rad)} + \sigma_R^2 \text{ (scat)};$$
$$\sigma^2 = \underbrace{\frac{1}{6} bL y_0^2 R^2}_{\text{Bremsstrahlung}} + \underbrace{\frac{2}{3} \Phi_0^2 \frac{R^4}{L}}_{\text{Scattering}}. \tag{22}$$

Here $\Phi_0^2 = E_s^2 / (0\beta c)^2 X_0$. This error, as a function of the length of measurement L, has a minimum when /132

$$L_{\text{opt}} = \frac{2E_s \sqrt{\ln 2}}{0.3 y_0 B} \tag{23}$$

(Figure 3, dashed curve); L_{opt} is the optimal length of the track and does not depend on particle energy and is insensitive to the working liquid in the chamber.

A method has thus been developed for obtaining the magnitudes of the optimal lengths of tracks suitable for measuring energy. Errors attributable to radiation within the context of the method are small on length L_{opt}. The following drawbacks in the Behr-Mittner method should be mentioned.

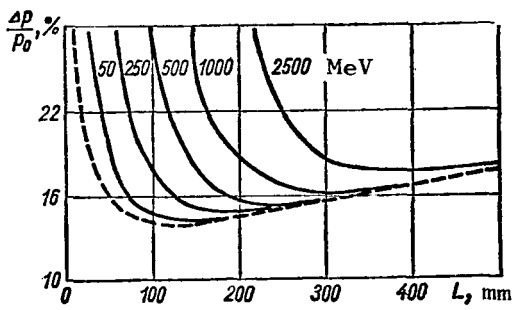

Figure 3. The error $\Delta p/p_0$ in terms of the measured length of the track [10] (B = 1.7 kg; y_0 = 1).

The solid curves were obtained with the error in measuring the deflection, Δf = 0.3 mm, taken into consideration. The dashed curve is that for Δf = 0. The numbers above the curves are the initial energies of the electrons.

1. Because y_0 is fixed, when group measurements are made some of the tracks are not sufficiently corrected, while others are over-corrected for radiation losses, something that would not matter if the radiation loss spectrum was symmetrical. It is not, however, and the results are systematic shifts in the energy value.

2. Measurement errors are not included in the expression for L_{opt}. To do so would increase L_{opt} by a factor of 1.5 to 2, the condition that $bL \ll 1$ might not be satisfied, and in such case the Behr-Mittner formulas would not apply.

3. The losses in the statistics will increase with reduction in the cutoff threshold. y_0 must be increased to compensate for these losses, but again up to a known limit.

The Behr-Mittner method was explored further in the paper by a Dubna team [10], which suggested a radiation loss spectrum cutoff method based on discarding during the measurements the part of the track in which the summed radiation losses exceed the specified cutoff threshold /133

$$E_r > E_0(1 - e^{-y_0}).$$

This condition superposes more rigid requirements on the permissible magnitude of radiation losses, and we can obtain a formula for correction factors for the same y_0 values that will have fewer errors

$$\left\langle \frac{p(L)}{p_0} \right\rangle = \frac{1}{L} \int_0^L dl \, \frac{\int_0^{y_0} \frac{p(y)}{p_0} w(y, l)\, dy}{\int_0^{y_0} w(y, l)\, dy} ; \qquad (24)$$

$$\left\langle \frac{p^2(L)}{p_0^2} \right\rangle = \frac{1}{L} \int_0^L dl \, \frac{\int_0^{y_0} \frac{p^2(y)}{p_0^2} w(y, l)\, dy}{\int_0^{y_0} w(y, l)\, dy} ; \tag{25}$$

$$\frac{\Delta p_r(L)}{p_0} = \left\{ \left\langle \frac{p^2(L)}{p_0^2} \right\rangle - \left\langle \frac{p(L)}{p_0} \right\rangle^2 \right\}^{1/2} \tag{26}$$

Upon integration with respect to y($0 \leq y \leq y_0 = \infty$)

$$\frac{\Delta p_r(L)}{p_0} = \left[\frac{1 - 3^{-bL}}{bL \ln 3} - \left(\frac{1 - 2^{-bL}}{bL \ln 2} \right)^2 \right]^{1/2} \tag{27}$$

If y_0 is finite, by writing $\Gamma(bl, ky_0) = \sum_{n=0}^{\infty} \frac{(-1)^n}{n!} \cdot \frac{(ky_0)^{n+bl}}{n+bl}$, we can obtain

$$\left.\begin{aligned} \left\langle \frac{p(L)}{p_0} \right\rangle &= \frac{1}{L} \sum_0^{\infty} \frac{(-1)^n (2y_0)^n}{n!} \int_0^L G(l, n)\, dl; \\ \left\langle \frac{p^2(L)}{p_0^2} \right\rangle &= \frac{1}{L} \sum_0^{\infty} \frac{(-1)^n (3y_0)^n}{n!} \int_0^L G(l, n)\, dl; \\ G(l, n) &= \frac{y_0^{bl}}{n + bl} \sum_0^{\infty} \frac{(-1)^n y_0^{n+bl}}{n!\,(n + bl)} . \end{aligned}\right\} \tag{28}$$

The error deriving from Eqs. (26) and (28) when $y_0 = 1$ is smaller than errors deriving from the Behr equations when $y_0 = 1$ and from Eq. (27) when $y_0 = \infty$ (Figure 4). /134

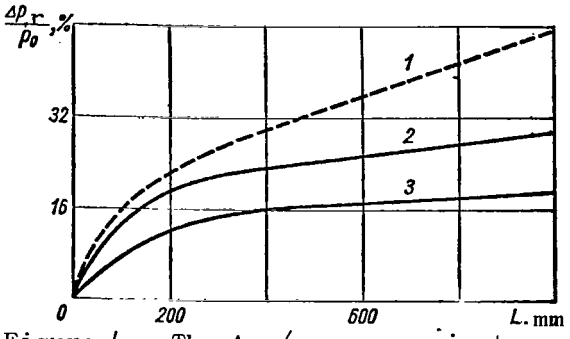

Figure 4. The $\Delta p_r/p_0$ errors in terms of measured length of a track.

1 - according to Behr (Eq. (20)] when $y_0 = 1$; 2 - according to Eq. (27) when $y_0 = \infty$; 3 - according to Eqs. (26) and (28) ($y_0 = 1$).

This eliminates the difficulty in the Behr-Mittner methodology associated with loss of statistics. Future development of the Behr methodology will be along the following lines:

(a) one, more effective, threshold cutoff value, y_0, will be compared with each electron track on the basis of an awareness that its trajectory is a more or less smooth curve;

(b) a track as long as possible and still containing useful information will be used for the measurements;

(c) the kinematic parameters will be established for the origin of the trajectory.

Herein lies the sense of the spiral method.

The spiral method. The momentum and angular parameters defining the trajectory over which a particle will move in a magnetic field usually are found by minimization of the sum of the squares of deviations by drawing the approximating curve through the experimental points of the track reconstructed in space from measurements of tracks on pictures.

The following functional is derived [11, 12]

$$Q = \sum_{i=1}^{n} [y_i - f(\mathbf{a}, x_i)]^2,$$

where

$f(a, x_i)$ is a function of the random quantities a $\{a_1, \ldots, a_m\}$, establishing the kinematic parameters;

x_i, y_i are the coordinates of the point of the track.

Errors in the coordinates associated with Coulomb scattering are taken into consideration by the introduction into the function of a Coulomb scattering matrix which has the form /135

$$F_{ik} = \frac{E_s^2 (m^2 + p^2)}{6 X_0 p^4} \sum_{j=1}^{i-1} \left[l^3_{j,\, j+1} \left(1 + \frac{3 l_{j+1,\, i}}{2 l_{j,\, j+1}} \right) \left(1 + \frac{3 l_{j+1,\, k}}{2 l_{j,\, j+1}} \right) + \right.$$
$$\left. + \frac{3}{4} l_{j,\, j+1} l_{j+1,\, i} l_{j+1,\, k} \right], \qquad (29)$$

where

X_0 is the radiative length;

l_{ij} are trajectory segment lengths.

The matrix of errors in coordinates, in which the errors in the coordinates attributable to the Coulomb scattering are summed with the errors attributable to inaccuracy in measurements and reconstruction of spatial coordinates, equals

$$S_{ik} = F_{ik} + \sigma^2 (\text{meas})\, \delta_{ik}, \qquad (30)$$

where

δ_{ik} is the Kronecker symbol.

The functional can then be written in the form

$$\chi^2 = \sum_{l,k=1}^{n} S_{lk}^{-1}(y_l - f(\mathbf{a}, x_l))[y_k - f(\mathbf{a}, x_l)]. \tag{31}$$

Here S_{ik}^{-1} is a matrix that is the inverse of the S_{ik} matrix.

Let us point out that the functional cannot be written in the form

$$\chi^2 = \sum_{l=1}^{n}\left(\frac{y_l - f(\mathbf{a}, x_l)}{\sigma_l}\right)^2;\ \sigma_l^2 = \sigma_l^2\,(\text{meas}) + \sigma_l^2\,(\text{scat}), \tag{31a}$$

because the errors in the coordinates attributable to the Coulomb scattering are not independent; σ_i^2 (meas) and σ_i^2 (scat) are standard deviations of the coordinates. (30) yields the elements of the matrix of errors, with $S_{ii} = \sigma_i^2$, but its non-diagonal elements represent the correlation of errors attributable to the Coulomb scattering at various points along the track. Minimization of Eq. (31) will reduce to a solution for the systems of equations

$$G_{ik}\Delta a_k^{(\nu)} = Y_i (k = 1, 2, \ldots, m). \tag{32}$$

Here

$$G_{ik} = \sum_{j,j'=1}^{n} S_{jj'}^{-1}\left[\frac{\partial f(\mathbf{a}^{(\nu-1)} x_j)}{\partial a_l}\ \frac{\partial f(\mathbf{a}^{(\nu-1)}, x_{j'})}{\partial a_k} + \frac{\partial f(\mathbf{a}^{(\nu-1)}, x_{j'})}{\partial a_l}\ \frac{\partial f(\mathbf{a}^{(\nu-1)}, x_j)}{\partial a_k}\right];$$

/136

$$Y_i = \sum_{j,j'=1}^{n} S_{jj'}^{-1}\left\{\frac{\partial f(\mathbf{a}^{(\nu-1)}, x_j)}{\partial a_l}\left[y_{j'} - f(\mathbf{a}^{(\nu-1)}, x_{j'})\right] + \frac{\partial f(\mathbf{a}^{(\nu-1)}, x_{j'})}{\partial a_l}\left[y_j - f(\mathbf{a}^{(\nu-1)}, x_j)\right]\right\};$$

where

$\Delta a_k^{(\nu)}$ are the corrections for the values $a_k^{(\nu-1)}$ found in the $(\nu - 1)^{\text{th}}$ approximation.

If f(a, x) is linearly related to a, the solution can be found at once in the zero approximation. The matrix of errors in the parameters a $\{a, .., a_m\}$ is equal to

$$\sigma_{ik}^2 = \overline{\Delta a_i \Delta a_k} = G_{ik}^{-1}. \qquad (33)$$

Bremsstrahlung leads to a reduction in particle energy and is strong in the forward direction. The set of conjugate arcs of circles, that is, a smooth curve, therefore is sufficiently accurate when the errors made in the measurements and in the scattering of the electron trajectory in a magnetic field are disregarded. This means we can select that analytical function that will sufficiently well describe the entire family of such smooth curves, and the value of the curvature of this function at the first point on the track will fix the unknown, initial value of electron track curvature. In practice, when drawing the approximating curve with variable radii of curvature, each point on the track must be assigned an error because of the errors attributable to the measurements and to the Coulomb scattering.

Now let us proceed to a quantitative consideration of the method of spirals [1], which involves the deformation of a circle into a spiral because of energy losses that occur during collisions and radiation.

Deformation of a circle attributable to ionization. At high energies, $\beta \approx 1$, so the mean losses per unit length are constant, and equal k. The change in momentum over length dx will be

$$\Delta p(x + dx) = -k dx,$$

where

pc = 0.3 BR ([p] = [MeV/c]; [B] = [kg]; [R] = [cm]);

$$\Delta R(x + dx) = -k' dx;$$
$$k' = k/0.3B;$$
$$R(x + dx) = R(x) + \Delta R(x + dx);$$
$$R(x + dx) = R(x)\left\{1 - \frac{k' dx}{R(x)}\right\}.$$

Considering that k' (dx/R(x)) $\ll$ 1, we obtain /137

$$\frac{1}{R(x + dx)} = \frac{1}{R(x)}\left\{1 + k'\frac{dx}{R(x)} + \left(k'\frac{dx}{R(x)}\right)^2 + \ldots\right\}.$$

During this time the tangent will rotate through the angle

$$\Delta\theta(dx) = \int_{x}^{x+dx} \left[\frac{1}{R(z+dz)} - \frac{1}{R(z)} \right] dz =$$

$$= k' \left(\frac{dx}{R(x)} \right)^2 \times \left\{ \frac{1}{2} + \frac{1}{3} \frac{k'\,dx}{R(x)} + \ldots \right\}.$$

The lateral displacement (the distance between a point on the circle and the corresponding point on the deformed curve) (Figure 5) will be

$$\varepsilon_{ion}(x) = \frac{k'}{R_0^3} \left(\frac{x^3}{6} + k' \frac{x^4}{12R_0} + \ldots \right). \tag{34}$$

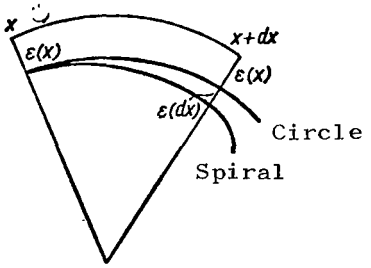

Figure 5. Deflection of particle track from a circle when ionization losses are taken into consideration.

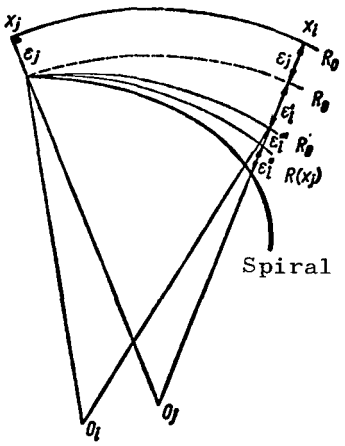

Figure 6. Deflection of particle track from a circle when radiation losses are taken into consideration.

Deformation of a circle attributable to radiation. Find the mean electron trajectory for specified initial curvature $1/R_0$, taking it that y_0 = constant over the entire trajectory; $\theta_0(x)$ is the angle of rotation of the tangent to the circle; $\theta(x)$ is the angle of rotation of the tangent to the deformed curve, $\Delta\theta(x) = \theta_0(x) - \theta(x)$; R_0, $R(s)$, p_0, $p(s)$ are radii and momenta at the initial point and at a point lying at distance s from the initial point (Figure 6). The lateral displacement of the trajectory can be written in the form

$$\varepsilon(x) = \int_0^x \varepsilon(ds)\,ds = \int_0^x dx \int_0^x \Delta\theta(ds)\,ds; \tag{35}$$

$$\Delta\theta(x) = \int_0^x \Delta\theta(ds)\,ds = \int_0^x \left[\frac{1}{R(s)} - \frac{1}{R_0} \right] ds. \tag{36}$$ /138

Since

$$\frac{E(x)}{E_0} = \frac{p(x)}{p_0} = \frac{R(x)}{R_0} = e^{-y},$$

then

$$\Delta\theta(x) = \frac{1}{R_0}\int_0^x (e^{y(s)} - 1)\, ds. \tag{37}$$

Let x_j, x_i be two points on the arc of the circle, and let ε_j and ε_i be the corresponding displacements (see Figure 6). Let us designate $R_i = R(x_i)$, $R_j = R(x_j)$. We have the following relationship for the ε_i displacement

$$\varepsilon_i = \varepsilon_j + \varepsilon_i' + \varepsilon_i'' + \varepsilon_i'''.$$

Here ε_i' is the displacement attributable to the rotation of the tangent to the circle at points $x = x_0$ and $x = x_j$. Putting $x_{ji} = x_i - x_j$, we obtain $\varepsilon_i' = x_{ij}\Delta\theta_j$, in which ε_i'' is the displacement attributable to the radiation along the path x_{ij}; $\varepsilon_i'' = e^{y(x_j)}\, x_{ji}$ ($E_j = E_0\, e^{y(x_j)}$); and ε_i''' is a correction factor required because ε_i'' must be equated to the circle with radius R_0, and not to the circle with radius R_j

$$\varepsilon_i''' = \frac{x_{ji}^2}{2R_0}(e^{y(x_j)} - 1).$$

ε_i can therefore be written in the form

$$\varepsilon_i = \varepsilon_j + x_{ji}\Delta\theta_j + e^{y(x_j)}x_{ji} + \frac{x_{ij}^2}{2R_0}(e^{y(x_j)} - 1). \tag{38}$$

Eqs. (37) and (38) provide the information needed to construct the mean electron trajectory.

In the case of fixed y_0, and after the integration of Eq. (37), we obtain

$$\langle \Delta\theta(x)\rangle = \frac{1}{R_0}\int_0^x \langle e^{y(s)} - 1\rangle\, ds = \frac{1}{R_0}\int_0^x (e^{A_1 bs} - 1)\, ds,$$

that is

$$\langle \Delta\theta(x)\rangle_{rad} = \frac{1}{R_0}\left(\frac{e^{A_1 bx} - 1}{A_1 b} - x\right), \tag{39}$$

$$\langle \varepsilon(x)\rangle_{rad} = \int_0^x \langle \Delta\theta(s)\rangle\, ds = \frac{1}{R_0}\int_0^x \left(\frac{e^{A_1 bs} - 1}{A_1 b} - s\right) ds = \tag{40}$$

$$= \frac{x^2}{R_0}\left\{\frac{e^{A_1 bx} - 1}{(A_1 bx)^2} - \frac{1}{A_1 bx} - \frac{1}{2}\right\}.$$

/139

Writing Eq. (37) in the form of a series

$$\Delta\theta(x)=\frac{L}{nR_0}\left\{\sum_{i=1}^{n}\left[\exp\left(\sum_{j=1}^{n+1-i}y_j\right)-1\right]\right\},$$

where

$$y_j = y(x_j),$$

we have

$$\left[\Delta\theta(x)\right]^2=\left(\frac{L}{nR_0}\right)^2\left\{\sum_{i=1}^{n}\left[\exp\left(\sum_{j=1}^{n+1-i}y_j\right)-1\right]^2+\right.$$
$$\left.+2\sum_{i=1}^{n}\sum_{j=i+1}^{n}\left[\exp\left(\sum_{k=1}^{n+1-i}y_k+\sum_{l=1}^{n+1-j}y_l\right)-\exp\left(\sum_{1}^{n+1-i}y_k\right)-\exp\left(\sum_{1}^{n+1-j}y_l\right)\right]\right\}.$$

Using this equation, and Eqs. (16) and (17), we obtain

$$<(\Delta\theta(x))^2>=\frac{L^2}{R_0^2}\left\{1+\frac{2}{(A_2-A_1)bx}\left(\frac{e^{A_2bx}-1}{A_2bx}-\right.\right.$$
$$\left.\left.-\frac{e^{A_1bx}-1}{A_1bx}\right)-2\frac{e^{A_1bx}-1}{A_1bx}\right\}, \qquad (41)$$

Similarly

$$<\varepsilon^2(x)>=\frac{2L^4}{R_0^2}\left\{\frac{1}{[(A_2-A_1)bx]^2}\left[\frac{e^{A_2bx}-1}{(A_2bx)^2}-\frac{e^{A_1bx}-1}{(A_1bx^2)}-\right.\right.$$
$$-\frac{1}{A_2bx}-\frac{1}{A_1bx}\Bigg]-\frac{1}{2}\left[\frac{e^{A_1bx}-1}{(A_1bx)^2}-\frac{1}{A_1bx}\right]+\frac{1}{8}+$$
$$+\frac{1}{(A_2-A_1)bx}\left[2\left(\frac{e^{A_2bx}-1}{(A_2bx)^3}-\frac{1}{(A_2bx)^2}\right)-\frac{1}{A_2bx}-\right.$$
$$\left.\left.-\left(\frac{e^{A_1bx}-1}{(A_1bx)^2}-\frac{1}{A_1bx}\right)\right]\right\}; \qquad (42)$$

$$<\varepsilon_i\varepsilon_j>_{rad}=<\varepsilon_j^2>-(x_i-x_j)<\varepsilon_i\Delta\theta_j>+$$
$$+<e^{y(x_j)}\varepsilon_j><\varepsilon_{jl}>-<\varepsilon_i><\varepsilon_j>+\frac{(x_l-x_j)^2}{2R_0}\times$$
$$\times[<\varepsilon_j e^{y(x_j)}>-<\varepsilon_j>]; \qquad (43)$$

/140

$$<\varepsilon(x)e^{y(x)}>_{rad}=\frac{x^2}{R_0}\left[\frac{1}{[(A_2-A_1)bx]^2}(e^{A_2bx}-e^{A_1bx})-\right.$$
$$\left.-e^{A_1bx}\left(\frac{1}{(A_2-A_1)bx}+\frac{1}{2}\right)\right]; \qquad (44)$$

$$<\varepsilon(x)\Delta\theta(x)>_{\text{rad}} = \frac{x^3}{R_0^2}\left\{\frac{1}{[(A_2-A_1)bx]^2}\left(\frac{e^{A_2bx}-1}{A_2bx} - \right.\right.$$
$$-\frac{e^{A_1bx}-1}{A_1bx}\Big) + \frac{1}{A_1bx} + \frac{1}{2} - \frac{e^{A_1bx}-1}{A_1bx}\left(\frac{1}{A_1bx}+\frac{1}{2}\right) +$$
$$+\frac{1}{(A_2-A_1)bx}\left[2\left(\frac{e^{A_2bx}-1}{(A_2bx)^2} - \frac{1}{A_2bx}\right) - \frac{e^{A_1bx}-1}{(A_1bx)^2} + \right.$$
$$\left.\left.+\frac{1}{A_1bx} - \frac{e^{A_1bx}-1}{A_1bx}\right]\right\} \tag{45}$$

Assuming that bL $\ll$ 1, Eqs. (39) through (45) yield

$$\left.\begin{aligned} <\Delta\theta(x)> &= \frac{x}{2R_0} A_1bx; \qquad <\varepsilon(x)> = \frac{x^2}{6R_0} A_1bx; \\ <(\Delta\theta(x))^2> &= \frac{x^2}{3R_0^2}(A_2-2A_1)bx; \\ <\varepsilon^2(x)> &= \frac{x^4}{20R_0^2}(A_2-2A_1)bx, \end{aligned}\right\} \tag{46}$$

and we have, for N equally spaced points along the track

$$\left.\begin{aligned} <\Delta\theta(x)> &= \frac{1}{2}\,\frac{N(N+1)}{N^2}\,\frac{x}{R_0} A_1bx; \\ <\varepsilon(x)> &= \frac{1}{6}\,\frac{N(N+1)(N+2)}{N^3}\,\frac{x^2}{R_0} A_1bx; \\ <(\Delta\theta(x))^2> &= \frac{1}{6}\,\frac{N(N+1)(2N+1)}{N^3}\,\frac{x^2}{R_0^2}(A_2-2A_1)bx; \\ <\varepsilon^2(x)> &= \frac{1}{60}\,\frac{N(N+1)(3N^3+12N^2+13N+2)}{N^5}\,\frac{x^4}{R_0^2}(A_2- \\ &\quad -2A_1)bx. \end{aligned}\right\} \tag{47}$$

The next step is the selection of y_0. Test tracks with various y_0 are constructed, and the natural track is used for calibration. The natural spiral that most closely approaches the measured spiral for the points must be selected from among the various spirals computed for $y_0 = y_0^1, y_9^2, \ldots$ The initial momentum approximation can be that obtained without consideration of the effects of collision and radiation, or, and this is better, that obtained through the use of the Behr-Mittern method. /141

If the χ^2 that results from the iteration is not good enough, this means that a hard quantum had been emitted. The assumption of the existence of some effective y_0 value (suitable for the case of the emission of several soft quanta) is then discarded. Now points on the track, beginning with the last, will be dis-

carded in succession until coincidence between test and experimental tracks is achieved.

Integral path method. The successive repetition of the processes involved in the radiation deceleration of electrons and in pair production while conserving bremsstrahlung quanta results in the formation of an electron-photon avalanche, or a shower (see Figure 1). Reference [4] reviews the feasibility of establishing γ-quanta energy from the integral path for all electrons and positrons in the shower

$$R = \sum R_i = \sum \left(\int \frac{dE}{-dE/dx} \right)_i ;$$

$$-\frac{dE}{dx} = \left(-\frac{dE}{dx}\right)_{\text{ion}} + \left(-\frac{dE}{dx}\right)_{\text{rad}} .$$

The energy of a quantum can then be found through the expression

$$E_\gamma = KR_i + 2nm_e c^2, \tag{48}$$

where

n is the number of electron pairs in the shower.

The path in xenon of an individual electron in terms of its energy between 0 and 75 MeV has been obtained (Figure 7). The feasibility of using this method for energies of from 20 to 1000 MeV has been reviewed in [13]. The measurements were made on a projection of the photograph. The sum of the paths of all electrons in the chamber was computed using the formula

$$\Sigma R = \frac{k \Sigma r}{\cos \psi} , \tag{49}$$

where

r is the length of a track on the projection;

k is the magnification factor;

ψ is the angle between the direction in which the photon is moving and the plane in which the photography was taken..

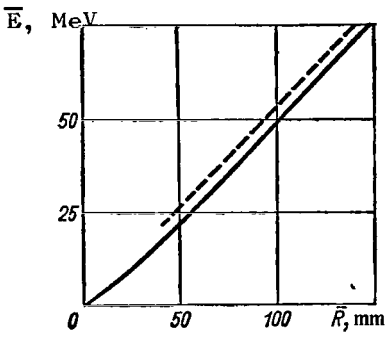

Figure 7. Mean free path of an electron in xenon in terms of energy.

Dashed curve - computed.
Solid curve - experiment.

Measurements were calibrated with respect to the positrons of a $\pi^+ \rightarrow \mu^+ \rightarrow e^+$ -decay. A comparison between the mean free path of the positrons and the mean expected energy provided the following for the coefficient /142

$$K = \frac{\bar{E}}{R} = (0.59 \pm 0.02) \text{ MeV/cm}$$

The theoretical positron spectrum was deformed assuming that various errors were made in measuring positron energies and then compared with the experimental spectrum. The best concordance was estimated to have taken place for the χ^2 criterion (Figure 8).

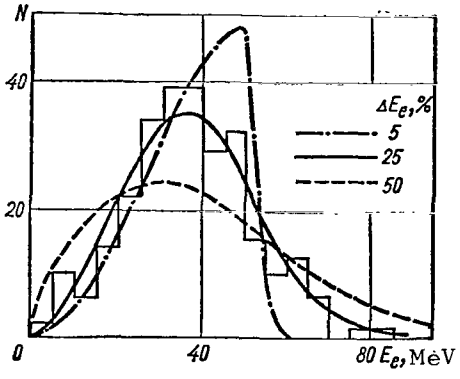

Figure 8. The energy spectrum, e^+, as a result of $\pi^+ \rightarrow \mu^+ \rightarrow e^+$ -decays.

There are a number of cases of partial shower development; some of the energy escapes from the chamber. Shower development length is the distance between the quantum conversion point and the chamber wall in the direction of γ-quantum flight. The summed length of the path in terms of the shower development length was determined in order to estimate how much of the energy leaves the chamber. The shower development length applied to showers that developed in whole, or in part, in the chamber. Each shower was artificially cut off at different development lengths, d. $\sum R = f(d)$ relationships were obtained for constant γ-quanta energies. Reference [14] took a somewhat different approach to this problem. Here it was assumed that the coefficient K in Eq. (48) was not a constant, and the following relationship was used.

$$T = T(E_\gamma), \tag{50}$$

where T is the total mean free path.

/143

This can be obtained empirically by making the measurements with beams of electrons with different energies. The mean electron path in a beam of electrons with a momentum of some 600 MeV/c was measured and compared with the computed path, arrived at through the use of the Monte Carlo method; $\bar{R}_{exp}$ = 131 cm for a half-width distribution of some 15%, and $\bar{R}_{com}$ = 128 cm.

The Monte Carlo method was used to create image electron showers under conditions approaching experimental conditions for other energies. The concor-

dance between the experiment and the Monte Carlo method computation was adequate for finding the "total path - energy" ratio. The advantage in measuring the energy of electrons and γ-quanta in terms of the total path is the possibility of measuring practically all events.

The following have an effect on the accuracy with which the energy of a γ-quantum is established from the $E_\gamma = f(R, d)$ curve [15]:

(a) fluctuations in that percentage of the γ-quantum energy lost in the form of ionization over the observed development length, d, and which are primarily associated with fluctuations in the longitudinal development of the shower. It should be emphasized that there is no ambiguity in R when showers are not cut off, so there are no errors of the type indicated;

(b) errors in measuring the projections of the integral lengths of paths with a curvometer in the plane of the photography;

(c) ambiguity in the minimum lengths of avalanche electron and positron tracks.

It has been established experimentally that $r_{min}^{\pm}$ does not depend on γ-quanta energy, so the unobserved percentage of the γ-quantum energy in a shower that is not cut off is practically identical for all E_γ, with the result that the error, ΔE_γ, attributable to the ambiguity in r_{min} is equal to about 6%. The error associated with fluctuations in the longitudinal development of a cutoff shower was established experimentally by measuring Σr_i at various lengths, d, in the case of artificial cutoff of showers with identical path lengths R. This error decreases with increase in d.

Measurement of energy E_γ in terms of the number of particles in the shower maximum. Reference [4] is devoted to methods that can be used to measure the energy of γ-quanta in a heavy-liquid bubble chamber and proved that it is possible to find energies $E_\gamma \geq 2$ GeV by using the characteristics of the development of photon-electron showers, that is, using the number of particles at the shower maximum, N_{max}, and the position of the maximum for the particles, t_{max}, according to the cascade theory

$$\left.\begin{aligned} t_{\max} &= k_1 (E/\beta) \ln (E/\beta); \\ N_{\max} &= k_2 (E/\beta)/(E/\beta) \sqrt{\ln (E/\beta)} \end{aligned}\right\} \qquad (51)$$

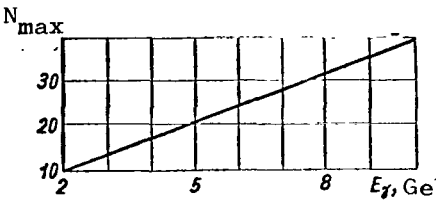

Figure 9. Number of particles at the shower maximum in terms of the γ-quantum energy.

(β is the boundary energy). Reference [16] contains the results of the development of this method for a xenon bubble chamber. Only those electrons with energies greater than some minimum, E_{min}, can be detected in the shower. The value E_{min} = 3.5 MeV was established by comparing the experimental mean free path distribution of the electrons with that computed using the cascade theory. Processing the experimental data by using Eq. (51) reduces to computing the $E_\gamma = f(N_{max})$ curve (Figure 9). Sources of errors in finding E_γ are the inaccuracies in computing the number of electrons, and fluctuations in the number of electrons in the shower. Verification of the correctness with which E_γ in the $\pi^0 \to 2\gamma$ decay was found was accomplished in a xenon bubble chamber [16]. The results are listed in Table 4.

/144

TABLE 4

Energy, E_γ, GeV			
Kinematics	$E_\gamma = f(N_{max})$	Kinematics	$E_\gamma = f(N_{max})$
5.98 ± 1.16	$5.75 \pm {}^{1.40}_{1.60}$	3.00 ± 0.86	$4.40 \pm {}^{1.60}_{1.40}$
3.72 ± 1.10	$3.65 \pm {}^{1.25}_{1.15}$	6.50 ± 1.60	$6.30 \pm {}^{1.70}_{1.30}$
3.22 ± 0.79	$3.65 \pm {}^{1.25}_{1.15}$		

In conclusion, we are including a summary table of the experimental results obtained during measurements made of the energies of electrons and γ-quanta in bubble chambers (Table 5). The validity of the methods used to measure the energies of γ-quanta and electrons in their corresponding energy ranges was verified in the course of reconstructing the masses of particles that, in the final analysis, decay into γ-quanta and electrons: π^0, η^0, K_2^0.

TABLE 5

Particle	Reaction	$\bar{M}$, MeV	Γ, MeV	$\frac{\Delta M}{M}$, %	$\frac{\Delta E_\gamma}{E_\gamma}$, %	Measurement Method	Chamber Charge	Reference
π^0	$\pi^- + p$, 1.15 GeV/c	138±3.7	100	19	22	Behr-Mittner method	50 Vol. % C_3H_8+50 Vol.% CF_3Br	[20]
η^0		573±26	235	18	22			
K_2^0	$K^+ + N \to K_2^0 + p + ...$, $K_2^0 \to 3\pi^0$, 0.9 GeV/c	487±25	—	~5	—	Same	CF_3Br	[19]
π^0	$\pi^- + p$, 4 GeV/c	138±2	40	7	30	Method of spirals	C_3H_8	[17, 18]
π^0	π^- + nuclei 2.8 GeV/c	135.1±2.3	50	13	15	Behr-Mittner method	Electron gas + C_3H_8	[8]
π^0	$\pi^- + p$, 5 GeV/c	133.4	40	10.5	—	Method of spirals	C_3H_8	[12]
π^0	$\pi^- + Xe$, 9 GeV/c	~150	100	—	25÷30	$E_\gamma = f(N_{max})$	Xe	[16]

REFERENCES

1. Morellet, D., Ecole Supérieure Laboratoire de l'Accelerateur Lineaire, 91-Orsay, France, 1968. /146
2. Gaytler, V., Kvantovaya teoriya izlucheniya, [The Quantum Theory of Radiation], Foreign Literature Press, Moscow, 1956.
3. Okhrimenko, L. S., et al., R13-3918, Dubna, 1968.
4. Konovalova, L. P., et al., Pribory i tekhn. eksperim, Vol. 6, 1961, p. 26.
5. Wilson, J., Fizika kosmicheskikh luchey, [Physics of Cosmic Rays], Foreign Literature Press, 1956.
6. Chudakov, A. Ye., Izv. AN SSSR. Ser. fiz., No. 19, 1955, p. 651.
7. Wilson, R. R., Phys. Rev., Vol. 84, No. 1, 1951, p. 100.
8. Pershin, I. I., et al., Pribory i tekhn. eksperim, Vol. 1, 1969, p. 30.
9. Behr, L., Mittner, P., Nucl. Instrum. and Methods, Vol. 20, 1963, p. 446.
10. Budagov, Yu. A., et al., Pribory i tekhn. eksperim, Vol. 1, 1966, p. 70.
11. Gramenitskiy, I. M., et al., P-2146, Dubna, 1965.
12. Budagov, Yu. A., et al., R10-3021, Dubna, 1966.
13. Danysh, L., et al., R-1144, Dubna, 1962.
14. Burmeister, H., et al., Proceedings of the Sienna International Conference on Elementary Particles, Bologna, 1963.
15. Ivanovskaya, I. A., et al., RI-3317, Dubna, 1967.
16. Nichiporuk, B., Strugal'skiy, E., R-1989, Dubna, 1965.
17. Grishin, V. G., R1-3677, Dubna, 1968.
18. Grishin, V. G., et al., R-2277, Dubna, 1965.
19. Aubert, B.,and Behr, L., Phys. Lett.,Vol. 10, No. 2, 1964, p. 250.
20. Behr, L., and Mittner, P., Phys. Lett., Vol. 4, No. 1, 1963, p. 22.

DEVELOPMENT OF A METHOD FOR STUDYING ELECTRON TRACKS IN BUBBLE CHAMBERS WITH A HEAVY LIQUID AND STRONG PULSE MAGNETIC FIELDS

V. K. Makar'in, N. N. Mukhin, A. S. Romantseva,
I. A. Svetlolobov, M. M. Sulkovskaya,
S. A. Chuyeva, R. S. Shlyapnikov.

ABSTRACT. A method for studying electron tracks in a xenon bubble chamber that is similar to that developed earlier for studying heavy, charged particles, and based on measuring the area of a segment over a short, initial section of the track, is described.

Approximate analysis methods, developed for use with tracks that have small /147 and constant curvatures, usually are used to interpret the tracks made by charged particles in bubble chambers filled with a light material and in those with weak magnetic fields. These methods are not suitable for interpreting the tracks of particles recorded in chambers with a heavy liquid and strong magnetic fields.

Our laboratory is now in the process of completing the building of a xenon bubble chamber 22 cm in diameter with an impulse magnetic field as strong as 70,000 oersteds. Tracks made by charged particles in this chamber should have large and variable curvatures. This was the basis for undertaking to develop a convenient and universal method for analyzing tracks of any curvature, a method which we have chosen to call the area method. The basis of the area method is the use of readily measured integral, or semiintegral, characteristics of particle tracks (length of arc, angle between the directions of the magnetic field and momentum, and area of the curved segment in the plane of the photograph). The area method for analyzing heavy charged particles has been described elsewhere [1]. The idea behind the use of this method is to compare the measured area of the segment Σ_{meas} with its computed values Σ_{com} for different sections of the path-momentum curve. A special program (for a computer) is used for the comparison, one that "moves" the measured segment of the track along the path-momentum curve to coincidence, $\Sigma_{meas} = \Sigma_{com}$. An experimental check of the method showed that it was more accurate than approximate methods, energy losses due to ionization not taken into consideration.

This article has undertaken to extend the area method to electron tracks, analysis of which requires additional consideration of energy losses due to radiation. Artificial electron tracks, modeled on the basis of the Monte Carlo method as applicable to the parameters of the chamber that is under construction, and to the conditions for making measurements with the semiautomatic equipment available in the laboratory [2], were used as the original material for development of the method. /148

1. The Methodology Used to Obtain Electron Tracks.

The electron tracks were selected in the energy range between 0 and 1000 MeV (more precisely, ending at the first energy value in excess of 1000 MeV). In order to simplify the computation, the end of each electron (corresponding to zero kinetic energy) was located in the coordinate origin and electron movement was considered in a plane normal to the direction of the magnetic field ($\Theta = \pi/2$).[15] Ionization losses were calculated and radiation losses were sampled every 0.1 cm (radiation losses were computed for energies in excess of 1 MeV). The program for the computation made it possible to derive the values of the X, Y coordinates for any point on the electron track, as well as the momentum p. A special program was used to introduce the correction for multiple scattering. This program "turned" the modeled track at each computed point through some angle Θ, found through the law of chance. Statistical errors ΔX and ΔY, the concrete values of which too were found through the Monte Carlo method, were introduced to take inaccuracies in measuring the derived coordinates into consideration.

Ionization losses were computed through the formula

$$-\frac{dE}{dx} = \frac{2\pi NZe^4}{mv^2}\left\{\ln\frac{mv^2E}{2I^2(1-\beta^2)} - (2\sqrt{1-\beta^2} - 1 + \beta^2)\ln 2 + \right.$$
$$\left. + 1 - \beta^2 + \frac{1}{8}(1-\sqrt{1-\beta^2})^2\right\},$$

15. When $\Theta \neq \pi/2$, the electron momentum will be larger by a factor of $1/\sin\Theta$.

where

NZ is the concentration of electrons in the medium;

E is the electron kinetic energy;

m is its mass;

v is the velocity;

$\beta = v/c$;

I is the mean ionization potential.

The radiation losses were sampled according to the formula

$$w(y)\,dy = \frac{e^{-y}\,y^{bl-1}}{\Gamma(bl)}\,dy,$$

which yielded the probability of a predetermined reduction in energy after the passage of an electron through a layer with thickness t. Here $y = \log(E_0/E)$, /150
where E_0 is the initial energy, E is the final energy, and b is a constant that depends on the medium.

The variables $y = (1/t - 1)^{1b/t}$ were substituted for purposes of eliminating divergence in W (y) for small t. The constant b was varied according to electron energy.

The ΔX and ΔY errors, and the multiple scattering angle Θ, were sampled according to the the cosine law, which is in good concordance with the central part of a Gaussian distribution. The values of the root-mean-square error, σ, and the root-mean-square angle of multiple scattering, Θ^2, were used for normalization. The latter was computed (for each point along the track) through the formula

$$\overline{\Theta}^2 = K \ln[1\ 13\cdot 10^4 Z^{4/3} z^2 A^{-1} t],$$

where

$$K = 0{,}157\ \frac{Z(Z+1)z^2}{A}\ \frac{t}{(pv)^2}\ ; \qquad /151$$

t is the thickness of the scattering layer, g/cm^2;

p and v are the momentum and the velocity of the scattered particle ([pv] = [MeV]);

Z and z are the charges of the scattering medium and of the scattered particle, respectively (measured in units of electron charge);

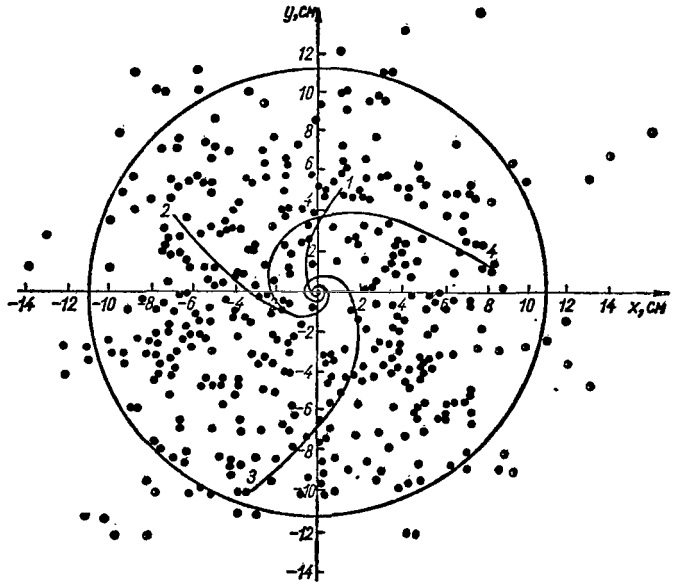

Figure 1. Distribution of the "ends" of 430 computed electron tracks uncoiling from the center of an xenon bubble chamber with a magnetic field of 70,000 oersteds from momentum $p = 0$ to $p \approx 1$ GeV/c.

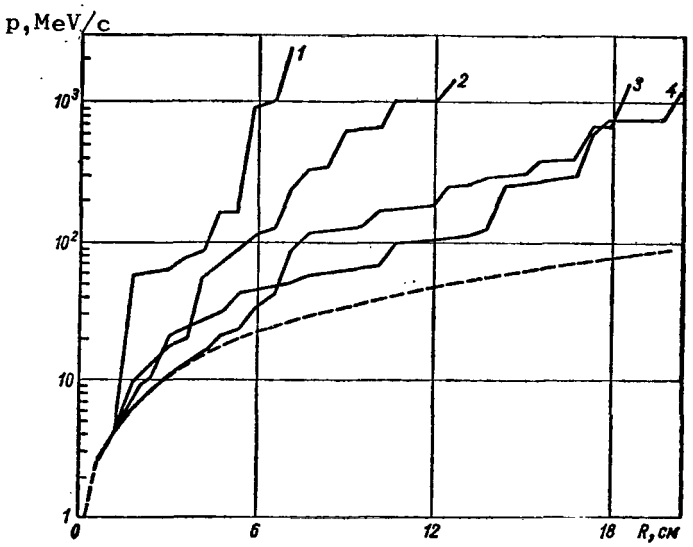

Figure 2. Momentum curves in terms of residual range for electron tracks 1, 2, 3, 4 (see Figure 1).

A is the atomic weight of the medium.

All computations were made using an M-20 electronic computer.

Figures 1 through 3 show some of the characteristics of the "tracks" obtained. Figure 1 shows the distribution of the "ends" of the electron tracks /152
uncoiling from the center of the chamber, and an overall view of several tracks (1, 2, 3, and 4) for some of the coordinates derived every 0.6 cm. As will be seen from the diagram, in a field of 70,000 oersteds, the electrons uncoil so strongly that they usually remain within the chamber limits, even after they "gain" a momentum of $p \approx 1$ GeV/c. Analysis of the distribution of the ends of the tracks through the chamber volume reveals that the percentage of stoppages of electrons in the chamber is 80%, and this is with the edge effect taken into consideration.

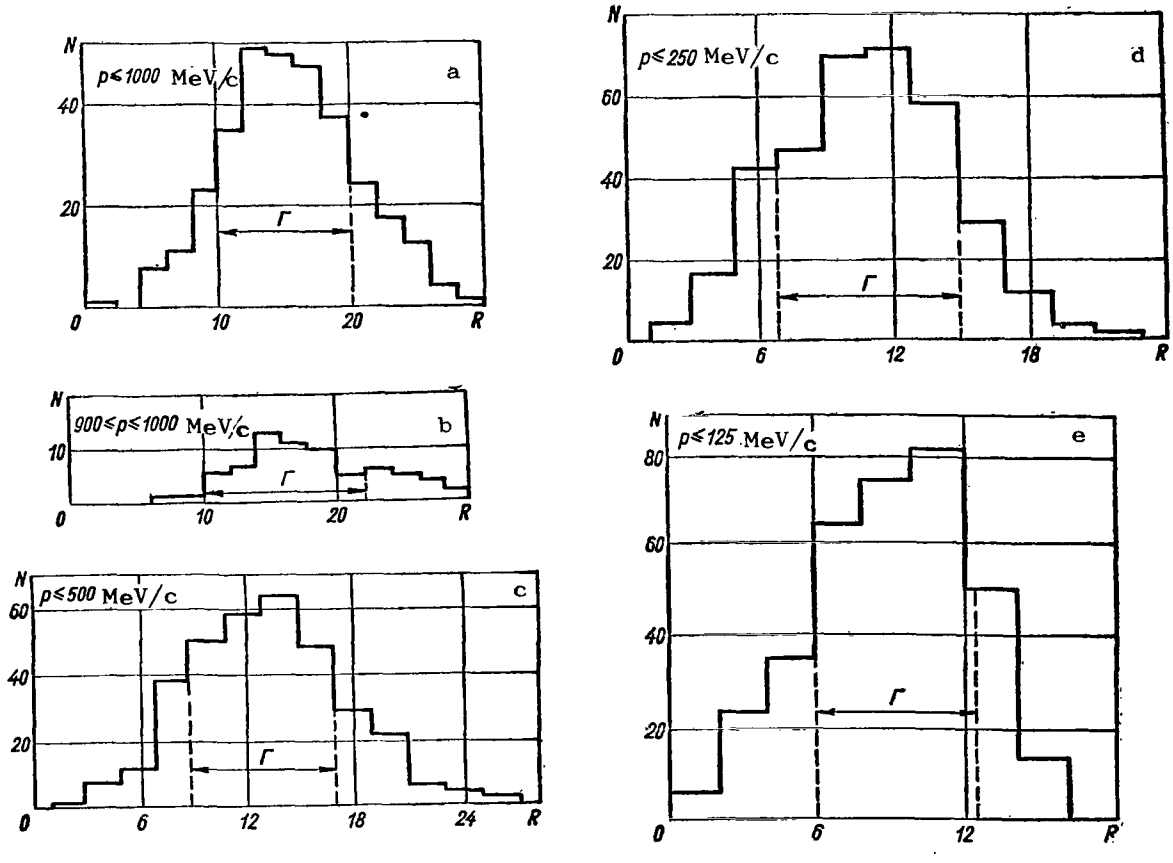

Figure 3. Distribution of paths of electrons with $p \lesssim 1$ GeV/c.

Figure 2 shows the "increase" in the momentum for the four tracks shown in Figure 1 in terms of the residual range, as well as the behavior of the momentum with range (dashed curve) in the case of the purely ionization mechanism of energy losses. As will be seen from the figure, there are individual cases when an electron can lose almost all of its energy immediately (track 1), others when an electron will lose its energy in comparatively small increments, despite the fact that in all cases the electron path is significantly shorter than the ionization path (the ionization path for an electron with initial momentum p = 1 GeV/c in xenon is R_{ion} = 202 cm).

Figure 3a is a histogram of the distribution of paths of electrons with momentum $p \leq 1$ GeV/c. The histogram covers the distance from R = 1 cm (3% of the cases with $R \leq 6$ cm) to R = 29 cm (3% of the cases with $R \geq 26$ cm). The highest probable path value is R = 15 cm.

The integral characteristic used for the distribution of electrons by paths was the width of the Γ band, containing 2/3rds (67%) of the electrons with the smallest deviations of their paths from the most probable value. As will be seen from Figure 3a, Γ = 10 cm, and the most probable range value, R_{prob}, lies in the middle of the band. If the histogram is constructed for electrons with momentum 0.9 GeV/c $\leq p \leq$ 1 GeV/c (Figure 3b), the maximum will remain in the same place, but the band will expand and become nonsymmetrical

$$R_{prob} = 15^{+7}_{-5} \text{ cm}.$$

Based on the sense of the magnitudes of Γ and R_{prob} introduced, the total range of an individual electron, R_{tot}, with an initial momentum p = 1 GeV/c equals $R_{tot} = 15^{+7}_{-5}$ cm (the confidence probability is 67%). A similar analysis, made for initial momenta of 0.5, 0.25, and 0.125 GeV/c, will provide the distributions shown in Figures 3c, d, and e. The characteristics of all four distributions are listed in Table 1, which contains the most probable values of total ranges, R_{prob}, for monoenergetic electrons.

2. Evaluation of Electron Momentum in Terms of the Magnitude of the Total Range.

Because the tracks of electrons with an initial momentum $p \leq 1$ GeV/c usually end within the chamber volume, it is useful to analyze the possibility of evaluating electron momentum in terms of the magnitude of its total range. A comparison of data listed in Table 1 reveals the most probable range, R_{prob}, is a very weak function of the initial momentum of monoenergetic electrons, with the range straggling near the most probable value extremely great. What follows is that the reverse operation of determining the momentum for monoenergetic electrons in terms of the nature of the distribution of their total ranges, R_{tot}, can be carried out with sufficient accuracy only with a very great many statistics. The momentum of a single electron in terms of the magnitude of its total range can be established on a tentative basis only.

TABLE 1

p, MeV/c	1000	500	250	125
R_{prob}, cm	15^{+7}_{-5}	13 ± 4	11^{+3}_{-4}	10^{+3}_{-4}

Distributions of electrons with these ranges as a function of the initial momentum (Figure 4a through e) were constructed in order to make a quantitative evaluation of the boundaries of the 67% confidence interval in which the momentum of an individual electron with the specified total range can be included. Electrons with initial momentum of $p \leq 1$ GeV/c (corresponding to the experiment in which the upper limit of the energies of the electrons forming was 1 GeV) were used for the distribution. The results of the interpretation of Figures 4a through e are listed in Table 2, where the most probable value of the momentum, p_{prob}, limited by the 67% confidence interval, is compared with each of the /154 values cited for total range. The momentum p_{ion}, corresponding to purely ionization losses, was used as the lower limit of the possible momentum for the 5 and 10 cm ranges).

As will be seen from the distributions and tables constructed, the total range (with the exception of very small and very large values) is a very poor characteristic of initial electron momentum, so the method of evaluating

the momentum in terms of the total range can be used only as a supplemental method. Analysis of the differential characteristics of the electron track can provide more accurate information about the electron momentum.

TABLE 2

Positions in Figure 4	a	b	c	d	e
R_{tot}, cm	5	10	15	20	25
p_{prob}, MeV/c	20 ± 3^{15}	100 ± 65^{100}	250 ± 150^{300}	550 ± 200	1000 ± 300^{0}
p_{ion}, MeV/c	17	35	56	78	100

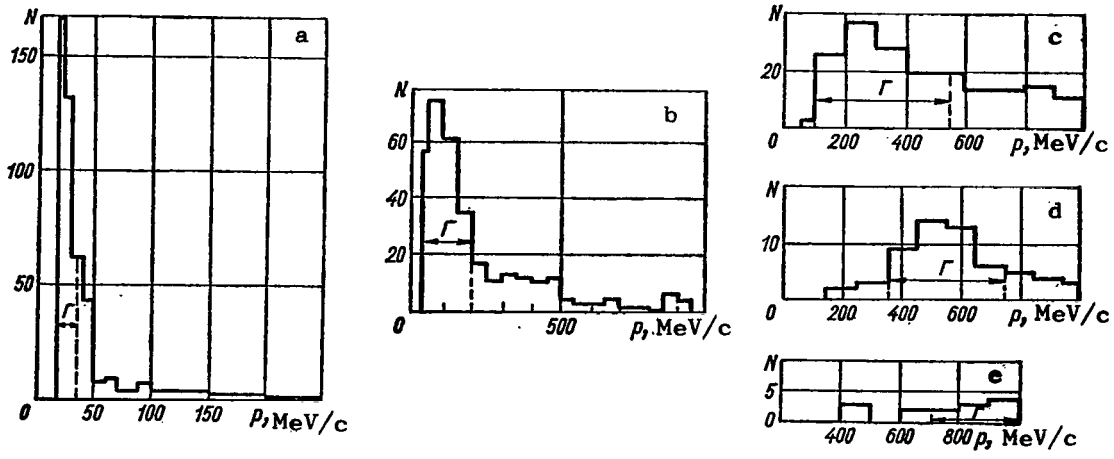

Figure 4. Distribution of electron momenta with specified range.

3. The Differential Area Method for Electrons.

Statement of the problem. The overall appearance of artificial electron tracks, their distribution in terms of total range (for a specified momentum), /155 and in terms of momentum (for a specified total range) concords with the radiation loss theory. Hence, artificial electron tracks can be used to develop a method for determining momentum for real electrons. A fast electron loses its energy in discrete portions, the magnitudes of which, ΔE, can attain the original energy value ($\Delta E \leq E_0$). The behavior of curvature with range, and the area of the curved segment, measured over the entire recorded section of

the range (both of which are good characteristics of the momentum for a heavy charged particle), therefore cannot be used to establish the electron momentum.

Some reliable data on electron momentum can be obtained by measuring the curvature of the very first section of the track ($\Delta l \sim 0.3\ X_0$, where X_0 is the radiative length of the track). The dimensions of this section, Δl, will depend on the parameters of the medium, the nature of the discharge of energy for the particular electron (see Figure 2), the intensity of the magnetic field, measurement errors, and on other factors. Thus, the following problems must be solved in developing the area method:

1. find the range of optimal values of Δl within the limits of which it is desirable to measure the track parameters;

2. establish a procedure for measuring track parameters that will be convenient to use and similar to that developed for heavy particles (the area of the segment $\Delta\Sigma$ on the section of track Δl, the angle Θ between the momentum and the direction of the magnetic field);

3. find a way to evaluate electron momentum in terms of measured values of track parameters and compose the corresponding program for the electronic computer. The program should provide for:

(a) varying the dimensions of the track section Δl during the measurements (within the limits of optimal values);

(b) analyzing several successive sections with lengths Δl_1, Δl_2, and Δl_3 for tracks with relatively low radiation losses (track 4 in Figure 2);

4. analyze the accuracy of the method, taking into consideration multiple scattering, measurement errors, inaccuracies in the magnitude of the magnetic field, computational approximations adopted, and others.

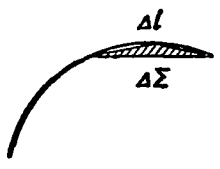

Figure 5. Differential Parameters of a track.

Computation methodology and results. The area of the segment $\Delta\Sigma$ was found for sections of the track limited by the segment of an arc of length Δl and a chord subtended by this arc (Figure 5). The segment was approximated by a triangle, two vertices of which coincide with the ends of the segment, and the third located in the center of the arc. This was done for

/156

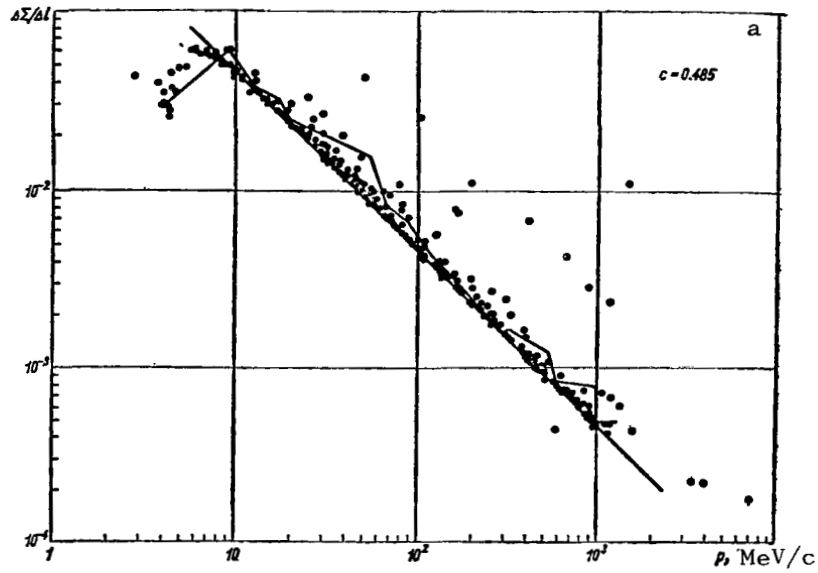

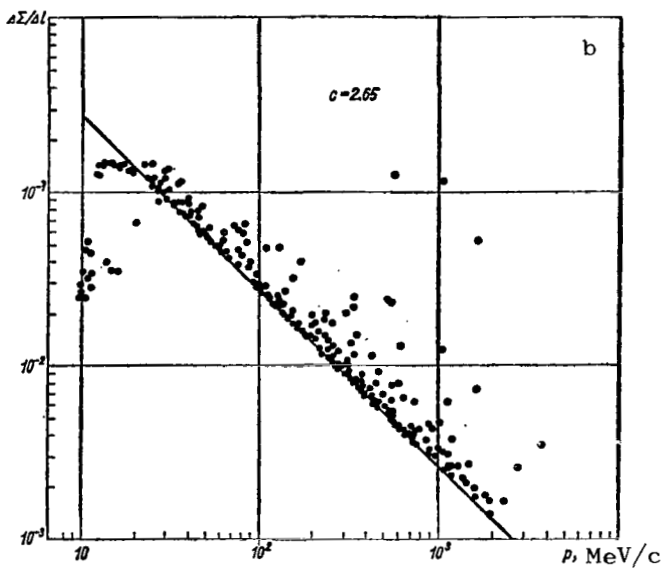

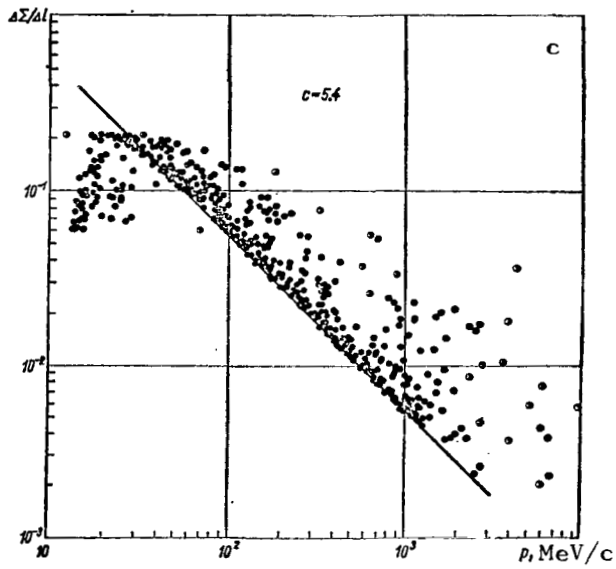

Figure 6. Spread in the $\Delta\Sigma/\Delta l$ values for electrons with a specified momentum when $\sigma = 0$ and $\Delta l = 0.6$ (a), 1.4 (b), 2 cm (c).

simplicity in making the measurements and computations. The computations were made for Δt = 0.6, 1.0, 1.4, 2.0 and 3 cm. /157

The values of $\Delta\Sigma/\Delta t$ as a function of the "true" (that is, obtained by sampling using the Monte Carlo method) value of momentum, p_{true}, are plotted in Figures 6a, b, and c for Δt = 0.6, 1.4, and 2.0 cm. There is a point in the graphic for each section, Δt_i, of the electron track (the broken line in Figure 6a connects all points on one track). As will be seen from the figures, the points are grouped near the straight lines

$$p_{true}\frac{\Delta\Sigma}{\Delta t} = c(\Delta t),$$

where

$c(\Delta t)$ is a factor that depends on Δt (the dispersion of the points can be explained by fluctuations in the bremsstrahlung).

A comparison of the results, equated to various Δt, revealed that $c(\Delta t)$ depended on Δt as the square of the relationship

$$c(\Delta l) = k\Delta l^2.$$

Here the constant $k = \frac{c(\Delta l)}{\Delta l^2} = \frac{5.4}{2^2} = \frac{2.65}{1.4^2} = \frac{0.484}{0.6^2} = 1.35.$

Now it is possible to find the electron momentum p_{meas} in terms of the value of $\Delta\Sigma$ (with accuracy to within the fluctuations in radiation losses) for a section of the track with arbitrary (within the limits of optimal values) length Δt[16] /158

$$p_{meas} = \frac{k\Delta l^2}{\Delta\Sigma/\Delta l} = k\frac{\Delta l^3}{\Delta\Sigma}.$$ [16]

Distributions of the magnitudes /159

$$\frac{\Delta p}{p} = \frac{p_{meas} - p_{true}}{p_{true}}$$

for Δt = 0.6, 1.0, 1.4, 2.0 and 3.0 cm were constructed to compare p_{meas} with p_{true}. Some of these are shown in Figures 7a through c. The histograms are not

16. See the note on page 156.

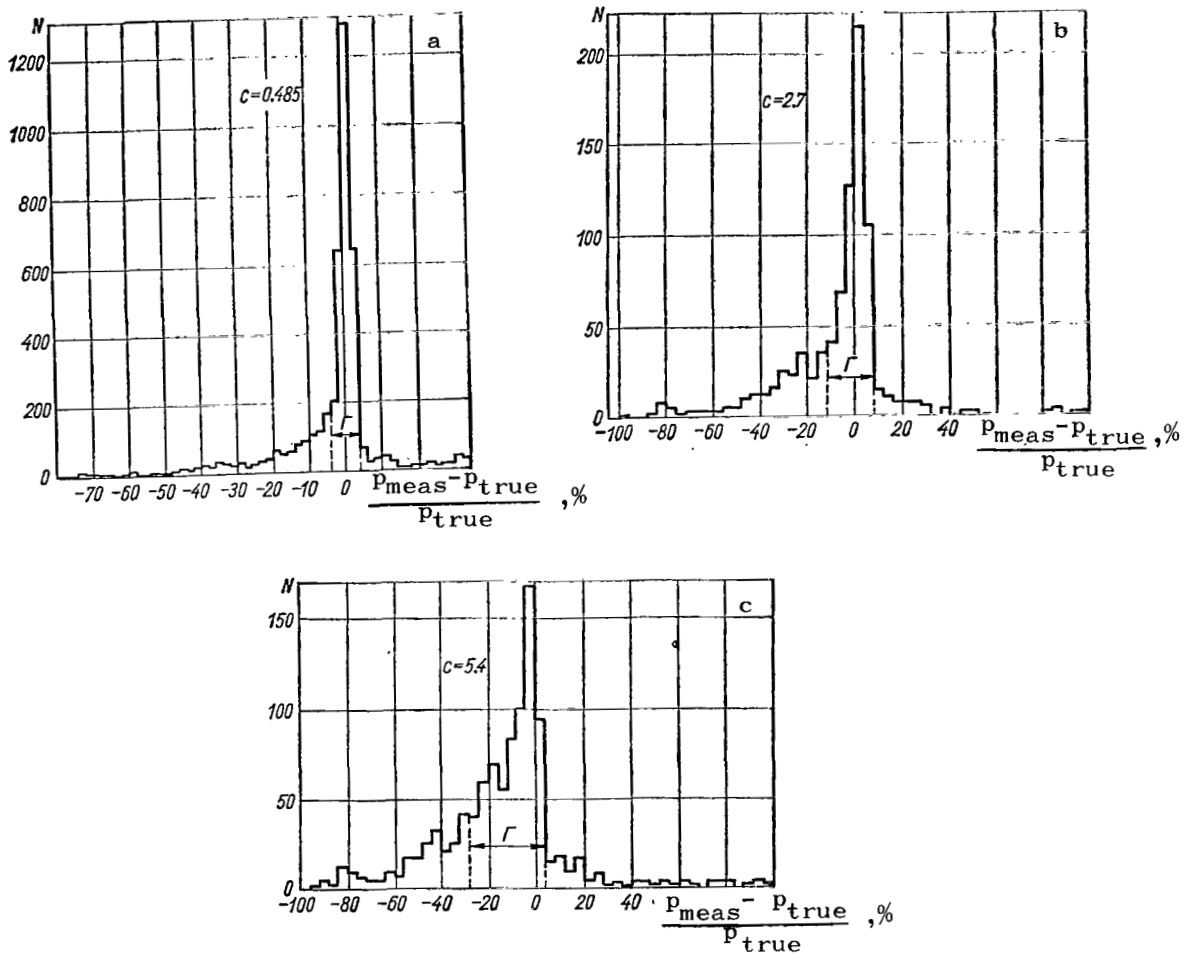

Figure 7. Distribution of the magnitude $\frac{p_{meas} - p_{true}}{p_{true}}$ when σ = 0 and Δt = 0.6 (a), 1.4 (b), and 2 cm (c).

symmetrical. They are characterized by a steep decline on the right and a broad, slow drop on the left. This histogram form can be explained by the sharp increase in the magnitude of $\Delta\gamma$ at those points on the track that correspond to high radiation energy losses by the electrons.

The width of the Γ band, within the limits of which are 2/3rds of the sampled cases with the highest probability of appearance, was used as the integral distribution characteristic. The width of the distribution is shown by the dashed lines in Figure 7. As will be seen from the Figures, the width of the Γ distribution is 8% when Δt = 0.6 cm, 20% when Δt = 1.4 cm, and 32% when Δt = 2.0 cm;

that is, it increases with increase in Δl. Once again, the explanation lies in the bremsstrahlung effect, the probability of which increases with increase in the length of the segment for the particular track segment.

The results given in the above were obtained assuming the absence of multiple scattering and measurement errors. Consideration of multiple scattering and measurement errors was a separate matter, considered as indicated in section 1. Computations were made for Δl = 0.6, 1.0, 1.4, 2.0, and 3.0 cm and for σ = 50, 100, and 200 microns, in order to take measurement errors into consideration. /160

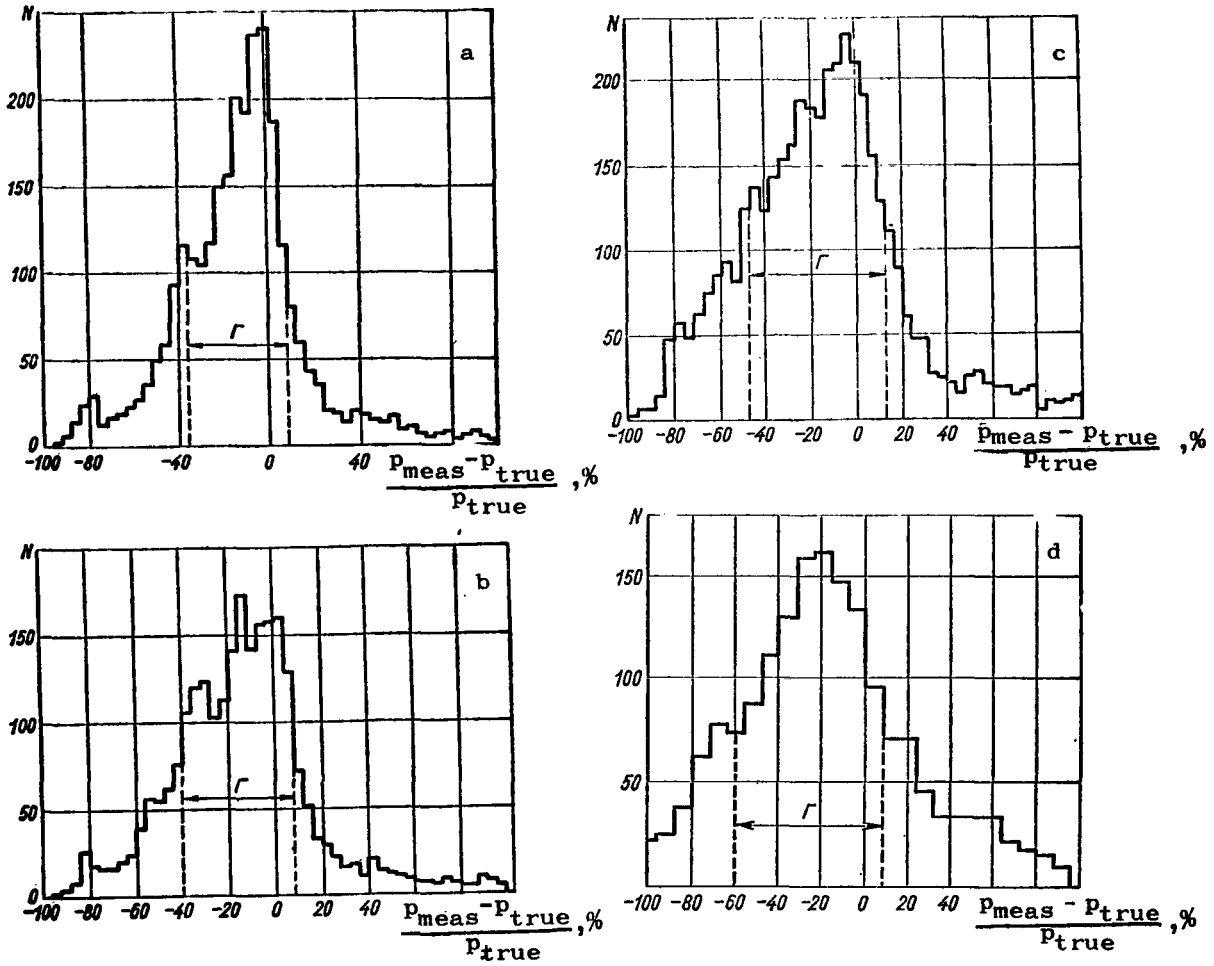

Figure 8. Distribution of the magnitude $\frac{p_{meas} - p_{true}}{p_{true}}$ when Δl = 2 cm and σ = 50 (a), 100 (b) and 200 microns (c), with multiple scattering not taken into consideration, and when σ = 200 microns (d) with multiple scattering taken into consideration.

The computations revealed that the $\Delta p/p$ distribution curves are expanded significantly as compared with the case of $\sigma = 0$ (particularly for small Δl). Figure 8 is an example showing the normalized $\Delta p/p$ distribution for $\Delta l = 2.0$ cm when $\sigma = 50$ microns (Figure 8a), 100 microns (Figure 8b), and 200 microns (Figure 8c). As will be seen from the figures, the distribution curves became more symmetrical, but the width of the Γ distribution increased from 32% for $\sigma = 0$ to 44, 48, and 60% for $\sigma = 50$, 100, 200 microns, respectively. Consideration of multiple scattering resulted in an additional increase in Γ. For example, Γ increased from 44 to 60% for $\Delta l = 2$ cm and $\sigma = 0$, from 48 to 64% when $\sigma = 50$ microns, and from 60 to 68% when $\sigma = 200$ microns (Figure 8d). /161 /162

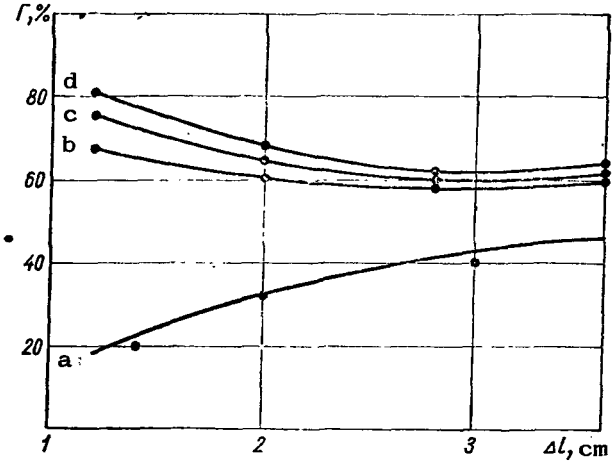

Figure 9. Γ in terms of Δl when $\sigma = 0$ without multiple scattering considered (a), and when $\sigma = 0$ (b), 50 (c), and 200 microns (d) with multiple scattering considered.

A comparative study of various distributions revealed that there is a region of Δl magnitudes for which the distribution width, Γ, and as a result the error in measuring the momentum, is minimal (Figure 9).[17] This region is $\Delta l = 2$ to 3 cm for $\sigma = 50$ to 200 microns. Therefore, the optimal distance between two successive points is the magnitude $\Delta l/2 = 1.5$ cm when measuring electron tracks.

The above distributions were obtained for electrons with momenta of 0 to 1 GeV/c. It is of interest to investigate the dependence of the width of the distribution of the magnitude $\Delta p/p$ within narrower energy intervals. The results of the corresponding computations made for $\Delta l = 1.2$ cm and $\sigma = 100$ microns are listed in Table 3.

17. Figure 9 also shows the curve for purposes of comparison for Γ in terms of Δl when $\sigma = 0$ without multiple scattering considered.

TABLE 3

p, MeV/c	Γ, %
0-100	72
100-200	72
200-400	68
400-800	56

As will be seen from Table 3, there is but slight dependence of the width of the Γ distribution on the initial momentum. It should be noted that the magnitude of Γ is made up of the inaccuracies in both signs, with the result that it is in excess of the normal error by a factor of approximately 2.

Conclusion. This article has described a method for studying electron tracks in a xenon bubble chamber that is similar to that developed earlier for heavy charged particles. The method is based on measuring the area of a segment $\Delta\Sigma$ over a short, initial section of a track, Δl. Analysis revealed a logarithmic linear dependence of $\Delta\Sigma/\Delta l$ on momentum p, and a square dependence on Δl. The simple nature of these dependencies is what makes it possible to make the measurements and to develop a convenient method. The universality of both methods (for heavy and light particles) greatly simplifies the compilation of programs for the computer. /163

REFERENCES

1. Mukhin, K. N., et al., V sb. Elementarnyye chastitsy i kosmicheskiye luchi, [IN Collection: Elementary Particles and Cosmic Rays], Atom Press, Moscow, 1967, p. 71.

2. Barkov, L. M., et al., Pribory i tekhn. eksperim., No. 6, 1963, p. 48.

THE NOBLE GAS SCINTILLATION MECHANISM

B. A. Dolgoshein and B. U. Rodionov

ABSTRACT. The noble gas scintillation mechanism is analyzed. Previous studies are reviewed, the elementary processes taking place along the track of an ionizing particle are discussed and properties of gas scintillators are described.

1. Introduction

The capacity of noble gases to light up when acted upon by ionizing particles is widely used in experimental nuclear physics. Let us list the most important properties of gas scintillators: /164

(1) gas scintillators efficiently record particles with various ionizing capabilities (from fission fragments to relativistic electrons);

(2) the rise time for a scintillation pulse is short (about 10^{-8} second);

(3) the linearity between the amplitude of the light flash and the energy lost by the ionizing particle in the gas is found to be good;

(4) the range of the particle (or the energy lost in the scintillator) can be controlled by changing the gas pressure, so recording of the more penetrating radiation can be avoided;

(5) scintillating gas can be used simultaneously as a target [for neutron spectrometry as a result of the $He^3(n, p)H^3$ reaction, for example];

(6) noble gas in ionization and spark chambers can be used simultaneously as a scintillator;

(7) a gas scintillator can be made in any size and shape.

The properties of gas scintillators known up to 1964, can be found in surveys of the subject [1, 2, 3 (chapter 14)]. A whole series of new properties, the most important of which will be cited in what follows, are being studied at this time.

The recent investigation of atomic processes taking place in plasma (see [4-6], for example) makes it possible to evaluate the role of these processes

in the kinetics of noble gas scintillation, as least qualitatively. Section 2 is devoted to the elementary processes taking place along the track of an ionizing particle. Section 3 describes the properties of gas scintillators. The principal purpose of this article is to analyze the mechanism involved in noble gas scintillation.

Let us pause to consider the individual stages that have taken place in /165
the study of the nature of noble gas scintillation. The work done by Pierre and Marie Curie stimulated the production of powerful radioactive preparations. The luminescence of the gas near these preparations was seen by the naked eye [7]. In 1906, Stark found that the fluorescence of a gas under the influence of α-particles was unresponsive to an electric field [8]. Pohl was concerned with the nature of the fluorescence of gases [9]. Interest in gas scintillation increased after the appearance of photoelectron multipliers, when it became possible to really record individual particles from the flashes of light in the gas. In 1951, Grün and Schopper studied scintillation as initiated by α-particles of polonium in argon, N_2, H_2, O_2, and CO_2 [10]. Maximum light yield was found in argon, and it was proven that this light did not depend on the presence of an electric field, and that most of the light was in the ultraviolet radiation region. The use of light converters for transforming the far ultraviolet radiation of a gas into visible light [11] made it possible to increase scintillation amplitude by a factor of almost ten. Because far ultraviolet radiation in a noble gas can occur only upon transition of an excited atom to the ground state, radiation from atoms should be absorbed resonantly in the gas itself. This is why Avivi and Cohen, in 1957, assumed that ultraviolet radiation occurs upon transition of excited atoms of a noble gas to the ground state [12].

Scintillator deexcitation time, according to this same reference [12], having been proven to be inversely proportional to the gas pressure and equalling about 10^{-6} to 10^{-7} second at normal pressure, pointed to the fact that ions forming along the track of an α-particle were excited to the metastable level. Lydia Koch [13-15] showed that two deexcitation processes can be observed in noble gases; rapid deexcitation, in approximately 10^{-9} second (the fast scintillation component), and slow deexcitation, in about 10^{-7} second (the slow component). Koch assumed that the slow component was associated with the

deexcitation of the metastable ions. Trace amounts of impurities (10^{-2}%) had a significant effect on gas scintillator deexcitation.

Northrop and Gursky [16] believe the cause of luminescence to be the recombination of ionized noble gas molecules forming along the particle track with the electrons (1958). Already known at that time was the fact that the ionized noble gases molecules, discovered by Tüxen in 1936 [17], have an unexpectedly high coefficient of recombination with electrons [18, 19]. The hypothesis advanced with respect to this recombination contradicted experiments in which the nonresponsiveness of a gas scintillator to an electric field had been shown [8, 10, 20, 21]. Tavendale successfully noted the reduction in the amplitude of scintillations in an Ar + N_2 mixture in 1961 [22]. The effect was about 3% when excitation was by α-particles, and 40% when excitation was by U^{235} fission fragments. /166

Reference [23] attempted to explain scintillation amplitude in helium in terms of electron and ion recombination pressure. Reference [24] found no electric field effect on scintillation in helium. The authors assumed the light to be the result of the excited He_2^* molecule. Reference [3] came to the conclusion that the complex conditions of Tavendale's experiments were not sufficient grounds for saying that recombination in noble gases had been proven. Gas scintillator literature [25] gives preference to the hypothesis that scintillation light is the result of the deexcitation of metastable ions.

Recently conducted, detailed, spectroscopic investigations made of scintillation in gases [26-29] confirm, in the main, the results of earlier investigations [14, 30]. Spectrum analysis indicates that noble gas scintillation is associated with the deexcitation of photons by excited noble gas atoms and molecules. Impurities (O_2, N_2, H_2O, Hg) that are always present within the scintillator (wall outgassing), even when the gas is very carefully purified, make a definite contribution. There are no lines for the excited ions, for all practical purposes.[18] Luminescence of ions is thus apparently unimportant in

---

18. A peak of 3093 Å in argon earlier had been assigned to the excited ion ArII [14], but reference [26] showed that this peak was associated with the deexcitation of the excited OH radicals.

gas scintillators.

Our paper [31] showed experimentally that recombination makes a significant contribution to noble gas scintillation (see section 2). This is the time, therefore, to review some of the previously made representations with respect to the nature of noble gas scintillation, because not one of the old scintillation models is capable of explaining, even qualitatively, all the known properties of gas scintillators.

2. Processes Along the Track of a Charged Particle

a. Formation of molecules and of molecular ions

Molecular ions. A charged particle, moving through a gas, will form atomic ions X^+, electrons e, excited atoms X^*, and excited ions along its track. Because ion lines have not been noted in the spectra of noble gas scintillations, excited ions are an insignificant part of the ions, and we will given them no special consideration.[19] /167

An atomic ion, X^+, colliding with the atoms of gas X, forms an ionized molecule, X_2^+ [32]

$$X^+ + 2X \rightarrow X_2^+ + X. \tag{1}$$

A third particle is needed to carry off the energy released during the formation of X_2^+. The characteristic time for the Eq. (1) reaction can be found through the formula

$$\tau \sim \frac{1}{\alpha_1 n^2},$$

where

n is the number of atoms of the gas per cm^3;

α_1 is a coefficient that is little dependent on gas temperature [33-35];

$\alpha_1 = 5(10^{-32}$ to $10^{-31})cm^6 sec^{-1}$.

The Eq. (1) reaction will take place in 10^{-8} second at normal pressure ($n = 2.7 \cdot 10^{19}$ $1/cm^3$), so in dense gases (pressure about 1 atmosphere) electrons, for all practical purposes, recombine only with ionized molecules. Incidentally,

19. According to the data contained in [12], the number of excited ions is 2 to 3% of the total number of ions.

the probability of the recombination of an electron with an ionized molecule is thousands of times greater than the probability of the recombination of an electron with an atomic ion of a noble gas [36].

The disassociation energy of the ionized molecule X_2^+ in the ground state is about 1 ev [37] (helium - 1 to 3 ev [27]), that is, the ionized molecule is extremely stable and evidently will disappear in gas scintillators only as a result of recombination with an electron.

Excited atoms. Now let us trace the fate of excited atoms. The excited atoms of a noble gas have two lower metastable levels, and two resonance levels ($^3P_2$, $^3P_0$ and $^3P_1$, $^1P_1$, helium has the metastable levels $^3S_1$, $^1S_0$ and the resonance levels $^3P_0$, $^1P_1$). Sooner or later, all the excited atoms in a dense gas will prove to be excited at one of the four lower levels. As a matter of fact, transitions of an electron between the upper excited states, leading to the emission of ultraviolet radiation, visible, or infrared light, will inevitably put a noble gas atom into one of the four excitation states mentioned.

If an atom moves from any of the upper excitation levels to the ground state, a photon will be emitted and it will be absorbed immediately by a neighboring atom. Radiation "capture" actually increases the lifetime of excited atoms in a gas in terms of transitions to the ground state. All such atoms finally fall, therefore, into the two lower metastable levels, or into the two resonance levels. Because of the capture of resonance radiation, the resonance levels will be populated for an extraordinarily long time (until diffusing light reaches the chamber walls, or the excited state is extinguished in collisions). /168

The interaction of excited atoms with neutral atoms. So, excited atoms in a pure noble gas cannot, practically speaking, make a transition to the ground state, and the result is that most of the energy expended by the ionizing particles in exciting the atoms is suppressed in the gas. The carriers of this energy, the atoms, excited at one of the four lower levels, will interact with the surrounding atoms [37-40]

$$X^* + 2X \rightarrow X_2^* + X. \qquad (2)$$

The time of this reaction, just as in the Eq. (1) reaction, is inversely proportional to the square of the gas density

$$\tau \sim \frac{1}{\alpha_2 n^2},$$

where α_2 will change from $2.5 \cdot 10^{-34}$ (helium [41]) to 10^{-31} cm^6/sec (krypton [42]). $\tau \sim 10^{-6}$ sec in light gases, and 10^{-7} to 10^{-8} sec in heavy noble gases at normal pressure. The photon emitted by the molecule during the transition to the ground state will not be a resonance photon for neutral atoms, and therefore leaves the gas freely.

The X_2 molecule ionization potential is approximately 1 to 2 ev less than the ionization potential for the atom [37, 43]. Hence, highly excited atoms are capable of forming ionized molecules when they collide with neutral atoms [43-45]

$$X^* + X \rightarrow X_2^+ + e. \qquad (3)$$

The energy released during the formation of the X^{2+} ion in this reaction is carried off by the electron, so a two-particle collision is sufficient. The Eq. (3) reaction should be completed prior to the transition of an electron of the atom to one of the four metastable levels, because at these levels the energies no longer suffice to detach the electron and form an ionized molecule; that is, the real time required for the Eq. (3) process to take place is not in excess of the deexcitation time for the atom (about 10^{-7} second).

So, we see that along the track of an ionizing particle the result of the Eq. (1) reaction is to convert all ions into ionized molecules, X_2^+, and all excited atoms, X^*, into excited molecules, X_2^* [the Eq. (2) reaction], or into ionized molecules, X_2^+ [the Eq. (3) reaction]. And only a slight amount of the energy is converted into heat (carried away by the atoms or electrons taking part in the triple collisions). /169

Mixtures of noble gases. Let us review the processes taking place along the track of an ionizing particle in a mixture of two noble gases (X is the lighter, Y the heavier). Since the levels of excitation (and the ionization potential) for the light gas always are higher than those for the heavy gas, there should be effective interception of the excitation energy by the atoms of the heavy gas in a mixture of two noble gases

$$X^* + Y \rightarrow X + Y^* \quad \text{or} \quad X_2^* + Y \rightarrow 2X + Y^*; \tag{4}$$

$$Y^* + 2X \rightarrow (XY)^* + X \quad \text{or} \quad Y^* + Y + X \rightarrow Y_2^* + X; \tag{5}$$

$$(XY)^* + Y \rightarrow Y_2^* + X. \tag{6}$$

Ionization of an atom of the heavy gas (the Penning effect) is possible

$$\text{or} \quad \left.\begin{array}{l} X^* + Y \rightarrow X + Y^+ + e \\ X_2^* + Y \rightarrow 2X + Y^+ + e. \end{array}\right\} \tag{7}$$

The reactions between the ions are energetically favorable

$$X_2^+ + Y \rightarrow (XY)^+ + X; \tag{8}$$

$$X_2^+ + Y \rightarrow Y^+ + 2X; \tag{9}$$

$$Y^+ + 2X \rightarrow (XY)^+ + X; \tag{10}$$

$$(XY)^+ + Y \rightarrow Y_2^+ + X. \tag{11}$$

Thus, as a result of the Eqs. (4) - (11) processes [as well as the Eqs. (1) - (3 processes] it is possible that there will be a pumping of almost all of the energy lost by the ionizing particle in a mixture of two noble gases to the molecules of the heavier gas (or to molecules of a mixed type). There is an effective energy pumping process when there are slight concentrations of the heavier gas. Mass spectrometric analysis of a Kr + 0.02% Xe mixture showed predominance of the $(KrXe)^+$ ions in the mixture [46]. Neon lines were predominant in the optical range in the He + 10^{-3}% Ne mixture [27].

Noble gas containing an impurity. If a noble gas, X, contains an atomic impurity, Y, all of the Eq. (4) - (11) reactions cited above are possible, obviously. For example, an impurity consisting of $2 \cdot 10^{-2}$% cesium vapors in helium will result in the cesium intercepting all the energy released in the discharge [47], and only cesium lines will be observed in the discharge spectrum. The presence of 0.002% mercury vapors in argon yields an intensive resonance line at 2536 Å in the noble gas scintillation spectrum in the optical region [14].

Molecular impurities have many excitation levels, therefore these impurities are particularly effective in intercepting the energy from the excited noble gas atoms (molecules). But it is possible to ionize the molecules of the impurity, or to excite the impurity, and equally possible are dissociation, dissociation with excitation of newly forming molecules, and the like. When noble gas ions interact with the impurity, charge exchange, with excitation of the ionized molecule of the impurity, is possible [6]. /170

The following are some of the reactions with the most widespread molecular impurities in noble gases [27]

$$X_2^+ + O_2 \rightarrow O_2^+ + 2X; \quad (12)$$

$$X_2^+ + N_2 \rightarrow N_2^+ + 2X; \quad (13)$$

$$X^* + N_2 \rightarrow N_2^+ + X + e; \quad (14)$$

$$X^* + N_2 \rightarrow N_2^* + X; \quad N_2^* \rightarrow N_2 + h\nu \quad \text{(a system of bands in the visible region)} \quad (15)$$

$$X^* + N_2 \rightarrow X + 2N; \quad (16)$$

$$X^* + H_2O \rightarrow X + OH^* + O; \quad OH^* \rightarrow OH + h\nu \quad \text{(band near 3064 Å)} \quad (17)$$

The formation of new, excited noble gas molecules, $(XO)^*$, for example, also can be observed [48]. As we see, there are a great many different processes that become possibilities during the interception of energy by the molecules in the impurity. They all result in the deexcitation of the gas atoms, and effectively convert the energy lost by the ionizing particles to the gas into heat. The Eq. (15) reaction takes place in argon with a large cross-section, and nitrogen (up to 10%) has been specially added to the early designs of gas scintillation counters to transform the energy of the excited argon atoms into visible light [10]. Let us follow the fate of ionized molecules in a pure noble gas.

b. Electron-ion recombination

The presence of electron-ion recombination, accompanied by luminescence along the tracks of ionizing particles in noble gases was shown experimentally in [31]. The proof is based on the following two experimental results.

1. The decrease in the amplitude of scintillation light is proportional to the number of electrons extracted from the track of the ionizing particle [31, 48, 49].

2. The increase in scintillating light in terms of time is proportional to the number of electron recombination events [31].

It is a known fact that recombination of electrons with the ionized molecules of a noble gas proceeds thousands of times more effectively than it does with atomic ions [18, 19, 32, 36, 50]. When the high rate at which ionized /171

molecules are formed is taken into consideration (see section 2a) it can be asserted that in gas scintillators the recombination of electrons with atomic ions is insignificant, and it can be taken that electrons recombine only with ionized molecules. Recombination is possible in one of the following processes

$$X_2^+ + e \rightarrow X_2^* + h\nu; \tag{18}$$

$$X_2^+ + e \rightarrow X^* + X; \tag{19}$$

$$X_2^+ + 2e \rightarrow X_2^* + e; \tag{20}$$

$$X_2^+ + e + X \rightarrow X_2^* + X. \tag{21}$$

There is little likelihood of the Eq. (18) radiative recombination because the time the electron interacts with the ionized molecule during collision is very much shorter than the photon emission time, so there is little likelihood that the energy for binding the electron to the ion will be carried away by the photon. The coefficient of radiative recombination is 10^{-11} to 10^{-12} cm^3/sec for thermal energy electrons [6].

The Eq. (19) dissociative recombination was long considered the most probable recombination process in noble gases. The coefficient of dissociative recombination has been estimated as in the range 10^{-6} to 10^{-8} cm^3/sec [6]. However, recent investigations made of noble gas plasma have shown that the role of dissociative recombination has been overestimated (see [51-54], for example). Apparently the principal recombination processes in noble gases must be considered to be the electron-ion recombinations in the Eq. (20) and Eq. (21) three-particle collisions.

A survey of the work done in accordance with the theory of triple collisions of an ion with electrons can be found in [5, 6, 55]. The electron recombines with the X_2^+ ion in the Eq. (20) reaction, and the potential energy released during electron capture is transferred to the other electron taking part in the collision. The recombination coefficient is approximately $10^{-26}\ n_e/T^{9/2}$ cm^3/sec (n_e is electron density, T is their temperature, ev [56, 57]). The Eq. (20) reaction can be the principal recombination process in plasma with a high electron density. For example, $n_e \approx 10^{15}$ to 10^{16} along the track of α-particles in helium at a pressure of 7 atmospheres [23]. Con-

sidering the electrons as being thermalized ($T \sim 1/40$ ev), we obtain a magnitude of about 10^{-4} cm^3/sec for the recombination coefficient.

The Eq. (21) reaction can become substantial in plasma with a low charge density. The energy released during recombination is carried off by an atom of gas X. The recombination coefficient is proportional to gas pressure p in this case. It is 10^{-11} p cm^3/sec in helium ([p] = [mm Hg]) [58]. The magnitude of the recombination coefficient is about 10^{-8} cm^3/sec at normal pressure. /172

So we see that the result of the recombination of an electron with the ion of Eqs. (18-21) is the formation of excited molecule X_2^*. In the case of the Eq. (20) dissociative recombination the excited atom will take part in the Eq. (2) or the Eq. (3) reaction, and, in the final analysis, the excited molecule X_2^* will be formed once again.

c. Formation of plasma along the track of an ionizing particle

The Eqs. (18) - (21) recombination processes are greatly dependent on the ion density formed along the track of the ionizing particle. There may not be any recombination when ionization density is low because the electrons leave the zone occupied by the positive ionized molecules quite rapidly as a result of diffusion. In fact, the electrostatic interaction of particles along the track can be ignored when ion density is low. Recombination is insignificant prior to electron thermalization, so the electron cloud leaks out during thermalization time t [59] such that the root-mean-square electron shift with respect to the trajectory of an ionizing particle $\sqrt{\overline{r_e^2}}$, is $\sqrt{\overline{r_e^2}} = \sqrt{4D_e t}$ (D_e is the diffusion coefficient for the electrons). The ions have a similar expression $\sqrt{\overline{r_i^2}} = \sqrt{4D_i t}$ [D_i is the diffusion coefficient for the ions, with $(D_e/D_i) \approx 1000$] [6]. The electron density in terms of the ion density along the trace can be established as approximately equal to $(\overline{r_i^2}/\overline{r_e^2}) \approx 10^{-3}$, very quickly; that is, only 10^{-3} of the electrons are in the volume occupied by the positive ions and can recombine with them.

Electrons and ions will interact electrostatically with each other when ion density is high. The diffusion leakage of electrons is checked by the electric field of the ions. Ions and electrons will diffuse together (ambipolar diffusion). It is a known fact [6] that the Debye shielding distance

characterizes the distance at which deviation from electrical neutrality is possible in a column of ionized gas. If the radius of the column of ionized gas, r, is greater than the Debye shielding distance λ_D, we will have the real plasma itself along the track of the ionizing particle. Let us suppose that in a column with radius r the ion density is uniform and equal to n_e. The total number of ions, N (or electrons), created by the ionizing particle in the gas in length l is equal to /173

$$N = l\pi r^2 n_e,$$

that is, $n_e = \frac{N}{e\pi r^2}$. From the expression for the Debye shielding distance

$$\lambda_D = \sqrt{\frac{\varepsilon kT}{4\pi e^2 n_e}},$$

where

$\varepsilon \sim 1$ is the gas permittivity;

n_e is ion density;

k is the Boltzmann constant;

T is gas temperature and thermalized electron temperature,

we find

$$\frac{\lambda_D}{r} = \sqrt{\frac{\varepsilon kTe\pi}{4\pi e^2 N}} = \sqrt{\frac{kT}{4e^2\eta}}, \qquad (1)$$

where

η is the number of ions per unit length of the track.

Eq. (1) shows that when the number of ions per unit length of the track is $\eta = 4.5 \cdot 10^4$ cm^{-1} quasineutrality of the plasma ($\lambda_D/r \approx 1$) begins to occur along the track of the ionizing particle.

Figure 1 shows the scintillation amplitudes in neon (a), krypton (b), argon (c), and xenon (d) in terms of gas pressure. Scintillations were observed as well when an electric field was applied, one that provided for maximum reduction in scintillation amplitude because of the extraction of some of the electrons from the α-particle track. Reference [31] notes that response to the field occurred in all gases when the number of ions per unit α-particle track was approximately $2 \cdot 10^5$ cm^{-1}, which corresponds to $\lambda_D/r \approx 1/2$. So it is only after the formation of plasma along the track of the ionizing particle that electron- /174

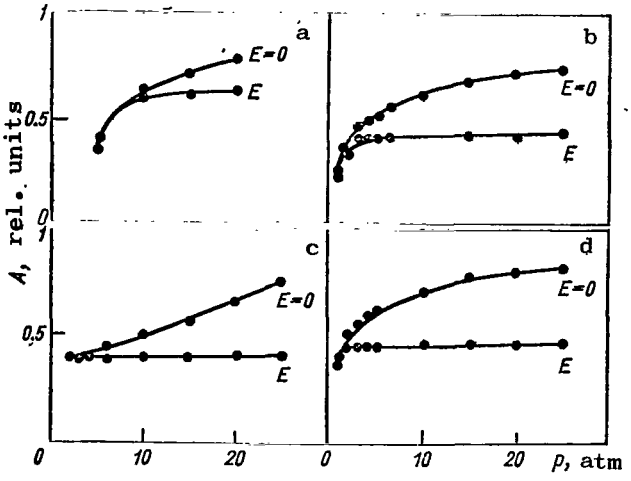

Figure 1. Scintillation amplitude A in various noble gases acted on by α-particles in terms of gas pressure, p.

ion recombination begins to make a definite contribution to noble gas scintillation (see Figure 1). The scintillation amplitude is not reduced in the electric field prior to the formation of plasma in a noble gas, and this concords with the results recorded in many other papers. If plasma has formed, there is a reduction in scintillation amplitude in an electric field [31, 49, 60]. The contribution of the recombination processes (as will be seen from Figure 1) increases with increase in gas density. In fact, if ion density along the track is $\eta > 2 \cdot 10^5$ cm^{-1}, recombination will continue until ion density is no longer equal to approximately $2 \cdot 10^5$ cm^{-1}, after which the electrons will separate from the ions and will depart from the track as a result of diffusion.

Thus, the recombination processes in gas scintillators are significantly dependent on ion density along the track of the ionizing particle. Recombination will not occur, practically speaking, when ionization densities are not adequate for plasma formation ($\eta < 2 \cdot 10^5$ cm^{-1}) because of the rapid diffusion of electrons from the track of the ionizing particle. Plasma will form along the track when $\eta > 2 \cdot 10^5$ cm^{-1}. Ion density in the plasma is determined by the percentage of recombining electrons and the rate at which the recombination process takes place.

d. Deexcitation of excited noble gas molecules

The spectral composition of molecular light. The result of the Eqs. (1) - (3) and (18) - (21) reactions is that the energy lost by the ionizing particle to a noble gas is, for the most part, transferred to the excited molecule. Very little of this energy can go to the deexcitation of photons of visible, soft ultraviolet, or infrared light during the transfer of electrons between the upper levels of excitation of noble gas atoms or molecules. Even if it is

assumed that all the upper levels are uniformly populated with electrons, the energy supplied to the upper levels is less than 30% in noble gases. The percentage of visible light in noble gas scintillators is less than 10% [31, 61, 62]. Basic light emitted by the molecules is vacuum ultraviolet ($\lambda < 2000$ Å). The shortwave limit of molecular light coincides with the wavelength of the photon emitted from the lower resonance level of a noble gas atom [63]. Ultraviolet light is distributed continuously from its shortwave limit to the longer /175
wave side. The distribution has a number of broad maxima. Reference [26] lists the molecular continuum for argon excited by α-particles. A survey of noble gas continuums when excitation is by an electric charge is contained in [64]. Deexcitation by an excited molecule of a shortwave photon is accompanied by the dissociation of the excited molecule

$$X_2^* \rightarrow h\nu + X + X. \qquad (22)$$

Time of deexcitation of light by molecules. The lifetime of the relative emission of an ultraviolet photon by an excited molecule of argon has been estimated in [40], as equal to $3.4 \cdot 10^{-6}$ sec ($p \leq 1$ atm). Reference [65] contains data to show the existence of metastable molecules, Ar_2^*, in argon, something that can explain the long deexcitation time at low pressures. Reference [42] made the assumption that the deexcitation of noble gas molecules takes place more rapidly than 10^{-6} second. The available data do not contradict the lifetimes of excited molecules relative to the emission of vacuum ultraviolet (10^{-5} to 10^{-7} second at a pressure close to atmospheric). The lifetime of excited molecules relative to the emission of soft ultraviolet or visible light is 10^{-7} to 10^{-8} second. The role of extinguishing collisions increases with increase in gas pressure, so the lifetime of excited atoms is shortened [3].

e. Deexcitation of noble gas molecules

Deexcitation of the molecules of molecular impurities. The processes involved in the interaction of excited atoms with molecular impurities were reviewed in subsection a of this section. Reactions similar to those of Eqs. (14) - (17) are valid for excited noble gas molecules. The deexcitation cross section is of the order of the gas kinetic cross section. The extinguishing

effect of molecular impurities is well known [4, 6, 50, 58], and we will not dwell upon it here. Let us consider the deexcitation of molecules in pure noble gases.

Deexcitation of molecules in collisions with electrons. When an excited noble gas molecule collides with an electron, the molecule can become even more highly excited, it can become ionized, or it can be deexcited (superelastic collision of the electron). The deexcitation cross section of a molecule in collision with an electron obviously is of the same order of magnitude as the deexcitation cross section for an atom; that is, 10^{-16} to 10^{-17} cm^2 [5]. Electron deexcitation has been reviewed in a number of papers (for example, [41, 52, 66]). Superelastic collision of electrons is one of the most important processes taking place in a noble gas plasma. But electron deexcitation can be a process /176 of lesser importance as compared with the deexcitation of molecules in collisions with atoms of the gas when concentrations of electrons in the plasma are small [65]. Reference [30] considers electron deexcitation to be of no moment in gas scintillators when pressures are low.

In fact, there is little likelihood of electron deexcitation in the case of those ionization densities along the track when no plasma is formed and when recombination of electrons with ions does not occur because electron density on the track is low. However, in plasma in which the Eqs. (18) - (21) recombination processes are taking place, the processes involved in the electron deexcitation of molecules should also be noted. The number of superelastic collisions of electrons in unit volume in unit time is readily found by the deexcitation cross section. The deexcitation coefficient is similar to the recombination coefficient, $(10^{-16}$ to $10^{-17})v_e$, where v_e is the electron velocity. When $T \sim 300°C$, $v_e \sim 10^7$ cm/sec, the deexcitation coefficient is about 10^{-9} to 10^{-10} cm^3/sec. What must be taken into consideration is that during recombination the electron emits only one shortwave photon, but that same electron can deexcite several molecules. Moreover, the number of excited molecules forming along the track exceeds the number of ions. But the presence of a linear relationship between the number of recombination events and the amplitude of the scintillation light [31] indicates that the effect of electron deexcitation does not exceed 10% of the scintillation amplitude.

Deexcitation of molecules in collisions with atoms. The effectiveness of deexcitation is maximum when the velocity of an incident particle is comparable with the velocity of the atomic electrons. The deexcitation cross section for a molecule in collision with a neutral atom therefore should be thousands of times smaller than the electron deexcitation cross section. According to the data contained in [5], the atom deexcitation cross section (like the atom excitation cross section) should be 10^{-20} to 10^{-22} cm^2 for an atom kinetic energy of about 10 ev.

Reference [67] evaluates the deexcitation cross sections for the four lower levels of neon in collisions with atoms and electrons (the distance between levels is in fractions of an electron volt). Only transitions between these levels are considered. The deexcitation cross section for collisions of atoms at 300°K is $5 \cdot 10^{-19}$ to $6 \cdot 10^{-20}$ cm^2. The deexcitation cross section $^3P_1$ to $^3P_2$ increases by an order of magnitude when the temperature is raised by a factor of almost two. The deexcitation of these same levels by thermal electrons takes place with cross sections of 10^{-13} to 10^{-14} cm^2. The deexcitation of noble gas atoms and molecules to the ground state should be much less likely because an energy of about 10 ev is removed in the case of this deexcitation. But reference [65] assumes that the main process involved in loss of energy by /177 an excited argon molecule ($p \sim 10$ mm Hg) is deexcitation in collisions with neutral atoms. The deexcitation probability is directly proportional to the gas pressure. The deexcitation cross section is about 10^{-20} cm^2 when T = 300°K, and a deexcitation time of about 10^{-4} second corresponds to normal pressure.

Deexcitation of molecules accompanied by ionization. An excited noble gas molecule can cause ionization of the three (or four) atoms that form during the collision of the molecule with the atoms (or an unexcited molecule) of a noble gas

$$X_2^* + X \rightarrow X_3^+ + e \qquad (23)$$

or

$$X_2^* + X_2 \rightarrow X_4^+ + e. \qquad (24)$$

The Eqs. (23) and (24) reactions are similar to the Eq. (3) reaction, and can be observed in nitrogen and hydrogen. There apparently are no reasons for the suppression of reactions of this type in dense noble gases, but the existence of the Eqs. (23) and (24) processes have not yet been confirmed experimentally.

f. Migration of excitation energy in noble gases

Light streaming through a noble gas can be absorbed by an atom of the gas. The probability of absorption is maximum if the photon energy coincides with the energy for excitation of the atom from the ground state. The atom absorbing the photon can emit it again, but in a different direction. The path followed by a photon that is repeatedly absorbed and then emitted by the atoms of the gas reminds one of the path of a particle diffused in the gas, so this type of energy migration is called the diffusion of light. If the coefficient of absorption is high, the diffusion of light locks the photons in the gas, in essence (radiation capture). Study of the diffusion of light in gases has been reported in a number of papers [67-74]. Expansion of atomic lines with increase in pressure plays an important role in the process involved in the diffusion of light [75]. Expansion of atomic lines results in an increase in the coefficient of absorption of light by the atoms, even well beyond the resonant frequency. Reference [76] suggests a linear increase in the width of the resonance level δ with gas pressure p (the mean lifetime of an electron at the $1/\delta$ level). The results have been confirmed experimentally in argon up to a pressure of approximately 200 mm Hg [77]. Reference [78] supports an expansion that is proportional to $\sqrt{p}$. The expansion in the lines can be determined in the main by the resonant energy transfer from atom to atom, and depends on the parameter $n\lambda\!\!\!^{-3}$, that is, on the number of atoms in a volume with linear dimensions of the order of the photon wavelength. In gas scintillators $n\lambda\!\!\!^{-3} \gg 1$ ($n \geq 10^{19}$ $1/cm^3$, $\lambda\!\!\!^{-} \sim 10^{-5}$ cm). Because of pair collisions with resonant energy transfer the shape of the line differs from the Lorentzian, and the excitation level can be shifted. Thus, the diffusion of light is intimately associated with the process involved in the migration of energy in collisions. The theoretical exposition of questions concerned with the migration of excitation energy in dense gases ($n\lambda\!\!\!^{-3} \gg 1$) is only beginning [79, 80]. Let us consider the role the migration of energy can have in gas scintillators.

/178

Capture of resonance radiation from atoms. The capture of resonance radiation from noble gas atoms, as has already been pointed out, facilitates the pumping of the energy of excited atoms to the four lower levels of excitation, or to the two lower resonance levels, which turn out to be the metastable levels, in essence. Only after excited noble gas molecules have been formed is it possible to convert the energy thus stored into nonresonant light.

The diffusion of light from the lower resonance levels lasts for tens and hundreds of microseconds when the pressure is about 100 mm Hg and the distance is 1 cm [72], and this corresponds to the time required for the formation of molecules in accordance with the Eq. (2) reaction. The diffusing light will be propagated more slowly at atmospheric pressure, with the rate at which the Eq. (2) reaction will take place being proportional to p^2, as we know. So it is obviously impossible to record resonance light in gas scintillators.

Resonance excitation energy transfer from atoms in collisions. The excitation energy stored on the lower resonance levels of the noble gas atoms is transferred rapidly from atom to atom in double collisions with cross section $\lambda\!\!\!^{-2}$ prior to the formation of molecules. This is why the lifetime of an excited atom, τ, in a dense gas is much shorter than the lifetime of an isolated atom. Migration of excitation energy (without photon deexcitation) increases the probability of energy transfer to the impurities contained in the gas. This takes place because of the expansion in the excitation level ($1/\tau$), that is resonance energy transfer to the impurity (cross section $\lambda\!\!\!^{-2}$) becomes possible, or because of the increase in the probability of an interaction between an atom (molecule) of the impurity and the excitation energy "diffused" in volume $\lambda\!\!\!^{-3}$.

Experimental data confirm the great magnitude of the energy interception cross section by impurities. Assuming a speed of deexcitation of the excited atoms of the basic gas of some 10^{-7} second (molecules form in approximately this time at normal pressure), we can find the cross section for interception of excitation energy by the impurities (atom velocity is approximately $3 \cdot 10^4$ cm/sec) in the examples considered earlier (normal pressure) /179

$$Kr + 0.02\%\ Xe\ [46];\ \sigma \geqslant 10^{-13}\ cm^2;$$
$$He + 10^{-3}\%\ Ne\ [27];\ \sigma \geqslant 10^{-12}\ cm^2;$$
$$Ar + 0.002\%\ Hg\ [14];\ \sigma \geqslant 10^{-12}\ cm^2.$$

A similar cross section ($\gtrsim 10^{-12}$ cm^2) is obtained for nitrogen intercepting all the excitation energy in noble gases when the concentration is some 10^{-3}% [61]. Accordingly, energy interception by impurities takes place more rapidly than can be explained by conventional collisions of atoms with gas kinetic cross sections ($\sim 10^{-15}$ cm^2). Energy interception time by the impurity when the concentrations of the latter are about 10^{-5} is obviously less than 10^{-7} second, and less than 10^{-8} second when the concentration is 10^{-4}.

The capture of molecular light. Since the shortwave limit of the noble gas molecular continuum coincides with the wavelength of the resonance line for the atom, the expansion of this line with increase in gas pressure should result in the diffusion of molecular light.

References [63, 81, 82] note a sharp reduction in the intensity of the light passing through xenon in the wavelengths near the resonance line for atomic xenon, 1470 Å. The reduction in intensity encompasses more and more of the spectrum with increase in xenon pressure (40 Å at normal pressure and about 100 Å when p = 20 atm). Thus, the shortwave section of the light of the molecular continuum is captured in the gas.

Absorption of light by noble gas molecules. Noble gas molecules can form elsewhere than along the track of an ionizing particle. The formation of molecules of two atoms (dimers) with a binding energy of about 0.01 ev is possible when unexcited atoms of noble gas X collide. Reference [83] found that the number of molecules of xenon per unit volume (when T = 300°K) was proportional to $2.16 \cdot 10^{-22}$ n, where n is the number of atoms of xenon per cm^3. The concentration of molecular xenon is about 1% at normal pressure. Molecular xenon scatters ultraviolet radiation (the scattering cross section is approximately $5 \cdot 10^{-22}$ cm^2 for the line 1215.7 Å). Absorption of light by noble gas molecules results in an additional expansion in the spectral lines [84].

Noble gas molecules can absorb the light from excited molecules, and this leads to the diffusion of the light from that part of the molecular continuum that will not absorb many of the gas atoms. The absorption of light by dimers /180 should increase with increase in pressure, and with decrease in gas temperature, because the probability of dissociation of the molecules decreases with decrease in temperature (the dissociation energy for a molecule of xenon is

about 0.03 ev [83]). The formation of trimers, X_3, or of heavier molecules (X_4 and other polymers) is possible when excited dimers collide with noble gas atoms. Since polymer ionization potential obviously will be reduced with increase in molecular weight, excited polymers can be readily ionized [the Eqs. (23) and (24) reactions]. The ions X_3^+ and X_4^+ will be formed at some distance from the particle track, where the concentration of electrons is low, and where, as a result, the electron-ion recombination is insignificant, when there is diffusion of molecular light. Therefore, the formation of the ions X_3^+ and X_4^+ is equivalent to the destruction of the diffusing photons.

g. Electron bremsstrahlung. Electrons forming along the track of an ionizing particle emit bremsstrahlung light during neutral atom dispersion [5, 85]. The intensity of the bremsstrahlung light decays rapidly over a period of time that is of the order of magnitude of thermalization time [59]. However, the electrons can acquire additional energy during superelastic collisions, so bremsstrahlung can last for the period of time required for electron recombination. The spectral composition of bremsstrahlung light can be characterized by a broad continuum. Intensity in the band of short wavelengths decays to photon energy below the first level excitation energy for a noble gas atom. This comes about because the number of electrons with energies exceeding the energy of the first excitation level for the atoms decays rapidly because of inelastic energy losses during collisions with atoms of the gas (10^{-9} to 10^{-10} sec at normal pressure). Further shift of the shortwave limit for bremsstrahlung toward the long wavelength side, together with simultaneous reduction in intensity, takes place because of elastic losses of energy by the electrons during thermalization (about 10^{-6} second). The intensity of bremsstrahlung light does not depend on photon energy to any great extent in the longwave band [5], but does depend very heavily on electron energy in the shortwave band.

G. A. Askar'yan [85] evaluated the output of bremsstrahlung light from a gas scintillator. The percentage of bremsstrahlung light is a few percentage points of the observed scintillation light. The rise time for the intensity of bremsstrahlung light is determined by the time required for the ionizing particle to pass through the gas.

3. Gas Scintillator Properties

a. Scintillation efficiency

The number of photons in a scintillation flash. The efficiency with which ionizing particles is recorded is determined by the number of photons occurring after the particle has passed through the scintillator. Reference [86] (see also [3]) evaluated the distribution of energy lost by a charged particle in the gas to ionization and excitation of atoms, as well as that carried off by electrons during ionization. In all noble gases approximately 60% of the energy is expended in ionization of atoms, 20% is carried off by the electrons (mean electron energy is about 0.3I, where I is the atom ionization potential), and 20% of the energy is expended in exciting the atoms. Since the energy for exciting noble gas atoms is of the order of 10 ev, a gas scintillator can emit about 10^4 photons per 1 MeV of energy lost by the ionizing particle (recombination and quenching not taken into consideration). What usually is observed is a value of 10^3 photons/MeV [3], and this is proof of the significant role played by the processes involved in quenching excited atoms (molecules) in gas scintillators.

The scintillation efficiency of various noble gases. The scintillation efficiency of a noble gas, while dependent on the type of gas, is also dependent on gas pressure, purity, and temperature, light recording time, and the ability of the particles recorded to ionize. This is why the relative scintillation efficiencies of noble gases, measured for a variety of conditions, can be very different from each other

Xe	Kr	Ar	Ne	He	90% He + 10% Xe	Literature
1	0.52	0.16	0.043	0.33	1.2	[16]
1	1	0.3	0.3	0.3	1.2	Our data

Despite some scattering, it will be seen that scintillation efficiency increases with increase in the atomic number for the gas. It seems that this is associated with the change in the rate at which excited molecules are formed, the deexcitation of which determines scintillation efficiency. The high degree of efficiency of scintillation of a mixture made up of 90% He + 10% Xe can be

explained by the efficient interception of the helium excitation energy by the xenon, with deexcitation of the xenon molecules relatively low because of the small concentration of xenon atoms (see section 2e and f). /182

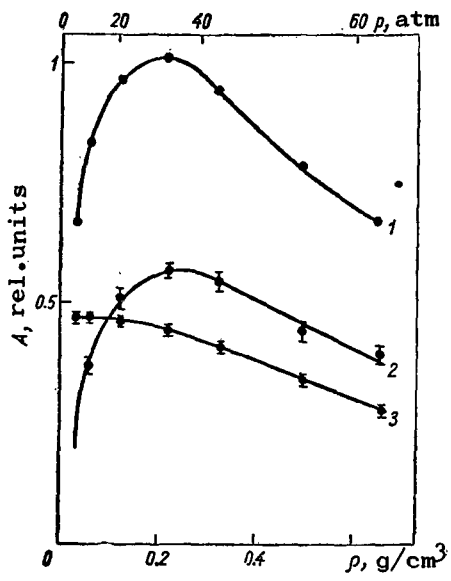

Figure 2. Scintillation amplitude, A, in terms of xenon density ρ (ionization by α-particles):

1 - total scintillation amplitude; 2 - recombination amplitude of scintillations depending on the field of the component; 3 - recombination amplitude of scintillations independent of the field of the component. Amplitudes are shown in relative units.

The contribution of electron-ion recombination. The data from Figure 1 can be used to evaluate the contribution made by recombination to the amplitude of a scintillation flash. Recombination will yield from 20 (neon) to 50% (xenon) of the light at pressures of about 10 atm along the track of an η-particle with an energy of 5.15 MeV. Figure 2 shows the change that takes place in scintillation amplitude in xenon in terms of gas density (curve 1). Curves 2 and 3 were obtained by extrapolation using the results of ionization measurements [31]. Let us now turn to the identical relative decay of both components with increase in xenon density, something that obviously points to the sameness of the quenching processes for both components. Since excited molecules form during electron-ion recombination, the sameness of the quenching processes for both components in turn means that the principal part of the scintillation quenching processes at high pressures takes place in the excited molecule stage, X_2^*.

Dependence of light yield on energy absorbed by the gas. The linearity of the light yield from gas scintillators, that is, the proportionality of the amplitude of the light flash of energy absorbed by the gas can be arrived at in the following cases:

(1) there is no recombination along the track (low gas pressures, particles with poor ionizing capabilities $\eta < 2 \cdot 10^5$ cm^{-1});

(2) recombination makes a maximum contribution to the scintillation amplitude (high gas pressure, particles with good ionizing capabilities

$\eta \gg 2 \cdot 10^5$ cm^{-1});

(3) particles have equal ionizing capabilities (arbitrary gas pressure); /183

(4) recombination light is not recorded. This can be done by simply recording the fast component of the scintillation (see c of this section).

It is possible to violate the linearity associated with the various contributions of the recombination components in the scintillation for particles with different ionizing capabilities when the conditions formulated above cannot be satisfied. Maximum flash amplitude is observed with strong ionizing particles when energy losses in the gas are identical. This is the type of behavior pattern obtained for electrons and α-particles [62, 87], and for α-particles and the fission fragments of U^{234} [22, 88, 89]. Moreover, reference [87] found that the nonlinearity of the light output increased in a mixture of He + Xe with increase in the xenon pressure, and reference [22] indicates that nonlinearity can be corrected by applying an electric field to the gas.

Dependence of the amplitude of the scintillation flash on gas pressure. Two processes, the rate at which excited molecules are formed, and the effectiveness of the processes involved in the deexcitation of atoms and molecules, determine the amplitude of the scintillation flash for the same ionization density, but different gas pressures (loss of energy by the particle to the gas the same).

Molecules form slowly in the low pressure region (see section 2a), and the excitation energy is intercepted and quenched by an impurity (see section 2e). The rate at which molecules form will increase with increase in gas pressure, and the energy capture by the impurities takes place with less efficiency. Scintillation amplitude increases too. But with a further increase in pressure comes the deexcitation processes associated with the capture of molecular light by the atoms and the absorption of light by the noble gas molecules. It is possible for the processes involved in molecule deexcitation in collisions to become substantial. The amplitude of scintillation light now should decrease slowly with increase in gas pressure (see Figure 2).

Change in pressure in a gas scintillator usually is accompanied by change in ionization density along the track. Let us, therefore, see how the re-

combination component behaves with increase in gas pressure. There is no recombination at low pressures. The recombination component increases with increase in pressure (see section 2c), then drops slowly because the deexcitation processes described above and forming during the recombination of noble gas molecules are included. The experimental data presented in Figures 1 and 2 thus can be explained very simply.

b. The spectral composition of scintillation light. /184

The spectral composition of scintillation light, as has already been noted, coincides with the molecule spectrum. Most of the scintillation light (90%) is vacuum ultraviolet ($\lambda \leq 2000$ Å). Impurities with low excitation levels, contained in a noble gas, can make a significant contribution to the optical portion of the spectrum. An impurity concentration of about 10^{-4} apparently ensures total interception of energy by the impurity (see section 2f) at normal pressure. It was at this concentration that reference [14] noted great brilliance of their lines, but noble gas molecular continuums were not noted.

Since excited molecules are formed upon the recombination of electrons with ionized noble gas molecules, the spectral composition of the recombination light coincides with the molecule spectrum, and this has been proven experimentally [31].

c. Deexcitation time for a gas scintillator. A pure gas can be characterized by intensive luminescence of noble gas molecules. The rate at which the molecules form is completely determined by gas pressure, so the probability of the interception of excitation energy by the impurity prior to the formation of a noble gas molecule will be reduced with increase in gas pressure, given the same partial pressure of the impurity. Accordingly, a gas can appear to be "pure" at increased pressure, and "contaminated" at reduced pressure, even if the measurement is made by the same installation. In a "pure" noble gas the impurities effect deexcitation only in terms of the deexcitation of the noble gas molecules. Thus, excitation time for a gas scintillator with no recombination will be determined by the time required to form the excited molecules, their deexcitation time, and the time required to diffuse part of the molecular light through the gas.

The time required to form excited molecules is proportional to $1/n^2$, and

is equal to 10^{-6} to 10^{-8} second at normal pressure (see section 2a). The time required to form helium molecules is 10^{-6} to 10^{-7} second [24] at pressures close to atmospheric, and changes in accordance with the $1/n^2$ law, while the deexcitation time for the He_2^* molecule is about 10^{-5} second. Our results, based on a study of xenon deexcitation time, agree with the molecule deexcitation time of about 10^{-7} second. Thus, deexcitation time for the scintillator is determined by the molecule formation time at low pressures. At high pressures the molecule formation time can be very short (the rise time for the amplitude /185 of a light pulse in xenon at a pressure of 10 atm is about 10^{-9} second), and the duration of the luminescence is determined by the molecule deexcitation time (approximately 10^{-6} second). This time will decrease somewhat with increase in pressure because of inelastic collisions.

Scintillator deexcitation will be much more rapid if only the optical portion of the spectrum ($\lambda > 2000$ Å), is recorded because in such case only the electron bremsstrahlung (about 10^{-9} second), and the light occurring with transition of the electrons between the excitation levels for the atoms (approximately) 10^{-8} second), are recorded. A part of the optical spectrum occurring during the formation of molecules can involve the luminescence of the scintillator in the optical region for molecule formation time. The deexcitation time for a noble gas with an impurity with low-lying excitation levels is almost completely determined by the rate of interception of the energy by the impurity, and can be very short (about 10^{-9} second). Rapid deexcitation of gas scintillators has been observed in [13, 83, 87, 90].

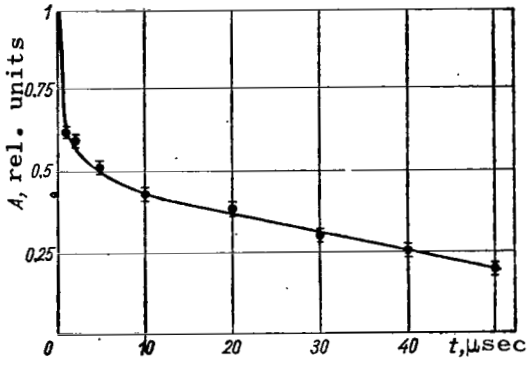

Figure 3. Decay in the number of electrons in xenon in terms of time.

The xenon (density 0.3 g/cm^3) has been ionized by a pulsed beam of X-rays, The pulse width was less than 1 μsec and the energy of the photoelectrons was less than 60 KeV.

Time required for the recombination of electrons and ions. The Eqs. (18) - (21) reactions take place along the track of an ionizing particle during the formation of plasma (see section 2b, c), and the result is the formation of excited noble gas molecules. We found the number of electrons

remaining along the track at any moment in time by experimental means [31] /186
(Figure 3). The xenon was ionized by X-rays with photon energy less than 60 KeV. As will be seen from Figure 3, initially recombination is quite rapid, then is extraordinarily slow. Recombination time is longer than 10 μsec. There was little change in the nature of the recombination when pressure was changed from 10 to 60 atm. The reason for so little change in recombination when the gas pressure was changed from 10 to 60 atm requires further study.

4. Conclusion

So, the main processes in gas scintillators apparently can be said to be:

(a) the formation of excited molecules and ionized molecules;

(b) electron-ion recombination in the plasma forming along the track of the ionizing particle;

(c) deexcitation of noble gas atoms and molecules.

These processes, as we have seen, explain the principal anomalies of scintillation in noble gases. It is obvious that study of the processes taking place in gas scintillators is very essential if gas scintillation counters are to be used to record particles. Moreover, gas scintillators can be useful in the study of the processes involved in the collisions of electrons and atoms in noble gases, and since the scintillation of noble elements can be observed in the liquid and solid phases as well [3, 49, 60], study of scintillation can help us to a better understanding of the nature of the electromagnetic interactions that occur in a substance.

REFERENCES

1. Brocklehurst, B., Atomic Energy Research Establishment Report, C/R 2669, 1963, pp. 1-55.
2. Teyssier, I. L. and Blanc, D., L'onde electrique, Vol. 44, 1964, pp. 446, 458.
3. Birks, I. B., The Theory and Practice of Scintillation Counting, Pergamon-press, 1964.
4. Hastead, D., Fizika atomnykh stolknoveniy, [The Physics of Atomic Collisions], Translated from the English, Mir Press, Moscow, 1965.
5. Zel'dovich, Ya. B. and Rayzer, Yu. P., Fizika udarnykh voln i vysoko-temperaturnykh gidrodinamicheskikh yavleniy, [The Physics of Shock Waves and of High-Temperature Hydrodynamic Phenomena], Nauka Press, Moscow, 1966.
6. MacDaniel, I., Protsessy stolknoveniy v ionizovannykh gazakh, [Collision Processes in Ionized Gases], Translated from the English, Mir Press, Moscow, 1967.
7. Curie, M., Traite de radioactivite, [Treatise on Radioactivity], Gauthier-Villars, Paris, 1910.
8. Stark, J. Z., Phys., Vol. 7, 1906, p. 892.
9. Pohl, R. J., Radioaktivitat, Vol. 4, 1907, p. 100.
10. Grun, A. E. and Schopper, E. Z., Naturforschung, Vol. 6a, 1951, p. 698.
11. Eggler, C. and Huddleston, C. M., Phys. Rev., Vol. 95, 1954, p. 600.
12. Avivi, P. and Cohen, S. G., Phys. Rev., Vol. 108, 1957, p. 972.
13. Koch, L., Acta Electronica, Vol. 5, No. 1, 1958, p. 103.
14. Koch, L. J., Phys. Radium, Vol. 21, 1960, p. 169.
15. Koch, L., Thesis, University of Paris, Rpt. CEA 1532, CEN Saclay, 1960.
16. Northrop, J. A. and Gursky, J. C., Nucl. Instr., Vol. 3, 1958, p. 207.
17. Tuxen, O. Z., Physik, Vol. 103, 1936, p. 463. /187
18. Biondi, M. A. and Brown, S. C., Phys. Rev., Vol. 76, 1949, p. 1697.
19. Biondi, M. A. and Holstein, T., Phys. Rev., Vol. 82, 1961, p. 962.
20. Greinacher, H. Z., Phys., Vol. 47, 1928, p. 344.
21. Audubert, R. and Lormeau, S., C.r.Acad. sci., Paris, Vol. 228, 1949, p. 318.
22. Tavendale, A. J., Rev. Sci. Instr., Vol. 32, 1961, p. 1398.
23. Easterling, R. and Lipman, N., Pribory dlya nauchnykh issledovaniy, No. 4, 1965.
24. Takanashi, T., et al., Phys. Lett., Vol. 23, No. 5, 1966.
25. Kalashnikova, V. I. and Kozodayev, M. S., Detektory elementarnykh chastits, [Elementary Particle Detectors], Nauka Press, Moscow, 1966, pp. 26-30.

26. Strickler, T. D. and Arakawa, E. T., J. Chem. Phys., Vol. 41, 1964, p. 1783.

27. Dondes, S., et al., Rad. Res., Vol. 27, 1966, p. 174.

28. Brocklehurst, B., Trans. Faraday Soc., Vol. 530, 1967, pp. 63, 274.

29. Kugler, E., Ann. Phys., Vol. 14, No. 3-4, 1964.

30. Bennett, W. R., Ann. Phys., Vol. 18, No. 3, 1962, p. 367.

31. Dolgoshein, B. A., et al., Zh. Eksperim. i. teor. fiz., Vol. 56, 1969, p. 1152.

32. Biondi, M. A., Phys. Rev., Vol. 83, 1951, p. 1078.

33. Phelps, A. V. and Brown, S. C., Phys. Rev., Vol. 86, 1952, p. 102.

34. Oskam, H. J., Phil. Res. Rep., Vol. 13, 1958, pp. 335, 401.

35. Beaty, E. C. and Patterson, P., 6th International Conference on Ionization Phenomena in Gases SERMA, Vol. 1, Paris, 1963, p. 289.

36. Biondi, M. A., Phys. Rev., Vol. 129, No. 3, 1963, p. 1181.

37. Samson, J. A. R. and Gairns, R. B. J., Opt. Soc. Amer., Vol. 56, No. 8, 1966, p. 1140.

38. Meyerott, R., Phys. Rev., Vol. 70, 1946, p. 671.

39. Phelps, A. V. and Molnar, J. P., Phys. Rev., Vol. 89, No. 6, 1953, p. 1202.

40. Colli, L., Phys. Rev., Vol. 95, No. 4, 1954, p. 892.

41. Phelps, A. V., Phys. Rev., Vol. 99, 1955, p. 1307.

42. Turner, R., Phys. Rev., Vol. 158, No. 1, 1967, p. 121.

43. Arnot, F. L. and McEwen, M. B., Proc. Roy. Soc., Ld., Vol. A 166, 1938, p. 543.

44. Hornbeck, J. A. and Molnar, J. P., Phys. Rev., Vol. 84, No. 4, 1951, p. 621.

45. Melton, C. E. and Hamill, W. H., J. Chem. Phys., Vol. 41, 1964, p. 1469.

46. Kaul, W. and Taubert, R. Z., Naturforsch., Vol. 17a, 1962, p. 88,

47. Morgulis, N. D. and Polushkin, I. N., Zh. tekh. fiz., Vol. 36, Issue 3, 1966, p. 542.

48. Cooper, C. D., et al., J. Mol. Spectr., Vol. 7, 1961, p. 223.

49. Hereford, F. L. and Moss, F. E., Phys. Rev., Vol. 141, No. 1, 1966, p. 204.

50. Loeb, L. B., Basic Processes of Gaseous Electronics, University of California Press, 1960.

51. Fergusson, E. E., et al., Phys. Rev., Vol. 138, No. 2A, 1965, p. 381.

52. Mosburg, E. R., Phys. Rev., Vol. 152, No. 1, 1966, p. 166.

53. Gusinow, M. A., et al., Phys. Rev., Vol. 149, No. 1, 1966, p. 91.

54. Gerber, R. A., et al., Phys. Lett., Vol. 19, No. 8, 1966, p. 656.

55. Atomnyye i molekukyarnyye protsessy, [Atomic and Molecular Processes], Translated from the English, Editor D. Bates, Mir Press, Moscow, 1964.

56. Pitayevskiy, L. P., Zh. eksperim. i teor. fiz., Vol. 42, 1962, p. 1326.

57. Gurevich, A. V. and Pitayevskiy, L. P., Ibid, Vol. 46, 1964, p. 1281.

58. Massey, G. and Barkup, E., Elektronnyye i ionnyye stolknoveniya, [Electron and Ion Collisions], Translated from the English, Mir Press, Moscow, 1967.

59. Brodskiy, V. B., et al., Zh. tekhn. fiz., Vol. 36, No. 4, 1966, p. 640.

60. Dolgoshein, B. A., et al., Pis'ma ZhETF, Vol. 6, 1967, p. 755.

61. Sayres, A. and Wu, C. S., Rev. Sci. Instr., Vol. 28, No. 10, 1957.

62. Shamu, R. E., Nucl. Instrum. Methods, Vol. 14, No. 3, 1961, p. 297.

63. Wilkinson, P. G. and Tanaka, Y. J., Opt. Soc. Amer., Vol. 45, No. 5, 1955.

64. Zaydel', A. N. and Shreyder, Ye. Ya., Spektroskopiya vakuumnogo ul'trafioleta, [Spectroscopy of Vacuum Ultraviolet], Nauka Press, Moscow, 1967.

65. Prince, J. F. and Robertson, W. W., J. Chem. Phys., Vol. 45, No. 7, 1966, p. 2577.

66. Ingraham, J. C. and Brown, S. C., Phys. Rev., Vol. 138, No. 4A, 1965, p. 1015. /188

67. Phelps, A. V., Phys. Rev., Vol. 114, No. 4, 1959, p. 1011.

68. Mitchell, A. C. G. and Zemansky, M. W., Resonance Radiation and Excited Atoms, New York, 1962.

69. Biberman, L. M., Zh. eksperim. i teor. fiz., Vol. 17, 1947, p. 416.

70. Biberman, L. M., Ibid., Vol. 59, 1948, p. 659.

71. Holstein, T., Phys. Rev., Vol. 72, 1947, p. 1212.

72. Holstein, T., Ibid., Vol. 83, 1951, p. 1159.

73. Veklenko, B. A., Zh. eksperim. i teor. fiz., Vol. 36, 1959, p. 204.

74. Barrat, J., Phys. Radium, Vol. 20, 1959, pp. 541, 633, 657.

75. Sobel'man, I. I., Uspekhi fiz. nauk, Vol. 54, 1954, p. 551.

76. Vlasov, A. A. and Fursov, V. S., Zh. eksperim. i teor. fiz., Vol. 9, 1939, p. 783.

77. Fursov, V. S., et al., Dokl. AN SSSR, Vol. 101, No. 3, 1955, p. 453.

78. Reck, G. P., et al., Phys. Rev., Vol. 137, No. 3A, 1965, p. 683.

79. Kazantsev, A. P., Zh. eksperim. i teor. fiz., Vol. 51, 1966, p. 1751.

80. Vdovin, Yu. A. and Galitskiy, V. M., Ibid., Vol. 52, 1967, p. 1345.

81. McLennan, J. C. and Turnbull, R., Proc. Roy. Soc., Ld., Vol. A 129, 1930, p. 266.

82. McLennan, J. C. and Turnbull, R., Proc. Roy. Soc. Ld., Vol. A 139, 1933, p. 683.

83. Shardanand, Phys. Rev., Vol. 160, No. 1, 1967, p. 67.

84. Wilkinson, P. G. J., Quant. Spectr. Rad. Transf., Vol. 5, 1965, p. 503.

85. Askar'yan, G. A., Zh. Eksperim. i teor. fiz., Vol. 39, 1960, p. 211.

86. Platzman, Intern. J. Appl. Rad. Isotopes, Vol. 10, 1961, p. 116.

87. Jenkin, J. G.,and Shamu, R. E., Nucl. Instrum. Methods, Vol. 34, 1965, p. 116.

88. Boicourt, G. and Brolley, I., Rev. Sci. Instru., Vol. 25, 1954, p. 1218.

89. Tavendale, A. J., Proc. Phys. Soc., Vol. 79, 1962, p. 652.

90. Schmidt, K. Z., Naturforsch., Vol. 11a, 1956, p. 1023.

Translated for the National Aeronautics and Space Administration
under contract No. NASw-2038 by Translation Consultants, Ltd.,
944 South Wakefield Street, Arlington, Virginia 22204.

☆ U. S. GOVERNMENT PRINTING OFFICE : 1972 720-403/321

"The aeronautical and space activities of the United States shall be conducted so as to contribute . . . to the expansion of human knowledge of phenomena in the atmosphere and space. The Administration shall provide for the widest practicable and appropriate dissemination of information concerning its activities and the results thereof."

—NATIONAL AERONAUTICS AND SPACE ACT OF 1958

NASA SCIENTIFIC AND TECHNICAL PUBLICATIONS

TECHNICAL REPORTS: Scientific and technical information considered important, complete, and a lasting contribution to existing knowledge.

TECHNICAL NOTES: Information less broad in scope but nevertheless of importance as a contribution to existing knowledge.

TECHNICAL MEMORANDUMS: Information receiving limited distribution because of preliminary data, security classification, or other reasons.

CONTRACTOR REPORTS: Scientific and technical information generated under a NASA contract or grant and considered an important contribution to existing knowledge.

TECHNICAL TRANSLATIONS: Information published in a foreign language considered to merit NASA distribution in English.

SPECIAL PUBLICATIONS: Information derived from or of value to NASA activities. Publications include conference proceedings, monographs, data compilations, handbooks, sourcebooks, and special bibliographies.

TECHNOLOGY UTILIZATION PUBLICATIONS: Information on technology used by NASA that may be of particular interest in commercial and other non-aerospace applications. Publications include Tech Briefs, Technology Utilization Reports and Technology Surveys.

Details on the availability of these publications may be obtained from:

SCIENTIFIC AND TECHNICAL INFORMATION OFFICE

NATIONAL AERONAUTICS AND SPACE ADMINISTRATION

Washington, D.C. 20546